

Max-Planck-Institut für Metallforschung
Stuttgart

Electron Microscopic Investigations of the Bonding Behaviour of Metals on SrTiO_3 Substrates

Klaus van Benthem

Dissertation
an der
Universität Stuttgart

Bericht Nr. 120
Juni 2002

Electron Microscopic Investigations of the Bonding Behaviour of Metals on SrTiO₃ Substrates

Von der Fakultät Chemie der Universität Stuttgart
zur Erlangung der Würde eines
Doktors der Naturwissenschaften (Dr. rer. nat.)
genehmigte Abhandlung

vorgelegt von

KLAUS VAN BENTHEM

aus Münster

Hauptberichter: Prof. Dr. Dr. h.c. M. Rühle

Mitberichter: Prof. Dr. F. Aldinger

Tag der Einreichung: 26. Februar 2002

Tag der Prüfung: 3. Juni 2002

MAX-PLANCK-INSTITUT FÜR METALLFORSCHUNG STUTTGART

2002

Bei Beobachtung sind selbst die Irrtümer nützlich,
indem sie aufmerksam machen
und dem Scharfsichtigen Gelegenheit geben,
sich zu üben.

J. W. von Goethe, 1784.

... dedicated to Pia

Parts of this thesis were published in the following papers:

- K. van Benthem, R. H. French, W. Sigle, C. Elsässer, and M. Rühle
Valence electron energy-loss study of Fe-doped SrTiO_3 and a $\Sigma 13$ boundary: electronic structure and dispersion forces
Ultramicroscopy **86**, 303 (2001).
- K. van Benthem, C. Scheu, W. Sigle, and M. Rühle
Electronic structure investigations of metal/ SrTiO_3 interfaces
Proc. of EUREM-12, Brno, Czech Republic, P421 (2000).
- K. van Benthem, R. H. French, and C. Elsässer
Bulk electronic structure of SrTiO_3 : Experiment and theory
J. Appl. Phys. **90** (2001) 6156.
- K. van Benthem, C. Elsässer, C. Scheu, W. Sigle, and M. Rühle
Electronic structure investigations of metal/ SrTiO_3 interfaces using EELS
Microscopy and Microanalysis **7**, Long Beach, Ca., USA (2001).
- K. van Benthem, W. Sigle, S. Krämer, and M. Rühle, Structural and Chemical Analysis of Materials with High Spatial Resolution
Mikrochimica Acta **138** (2002) 181.

Contents

List of Abbreviations	8
Abstract	10
Zusammenfassung	13
1 Introduction	17
2 Basics	20
2.1 Interface Structures	20
2.1.1 Orientation Relationships	20
2.1.2 Lattice Mismatch	21
2.1.3 Coherence State between Film and Substrate	21
2.2 Wetting Mechanisms	22
2.3 Materials Properties	25
2.3.1 Bulk SrTiO ₃	25
2.3.2 Palladium	27
2.3.3 Nickel	28
2.3.4 Chromium	28
2.4 Bonding Mechanisms	29
2.4.1 Ionic Bonding	29
2.4.2 Covalent Bonding	29
2.4.3 Metallic Bonding	29
3 Literature Survey	31
3.1 Metals on Surfaces of Oxide Substrates	31
3.1.1 Metals/SrTiO ₃	32
3.1.2 Pd/Ceramic Interfaces	37
3.1.3 Ni/Ceramic Interfaces	41
3.1.4 Cr/Ceramic Interfaces	42
3.2 Spatially resolved EELS/ELNES	44
3.3 Goal of the Thesis	46

4	Methods	48
4.1	Experimental Details	48
4.1.1	Scanning Transmission Electron Microscopy	48
4.1.2	Electron Energy-Loss Spectroscopy	54
4.1.3	Spatial Difference Technique	59
4.2	Computational Details	63
4.2.1	Local Density Functional Theory	64
4.2.2	The Mixed-Basis Pseudopotential Program	66
4.2.3	Multiple Scattering Approach	69
5	Specimen Preparation	72
5.1	Molecular Beam Epitaxy	72
5.2	TEM-Specimen Preparation	73
6	Bulk SrTiO₃	79
6.1	VEELS-Investigations	79
6.1.1	VUV Spectroscopy and Spectroscopic Ellipsometry	81
6.1.2	VEELS-Results	84
6.1.3	Band structure calculations	85
6.2	Discussion of the VEELS Data	87
6.2.1	UV optical Constants and Band Gaps	88
6.2.2	Valence Electron Counts in SrTiO ₃	88
6.2.3	Transitions from the Upper Valence Band	89
6.2.4	Transitions from the Lower Valence Band	89
6.2.5	Shallow Core Level transitions	89
6.2.6	Schematic Energy Level Description	90
6.2.7	Comparison to Results from the Literature	90
6.2.8	Comparison of VEELS and VUV Spectroscopy	91
6.3	EELS-Ionization Edges	92
6.4	Core-hole-Effects in SrTiO ₃	95
6.4.1	LDFT-based Calculations	96
6.4.2	Multiple Scattering-based Calculations	100
6.5	Discussion of the Core-hole-Effects	104
7	The Pd/SrTiO₃ Interface	111
7.1	Experimental Results	111
7.1.1	Diffraction and Imaging Studies	111
7.1.2	EELS Results	116
7.2	Computational Results	121
7.3	Discussion	131
7.3.1	Interface Structure	131
7.3.2	ELNES-Analysis: Experiment and Theory	132

7.3.3	Bonding Analysis	138
8	The Ni/SrTiO₃ Interface	146
8.1	Experimental Results	146
8.1.1	Diffraction and Imaging Studies	146
8.1.2	EELS Results	148
8.2	Computational Results	153
8.3	Discussion	155
8.3.1	Interface Structure	155
8.3.2	ELNES-analysis: Experiment and Theory	156
9	The Cr/SrTiO₃ Interface	160
9.1	Experimental results	160
9.1.1	Diffraction and Imaging Studies	160
9.1.2	EELS Results	162
9.2	Discussion	166
9.2.1	Interface Structure	167
9.2.2	ELNES-analysis	168
10	Final Discussion	170
10.1	Bulk SrTiO ₃	170
10.2	The metal/SrTiO ₃ Interfaces	172
A	Image Formation Theory in the STEM	175
B	Characterization of the PEELS Detectors	182
	List of Tables	186
	List of Figures	186
	Bibliography	190
	Epilogue	205
	Curriculum vitae	207

List of Abbreviations

ADF	=	Annular Dark Field
AEM	=	Analytical Electron Microscopy
AES	=	Auger Electron Spectroscopy
AFM	=	Atomic Force Microscopy
CBED	=	Convergent Beam Electron Diffraction
CCD	=	Charge-Coupled Device
CTEM	=	Conventional Transmission Electron Microscopy
DOS	=	Density of States
EDXS	=	Energy Dispersive X-Ray Spectroscopy
EEL	=	Electron Energy-Loss
EELS	=	Electron-Energy-Loss Spectroscopy
ELNES	=	Energy-Loss Near-Edge Structure
EXAFS	=	Extended X-Ray Absorption Fine Structure
GIXS	=	Grazing Incidence X-ray Scattering
HAADF	=	High Angle Annular Dark Field
HeAS	=	He-atom scattering
HRTEM	=	High Resolution Transmission Electron Microscopy
LDFT	=	Local Density Functional Theory
MBE	=	Molecular Beam Epitaxie
PEELS	=	Parallel Electron Energy-Loss Spectrometer
PSF	=	Point Spread Function
RHEED	=	Reflection High Energy Electron Diffraction
SAD	=	Selectred Area Diffraction
SEELFS	=	Surface Extended Energy-Loss Fine Structure
SEM	=	Scanning Electron Microscopy
STEM	=	Scanning Transmission Electron Microscope
STM	=	Scanning Tunneling Microscopy
STS	=	Scanning Tunneling Spectroscopy
TEM	=	Transmission Electron Microscopy
UHV	=	Ultra High Vacuum
UPS	=	Ultra-Violet Photoemission Spectroscopy
VEELS	=	Valence Electron Energy-Loss Spectroscopy
VUV	=	Vacuum Ultra-Violet Spectroscopy
XPS	=	X-ray Photoelectron Spectroscopy

Abstract

The microscopic and electronic structure of interfaces between SrTiO_3 in its cubic phase and thin films of Pd, Ni and Cr have been investigated to gain insights into the bonding characteristics between the ceramic substrate and the different 3-d transition metals. The interfaces were investigated by various transmission electron microscopy (TEM) techniques, such as conventional TEM, high-resolution transmission electron microscopy (HRTEM), and electron energy-loss spectroscopy (EELS). The electronic structure of the different interfaces was analysed in terms of the electron energy-loss near-edge structures (ELNES). ELNES spectra are theoretically described in terms of the site and symmetry projected unoccupied densities of states. The inelastic scattering process within the electron microscope, which leads to the ELNES measurement, produces an electron-hole pair within the local bandstructure of the investigated material. This effect is called *core-hole effect* and can modify the local unoccupied densities of states. The influence of the core-hole effects on the local unoccupied band structure was investigated in detail for the Ti $L_{2,3}$ -edge, the O K-edge and the Sr $L_{2,3}$ -edge in bulk SrTiO_3 . A comparison of the experimental ELNES spectra to the calculated local symmetry projected unoccupied densities of states (PDOS) showed that consideration of the core-hole effects is crucial for the Ti $L_{2,3}$ -edge and the O K-edge, but can be neglected for the Sr $L_{2,3}$ -edge within the current limits of experimental energy resolution.

The valence electronic structure of bulk SrTiO_3 was investigated in terms of interband transitions between the occupied valence bands and the unoccupied conduction bands. The interband transition strength is calculated from the complex dielectric function, which can be extracted from the low energy regime in energy-loss spectra. By a comparison of the interband transition strength to calculated densities of states, assignments of the initial and final states for the observed excitations became possible. In addition, it is demonstrated how optical properties can be determined from valence electron energy-loss spectroscopy (VEELS). Results are compared to experimental data measured by R.H. French using optical spectroscopy methods, such as spectroscopic ellipsometry and vacuum ultraviolet spectroscopy [van Benthem, 2001a] [van Benthem, 2001b]. The comparison showed that all three experimental methods revealed equivalent results, although the energy resolution in optical spectroscopy is by a factor 3 better than in VEELS.

Pd, Ni and Cr were deposited by molecular beam epitaxy on (100) SrTiO_3 surfaces. Prior to the deposition, the surface was prepared in such way that predominantly TiO_2 terminated (100) surfaces of SrTiO_3 are expected to occur [Kawasaki, 1994]. Richter [Richter, 2000] has performed growth studies for Pd on the (100) SrTiO_3 interface. He found that, for substrate temperatures of 650°C, Pd is growing epitaxially in a 3-dimensional mode as islands on the

SrTiO₃ surface. Pd islands showed a cube-on-cube orientation relationship, denoted by

$$100_{Pd} \parallel 100_{SrTiO_3}.$$

In the present study, by conventional TEM and HRTEM the mentioned results by Richter [Richter, 2000] were reproduced. Due to the corresponding lattice mismatch of $m = -0.4\%$, the Pd/SrTiO₃ interface showed a coherent interface structure under high-resolution imaging conditions in the TEM. However, experimental atomistic structure studies, such as qualitative HRTEM or atomic column resolved high-angle annular dark-field imaging, could not resolve whether the (100)SrTiO₃ surface is TiO₂ terminated or SrO terminated.

In a previous study Ochs and co-workers [Ochs, 2000] [Ochs, 2001] have developed an atomistic structure model of the Pd/SrTiO₃ interface using local density functional theory. In the present study, this atomistic structure model was used to calculate the local symmetry projected unoccupied densities of states for the Pd/SrTiO₃ interface. Due to an agreement of the experimentally determined interface specific O K-ELNES component with the calculated interfacial O p-projected DOS, the theoretically proposed structure model could be evaluated. In addition, the SrTiO₃ substrate was found to be TiO₂ terminated. The calculated occupied densities of states were then analysed to determine bonding characteristics at the Pd–SrTiO₃ interface. Covalent σ -bonds, formed by O p_z–Pd d_{z²} hybridizations, were found between O atoms of the substrate and Pd atoms. In addition, an amount of intermetallic bonding between Ti and Pd atoms was observed. The contact between the metal and the insulating SrTiO₃ substrate produced metal-induced states within the band gap region of the ceramic. The calculations showed that these metal-induced gap-states are present only within the interface and exponentially decay inside the bulk materials.

For Ni atoms, an epitaxial island growth was observed on the (100)SrTiO₃ surface for substrate temperatures of 650°C. Conventional TEM experiments revealed that the islands possessed a cube-on-cube orientation relationship to the (100) substrate surface:

$$100_{Ni} \parallel 100_{SrTiO_3}.$$

HRTEM investigations showed a semi-coherent interface structure with misfit dislocations accommodating the lattice mismatch of $m = -9.8\%$. In the interfacial region, additional contrasts could be observed, which may indicate a reaction between Ni and SrTiO₃. However, an extended reaction layer could not be resolved.

Since Ni atoms have a similar valence electron structure as Pd atoms, the atomistic structure model for the Pd/SrTiO₃ interface was taken to perform PDOS calculations for the Ni/SrTiO₃ interface. It was found, that the calculated PDOS do not agree with the experimental ELNES data, indicating that the used atomistic structure model is not valid for the Ni/SrTiO₃ interface. The interfacial O K-ELNES showed a similar line shape compared to reference spectra for stoichiometric bulk NiO. Thus, the formation of Ni–O bonds across the interface with a bonding character comparable to bulk NiO was concluded. In combination to HRTEM observations, the Ni–SrTiO₃ adhesion can be described by the formation of a 2-dimensional NiO phase within the interfacial plane. The formation of intermetallic Ni–Ti bonds across the interface cannot be neglected by the applied experimental techniques.

For the Cr/SrTiO₃ system, Cr was observed to grow 3-dimensionally on the (100)SrTiO₃ surface at a substrate temperature of 65°C. For a film thickness of 35 nm, conventional TEM investigations showed continuous Cr films on the substrate surface. For the Cr/SrTiO₃ interface, an epitaxial orientation relationship between the film and the substrate was found, denoted by

$$[110](100)_{Cr} \parallel 100_{SrTiO_3}.$$

HRTEM micrographs showed an abrupt interface with a semi-coherent structure, originating from the corresponding lattice mismatch of $m = +4.3\%$ between *bcc* Cr and the SrTiO₃ substrate. Since for the Cr/SrTiO₃ interface no atomistic structure model was achievable, calculations of the unoccupied densities of states were not performed. However, the bonding characteristics were analysed by an experimental ELNES analysis. The interface specific O K-ELNES component showed a similar line shape compared to chromium oxides of CrO_x composition, indicating the formation of Cr–O bonds across the interface. The Ti L_{2,3}-edge possessed a significant reduction in the nominal oxidation state for Ti at the interface, whereas the Cr L_{2,3}-edge reflected an oxidation of Cr and an electron transfer from Cr to oxygen. Therefore, the Cr–SrTiO₃ adhesion can be understood by a bonding between Cr and O, including a charge transfer and thus some ionic bonding contributions. Also for this system, intermetallic bonds between Cr and Ti could not be neglected.

Comparing the results obtained for the different metal/SrTiO₃ interfaces, it becomes obvious that the wetting of the (100)SrTiO₃ surface is best for Cr depositions near room temperature. The Cr–O bonds are suggested to be stronger than the Ni–O and Pd–O bonds, since not only a covalent but also a significant ionic bonding characteristic is present. The wetting by Ni is still stronger than for Pd, both deposited at the same substrate temperature of 650°C. This might be due to the formation of a 2-dimensional reaction layer between the film and the substrate in the case of the Ni/SrTiO₃ interface. An ionic bonding was not observed, neither for Ni nor for Pd.

Zusammenfassung

Der technologische Einsatz von Hochleistungs-Funktionskeramiken erfordert die Kontaktierung der Keramiken mittels verschiedener Metallelektroden. Die Eigenschaften der so gebildeten Metall/Keramik Grenzflächen beeinflussen somit erheblich die Leistungsfähigkeit der hergestellten Bauteile. Aufgrund ihrer hohen Dielektrizitätskonstanten erringen speziell elektrokeramische Materialien, wie z.B. Barium-Strontium-Titanat oder Blei-Zirkonat-Titanat, immer mehr technologisches Interesse als funktionelle Keramiken in mikroelektronischen Bauteilen [Setter, 2000]. Generell finden Titanate, die in der kubischen Perovskit-Struktur kristallisieren, Anwendung in Sensoren, Aktuatoren, Sperrschichtkondensatoren und in elektro-optischen Bauteilen [Hönlein, 1999] [Meixner, 1995]. Insbesondere SrTiO_3 , welches den prominentesten Vertreter der Perovskite darstellt, wird im Bereich der Katalyse [Henrich, 1978], der Sensortechnik [Meixner, 1995], aber auch als Substratmaterial für Hochtemperatur-Supraleiter verwendet [Chaudhari, 1987].

In der wissenschaftlichen Grundlagenforschung sind Metall/Keramik-Grenzflächen äußerst interessant, da an diesen Grenzflächen zwei unterschiedliche Materialien mit weitgehend unterschiedlichen physikalischen wie chemischen Eigenschaften aufeinander treffen. Keramiken sind meist gekennzeichnet durch ein gemischt ionisch-kovalentes Bindungsverhalten, wohingegen in Metallen die Bindungen durch delokalisierte Valenzelektronen beschrieben werden können. Somit ist das Bindungsverhalten an Metall/Keramik-Grenzflächen nicht durch einfache Bindungsprozesse zu beschreiben.

In der vorliegenden Arbeit wurde das Bindungsverhalten der Metalle Pd, Ni und Cr auf der (100) Oberfläche von SrTiO_3 mit elektronenmikroskopischen Methoden untersucht. Der Schwerpunkt lag hierbei auf der Untersuchung der elektronischen Strukturen der Grenzflächen hinsichtlich der Analyse des Bindungsverhaltens. Die Morphologie der mittels Molekularstrahlepitaxie aufgewachsenen Metallfilme wurde zunächst anhand der konventionellen Transmissionselektronenmikroskopie (TEM) untersucht. Die atomistische Struktur der erzeugten Grenzflächen wurde mit Hilfe der hochauflösenden TEM analysiert. Die kantennahen Feinstrukturen von Absorptionskanten im Elektronen-Energieverlustspektrum (ELNES) beinhalten Informationen über den lokalen Bindungszustand an der Grenzfläche. Diese Feinstrukturen können theoretisch durch die lokale symmetrieprojierte unbesetzte Zustandsdichte beschrieben werden. Hierzu müssen jedoch Effekte, die durch die Messung bedingt werden, berücksichtigt werden. Durch den inelastischen Streuprozess, der zur Messung der ELNES führt, werden im Material Elektron-Loch Paare erzeugt, die zu einer modifizierten Bandstruktur und damit auch zu veränderten unbesetzten Zustandsdichten führen können. Dieser Effekt wird in der Literatur auch als *Core-hole-Effekt* bezeichnet. Der Einfluß dieses

Effektes auf die Interpretation der Ti $L_{2,3}$ -Kante, der O K-Kante sowie der Sr $L_{2,3}$ -Kante durch Berechnungen der entsprechenden Zustandsdichten wurde für massives SrTiO_3 untersucht. Das Ergebnis dieser Untersuchungen ist, daß sowohl für die Berechnung der Ti $L_{2,3}$ -Kante als auch für die Berechnung der O K-Kante die Berücksichtigung des Core-hole-Effekts wichtig ist und zu einer besseren Übereinstimmung mit experimentellen ELNES Spektren führt. Für die Sr $L_{2,3}$ -Kante ist der Core-hole-Effekt weniger bedeutend, da die zu verzeichnenden Modifikationen der unbesetzten Zustandsdichten aufgrund der momentan verfügbaren experimentellen Energieauflösungen innerhalb der ELNES nicht zugänglich sind.

Die valenzelektronische Struktur von massiven SrTiO_3 wurde anhand der Interbandübergangswahrscheinlichkeit für elektronische Anregungen vom besetzten Valenzband in das unbesetzte Leitungsband untersucht. Die Interbandübergangswahrscheinlichkeit kann aus der komplexen dielektrischen Funktion berechnet werden, die wiederum aus dem Niederenergieverlustbereich eines Energieverlustspektrums ermittelt werden kann. Durch einen Vergleich der experimentell bestimmten Übergangswahrscheinlichkeit mit berechneten totalen Zustandsdichten für SrTiO_3 konnten die Anfangs- und Endzustände der beobachteten Elektronenübergänge bestimmt werden. Die Kenntnis der komplexen dielektrischen Funktion erlaubt zusätzlich die Berechnung der optischen Eigenschaften von SrTiO_3 , wie z.B. dem komplexen Brechungsindex und der Reflektivität. In einer parallelen Studie wurden diese Größen zusätzlich mit Hilfe von optischer Ellipsometrie und Vakuum Ultra-Violett Spektroskopie von R.H. French bei der Firma DuPont Inc. in Wilmington, Delaware, USA, bestimmt [van Benthem, 2001a] [van Benthem, 2001b]. Im Vergleich zeigten alle drei Methoden äquivalente Ergebnisse, wobei die Energieauflösung innerhalb der optischen Spektroskopie um etwa einen Faktor 3 besser ist als in der Elektronen-Energieverlustspektroskopie.

Das Aufwuchsverhalten von Pd auf der (100) SrTiO_3 Oberfläche wurde in einer vorhergehenden Studie von G. Richter [Richter, 2000] untersucht. In dieser Studie wurde ein 3-dimensionales Wachstum (Inselwachstum) bei einer Substrattemperatur von 650°C beobachtet. Die Inseln wiesen hierbei die folgende epitaktische Orientierungsbeziehung zum Substrat auf:

$$100_{Pd} \parallel 100_{\text{SrTiO}_3}.$$

Diese Ergebnisse konnten in der vorliegenden Arbeit mittels der konventionellen TEM und der HRTEM reproduziert werden. T. Ochs [Ochs, 2000] berechnete im Rahmen der lokalen Dichtefunktionaltheorie ein voll relaxiertes atomistisches Strukturmodell für die Pd/ SrTiO_3 Grenzfläche. Dieses Strukturmodell sagt eine Nukleation der Pd Atome oberhalb der O Säulen der TiO_2 terminierten (100) SrTiO_3 Oberfläche voraus. Das von Ochs entwickelte Modell wurde im Rahmen dieser Arbeit verwendet, um die lokale symmetrieprojierten Zustandsdichten zu berechnen. Durch die beobachtete Übereinstimmung der berechneten unbesetzten Zustandsdichten mit den experimentell beobachteten ELNES-Spekten der Ti $L_{2,3}$ -Kante, der O K-Kante sowie der Sr $L_{2,3}$ -Kante konnte das theoretisch entwickelte Strukturmodell evaluiert werden. Zusätzlich konnte durch die Kombination von Theorie und Experiment die TiO_2 Terminierung der (100) SrTiO_3 Oberfläche nachgewiesen werden. Schliesslich wurden berechnete besetzte Zustandsdichten für eine Analyse des tatsächlichen Bindungsverhaltens

an der Pd/SrTiO₃ Grenzfläche herangezogen. Es zeigte sich, daß die Adhäsion zwischen dem Pd Film und dem SrTiO₃ Substrat zum einen durch eine σ -Bindung, d.h. durch eine Hybridisierung von O p_z und Pd d_{z²} Orbitalen, hervorgerufen wird. Zusätzlich wurde eine intermetallische Bindung zwischen Ti und Pd beobachtet. Durch den Kontakt des metallischen Pd Films zu dem isolierenden SrTiO₃ Substrat konnten außerdem metallinduzierte Zustände innerhalb der Bandlücke des SrTiO₃ direkt an der Grenzfläche nachgewiesen werden, deren Aufenthaltswahrscheinlichkeit in den angrenzenden Materialien exponentiell abfällt.

Für Ni wurde ebenfalls ein epitaktisches Inselwachstum festgestellt. Die Orientierungsbeziehung der Ni Inseln im Vergleich zum Substrat kann wie folgt beschrieben werden:

$$100_{Ni} \parallel 100_{SrTiO_3}.$$

HRTEM Aufnahmen der Ni/SrTiO₃ Grenzfläche zeigten eine semi-kohärente Struktur, in der Misfit-Versetzungen innerhalb des Ni Films auftreten. Diese Versetzungen kompensieren Verzerrungen des Ni Films, die durch eine Gitterfehlpassung von $m = -9.8\%$ hervorgerufen werden. An der Grenzfläche treten zusätzliche Kontraste auf, die auf eine Reaktion des Ni Films mit dem Substrat schließen läßt. Eine ausgedehnte Reaktionsphase konnte jedoch nicht beobachtet werden. ELNES Untersuchungen zeigten eine Reduktion des nominellen Oxidationszustandes von Ti Atomen an der Grenzfläche. Die O K-Kante wies eine Feinstruktur auf, die große Ähnlichkeiten zur O K-ELNES von stöchiometrischem NiO zeigt. Dies deutet auf Ni-O Bindungen hin, die einen ähnlichen Bindungscharakter wie in NiO aufweisen. Da Ni eine ähnliche Valenzelektronenstruktur besitzt wie Pd, wurden *ab initio* Berechnungen der unbesetzten lokalen p-projizierten Zustandsdichte durchgeführt, die auf dem Strukturmodell für die Pd/SrTiO₃ Grenzfläche basieren. Der Vergleich von Experiment und Theorie zeigte keine Übereinstimmung der Spektren mit den entsprechenden Zustandsdichten. Aus diesem Grund ließ sich schlußfolgern, daß die atomare Struktur der Ni/SrTiO₃ Grenzfläche von der für die Pd/SrTiO₃ Grenzfläche verschieden ist. Eine mögliche Erklärung für das Bindungsverhalten zwischen Ni und der (100)SrTiO₃ Oberfläche ist die Bildung einer 2-dimensionalen NiO Reaktionsschicht, die zum einen eine O K-ELNES ähnlich zu stöchiometrischem NiO aufweist, und zum zweiten zusätzliche Kontraste in HRTEM Aufnahmen hervorrufen könnte.

Für Cr wurde ein 3-dimensionales Aufwuchsverhalten auf der (100)SrTiO₃ Oberfläche bei einer Substrattemperatur von 65°C beobachtet. Konventionelle TEM Aufnahmen zeigten jedoch bereits eine kontinuierlichen Cr Bedeckung für eine Schichtdicke von 35 nm. Aus diesen Untersuchung läßt sich bereits eine erhöhte Nukleationsdichte für Cr im Vergleich zu Pd und Ni ableiten. Die untersuchten Cr Filme hatten die folgende epitaktische Orientierungsbeziehung zum Substrat:

$$[110](100)_{Cr} \parallel 100_{SrTiO_3}.$$

Hierbei handelt es sich nicht wie im Fall von Pd und Ni um eine sog. Würfel-auf-Würfel Beziehung, da die Cr Einheitszelle um 45° um die Grenzflächennormale gedreht ist. Durch diese Konfiguration wird die Gitterfehlpassung zwischen bcc Cr und dem Substrat auf $m = +4.3\%$ reduziert. HRTEM Untersuchungen zeigten eine semi-kohärente Struktur der Cr/SrTiO₃ Grenzfläche. Diese ist abrupt in den HRTEM Aufnahmen, so daß das Auftreten

einer ausgedehnten Reaktionsschicht ausgeschlossen werden konnte. Da bislang für die Cr/SrTiO₃ Grenzfläche keine relaxierte atomistische Struktur vorliegt, konnten im Rahmen dieser Arbeit keine *ab initio* Bandstrukturberechnungen der unbesetzten Zustandsdichten durchgeführt werden. Aus diesem Grund wurde ein Modell für das Bindungsverhalten an dieser Grenzfläche basierend auf den experimentellen ELNES Untersuchungen erstellt. Die grenzflächenspezifische Ti L_{2,3}-Kante zeigte eine signifikante Reduktion des nominellen Oxidationszustandes der Ti Atome an der Grenzfläche. Die Struktur der kantennahen Feinstruktur der O K-Kante an der Grenzfläche ist in ihrem Verlauf sehr ähnlich zu der ELNES, die für vollständig oxidierte Cr Inseln der Zusammensetzung CrO_x gemessen wurde. Somit kann auf Cr–O Bindungen an der Grenzfläche geschlossen werden. Die Cr L_{2,3}-Kante wies ein signifikantes Signal für oxidiertes Cr an der Grenzfläche auf. Zusätzlich konnte aufgrund eines vergrößerten Intensitätsverhältnisses der Cr L₃ und L₂ Kanten ein Elektronenübergang vom Cr auf benachbarte Bindungspartner nachgewiesen werden. Es zeigte sich, daß die Adhäsion zwischen dem Cr Film und dem SrTiO₃ Substrat durch Cr–O Bindungen hervorgerufen wird, die einen signifikanten ionischen Charakter aufweisen.

Die Untersuchung deutet darauf hin, daß eine bessere Benetzung der (100) Oberfläche von SrTiO₃ durch Cr im Vergleich zu Pd und Ni vorliegt. Die Gründe hierfür liegen in relativ starken Cr–O Bindungen, die, im Vergleich zu Pd–O und Ni–O Bindungen, zusätzlich einen ionischen Charakter aufweisen. An der Ni/SrTiO₃ Grenzfläche wurde eine NiO-ähnliche 2-dimensionale Reaktionsschicht vorgeschlagen, die im Vergleich zur Pd/SrTiO₃ Grenzfläche die Adhäsion verbessert.

Chapter 1

Introduction

The deposition of metals on substrates of oxides, which leads to the formation of metal /ceramic interfaces, is of great technological and academic interest. Electroceramic materials like barium-strontium-titanates and lead-zirconate-titanates are considered as functional ceramics [Setter, 2000], mainly because of their high dielectric constants and partially because of their ferro-, piezo-, or pyro-electrical properties. These ceramic materials are technologically used, for example, as sensors and actuators [Meixner, 1995], as capacitors, as memory devices [Hönlein, 1999], and in opto-electronic devices [Uchino, 1994]. SrTiO_3 is used in the framework of catalysis [Henrich, 1978], for gas-sensors [Meixner, 1995], and as a substrate for high T_c superconductors [Chaudhari, 1987]. For most of these applications, the ceramic materials have to be in contact with electrodes. The performance of these devices strongly depends on the interface between the ceramic and the metallic electrodes.

From the academic point of view, a metal/ceramic interface is a contact between two classes of materials, which usually differ extremely in most materials properties due to their different bonding characteristics. Metallic bonding originates from delocalization of electrons, whereas most ceramics and especially perovskites are characterized by mixed ionic-covalent bonds. So far, the interaction of the different types of bonding across the interface forming the adhesion between the metal films and the ceramic substrates is, however, not understood in general [Finnis, 1996].

Conventional transmission electron microscopy (CTEM), high-resolution transmission electron microscopy (HRTEM), and analytical electron microscopy (AEM), such as electron energy-loss spectroscopy (EELS), have become important tools for the analysis of the atomistic structure [Ernst, 1995] and the electronic structure [Muller, 1999] of metal/ceramic interfaces, especially in combination with *ab initio* bandstructure calculations [Finnis, 1996]. In the literature a large number of publications concerning metal/ceramic interfaces is available. In most studies the substrate materials are $\alpha\text{-Al}_2\text{O}_3$, MgO, SiO_2 , TiO_2 , and ZnO [Ernst, 1995] [Finnis, 1996] [Bäumer, 1999]. In these investigations mainly the 3d- and 4d-transition metals as well as alkali-metals were considered in the contact to the ceramic substrate. Experimental methods were predominantly (*in situ*) surface science techniques, such as reflection high energy electron diffraction (RHEED), Auger electron spectroscopy (AES),

atomic force microscopy (AFM), scanning tunneling microscopy and spectroscopy (STM and STS), and X-ray diffraction measurements. Only in few investigations TEM techniques were applied (for an overview see for example [Rühle, 1989], [Rühle, 1990] and [Howe, 1997]). For the metal/SrTiO₃ system, some investigations for the metals Ni, Ti, Y, Ba, Cu, Pt, and Al can be found in the literature [Chung, 1979] [Hill, 1989] [Andersen, 1990] [Jackson, 1998] [Stanzick, 1998] [Kido, 2000] [Polli, 2000] [Richter, 2000] [Wagner, 2001a] [Wagner, 2001b]. Also for this system, the investigations were focussed on the growth mechanisms and on the resulting film morphology rather than on the analysis of the bonding characteristics between the metal and the ceramic across the interface. Due to the preparation of the (100) substrate surface following a routine provided by Kawasaki et al. [Kawasaki, 1994], TiO₂ terminated (100) surfaces of SrTiO₃ were formed. However, so far no experimental evidence based on cross-sectional TEM investigations was found, confirming the presence of a TiO₂ terminating layer of the (100) surface of SrTiO₃.

In the present study, SrTiO₃ with a cubic perovskite structure was chosen as a model substrate, on whose (100) surface thin metal films were deposited by molecular beam epitaxy (MBE). To perform self-consistent *ab initio* band structure calculations of the metal/ceramic interfacial structures, materials systems with a short spatial periodicity length are required to keep the number of atoms as small as possible within the calculated supercells, i.e. below ~ 50 . Therefore, only coherent interfaces can be considered. One candidate is the Pd/SrTiO₃ system, in which the lattice parameters of both Pd and bulk SrTiO₃ are 0.389 nm and 0.391 nm, respectively, i.e., nearly identical. In a theoretical study based on local density functional theory (LDFT), atomistic structure models of the Pd/SrTiO₃ interface were provided for the two different terminations of the (100)SrTiO₃ surface [Ochs, 2000] [Ochs, 2001]. The aim of the present study is to use these structure models to calculate the site and symmetry projected unoccupied densities of states of the Pd/SrTiO₃ interface, and compare these to experimentally determined electron energy-loss near-edge structures of different absorption edges (ELNES). By a synthesis of experiment and theory the supposed structure model can be verified and the terminating layer of the substrate is determined. Using the evaluated atomistic structure model to calculate the occupied densities of states, the analysis of the bonding characteristics between the Pd film and the SrTiO₃ substrate becomes possible.

In a further study, it is proven whether the theoretical results obtained for the Pd/SrTiO₃ can be used to investigate the adhesion of Ni on the (100)SrTiO₃ surface, which has a similar valence electronic structure compared to Pd. To consider a more reactive system, the Cr/SrTiO₃ interface was studied since Cr has a significantly larger oxygen affinity compared to Pd and Ni.

In order to interpret changes in the interfacial ELNES, line shapes compared to the bulk materials, the ELNES of the Ti L_{2,3}-edge, the O K-edge and the Sr L_{2,3}-edge in bulk SrTiO₃ are investigated in a comparative study by both experiment and theory. Therein, the importance of considering final state effects, such as the core-hole effect, in ELNES investigations is analysed. Furthermore, the valence electronic structure of bulk SrTiO₃ is determined in terms of the interband transition strength, extracted from valence electron energy-loss spectroscopy (VEELS) measurements. The experimental results are interpreted

by a comparison to the calculated total density of states of bulk SrTiO_3 .

Outline of the Thesis

After this introduction, fundamental aspects of metal/ceramic interfaces, which are important in the context of this work, are reported in chapter 2. Furthermore, important materials properties of bulk SrTiO_3 and the metals Pd, Ni, and Cr are summarised.

In chapter 3, a literature survey is given concerning metal/ceramic interface investigations in general. The main focus is however on Pd/ceramic, Ni/ceramic, Cr/ceramic, and metal/ SrTiO_3 interfaces. In addition, current state-of-the-art methods concerning spatially resolved EELS and ELNES measurements are discussed.

The experimental and calculational methods used in this work are presented in detail in chapter 4. In section 4.1, the experimental details are given in section 4.1, whereas the calculational details are presented in section 4.2. The latter include the LDFT approach for the bandstructure calculations as well as a full multiple scattering approach.

In chapter 5 the preparation of the investigated metal/ SrTiO_3 interfaces by MBE as well as the following TEM specimen preparation techniques are reported.

VEELS investigations of bulk SrTiO_3 are described in chapter 6 and are discussed in terms of interband transitions between the occupied valence band and the unoccupied conduction band. In the second part of this chapter, the ELNES of the Ti $L_{2,3}$ -edge, the O K-edge, and the Sr $L_{2,3}$ -edge is investigated by both experiment and theory. Therein, the importance of considering final-state effects, such as the core-hole effects, in the calculations is investigated.

In chapters 7, 8, and 9 the experimental and calculational results obtained for bulk SrTiO_3 , and for the Pd/ SrTiO_3 , the Ni/ SrTiO_3 and the Cr/ SrTiO_3 interfaces, respectively, are reported. Each of these chapters includes both the presentation of the obtained results and the corresponding discussion concerning the bonding characteristics.

Finally, the results, which were obtained for the different materials systems, are discussed in general in chapter 10 to develop a basic trend in the wetting behaviour for Pd, Ni, and Cr with respect to the (100) surface of bulk SrTiO_3 .

Chapter 2

Basics

In this chapter the basics for the description of metal/ceramic interfaces are presented with respect to the wetting mechanisms and the crystallography of the interfaces. Subsequently, the materials properties of bulk SrTiO_3 and of the metals Pd, Ni, and Cr, which are relevant for this work, will be reviewed. Finally some remarks concerning different bonding mechanisms will be given in section 2.4.

2.1 Interface Structures

2.1.1 Orientation Relationships

If two materials with different chemical and crystallographic structures are in contact, a so-called heterophase interface is formed. The crystallographic orientation relationship describes the orientation of one material with respect to the other material [Baluffi, 1981]. A heterophase interface can be fully described by five microscopic and five macroscopic degrees of freedom. The macroscopic degrees of freedom cover, for instance, the normal vectors \vec{n}_1 and \vec{n}_2 of the two crystal surfaces and the rotation angle θ_{twist} of crystal 1 around \vec{n}_1 with respect to crystal 2. Since \vec{n}_1 and \vec{n}_2 are unit vectors, 5 degrees of freedom are consumed with this description: two Euler angles for each normal vector in spherical coordinates plus the rotation angle θ_{twist} . The microscopic degrees of freedom are given by the 3-dimensional translation vector of the two half-crystals $\vec{T} = (t_x, t_y, t_z)$ and one parameter for each crystal determining the terminating layer of the crystal (in case that the basis consists of > 2 atoms). Therefore the minimum number of geometric variables is 10 for a complete description of a heterophase interface. Since a pure metal has only one atom in its crystal basis, the number of desired degrees of freedom is reduced to 9.

In this work, orientation relationships between the metal film and the substrate are given by

$$[uvw](hkl) \parallel [u'v'w'](h'k'l'), \quad (2.1)$$

where (hkl) and $(h'k'l')$ denote planes parallel to the interface and $[uvw]$ and $[u'v'w']$ are directions, which are parallel to each other.

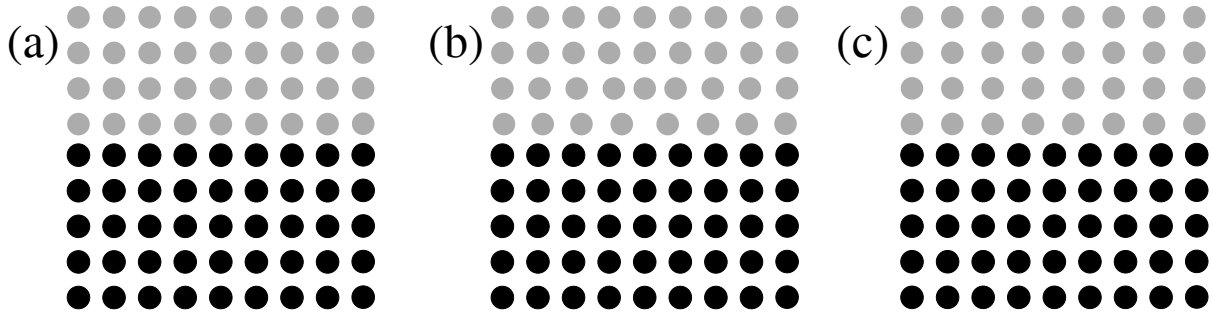


Figure 2.1: Schematic drawing of a) a coherent, b) a semi-coherent, and c) of an incoherent interface structure.

2.1.2 Lattice Mismatch

The lattice mismatch m between the thin metal film and the ceramic substrate is defined as

$$m = \frac{a_{film} - a_{substrate}}{a_{substrate}}, \quad (2.2)$$

where $a_{substrate}$ is the lattice parameter of the substrate and a_{film} is the lattice parameter of the metal overlayer. Apart from the lattice mismatch, differences in the thermal expansion coefficients can also affect a mismatch during the growth process at high temperatures. In this case, the lattice parameters can simply be replaced by the corresponding thermal expansion coefficients in equation 2.2.

2.1.3 Coherence State between Film and Substrate

The state of coherency of a heterophase interface can be divided into three cases, which are denoted as coherent, semi-coherent, and incoherent [Hull, 1984]. If a film grows epitaxially on the substrate without forming any defects, the interface is called a coherent interface. In the case that the system provides a non-zero mismatch in the lattice parameters of the two materials (compare section 2.1.2), homogeneous strains can be introduced into the thin film to compensate for the mismatch. Therefore the same periodicity of lattice planes as in the substrate material can be achieved. However, the elastic strain energy will be increased with increasing film thickness and increasing mismatch. For large values of m or high film thicknesses it is energetically favourable to introduce misfit dislocations to the interfacial structure to compensate for high elastic strain fields. These interfaces are called semi-coherent. In the case that no strains appear, the interfacial structure is called incoherent. These three cases are sketched in Figure 2.1. There exist no well-defined limits between semi-coherent and incoherent interfacial structures. However, an incoherent structure can be described by delocalization of the cores of misfit dislocations [Ernst, 1995] [Romanov, 1998].

The distance between two misfit dislocations is inversely proportional to the lattice mismatch of the two materials. For instance, for a mismatch of $m = 4\%$, a misfit dislocation will appear every 25 lattice planes.

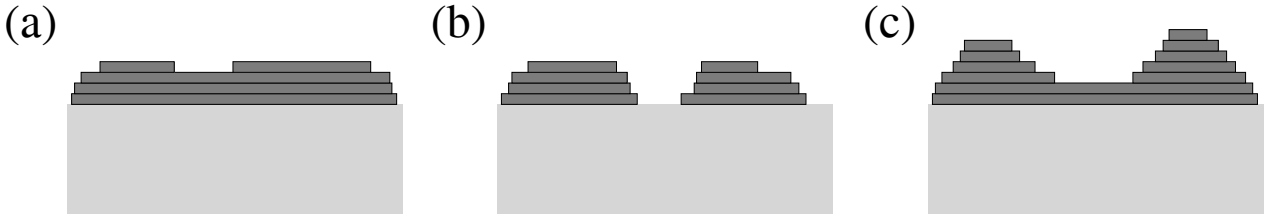


Figure 2.2: Three different growth mechanisms of a thin film on a substrate exist: a) Frank-van-der-Merwe-growth (layer growth), b) Volmer-Weber-growth (island growth), and Stranski-Krastanov-growth (combination of island-growth and layer-growth).

2.2 Wetting Mechanisms

For the preparation of heterophase interfaces three main methods are used: internal oxidation/reduction [Meijering, 1971], diffusion bonding [Fischmeister, 1993, Elssner, 1990], and epitaxial growth of thin films on single crystalline substrates by physical vapour deposition [Tsao, 1993]. In the present study the latter technique is used for the preparation of metal/SrTiO₃ interfaces, which were produced by MBE. In the MBE process the metals Pd, Ni, and Cr were evaporated under ultra-high vacuum (UHV) conditions on (100)SrTiO₃ surfaces at different substrate temperatures $T_{\text{substrate}}$. The orientation of the resulting interfacial plane of the substrate is then given by the substrate surface. The orientations of the deposited metal films can be influenced by the growth parameters, such as the substrate temperature and the deposition rates [Bauer, 1958] [van der Merwe, 1993] [Richter, 2000].

Bauer [Bauer, 1958] has described the wetting behaviour by three different phenomenological growth processes. One is a 2-dimensional growth mode in which a continuous layer of the wetting material is formed on the substrate surface before a second layer is starting to grow. This behaviour is also referred to as the Frank-van-der-Merwe growth mode [van der Merwe, 1993] or layer growth mode and is sketched in Figure 2.2a. From the energetic point of view, for this wetting mechanism the formation of a heterophase interface is energetically favoured compared to the formation of a free surface of the wetting material. In contrast to this mode, materials can also grow 3-dimensionally on a substrate surface [Bauer, 1958]. In this case, new layers of the wetting material are formed before the previous layer are completed, leading to island formation on the surface of the substrate (cf. Figure 2.2b). This mode is called the Volmer–Weber growth mode [van der Merwe, 1993] or is simply denoted by island growth. In this case, the formation of free surfaces of the wetting material is energetically favoured compared to the interface formation. However, a third process can appear called Stranski-Krastanov growth, which is a combination of the 2-dimensional and the 3-dimensional growth modes [van der Merwe, 1993]. In this process, after the growth of a few continuous layers of the wetting material, islands start growing on top of these layers. The reasons for a combination of layer growth and island growth can be electronic interactions between the film and the substrate [Doben, 1988] [Gossmann, 1991] [van der Merwe, 1993] or strains within the grown film due to a large lattice mismatch m between the continuous

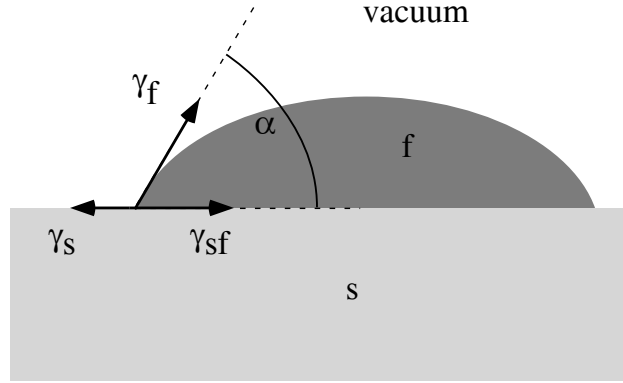


Figure 2.3: A drop of a liquid metal film (f) on a solid substrate (s). In thermodynamic equilibrium the contact angle α is given by the surface energies γ_s, γ_f and by the interface energy γ_{sf} .

film and the substrate [van der Merwe, 1993].

As mentioned above, the type of growth mode which takes place depends on the interface energy γ_{sf} and on the free surface energies of both film, γ_f , and substrate, γ_s . These energies are related by the so-called Young-Dupré equation [Sutton, 1995]:

$$\gamma_{sf} = \gamma_s - \gamma_f \cos \alpha. \quad (2.3)$$

Therein, α denotes the contact angle between the film and the substrate as defined in Figure 2.3. The description of the wetting behaviour in terms of the Young-Dupré equation is originally based on the model of a liquid metallic drop on a flat solid substrate (see Figure 2.3). Equation 2.3 is determined by considering the change in the free enthalpy due to the interface formation [Ohring, 1992] and is only valid in thermodynamic equilibrium [Sutton, 1995]. A contact angle of $\alpha \leq 90^\circ$ denotes wetting of the substrate surface in which the interface formation is energetically favoured. Therefore, for 2-dimensional growth the corresponding interface energy behaves like

$$\gamma_{sf} \leq \gamma_s - \gamma_f. \quad (2.4)$$

For the 3-dimensional growth mode, denoted by $90^\circ < \alpha \leq 180^\circ$, interface formation is energetically unfavourable compared to free surface formation of the wetting film and therefore the interface energy fulfills the condition

$$\gamma_{sf} > \gamma_s - \gamma_f. \quad (2.5)$$

For a contact angle of $\alpha = 90^\circ$, neither the formation of a free substrate surface nor the formation of an interface is energetically favoured, defining the turning point between layer growth and island growth.

The Young-Dupré equation is valid for liquid drops on solid substrates where surface energies are isotropic. This model has to be modified if solid films are in contact with

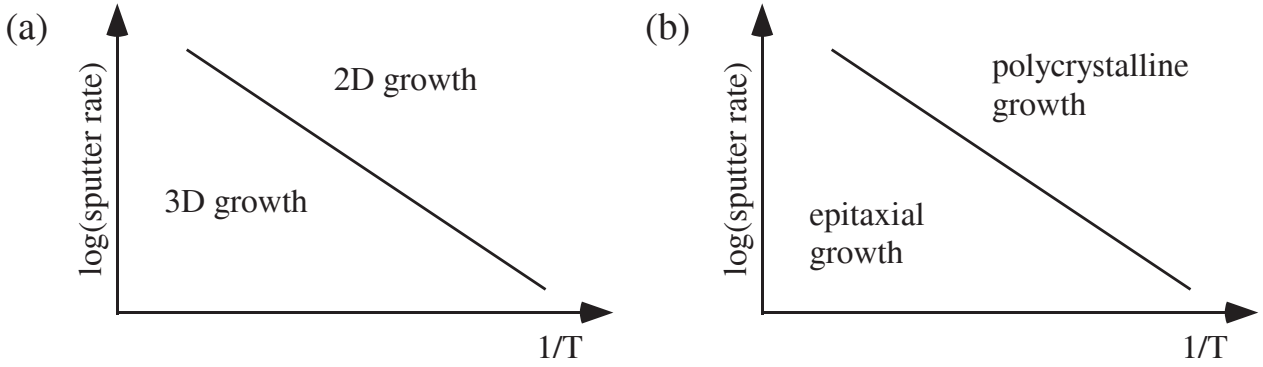


Figure 2.4: Sketches of the different growth modes as a function of sputter rate and substrate temperature $T_{\text{substrate}}$ after [Wagner, 2001a]. In both plots the logarithmic sputter rate is plotted versus the reciprocal substrate temperature $T_{\text{substrate}}$.

the substrate surfaces, as for example, for the solid/ceramic interfaces which are investigated in this work. In general, surface energies are anisotropic. Small crystals will therefore create facets along low-index crystallographic planes to minimize the total surface energy [Winterbottom, 1967]. The crystallographic structure of the solid particle is then given by the Wulff-construction [Wulff, 1901], which can directly be transferred to the case of small particles on a solid substrate. These suggestions lead to the modified Young-Dupré equation

$$\gamma_{sf} = \gamma_s + \gamma_{f(hkl)} \frac{r_2}{r_1}. \quad (2.6)$$

$\gamma_{f(hkl)}$ is the surface energy of the (hkl)-facet. r_1 and r_2 are the distances of the particles' surface plane and the interfacial plane from the Wulff point, respectively, which is given by the symmetry centre of the particle [Wulff, 1901].

However, in MBE the processing conditions are usually far from thermodynamic equilibrium. Therefore, the criterion of Bauer [Bauer, 1958] and also the Young-Dupré equation have to be modified with respect to the substrate temperature $T_{\text{substrate}}$ [Markov, 1976] [Markov, 1976] and the sputtering rate, i.e., with respect to the ratio $\xi = \frac{R_a(T_s)}{R_d(T_s)}$ of adsorbed and desorbed ad-atoms on the substrate surface [van der Merwe, 1993]. For small values of ξ , an adatom can easily reach a site which is energetically favoured. Therefore the growth process will be near thermodynamic equilibrium and the film will grow with an epitaxial orientation relationship to the substrate. For larger values of ξ , the diffusion length of the adatoms on the surface is short, which can lead to a polycrystalline growth far away from thermodynamic equilibrium. The ratio ξ also influences the mode of growth. The higher the substrate temperature $T_{\text{substrate}}$ and the higher the deposition rate, the more favourable will the three dimensional growth mode be, i.e. the Volmer-Weber type (cf. Figure 2.4).

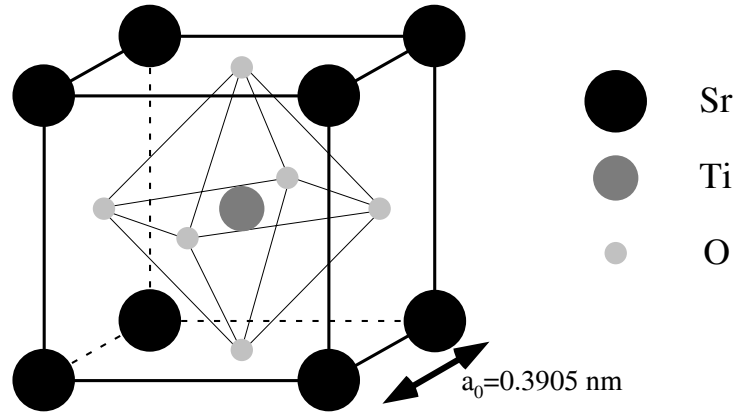


Figure 2.5: Crystal structure of bulk SrTiO_3 at room temperature. The size of the spheres representing the atoms are arbitrary and are not related to atomic radii.

2.3 Materials Properties

In this section the materials properties for bulk SrTiO_3 and for the metals Pd, Ni and Cr, which were deposited on the (100) surface of SrTiO_3 , are reviewed.

2.3.1 Bulk SrTiO_3

Atomistic Structure

At room temperature bulk SrTiO_3 crystallizes in the cubic perovskite structure [Landoldt, 1981] [Nassau, 1988]. The space-group symmetry of this structure is $Pm3m$. The Ti^{4+} ions are sixfold coordinated by O^{2-} ions, whereas each of the Sr^{2+} ions is surrounded by four TiO_6 octahedra. Therefore, each Sr^{2+} ion is coordinated by 12 O^{2-} ions. The crystal structure is sketched in Figure 2.5. Within the TiO_6 octahedra a high amount of covalent bonding is present [Leapman, 1982] [de Groot, 1989]. At room temperature, the lattice parameter of bulk SrTiO_3 is 0.3905 nm. At 105 K a phase transition is observed in which the TiO_6 octahedra are slightly tilted and therefore a tetragonal structure with the space-group symmetry $I4/mcm$ is formed [Heidemann, 1973, Fujishita, 1979]. At 65 K again a phase transformation takes place to an orthorhombic structure [Lytle, 1964].

The cubic unit cell for bulk SrTiO_3 at room temperature is completely described by the space-group $Pm3m$ and the following basis of atoms at the following positions: Sr: $[0, 0, 0]$, Ti: $[\frac{1}{2}, \frac{1}{2}, \frac{1}{2}]$, and O: $[\frac{1}{2}, \frac{1}{2}, 0]$, $[\frac{1}{2}, 0, \frac{1}{2}]$, and $[0, \frac{1}{2}, \frac{1}{2}]$ [Landoldt, 1981].

It can easily be recognized from the crystal structure (Figure 2.5) that the (100) SrTiO_3 surface can exhibit two different terminations. One is formed by a TiO_2 plane and the other by a SrO plane, respectively. In Figure 2.6 the two different terminations for the (100) surfaces of SrTiO_3 are sketched in a side view (Figure 2.6a) and in a top view (Figure 2.6b).

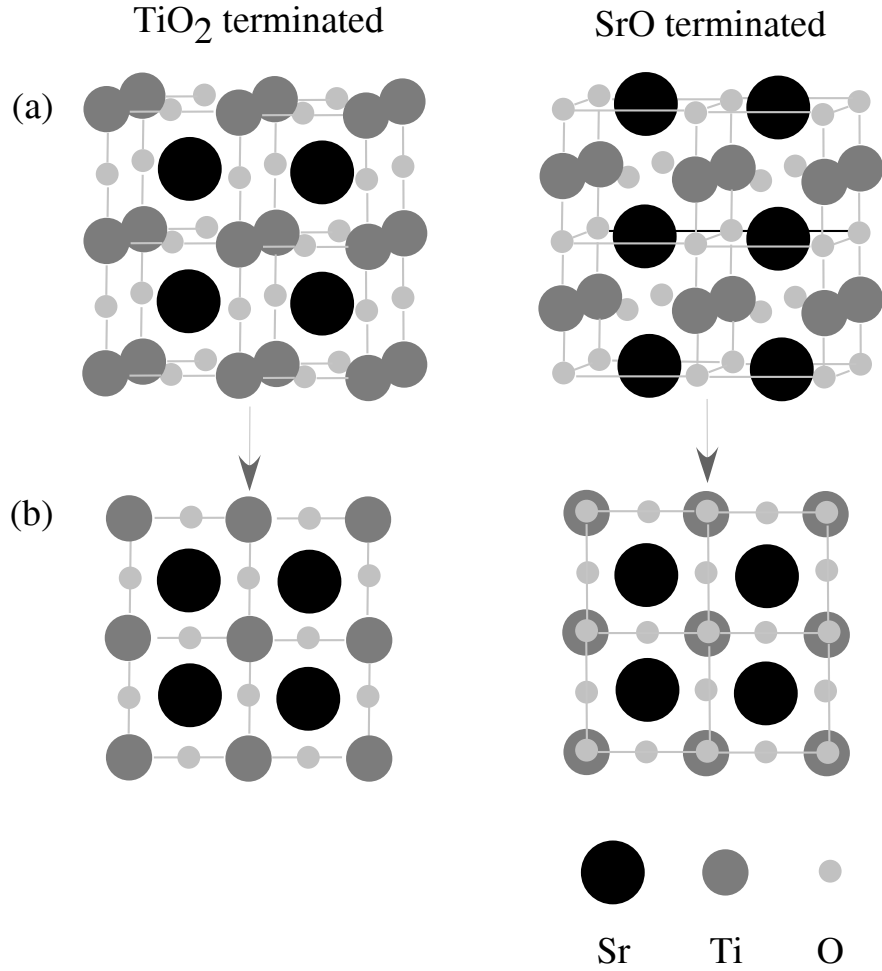


Figure 2.6: Two different surface terminations exist for the (100)SrTiO₃ surface. TiO₂ and SrO termination in a side view (a) and in a top view (b). The size of the spheres representing atoms have no physical meaning.

Electronic Structure

Pure stoichiometric SrTiO₃ is an insulating material with a band gap of 3.1 – 3.2 eV, separating the valence bands from the conduction bands [Cardona, 1965] [Waser, 1990].

SrTiO₃ is a material with mixed ionic–covalent bonds and is formed by nominally Sr⁴⁺, Ti²⁺ and O²⁻ ions. Due to the sixfold coordination of Ti ions by surrounding O ions (cf. Figure 2.5), a crystal field splitting of the degenerated Ti-3d states of 2.4 eV appears [Cox, 1995]. These separated states are called Ti-3d t_{2g} and Ti-3d e_g , respectively. A hybridization of oxygen-2p states with the Ti-3d t_{2g} and e_g states leads to a pronounced covalent bonding contribution to the Ti–O bonds [Leapman, 1982] [de Groot, 1989] [Brydson, 1992]. The electronic structure of bulk SrTiO₃ will be discussed in more detail in chapter 6 in terms of electron densities of states.

The presence of intrinsic defects, such as vacancies, and the appearance of extrinsic

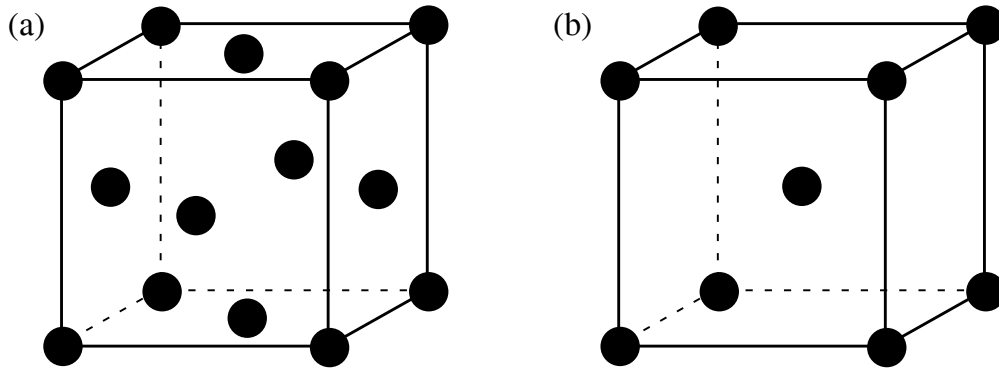


Figure 2.7: Crystal structure of (a) face-centered cubic and (b) body-centered cubic materials.

defects like dopants lead to modifications of the electronic structure and the electronic conductivity of the material. In SrTiO_3 intrinsic defects are O and Sr vacancies, whereas Ti vacancies are of minor importance due to the high value of the energy of formation. Extended reviews of the chemistry of intrinsic defects in SrTiO_3 can be found in references [Waser, 1991] [Denk, 1995] [Moos, 1997]. Atomistic calculations of Akhtar et al. [Akhtar, 1995] reveal the lattice sites which will be occupied by different dopants. They showed that single or double charged cations will substitute Sr-ions. The cation radius of triple charged cations mainly determines the site where the dopant is substituted. Large cations, e.g. La^{3+} and Y^{3+} , substitute Sr, whereas smaller cations, e.g. Fe^{3+} , substitute Ti and act as acceptors [Akhtar, 1995]. In SrTiO_3 mainly the acceptor-type impurities Fe^{3+} , Al^{3+} , Cr^{3+} , Ni^{2+} , and Mn^{2+} are found [Chiang, 1990].

2.3.2 Palladium

Palladium (Pd, $Z=46$) belongs to the metals in the 10th group of the periodic table of the elements. Pd has the atomic valence electron configuration $[\text{Kr}]4d^{10}$ and crystallizes in the face-centered cubic structure (cf. Figure 2.7a), corresponding to the space-group: $Fm\bar{3}m$. The lattice parameter at room temperature is $a_0 = 0.389 \text{ nm}$. Therefore, the lattice mismatch is $m = -0.4\%$ for a cube-on-cube orientation relationship to bulk SrTiO_3 on top of the (100) surface. The melting point and the boiling point for Pd are at 1554°C and at 3236°C , respectively. The vaporization enthalpy is 377 kJmol^{-1} . However, even below the melting point the partial pressure for Pd is so high that evaporation experiments can easily be performed [Brandes, 1992].

The oxide PdO has a heat of formation of $-\Delta H^0 = (87.923 \pm 8.374) * 10^{-6} \text{ kJmol}^{-1}$ [Samsonov, 1973], which is small compared to the corresponding $-\Delta H^0$ values for Cr and Ni oxides in Table 2.1. Therefore, the probability for interfacial reactions of Pd on oxide surfaces is regarded to be significantly smaller compared to Ni and Cr, which are also investigated in this work.

Table 2.1: Heat of formation $-\Delta H^0$ for the different Chromium oxides, and for NiO and PdO ([Samsonov, 1973] and therein) In addition, the oxygen affinities $pO = -\log p_{O_2}$ are plotted for the case of oxygen in equilibrium at 1000°C [Reed, 1971].

	CrO	Cr ₂ O ₃	CrO ₂	CrO ₃	NiO	PdO
$-\Delta H^0$ 10^{-6}kJmol^{-1}	389.372	272.142	590.339	579.453	244.509	87.923 ± 8.374
$-\log p_{O_2}$		30.1			16.2	-1.1

2.3.3 Nickel

Nickel (Ni, Z=28) is also located in the 10^{th} group of the periodic table. Its crystal structure is face-centered cubic as for Pd (Figure 2.7a) with the space group $Fm\bar{3}m$. The atomic valence electron configuration is $[\text{Ar}]3d^84s^2$. The lattice parameter at room temperature is $a_0 = 0.352\text{nm}$, resulting in a lattice mismatch of $m = -9.9\%$ with respect to the lattice parameter of SrTiO_3 for a cube-on-cube orientation relationship. The melting point for Ni is at 1728°C , whereas the boiling point is at 3186°C . The vaporization enthalpy for Ni is 378kJmol^{-1} . Only the oxide NiO is known to exist, whose heat of formation is $-\Delta H^0 = 244.509 \times 10^{-6}\text{kJmol}^{-1}$ [Samsonov, 1973].

The valence electronic structure of Ni is similar to that of Pd, since both metals are located in the 10^{th} group of the periodic table. Therefore, the bonding characteristics are expected to be similar since only the valence electrons are expected to form bonds.

2.3.4 Chromium

Chromium (Cr, Z=24) is a metal from the 6^{th} group of the periodic table of the elements. At room temperature, Cr crystallizes in the body-centered cubic structure (cf. Figure 2.7b). The space group is $Im\bar{3}m$. The valence electronic structure is $[\text{Ar}]3d^54s^1$. The lattice parameter of cubic Cr is $a_0 = 0.288\text{nm}$ at room temperature. Therefore, the lattice mismatch m with respect to the (100) SrTiO_3 surface is $m = -26.2\%$ for a cube-on-cube orientation relationship, which can be reduced to $m = +4.3\%$ by rotating the Cr unit cell by 45° around the axis perpendicular to the interfacial plane.

The melting point and the boiling point of Cr are at 2180°C and 2944°C , respectively. The vapourization enthalpy is 350kJmol^{-1} . The following oxides of Chromium are known: CrO, Cr₂O₃, CrO₂, and CrO₃. Therefore, the possible oxidation states for Cr are +II, +III, +IV, and +VI. The corresponding heats of oxide formation $-\Delta H^0$ and the oxygen affinities are given in Table 2.1.

From the values of the heat of oxide formation and the values of the oxygen affinities for the different metals in Table 2.1, one can infer that Cr has the highest probability to chemically react with oxygen, followed by Ni and Pd. This is an important point for the later

interpretation of the bonding effects at the different metal/SrTiO₃ interfaces.

2.4 Bonding Mechanisms

In the following the different bonding characteristics such as ionic bonding, covalent bonding, and metallic bonding will be briefly reviewed.

2.4.1 Ionic Bonding

In the simplest model of an ionic crystal all ions are treated as impenetrable charged spheres. Bonds between negatively and positively charged ions are formed by the electrostatic attraction, i.e. by the Coulomb interaction. A collapsing of the ions is thereby prevented by the Pauli exclusion principle due to an overlap of the electronic charge distributions. In addition, the stable closed-shell electronic configurations of the ions avoid collapsing [Ashcroft, 1976]. In an ionic crystal, each ion is embedded in an effective electrostatic potential, which is described by the so-called Madelung correction with respect to the two-body Coulomb interaction [Ashcroft, 1976]. Typical examples for ionic crystals are e.g. NaCl and CaCl₂.

2.4.2 Covalent Bonding

In the case of covalent bonding the atoms in the crystal structure share their valence electrons with their nearest neighbours in order to achieve the noble gas configuration. This behaviour is called hybridization in the atomic orbital model. The valence electrons are localized between the atoms and the corresponding total energy of the system is lower to that where the electrons are localized on one atomic site. Therefore, the basis of covalent bonding is also the electrostatic interaction between the atomic nuclei and the negatively charged electron clouds in between the nuclei.

A covalent bond forms between two atoms of the same species or between atoms which are located next to each other in the periodic table of the elements. In general, covalent bonding prefers a distinct orientation in the crystal. In most of the cases the coordination number is 4 instead of 12 for a close-packed structure. Typical examples for crystals possessing this bonding character are C, Si, Ge, and SiC.

If the electron affinity/electronegativity of one atom is higher than that of the other bonding partner, then the valence electrons which are shared are more localized at the atomic site of the bonding partner with the higher electron affinity. Thus, the covalent amount of the bonding decreases whereas an ionic amount is strongly increased.

2.4.3 Metallic Bonding

In a metal, the valence electrons originating from the conduction bands, are no longer localized at the atomic sites. In this case, all valence electrons form a negatively charged gas, in which the nuclei are incorporated with no preferential bonding orientations. Therefore most of the

metals crystallize in close-packed crystal structures with high coordination numbers. The bonding energy is given by the lowering of the total energy of the valence electrons due to their delocalization. In the case of transition metals, whose d-bands are not completely filled, a covalent bonding contribution occurs.

Chapter 3

Literature Survey

In this chapter the literature concerning investigations of heterophase interfaces between metals and oxidic substrates is reviewed. Therein, the focus is not on metal/ceramic interfaces in general; instead only the most relevant papers concerning the metals Pd, Ni, and Cr used for deposition on different oxidic ceramic substrates as well as papers concerning investigations of different metals on SrTiO_3 will be discussed. In addition, since spatially resolved EELS analysis was the main experimental method used in this work, different attempts of performing EELS measurements at high spatial resolution will be discussed.

3.1 Metals on Surfaces of Oxide Substrates

Reviews of the scientific progress in the investigation of metal/ceramic interfaces from both the experimental and the theoretical point of view, can be found in the articles by Ernst [Ernst, 1995], Bäumer and Freund [Bäumer, 1999], Finnis [Finnis, 1996], as well as in the textbooks by Sutton and Balluffi [Sutton, 1995] and by Howe [Howe, 1997].

In the literature a large number of publications concerning metal/ceramic interfaces is available. The most prominent substrate materials are TiO_2 , ZnO , MgO , Al_2O_3 , and SiO_2 (see e.g. [Ernst, 1995], [Finnis, 1996] and [Bäumer, 1999]). The investigated metals were mainly 3d and 4d transition metals as well as alkali-metals. The used characterization methods were predominantly *in-situ* surface methods RHEED, AES, AFM, and STM, as well as X-ray diffraction and (high-resolution) TEM after a cross-sectional preparation of the interfaces. Different interface preparation methods such as internal oxidation techniques [Meijering, 1971], diffusion bonding [Fischmeister, 1993] [Elssner, 1990] and molecular beam epitaxy [Tsao, 1993] are reported throughout the literature.

The main focus of TEM based investigations was in the analysis of the wetting and growth behaviour in terms of the contact angle concept (cf. chapter 2.2), as well as on the analysis of the atomistic structure of the interfaces. Detailed quantitative HRTEM studies with picometer accuracy are reported for Ag/MgO [Trampert, 1992], Nb/ Al_2O_3 [Gutekunst, 1997a] [Gutekunst, 1997b], Al/ Al_2O_3 [Inkson, 1999], Cu/ Al_2O_3 [Dehm, 1995] [Dehm, 1997] [Scheu, 2000] and for Al/ MgAl_2O_4 and Ag/ MgAl_2O_4 [Schweinfest, 1998]. The Si/ SiO_2 in-

terface was studied by Batson and co-workers [Batson, 1994] using incoherent electron scattering experiments, combined with a chemical analysis using EELS. For metal/SrTiO₃, or metal/perovskite interfaces in general, no quantitative atomistic structure investigations are reported so far.

Only a few investigations were published concerning detailed EELS analyses of metal/ceramic interfaces. Batson et al. [Batson, 1994] were able to show a change in the electronic structure on the atomic level for Si at Si/SiO₂ interfaces. For the Cu/MgO system, spatially resolved EELS/ELNES measurements were performed by several authors ([Imhoff, 1999] [Muller, 1998] [Shashkov, 1999]). Muller et al. [Muller, 1998] identified metal-induced gap states (MIGS) at the Cu/MgO interface by both, EELS measurements and local density functional theory (LDFT). Shashkov et al. [Shashkov, 1999] furthermore studied the segregation behaviour of Ag in the Cu/MgO system by quantitative EELS. Imhoff and co-workers [Imhoff, 1999] performed ELNES measurements with high spatial resolution on the Cu/MgO system. Analysing the interfacial electronic structure they found Cu-O bondings together with a significant charge transfer across the interface.

Systematic studies of the electronic structure of Al/Al₂O₃ and Cu/Al₂O₃ using EELS/ELNES were performed by several authors [Brydson, 1995] [Scheu, 1995] [Scheu, 1998]. Brydson et al. [Brydson, 1995] and Scheu et al. [Scheu, 1995] [Scheu, 1996a] [Scheu, 1996b] investigated the electronic structure in this system for different substrate terminations and interface preparation methods. They performed spatially resolved ELNES measurements using the so-called spatial-difference method [Bruley, 1993] [Mülleijans, 1995] in comparison to ELNES calculations using a multiple scattering approach [Durham, 1982] [Vvedensky, 1986]. For the Al/Al₂O₃ interface the authors found that Al atoms are coordinated by three O atoms and one Al atom at the interface, where the Al-Al bond length is larger than for Al-O. For the Cu/Al₂O₃ system, a Cu-O bond was determined at the interface with Cu in the nominal oxidation state of +I.

After a discussion of the literature with a focus on the materials systems investigated in this work, different methods for ELNES measurements with high spatial resolution, which are reported in the literature, are discussed in section 3.2.

3.1.1 Metals/SrTiO₃

Several investigations of various metals such as Ni, Ti, Y, Ba, Cu, Pt, and Al, in contact with the (100)SrTiO₃ surface have been performed [Hill, 1989] [Andersen, 1990] [Jackson, 1998] [Stanzick, 1998] [Kido, 2000] [Polli, 2000]. Therein, mainly the growth behaviour and epitaxy of the metal films were analysed as a function of substrate termination, processing method and temperature, and reactivity of the corresponding metal. The main techniques are in the field of surface science, such as RHEED, XPS, AES, scanning tunneling spectroscopy (STS), AFM, and STM. Only a few experiments on the interface in cross-section, such as TEM and EELS, are reported.

After reporting investigations performed on the termination of the (100)SrTiO₃ the results for the metal/SrTiO₃ interfaces (metal=Ni, Ti, Y, Ba, Cu, Pt, and Al) are reviewed

and discussed in detail.

Substrate Termination

The preparation of the (100)SrTiO₃ surface, prior to the metal deposition, is critical with respect to the termination and the chemistry of the substrate surface and therefore also for the atomistic and electronic structures of the resulting metal/SrTiO₃ interface. In general, three different preparation techniques of the (100)SrTiO₃ surface are reported in the literature: (i) cleaning of the surfaces by sputtering with Ar⁺ ions, (ii) single or multiple annealing cycles of the substrates, and (iii) etching of the crystals.

Ar⁺ ion bombardement experiments are reported by Henrich et al. [Henrich, 1978] and Adachi et al. [Adachi, 1999]. During the sputtering process, defects, such as strontium vacancies and oxygen vacancies, are induced in the SrTiO₃ surface, which could not be removed afterwards by additional annealing processes.

Liang and Bonnell ([Liang, 1995] and therein) as well as Matsumoto and Tanaka [Matsumoto, 1992] [Tanaka, 1994] used a single annealing process of the crystals for the surface preparation. Both groups observed mixed TiO₂ and SrO terminations of the (100)SrTiO₃ surface as well as a ($\sqrt{5} \times \sqrt{5}$) surface reconstruction caused by oxygen vacancy diffusion [Matsumoto, 1992] [Tanaka, 1994]. Jiang and Zegenhagen [Jiang, 1996] used two steps of annealing. The surface showed terraces with a $c(6 \times 2)$ -reconstruction.

Kawasaki and co-workers [Kawasaki, 1994] etched the (100)SrTiO₃ surface in HF-acid, which was buffered with NH₄F. The pH-value of the buffered acid was 4.5. Using this technique they were able to produce a regularly stepped surface. After etching, ion scattering spectroscopy measurements showed the surface to be purely TiO₂ terminated [Yoshimoto, 1994] [Kawasaki, 1994], compared to 75% to 95% TiO₂-termination prior to etching [Kawasaki, 1994]. The authors do not comment on the detailed structure of the surface, regarding e.g. oxygen vacancies. Kawasaki et al. [Kawasaki, 1994] report that in order to obtain a SrO-terminated (100)SrTiO₃ substrate, one monolayer (ML) of SrO has to be deposited on a previously etched TiO₂ terminated surface.

Polli and co-workers [Polli, 1999] and Richter [Richter, 2000] used a combination of etching and heat treatment to prepare well-defined (100)SrTiO₃ TiO₂ terminated surfaces. They found that this technique leads to a homogeneous morphology of the substrate surface with steps of one unit cell in height.

Ni/SrTiO₃

Kido and co-workers [Kido, 2000] investigated the termination of the (100) surface of SrTiO₃ as well as the nucleation of Ni atoms on this surface by high-resolution medium-energy ion scattering (MEIS), RHEED and by UPS measurements. They prepared the surfaces by etching them in an *pH*-controlled NH₄F-HF solution (*pH* = 3.5 – 3.8). After this process they additionally used a heat-treatment at temperatures up to 650°C. The termination was $(88 \pm 2\%)$ TiO₂ for temperatures below 600°C. For temperatures higher than 600°C, UPS

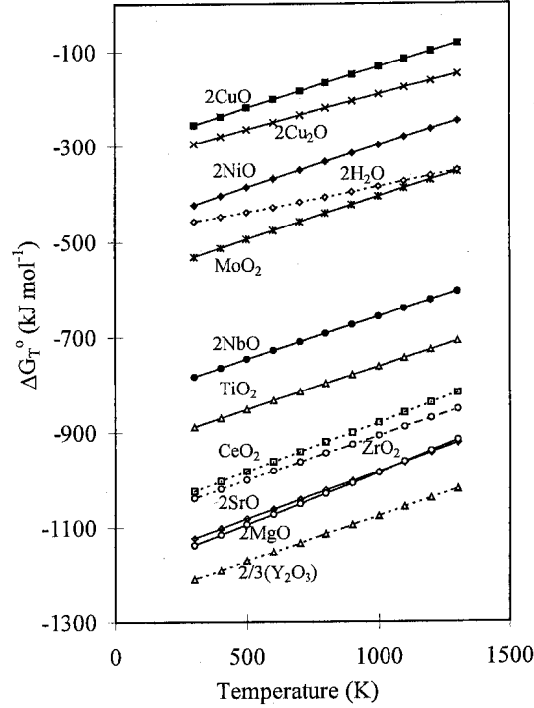


Figure 3.1: The standard free energy change for the formation of selected metal oxides, ΔG_T^0 , between 300 K and 1300 K [Jackson, 1998]. The units of ΔG_T^0 are KJ (mol O_2)⁻¹. The data for the formation of water is included for comparison.

experiments showed an electronic surface state, whose energy level lies about 1.3 eV below the Fermi level due to reduction processes. A quantification of these data showed that 14% of oxygen sites appear to be vacant in the top layer of the substrate, leading to a reduction of the amount of TiO_2 termination of 5%-6%. After a deposition of 1 monolayer Ni on top of the predominantly TiO_2 terminated (100) surface at room temperature, RHEED experiments showed a random distribution of Ni on the surface. UPS spectra exhibited a metallic nature of the Ni. Annealing of the as-deposited samples at 400°C for 30 minutes leads to the formation of Ni clusters on the substrate surface. Kido et al. did neither comment on thicker Ni films nor on the atomistic or electronic structure of the Ni/ $SrTiO_3$ interface. Besides that, they also did not analyse the growth behaviour of the metal films.

Jackson and co-workers [Jackson, 1998] applied a thermodynamic description in terms of the standard Gibbs free energy to the formation of thin ceramic films on pure metal substrates. Neglecting any effects due to a non-zero oxygen partial-pressure inside the deposition chamber, Jackson et al. claimed that from the thermodynamic point of view, metallic Ni should be stable with respect to oxidation in contact to $SrTiO_3$, or simplified in contact to TiO_2 (cf. Figure 3.1 and references [11] & [12] in [Jackson, 1998]). The authors report that under reducing conditions inside the UHV deposition chamber, metallic Ni can be kept stable

against oxidation by incorporation of hydrogen as a process gas [Jackson, 1998]. However, Jackson et al. only addressed data for bulk materials and not surface enthalpies and surface entropies. Furthermore, influences of deposition rates and, therefore, also of the nucleation rates were not considered.

Ti, Y and Ba on SrTiO₃

Hill and co-workers [Hill, 1989] investigated different metals deposited on the (100)SrTiO₃ surface using XPS. The surface preparation was done by Ar⁺-ion sputtering followed by a heat-treatment at 900°C. LEED experiments showed a (1 × 1)-reconstruction of the substrate surface. XPS measurements of the Ti-2p lines clearly showed a shoulder on their low-energy side, which is formed by Ti³⁺ and Ti²⁺ states, indicating defect states like oxygen vacancies in the terminating layer of the substrate.

Ti/SrTiO₃: Hill et al. found characteristic shifts of the Ti-2p lines in the XPS data, which they interpret as a complete oxidation of Ti in the deposited layer for nominal film thicknesses below 0.12 nm. For higher film thicknesses, the Sr-3d and O-1s lines are nearly damped linearly with increasing film thickness. From these observations, the authors conclude a 2-dimensional growth behaviour of metallic Ti films on thin Ti–O compounds formed during the initial stages of the Ti deposition on the (100)SrTiO₃ surface.

Y/SrTiO₃: Similar to Ti, Y shows a significant shift in energy of the Y-3d lines in the XPS-spectra with increasing film thickness. Binding energies determined at a nominal film thickness of 0.05 nm already correspond to those found for yttrium oxide. With increasing film thickness the Ti-2p lines show a pronounced shoulder on the low-energy side. This shoulder reflects that the Ti in the substrate surface is reduced due to an oxidation of Y inside the film. Also for this system, the authors observed linearly decreasing XPS intensities from the substrate with increasing film thickness reflecting a 2-dimensional growth mode for Y on SrTiO₃.

Ba/SrTiO₃: Ba shows the same behaviour in the XPS data as Ti and Y indicating a reaction of Ba with the O from the SrTiO₃. Besides that, layer growth is concluded for this metal/ceramic interface.

Hill and co-workers [Hill, 1989] performed a detailed XPS study of Ti, Y and Ba on the (100)SrTiO₃ surface. However, they gave no information concerning the processing temperatures, the structure, the morphology, and the epitaxy of the metal films. Moreover, they only give evidence for an oxidation of the different metal layers without any comment on the bonding behaviour between film and substrate.

Cu/SrTiO₃

Hill et al. [Hill, 1989] also investigated the Cu/SrTiO₃ system. In contrast to Ti, Y and Ba, they did not find any shifts of the Cu-2p energy levels in their XPS data sets. Therefore, no indication of an oxidation process of Cu atoms at the interface could be revealed. Hill et al. consider Cu to be a non-reactive metal with respect to SrTiO₃. From the analysis of

the normalised intensities of their XPS spectra they concluded that Cu does not grow in a two-dimensional mode on the SrTiO_3 surface.

Conard and co-workers [Conard, 1996] investigated this system using both reduced and stoichiometric substrate surfaces by XPS, low-energy electron diffraction (LEED) and surface EELS. They prepared the substrate surfaces by heating the crystals in UHV at $T = 1000^\circ\text{C}$ and partially reoxidized them in an oxygen atmosphere afterwards. After both preparation steps the surface was found to be TiO_2 terminated. Through an analysis of the normalized XPS-intensities for Ti, O, Sr, Cu, and by a comparison to a theoretical model, the authors concluded an oxidation of Cu in the first atomic layers, and a growth behaviour, which is similar to the Stranski-Krastanov mode. Conard et al. also showed that the growth modes were identical for the stoichiometric and for the non-stoichiometric surface. The only difference is, that for the stoichiometric, i. e. the oxidised surface, which has less oxygen vacancies, less Cu atoms are in the 2D-layer, and the number of islands on top of this layer is decreased [Conard, 1996].

Andersen and Møller [Andersen, 1990] also performed XPS, UPS, surface EELS and Auger Electron Spectroscopy (AES) measurements for the Cu/SrTiO_3 system. They prepared the substrate surface by multiple sputter-heating cycles. Cu was deposited at room temperature onto the (100) SrTiO_3 surface. During the deposition they found a 3-dimensional growth behaviour for Cu. A well-defined orientation relationship between the Cu film and the perovskite substrate could not be observed. XPS and UPS measurements showed almost no bending of energy bands, which Andersen and Møller interpreted as a weak bonding between Cu and the substrate [Andersen, 1990].

All three studies of the Cu/SrTiO_3 system mentioned used the same analytical surface science methods to determine the growth of Cu and the bonding between the film and the substrate. Conard et al. [Conard, 1996] observed a Stranski-Krastanov growth mode whereas the other two groups ([Hill, 1989] and [Andersen, 1990]) observed a Volmer-Weber growth mode. However, these observations were not further confirmed by imaging techniques like SEM, AFM or TEM. In addition, Conard et al. [Conard, 1996] as well as Andersen and Møller [Andersen, 1990] did not comment on any specific orientation relationship. All three authors only give qualitative statements regarding the bonding. Differences in the bonding strength and in the observed growth modes might be caused by the different temperatures used during the deposition.

Pt/ SrTiO_3

Chung and Wessbard [Chung, 1979] investigated the growth of Pt on the (100) SrTiO_3 surface, which was cleaned before by an Ar^+ ion bombardment and showed a (1×1) -reconstruction. The applied techniques covered AES, LEED, surface EELS, and UPS. Auger-electron spectroscopy analyses exhibited a loss of Sr in the surface layer above 240°C . After this detailed surface analysis, Pt was deposited at room temperature. *In-situ* AES measurements showed a charge transfer from Ti to Pt. Apart from that, the Pt atoms showed a high level of ordering on the substrate surface [Chung, 1979].

Polli and co-workers [Polli, 2000] investigated the Pt/SrTiO₃ interface for both possible terminations of the (100) substrate surface. The surface preparation for the TiO₂ termination was done using the methods described by Kawasaki et al. [Kawasaki, 1994]. To obtain a SrO terminated substrate, Polli et al. deposited nominally 0.5 and 2.0 monolayers of SrO on the substrate surface of different samples, respectively, which was growing with an epitaxial orientation relationship. Pt was then deposited on the two differently prepared substrates and for both experiments a 3-dimensional growth of Pt was observed. On the TiO₂ terminated substrate, Pt showed a cube-on-cube orientation relationship to the substrate, whereas for the 2.0 monolayer SrO terminated substrate a (111) orientation relationship was found. Polli et al. [Polli, 2000] addressed this behaviour to the higher interface energy for the (100)SrTiO₃ surface with a 2.0 monolayer SrO layer. Polli and co-workers performed the first systematic study of growth modes of a metal on both possible surface terminations of SrTiO₃.

Al/SrTiO₃

Stanzick [Stanzick, 1998] investigated the growth behaviour of Al on the (100)SrTiO₃ surface. The surface preparation was performed by chemical etching [Kawasaki, 1994] followed by an annealing process in an O₂-atmosphere. A Volmer-Weber growth was observed for substrate temperatures between 573 K and 773 K. The observed orientation relationship was a combination of a {111}-texture and a cube-on-cube relationship between film and substrate. The author found steps in the (100)SrTiO₃ surface due to the etching processes, which were regarded to cause the observed wetting behaviour.

3.1.2 Pd/Ceramic Interfaces

Since Pd is commercially used in catalytic systems [Henry, 1998], a large number of Pd/ceramic interfaces have been investigated. Table 3.1 summarises the different Pd/ceramic systems, which are of interest for the present study. There exist both experimental and theoretical studies of the different materials systems.

In the following, the investigations of Pd on the cubic substrates listed in Table 3.1 are discussed in more detail, whereas the lower symmetry substrates like rhombohedral α -Al₂O₃ and hexagonal ZnO are of minor interest for this work, and are not considered further.

Pd/MgO

Moodie et al. [Moodie, 1977] investigated reactions between Pd and MgO by TEM at temperatures below the melting point of each of the components, i.e., at temperatures below 1827 K. An observed reaction phase exhibited liquid-like characteristics, whereas the ceramic remained strain-free, both during and after the reaction. The authors describe the reaction to be a surface phenomenon rather than a bulk one.

Henry and co-workers [Chapon, 1985] [Goyhenex, 1996] [Henry, 1991] [Henry, 1998] performed studies about the growth and the morphology of Pd/(100)MgO using different TEM-techniques. In their studies Pd was deposited onto the (100) surface of MgO at temperatures

Table 3.1: Overview for investigations performed on different Pd/ceramic interfaces. The abbreviations VW and SK in the second column denote Volmer-Weber growth and the Stranski-Krastanov growth, respectively. The substrate temperatures $T_{\text{substrate}}$ during the experimental growth process are also listed.

Substrate	Growth	Epitaxy	$T_{\text{substrate}}$	Method	References
(0001) α -Al ₂ O ₃	VW		300 K	XPS/AES	[Ogawa, 1995]
(100)MgO			< 1827 K	TEM	[Moodie, 1977]
(100)MgO	VW	(100)	≤ 630 K	TEM	[Chapon, 1985]
(100)MgO	VW	(100)	423 – 473 K	TEM	[Henry, 1991]
(100)MgO	VW/SK	(100)	273 K-523 K	AES/HeAS TEM	[Goyhenex, 1996]
(100)MgO				theory	[Goniakowski, 1998] [Goniakowski, 1999a]
				theory	[Matveev, 1999]
(100)MgO	VW	(100)	293 K	TEM/GIXS SEELFS	[Renaud, 1999]
(111)MgO				theory	[Goniakowski, 1999b]
(110)TiO ₂	SK	(111)	300 K – 800 K	XPS/LEED	[Evans, 1996]
(110)TiO ₂	VW	(111)	300 K	STM	[Xu, 1997]
(110)TiO ₂				theory	[Bredow, 1999]
(0001)ZnO	VW	(111)	≥ 573 K	AES	[Jacobs, 1985]

of $T_{\text{substrate}} = 423 - 673$ K. To ensure that most of the islands already had undergone a coalescence process, relatively large deposition times of 10-15 minutes were chosen. Selected area diffraction experiments showed a $[100](001)_{\text{Pd}} \parallel [100](001)_{\text{MgO}}$ epitaxy, i.e. a cube-on-cube orientation relationship. The Pd islands showed $\{111\}$, $\{110\}$ and $\{100\}$ facets. At substrate temperatures above 573 K, the authors found that less Pd atoms condense on the substrate surface. Therefore, the island density is significantly decreased and the island morphology is changed to pyramids with $\{111\}$ and $\{100\}$ facets. In addition, Chapon et al. [Chapon, 1985] investigated the initial stages of Pd growth. By TEM investigations they found Pd clusters randomly distributed over the whole surface. They determined activation energies from maximum island densities for different deposition temperatures [Chapon, 1985]. At room temperature, Goyhenex and co-workers [Goyhenex, 1996] found by AES and by Helium-atom Scattering (HeAS) that 2-dimensional growth occurs below a critical coverage which was determined to be one monolayer.

Renaud et al. [Renaud, 1999] performed in-situ Grazing Incidence X-ray Scattering (GIXS) and Surface Extended Energy-Loss Fine Structure (SEELFS) measurements of the

Pd/(100)MgO interface to investigate the growth behaviour, and TEM measurements to obtain information about the morphology and atomistic structure of the interface. They found that at room temperature Pd grows in the Volmer-Weber mode with a cube-on-cube epitaxy. For coverages below 4-5 monolayers the Pd film is coherent with the MgO substrate because of strain relaxations at the edges and on the free surfaces of the islands. Above 5 monolayers, misfit dislocations were found and the islands start to grow laterally on the surface and finally undergo some coalescence processes. For a coverage of approximately 35 monolayers the film becomes continuous. The adsorption site of Pd is shown to be on top of O ions of the terminating MgO(001) layer, and the steady-state value of the interfacial distance is found to be $d_{Pd-MgO} = (0.222 \pm 0.003)$ nm [Renaud, 1999].

Goniakowski [Goniakowski, 1998] performed *ab initio* full-potential linear muffin-tin-orbital calculations of the Pd/(100)MgO interface to investigate the electronic and the atomistic structure. For a model of one monolayer Pd on top of the (100)MgO surface, the author found that for energetic reasons Pd prefers nucleation on top of O. His calculations exhibit a bond length for Pd-O of 0.218 nm. Goniakowski states that the preferential adsorption site is determined by the polarization of the Pd film in the field of the MgO surface rather than by chemical bonding. In another study, Goniakowski claims that all 4d transition metals show a tendency to favour adsorption on top of the surface oxygen of (100)MgO [Goniakowski, 1999a]. For the polar (111) surface of MgO Goniakowski and Noguera [Goniakowski, 1999b] found gap states appearing for both possible surface terminations. The adsorption characteristics of Pd are controlled by the strong polar character of the surface and therefore differ substantially from those observed for the (100) surface [Goniakowski, 1998]. In particular, strong electron transfers and/or orbital hybridization between the Pd and the substrate take place, inducing significant changes of the local densities of states near the Fermi level [Goniakowski, 1999b].

Also Matveev and co-workers [Matveev, 1999] calculated the atomistic and the electronic structure of Pd/(100)MgO using a density functional approach. From a calculation of adsorption energies they found that Pd adsorbed on a non-charged oxygen vacancy position is energetically favoured compared to a regular O^{2-} site as a consequence of reduced Pauli repulsion [Matveev, 1999]. In addition, the authors calculated an interfacial distance (Pd-O bond length) of 2.11 Å, which is somewhat smaller than the value found by Renaud and co-workers [Renaud, 1999]. The smaller value, provided by the theory, is considered to be a coverage effect since the calculations were performed in the "zero-coverage limit" [Matveev, 1999].

In conclusion, there exists a wide range of both experimental and theoretical studies of the growth processes and the bonding of Pd/(100)MgO [Moodie, 1977] [Chapon, 1985] [Henry, 1991] [Goyhenex, 1996] [Goniakowski, 1998] [Goniakowski, 1999b] [Matveev, 1999] [Renaud, 1999] [Goniakowski, 1999b]. All authors found Volmer-Weber growth modes for Pd in an extended temperature range. The 2-dimensional growth reported by Goyhenex [Goyhenex, 1996] is only valid for coverages below one monolayer where no extended layer can be formed. This interpretation conforms with observations by Renaud and co-workers [Renaud, 1999]. Theoretical investigations provide a detailed understanding of the nucleation sites for Pd and the corresponding electronic structures. Bond lengths of (2.22 ± 0.03) Å

[Renaud, 1999] and 2.11\AA [Matveev, 1999] from experiment and theory, respectively, correspond to each other within the assumptions and restrictions in the theoretical approaches. However, the electronic structure in terms of the unoccupied local densities of states has not been addressed so far. The study of Moodie et al. [Moodie, 1977] is not directly comparable to the other cited investigations since they observed the reaction behaviour for this interface at very high temperatures while the other reported studies used much lower temperatures (cf. Table 3.1).

Pd/TiO₂

Evans et al. [Evans, 1996] investigated the adsorption of carbon monoxide on (110)TiO₂ supported palladium films. They investigated the growth behaviour of Pd on the rutile substrate by LEED and XPS. For low Pd coverages of the substrate (< 3 monolayers) Evans and co-workers did not find a significant ordering of the adatoms on the substrate surface at 300K . However, an additional annealing process at 500K showed a clustering of the metal atoms up to a size of 1 nm leading to a highly dispersed Pd coverage of the substrate surface. At higher coverages (10-20 monolayers) they observed a nucleation of Pd already at 300K . Annealing at 500K again led to a clustering with high dispersions. For coverages above 10 monolayers Evans and co-workers [Evans, 1996] observed Pd islands with their (111) facets parallel to the (110) plane of the TiO₂-substrate. The observed growth mode was reported to be of Stranski-Krastanov type.

Xu et al. [Xu, 1997] performed a STM and STS study concerning the nucleation, growth and structure of Pd/(110)TiO₂ under UHV conditions. They deposited Pd at $T_{\text{substrate}} = 300\text{K}$ on well-defined (1×1) -reconstructed (110) surfaces of TiO₂. Pd was observed to grow 3-dimensionally (Volmer-Weber growth mode) on the substrate surface. The initial adsorption site for Pd on the (110)TiO₂ surface was found to be the fivefold-coordinate Ti rows. Due to the presence of $1 \times 10^{-6}\text{ Torr CO}$, cluster growth for Pd was also observed [Xu, 1997]. The electronic structure, investigated by STS, exhibited a transition from a non-metallic to a metallic nature for an atomic cluster size of $250 - 350$ atoms.

Bredow and Pacchioni [Bredow, 1999] performed a theoretical study of the nucleation of Pd on top of the non-reconstructed (100)TiO₂ surface using a density functional approach. Their calculations showed that for isolated Pd atoms or for dimers, nucleation is preferred on top of Ti rows of the substrate, whereas for a full coverage the calculations show that the oxygen sites are energetically favoured. Bredow and Pacchioni [Bredow, 1999] describe these different results to be effects of interactions of different adatoms. Therefore, they claimed that correlation effects between the Pd atoms dominate the choice of the nucleation sites. However, the authors found Pd to be covalently bonded to the TiO₂ substrate, while no charge transfer is observed.

All three investigations, which were reported in this section, showed a 2-dimensional growth of Pd on the (110)TiO₂ surface for low coverages (single atom [Bredow, 1999] up to 3 monolayers [Evans, 1996]). The experiments showed a clustering at higher temperatures (500K [Evans, 1996] [Xu, 1997]) and a 3-dimensional growth at higher coverages (above 10

Table 3.2: Overview for investigations performed on different Ni/ceramic interfaces.

Substrate	Growth	Epitaxy	$T_{\text{substrate}}$	Method	References
(100)MgO		(100)	293 K	TEM	[Gao, 1988]
(100)MgO		(100)	580 K	HRTEM	[Nakai, 1995]
(100)MgO	VW	(100) & (110)	293 K	GIXS	[Barbier, 1998]
(100)SrTiO ₃				theory	[Jackson, 1998]
(100)SrTiO ₃		293 K		UPS, RHEED	[Kido, 2000]

monolayers [Evans, 1996]). Bredow and Pacchioni [Bredow, 1999] explained this behaviour to be a correlation effect of the different adatoms with each other. However, in none of the reported papers the authors comment on a quantitative bonding analysis between the film and the substrate. Also, a comparison of experimentally and theoretically determined bonding energies could not be performed since no experimental values exist.

3.1.3 Ni/Ceramic Interfaces

Investigations of interfaces between Ni and different oxidic substrates, which are related to the present study, are summarized in Table 3.2. A large number of experimental investigations of the morphology and the growth behaviour exist for the Ni/MgO system. Most of these investigations demonstrated that at room temperature Ni grows polycrystalline on the (100)MgO surface (cf. [Barbier, 1998], [Bialas, 1977], [Bialas, 1994], [Fitzsimmons, 1994], [Hoel, 1990], [Hussain, 1989], [Kiselev, 1989], [Maruyama, 1995], [Nakai, 1995], [Pacchioni, 1996], [Qiu, 1994], [Reniers, 1996], [Raatz, 1989], and [Sato, 1962]). Theoretical investigations [Pacchioni, 1996] [Rösch, 1997] showed that Ni is expected to interact strongly with the (100)MgO surface. For this system a relatively large adhesion energy of 0.62 eV/atom was calculated in the case of Ni above an O site of the substrate surface [Pacchioni, 1996] [Rösch, 1997].

Gao et al. [Gao, 1988] studied the condensation of MgO smoke on a (100)Ni surface at room temperature. By TEM they observed small MgO clusters ($0.02 \mu\text{m}$ - $0.2 \mu\text{m}$) randomly spread over the metal surface, each with their (100)surfaces parallel to the (100) surface of Ni. After annealing at 873 K for 9 hours the authors observed that the MgO particles rotated into an orientation corresponding to a local minimum in energy. A detailed analysis showed that these low-energy orientations correspond to defined coincident site lattice orientations [Gao, 1988].

Nakai and co-workers [Nakai, 1995] performed HRTEM studies of the Ni/(100)MgO interface in which they found a cube-on-cube epitaxy between the film and the substrate, combined with a dislocation network. In their study, the Ni films were deposited by sputtering at substrate temperatures of 580 K.

Table 3.3: Overview for investigations performed on different Cr/ceramic interfaces.

Substrate	Epitaxy	Method	References
(10 $\bar{1}$ 0)Al ₂ O ₂	(110)	SEM & TEM	[Backhaus-Ricoult, 1988] [Backhaus-Ricoult, 1994]
(0001)Al ₂ O ₂	(110) & (111)	SEM & TEM	[Backhaus-Ricoult, 1994]
(10 $\bar{1}$ 0)Al ₂ O ₂	(110)	AES	[Gautsch, 1995]
(10 $\bar{1}$ 0)Al ₂ O ₂	(110)	TEM & EDXS	[Gaudette, 1997]

The growth of Ni on (100)MgO was studied by Barbier et al. [Barbier, 1998] by GIXS at room temperature. The authors found a 3-dimensional island growth (Volmer-Weber growth mode) of Ni on the (100) substrate surface. A mixed epitaxial orientation relationship of (100)_{Ni} || (100)_{MgO} (cube-on-cube) and (110)_{Ni} || (100)_{MgO} was found, favouring strain relaxation within the Ni film. Barbier et al. claimed that Ni nucleates over the O sites of the substrate surface and that coalescence processes of the Ni islands take place for coverages between 10 and 27 monolayers. An anisotropic relaxation and no misfit dislocations were observed. After annealing of the interfaces at 1223 K, a single crystalline Ni film was observed on the (100)MgO surface with a cube-on-cube orientation relationship.

In conclusion, several systematic experimental and theoretical studies were performed to investigate the growth behaviour of Ni on the (100)MgO surface and the bonding between the film and the substrate. The authors cited above agree about the growth behaviour and the strong interaction, i.e., the strong bonding between Ni and the substrate. Differences in the film morphology and the epitaxial orientation relationships are due to different processing parameters such as the substrate temperatures, the sputter rates, etc. However, no experimental evidence of the adsorption site was given.

Investigations have also been reported for Ni/SrTiO₃ interfaces [Jackson, 1998] [Kido, 2000], which were addressed in section 3.1.1.

A detailed study of the local electronic structure by a combination of experiment and theory has not been performed for any Ni/oxide-ceramic interface. Therefore, it is not clear whether a formation of a thin layer of NiO or only a strong hybridization between Ni and O is present at the different Ni/ceramic interfaces. Also the possibility of a charge transfer across the interface has not yet been discussed.

3.1.4 Cr/Ceramic Interfaces

In the literature, there exist only few reports of interfaces between Cr and ceramic materials. Concerning oxide ceramics, only investigations of Cr/Al₂O₃ interfaces are reported, which are based on internal oxidation processes and are summarised in Table 3.3. Backhaus-Ricoult and co-workers [Backhaus-Ricoult, 1988] [Backhaus-Ricoult, 1994] investigated Cr-

doped single crystalline α - Al_2O_3 after internal reduction. The crystals were reduced in an $\text{Al}/\text{Al}_2\text{O}_3$ buffer for time periods of 1 to 100 hours. They were then analysed by SEM and TEM. The authors observed needle-shaped and spheroidal-shaped precipitates of metallic Cr [Backhaus-Ricoult, 1994]. The number of spheroidal precipitates was found to be larger than the number of the needle-shaped ones. All needle-shaped precipitates provided the same type of elongated interfaces, which consisted of the prismatic $(10\bar{1}0)$ plane of Al_2O_3 and the (110) plane of the bcc-structured Cr. For both crystals, these planes have a high atom density and therefore a low interfacial energy. In contrast to that, the top and bottom interfaces of the needles never showed this interfacial configuration. For the spheroidal precipitates, the interfacial planes were always high-density planes in Al_2O_3 . Sometimes the interfaces were also formed by high-density planes in Cr [Backhaus-Ricoult, 1994]. The authors stated that even though the atom density in the interfacial plane is high and the interface energy is low, the final size of the spheroidal precipitates is limited by a rather bad match of the two crystal lattices. However, the largest interfaces for these precipitates again had the same configuration as those observed for the needle-shaped structures [Backhaus-Ricoult, 1994].

By AES, Gautsch [Gautsch, 1995] investigated the mixing of Al and Cr at a $\text{Cr}/\text{Al}_2\text{O}_3$ interface, which was induced by ion bombardement with 100 keV-200 keV Ar^+ -ions. For polycrystalline films the author observed migration distances of Cr and Al across the sharp interface of 100 nm to 200 nm, induced by thermal and/or radiation induced processes.

Gaudette and co-workers [Gaudette, 1997] performed investigations of the influence of Cr addition on the toughness of $\text{Ni}/(10\bar{1}2)\text{Al}_2\text{O}_3$ interfaces in a moist environment. They observed that Cr forms precipitates of chromium carbide at the interface by gettering carbon due to contamination effects of the specimens, e.g. inside the electron microscope. Another possible process postulated by the authors is the dissolution of Al_2O_3 in the alloy which disperses the interface contaminants, and thereby enabling a strong bonding [Gaudette, 1997]. In general, the authors claimed that adding Cr to a $\text{Ni}/(10\bar{1}2)\text{Al}_2\text{O}_3$ composite enhances the interface toughness by eliminating the sensitivity of the interface to stress corrosion.

In summary, there exist only few papers reporting investigations of Cr/ceramic interfaces. Due to its high reaction probability (cf. Table 2.1), Cr is used to stabilize or to enhance the bonding of other metal/ceramic interfaces [Gaudette, 1997]. In fact, this is done for many Ni/ceramic composites [Calow, 1971a][Calow, 1971b]. However, a systematic study of the bonding at Cr/ceramic interfaces has not been performed so far, neither with surface science techniques nor with TEM or theoretical methods. In addition, the above mentioned authors, except Backhaus-Ricoult et al. [Backhaus-Ricoult, 1994], did not comment on epitaxial orientation relationships between Cr and the ceramic. Also, a study of the growth behaviour of Cr on oxidic substrates is not reported in the literature, except from some oxidation studies of Cr [Graham, 1995]. In this study different chromium oxides were found to grow with an epitaxial orientation relationship on metallic Cr. Dependent on the temperature, *fcc*, *bcc* and tetragonal oxides were formed, which was determined by RHEED experiments [Graham, 1995].

3.2 Spatially resolved EELS/ELNES

Electron Energy-Loss Spectroscopy (EELS) has become an important tool in materials science for the analysis and characterization of materials with respect to their chemical composition and their electronic structure [Egerton, 1996] [Reimer, 1994]. Since the development of the dedicated STEM [Crewe, 1971][Isaacson, 1975], EELS experiments have become possible at high spatial resolution of 1 Å-10 Å [Brown, 1981] [Batson, 1993] [Batson, 1994]. To obtain high spatial resolution, there are three different attempts discussed in the literature for measuring electron energy-loss spectra, or more specifically, the electron energy-loss near-edge structures (ELNES) of the absorption edges: the spatial difference technique [Berger, 1982] [Bruley, 1993] [Müllejans, 1994], the atomic column resolved EELS technique [Browning, 1993a] [Browning, 1993b] [Batson, 1993] [Batson, 1994] [Duscher, 1998], and the acquisition of EELS linescans [Colliex, 1984] across a 2-dimensional defect, e.g. an interface.

Berger and Pennycook [Berger, 1982] provided a method to detect nitrogen in {100} platelets in diamond. They acquired EELS data in the energy-loss range of 250 eV to 500 eV, in which the C K-edge due to the carbon support film and the N K-edge appear. The electron beam was scanned over areas of 1 nm² in size, first on the diamond platelet and afterwards using the same acquisition parameters in a region nearby. By subtracting the two spectra after the acquisition, the authors were able to detect the N K-edge at approximately 406 eV, which was superimposed by the strong C K-edge intensities before applying the difference technique.

Bruley and Müllejans [Bruley, 1993] [Müllejans, 1994] further developed this technique for the determination of interfacial ELNES data. Bruley [Bruley, 1993] was able to determine interface specific ELNES data of the Al L_{2,3}-edge of a $\Sigma = 11$ grain boundary in α -Al₂O₃ by gradually subtracting bulk spectra from the spectra acquired in a region containing the interface. In these studies, the amount of the subtracted bulk intensities was determined by trial-and-error methods. This technique is referred to as the so-called *spatial difference technique*, and was used by several authors to investigate the near-edge fine structure of internal interfaces in ceramics [Müllejans, 1995] [Gu, 1999a] [Gu, 1999b] [Nufer, 2001b], and of metal/ceramic interfaces, predominantly of the Cu/Al₂O₃ system [Scheu, 1995].

Gu [Gu, 1999a] [Gu, 1999b] developed an advanced method based on the spatial difference technique to reduce the subjective nature of gradually subtracting bulk intensities. This method regards the subtraction of spectra as a vector orthogonalization procedure to separate two dissimilar ELNES patterns [Gu, 1999a]. However, Gu did not achieve a complete elimination of the subjectivity of this technique.

Imhoff et al. [Imhoff, 1999] acquired ELNES linescans perpendicular to a Cu/MgO interface. By comparing spectra recorded in the bulk materials to spectra from the interface region, differences are regarded as belonging to the interface specific ELNES component. To finally extract this component they used the spatial difference technique [Bruley, 1993] [Müllejans, 1994]. In their application they used a normalization routine to scale the spectra in intensity for a further quantitative EELS analysis. However, no reduction of the subjective nature of the spatial difference technique could be obtained.

A more quantitative way to extract interface specific ELNES components was provided by Scheu and co-workers [Scheu, 2000], who calculated approximates of scaling factors finally used in the spatial difference technique. Their attempt is presented and further discussed in section 4.1.3, since this technique is also used in this work.

Nufer et al. [Nufer, 2001b] showed that the percentage ratio of bulk versus interfacial intensities can be obtained by counting atom columns in the probe region for interfaces with atomic structure models derived by alternative means (HRTEM, LDFT).

Muller recently has shown that core-level shifts of ELNES data due to changes in bond lengths and coordination of atoms probably can produce artifacts by using the spatial difference method [Muller, 1999]. He claims that the subtraction of ELNES data leads to the calculation of the first derivative of the spectrum in the case of appearing core-level shifts. This would introduce extra intensities into the so-called interface specific line shape, which are not related to the real interfacial electronic structure. Nufer however showed that such artifacts can be distinguished from the true interfacial spectra [Nufer, 2001b].

Browning and co-workers [Browning, 1993a] [Browning, 1993b] and Batson et al. [Batson, 1993] provided the so-called atomic column resolved EELS method. Using this technique in a STEM, the so-called Z-contrast image is used to place the electron beam on distinct atomic columns after tilting the specimen in a low-indexed zone-axis. Spectra were acquired by scanning the probe along the planes parallel to an interface [Browning, 1993b]. If the probe size is smaller than the interatomic distances, the authors claim that spectra of individual atomic columns can be acquired to analyse the local unoccupied densities of states [Browning, 1993b].

So-called atomic column resolved EELS investigations have been reported for different materials such as Si/SiO₂ interfaces [Batson, 1994], [001] tilt grain boundaries in SrTiO₃ [Browning, 1996] and TiO₂ [Browning, 1997], and doped grain boundaries in MgO and SrTiO₃ [Duscher, 1998]. Duscher et al. were able to analyze ELNES data by atomic column resolved EELS [Duscher, 1998]. However, atomic column resolved HAADF images and ELNES data were not acquired simultaneously under the same experimental conditions [Duscher, 1998].

Loane et al. [Loane, 1988] have shown that the current density distribution throughout the sample is not only concentrated on one atomic column but is spread over multiple atomic columns as a function of specimen thickness. Therefore, atomically resolved EELS data contain signals also originating from electrons channeling through atomic columns nearby (cf. Figure 3.2 taken from [Egerton, 1996]). An additional effect is the beam blurring inside the sample [Titchmarsh, 1989]. Thus, data measured by this technique also consist of a mixture of interface specific data and the adjacent bulk data.

Colliex and Mory [Colliex, 1984] measured EELS and ELNES line-profiles across interfaces by scanning the beam perpendicular to the interface, while the interface was tilted edge-on to the incident electron beam. By this technique they were able to obtain high spatial resolution by decreasing the step-width between two acquisitions. Changes of the spectral line-shape at the interface compared to the pure bulk spectra are interpreted as interface specific signals. However, this technique always provides a mixture of the interfacial signal with the pure bulk signal, especially for larger specimen thicknesses due to the beam

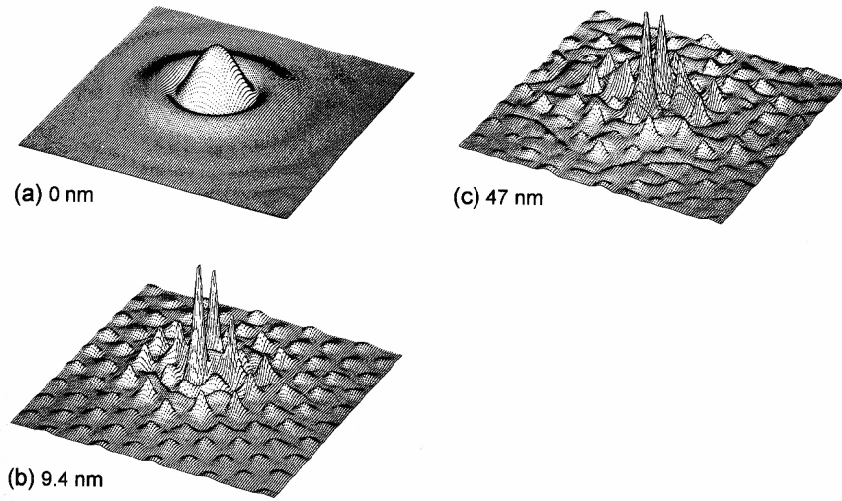


Figure 3.2: Amplitude of the fast-electron wavefunction (square root of current density) for (a) 100 keV STEM probe randomly placed at the $\{111\}$ surface of a silicon crystal, (b) the same electrons after penetration to a depth of 9.4 nm, and (c) after penetration by 47 nm. Channeling has largely concentrated the electron flux along $\langle 111 \rangle$ rows of Si atoms [Loane, 1988].

blurring [Titchmarsh, 1989]. A disadvantage of this technique is that one gets no image of the interface during acquisition in contrast to the spatial difference method. Therefore, a manual compensation for spatial drift is impossible, which can cause unreliable results for non-stable acquisition conditions with respect to spatial drift.

3.3 Goal of the Thesis

The aim of this thesis is a detailed analysis of the electronic structure of the Pd/(100)SrTiO₃ interface. For this metal/ceramic system the growth behaviour and the atomistic structure of the interface was previously investigated with surface science techniques [Richter, 2000] and theoretically by Ochs [Ochs, 2000]. The methods used in the present work are transmission electron microscopy techniques, such as CTEM, HRTEM and STEM-EELS/ELNES, and the local density functional theory to model the local densities of unoccupied states and to compare them to ELNES data. For this study, it was advantageous to use the results from earlier studies of Richter [Richter, 2000] and Ochs [Ochs, 2000] to get a detailed understanding of the atomistic and the electronic structure of the Pd/SrTiO₃ interface. In addition, the obtained results for this non-reactive materials system should be transferable to some extent for the understanding of the interfacial structures at the Ni/(100)SrTiO₃ and the Cr/(100)SrTiO₃ interfaces.

From the methodical point of view, the comparison of ELNES data with local densities of unoccupied states data, calculated by using LDFT, is of particular scientific interest. By a

combination of both experiment and theory an experimental verification of the theoretically obtained models [Ochs, 2000] becomes possible. Moreover, this synthesis of experiment and theory should be able to verify the validity of the spatial difference technique used in this work, which has been critically discussed in the scientific community.

Chapter 4

Methods

In this chapter the methods applied in this work will be described in detail. On the experimental side, the metal/ceramic interfaces were investigated using various TEM techniques (Section 4.1), such as conventional TEM, HRTEM (Subsection 4.1.1) and EELS (Subsection 4.1.2). In Section 4.2 the theoretical approaches will be described in detail. These cover the local density functional theory (Section 4.2.1) and a multiple scattering approach (Section 4.2.3).

4.1 Experimental Details

In this work a JEOL JEM2000FX (200kV accelerating voltage, point-to-point resolution of 0.28 nm, information limit at ~ 0.14 nm [Jeol]) was used to investigate the film morphology, and a JEOL ARM1250 (1250kV accelerating voltage, point-to-point resolution of 0.12 nm, information limit at ~ 0.09 nm, [Phillipp, 1994], [Dehm, 1996]) with the side-entry pole piece ($C_s = 2.7$ mm) was used for high-resolution investigations. The electronic structure of the interfaces was investigated in terms of the electron energy-loss near-edge structures using a VG HB501UX STEM. Since the main focus of this work was on the electronic structure of the interfaces, the STEM is described in more detail than the conventional TEM instruments. In the next section, the limiting experimental factors such as spatial resolution and energy resolution in the STEM will be described. The image formation theory, i.e. the propagation of fast electrons through the STEM, is described more generally in Appendix A.

4.1.1 Scanning Transmission Electron Microscopy

A VG HB501UX dedicated STEM was used to acquire EELS data and Energy Dispersive X-ray spectroscopy (EDXS) data of metal/ceramic interfaces at high spatial resolution. Using this instrument, it is possible to acquire EELS and EDXS spectra simultaneously, while recording images of the specimen on two different annular detectors. A schematic drawing of the STEM is given in Figure 4.1. The microscope is operated in UHV at an accelerating voltage of 100 kV and is equipped with a cold field-emission gun. The microscope has an

ultra-high resolution top-entry pole-piece with a C_s -value of 1.3 mm.

The STEM contains two different condensor lenses (C1 & C2, cf. Figure 4.1). In the standard operating mode only the lens denoted with C2 is used. In addition, C1 can be used optionally to further increase or decrease the beam current. As can be inferred from Figure 4.1, in a dedicated STEM the objective lens is situated in front of the specimen with respect to the electron beam direction. In contrast to that, in a conventional TEM the image formation lens is placed behind the specimen. This aspect is pointed out in more detail in Appendix A.

The Stuttgart VG STEM is equipped with an energy dispersive X-ray spectrometer to acquire X-rays, which are emitted from the specimen due to the electron irradiation. The detector (Noran Voyager) is situated in front of the specimen (cf. Figure 4.1) and consists of a Li-doped Si semiconducting crystal.

For recording EELS data, a Gatan DigiPEELS766 parallel electron energy-loss spectrometer (PEELS) is adapted on top of the microscopes column. The PEELS consists of a magnetic prism and a system of four quadrupole lenses [Krivanek, 1987]. The magnetic prism disperses the electrons in energy, forming an electron energy-loss spectrum. This spectrum is then imaged on a Yttrium-Aluminium-Garnet (YAG) scintillator by the four quadrupole lenses. The YAG is coupled via a fiber optic to a photodiode array or a CCD¹ camera. The majority of the spectra presented in this work were acquired using a photodiode array (PDA, Hamamatsu Inc.) consisting of 1x1024 photodiodes. Some spectra were recorded using the new UHV Enfina system (Gatan Inc.) [Hunt, 2001], which detects the signals coming from the scintillator by a 100x1370 pixel CCD camera. Unless stated otherwise, all spectra shown in the following were detected using the photodiode detector. A characterization of the new CCD-based PEELS detector in comparison to the formerly used system is given in Appendix B.

In a VG STEM images can be acquired by three different detectors. One is a removable bright-field detector which collects electrons scattered in semi-angles up to 19 mrad. Removing the bright-field detector one can choose between two different PEELS entrance apertures of 2 mm and 4 mm width. In these cases, an annular dark-field detector (ADF) is used instead of the bright field-detector, collecting electrons scattered in semi-angles of 12 mrad to 38 mrad (2 mm aperture) and 19 mrad to 38 mrad (4 mm aperture), respectively. In addition to these setups, signals from a high-angle annular dark-field detector (HAADF) are available, which are due to electrons scattered in semi-angles between 53 mrad and 173 mrad. For the electrons registered by the HAADF detector, coherent scattering effects are negligible. Therefore, the intensity in the acquired HAADF-images is approximately proportional to the square of the atomic number of the elements in the specimen, corresponding to the Rutherford scattering process. This results in a compositional map of the sample with high atomic number contrast, a so-called Z-contrast image [Pennycook, 1988].

To perform EELS investigations at high resolution, one has to take into account two different resolution limits of the microscope: the spatial resolution and the energy resolution.

¹CCD = charge coupled device

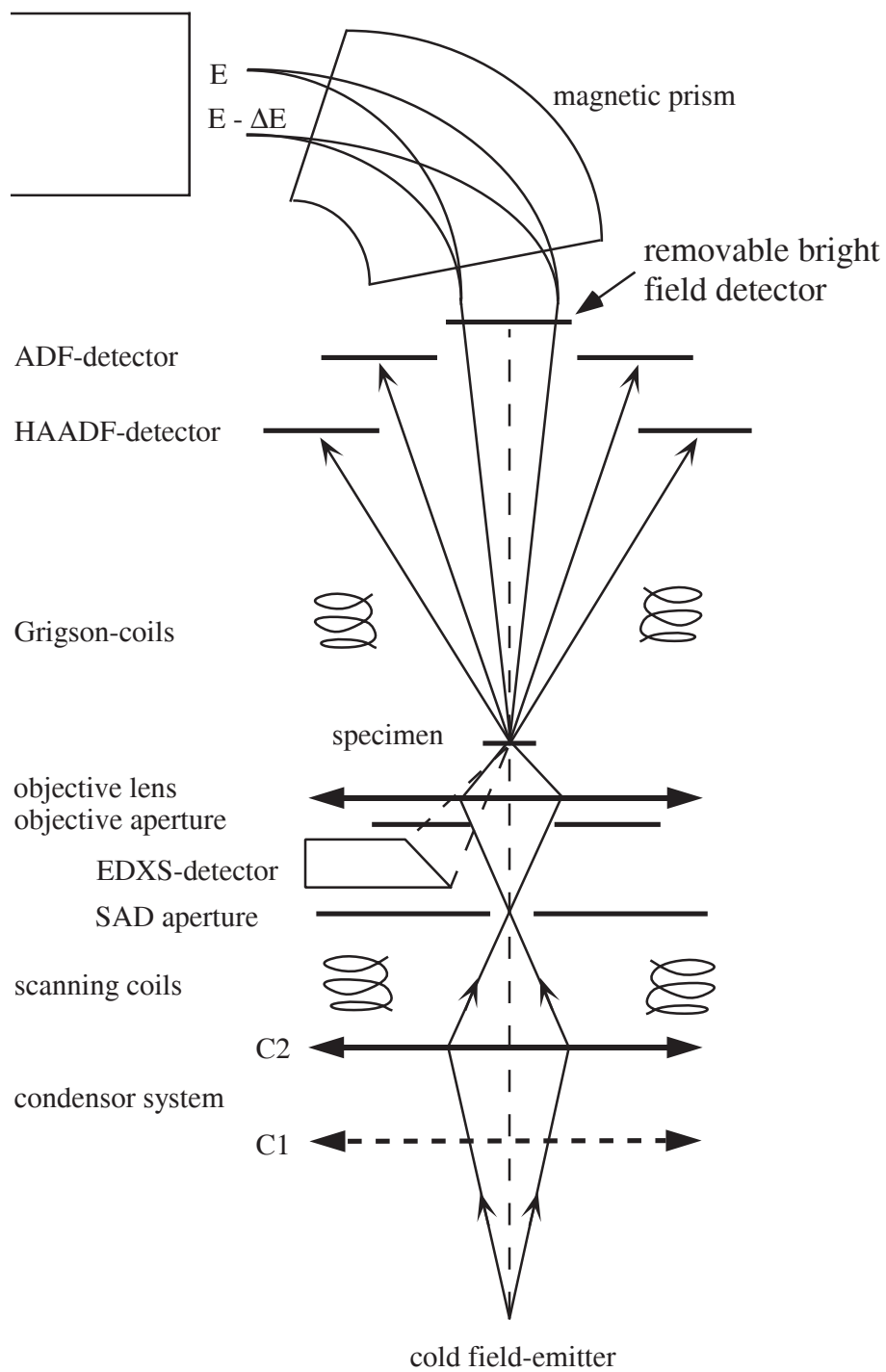


Figure 4.1: Schematic drawing of the VG HB501 UX dedicated STEM used in this work.

The spatial resolution can be expressed by the effective diameter of the electron beam in the specimen plane, whereas the energy resolution is given by the full-width at half-maximum (FWHM) of the energy distribution of the electron beam. Both are discussed in detail in the next two paragraphs.

Spatial Resolution in the STEM

In the STEM the diameter of the electron beam hitting the specimen determines the spatial resolution in the corresponding experiment. Several electron optical lenses are used in the STEM to demagnify the image of the tip and for focussing it onto the specimen surface. In an ideal microscope without any aberrations the limiting factor for the beam diameter is the beam current density. Assuming a rotation-symmetry of a gaussian current density distribution for the electron beam, the diameter of the beam is then given by [Reimer, 1997]

$$d_0 = \sqrt{\frac{4I_0}{\pi^2 B}} \cdot \frac{1}{\alpha}. \quad (4.1)$$

I_0 denotes the beam current, B the brightness of the electron gun and α the semi-angle of the effective aperture of the microscope. For analytical TEM, especially for EELS, high beam currents are required to obtain large signal-to-noise ratios in the detector plane. In a standard alignment of the STEM used in this work, the beam current I_0 is approximately 1 nA [Thomas, 1993]. The brightness B of the cold FEG is in the range of $B = 10^9$ A/cm²sr. In the standard setup, an objective aperture of 50 μ m, corresponding to a semi-angle of $\alpha = 10$ mrad, is used. Therefore the resulting diameter of the electron beam hitting the sample in the standard setup has a minimum value of $d_0 = 0.6$ nm.

As shown in Appendix A, in a *real* microscope lenses suffer from aberrations similar to those of glass lenses in light optics, which limit the spatial resolution and therefore have to be considered in the determination of the diameter of the electron beam.

1. *spherical aberration*: Comparable to the optical microscope, electron beams having a large distance from the optical axis (axis through the center of the lens), have a smaller focal length than those running close to the optical axis. Therefore, a circular focus disk rather than a focus spot is formed in the back focal plane of the lens. The diameter of this disk d_s is determined by [Reimer, 1997]

$$d_s = \frac{1}{2} C_s \alpha^3. \quad (4.2)$$

C_s is the aberration coefficient for the spherical aberration. Therefore, d_s becomes 0.65 nm for an objective aperture of $\alpha = 10$ mrad.

2. *chromatic aberration*: Electrons with different wavelengths, i.e. different kinetic energies, are refracted differently by the magnetic lenses of the microscope. Thus, for an energy spread ΔE of the high-energy electrons, a circular disk with the diameter d_c is

formed in the back focal plane. d_c is given by [Reimer, 1997]

$$d_c = \frac{1}{2} C_c \frac{\Delta E}{E_0} \alpha. \quad (4.3)$$

E_0 denotes the primary energy of the electrons ($E_0 = 100$ keV in this work) and C_c is the chromatic aberration coefficient. Since in a dedicated STEM the electron beam does not penetrate through a further lens system after transmitting through the specimen, the energy spread of the electron gun determines the chromatic aberration. For a kinetic electron energy of 100 keV and assuming $C_c = 2.0$ mm [Reimer, 1997], d_c becomes 0.06 nm. Therefore, for a dedicated STEM the chromatic aberration is by one order of magnitude smaller than the spherical aberration and thus negligible.

3. *axial astigmatism*: Inhomogenities in the polepiece material, ellipticities of the polepiece bore and charging of the specimen and aperture diaphragms result in astigmatism. In this case, electron waves in sagittal and meridional bundles are focussed at different focal distances, which result in crossed line foci. For many bundles a sperical focus disk is formed whose diameter d_A is given by

$$d_A = \Delta f_A \alpha. \quad (4.4)$$

d_A is proportional to the astigmatic focus length difference Δf_A . This aberration can be compensated by stigmators, which consist of a magnetic quadrupole lens. In the VG the axial astigmatism of the condensor lens system and the objective lens is compensated by aligning a condensor stigmator and an objective stigmator, respectively. Therefore, the axial astigmatism is not a limiting factor for the spatial resolution.

4. *diffraction aberration*: Diffraction effects of electron waves at apertures or pole-pieces result in an Airy-disk in the back focal plane with the diamter d_B :

$$d_B = 0.6 \frac{\lambda}{\alpha}. \quad (4.5)$$

λ is the wavelength of the electrons, which has a value of approximately 3.70 pm for an accelerating voltage of 100 keV. For the standard alignment of the microscope, d_B becomes 0.2 nm.

To determine the total lens aberrations in the microscope, the different aberrations are considered to be independent. Therefore, the total minimum beam diameter d_{total} can be calculated by [Reimer, 1997]

$$d_{total}^2 = d_0^2 + d_s^2 + d_c^2 + d_B^2 \quad (4.6)$$

This reveals a minimum obtainable beam diameter of $d_{total} = 0.91$ nm for the standard setup of the STEM with a 10 mrad objective aperture and a beam current of $I_0 = 1$ nA. This value was also proved experimentally by Thomas and co-workers [Thomas, 1993]. The highest obtainable spatial resolution of the VG HB501 UX is 0.22 nm, which is in general accessible

by a high-resolution setup of the microscope in which, e.g., the beam current is significantly reduced. For this setup, Z-contrast imaging with atomic resolution of, e.g., the Pd/SrTiO₃ interface is not possible in $\langle 100 \rangle$ zone-axis orientation because of the too small lattice spacing within the Pd film. However, also for HAADF imaging of bulk SrTiO₃ the stability of the Stuttgart VG STEM is not sufficient to obtain these high-resolution conditions due to electrical and mechanical vibrations within the environment of the laboratory.

Energy Resolution in the STEM

For investigations of the fine structure and of the low-loss regime in EEL-spectra a high energy resolution is required so that sharp spectral features can be observed. In this section the instrumental energy broadening is discussed, whereas effects due to the investigated material, such as lifetime effects, are discussed later (see sections 4.2.1 and 4.2.2). The highest energy resolution δE_0 which is achievable in a measured energy-loss spectrum is determined by four factors: The width of the energy distribution provided by the electron gun (δE_{tip}), the energy resolution of the spectrometer (δE_s), the spatial resolution of the detector array s , and the dispersion of the spectrometer D . δE_0 is then given by [Egerton, 1996]

$$(\delta E_0)^2 = (\delta E_{tip})^2 + (\delta E_s)^2 + (s/D)^2 \quad (4.7)$$

The width of the energy distribution of the tip δE_{tip} is given by the natural energy width of the beam electrons, instabilities of the acceleration voltage, and by the so-called Boersch-effect [Boersch, 1954]. This effect describes the increase in the energy broadening due to electrostatic interactions of the beam electrons at the cross-overs in the microscope. For a cold field-emission gun, δE_{tip} is in the range of 0.2 eV to 0.3 eV.

The energy resolution of the spectrometer δE_s is determined by the electron optics in the PEELS. Since the spectrometer is located beyond the specimen, the beam electrons penetrating the PEELS have different kinetic energies due to inelastic scattering processes within the sample. This results in chromatic aberrations of the spectrometer lenses and therefore finally in a defocussed beam on the scintillator, which is located in the energy dispersive plane of the spectrometer. This leads to a lower energy resolution at high energy-losses. In a modern energy-filtering TEM (EFTEM), this effect is avoided by increasing the accelerating voltage of the electrons by the same value as the energy-loss measured in the detector. In this case, all the electrons penetrating the spectrometer have almost the same kinetic energy and chromatic aberrations are negligible. In a VG STEM this technique is not available and therefore, δE_s shows a $1/\Delta E$ dependence.

The spatial resolution of the detector array s is determined by the so-called point-spread-function (PSF). This function describes the resulting intensity distribution after illuminating only one pixel of the detector array. It is a characteristic function for each detector. The influence of the PSF on the measured spectra can be compensated by a deconvolution of the spectra with the PSF after the acquisition. In this work, this technique was not applied since a deconvolution significantly decreases the signal-to-noise ratio of the EELS data. A more

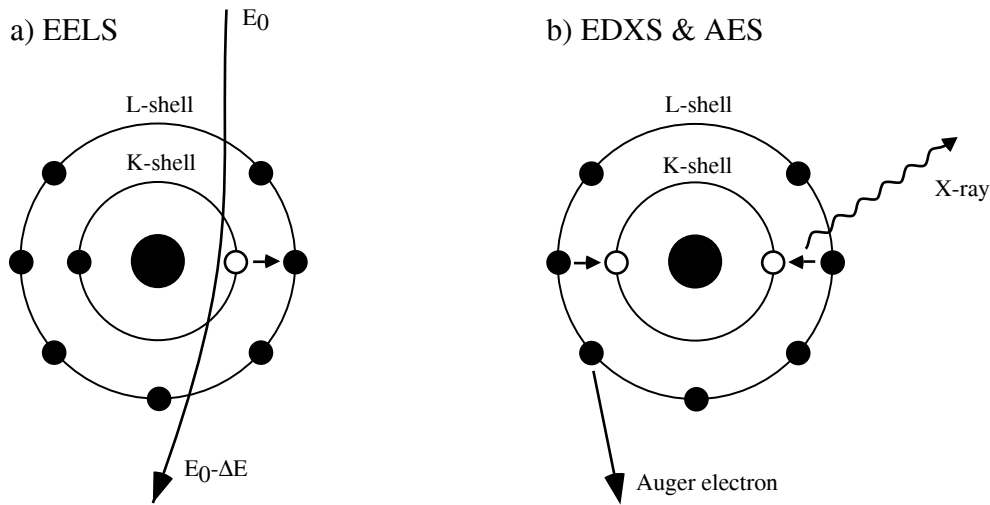


Figure 4.2: Schematic drawing of an inelastic scattering process on a single atom. a) EELS: excitation of a core-electron by an electron of the electron beam. The primary beam has the kinetic energy E_0 and $E_0 - \Delta E$ before and after the interaction with the specimen, respectively. b) EDXS: Characteristic X-ray photons are emitted due to the relaxation of an excited atom. Alternatively, also an Auger electron can be emitted. These two processes are regarded to be secondary processes.

detailed analysis of the PSF functions for the detectors used in this work is given in appendix B.

The energy resolution in the experiment can be measured as the FWHM of the zero-loss peak (see chapter 4.1.2). In a standard setup of the microscope the energy resolution is 0.7 eV (dispersion: 0.1 eV/channel) or 0.9 eV for a dispersion of 0.3 eV/channel.

4.1.2 Electron Energy-Loss Spectroscopy

The electrons of the primary beam of the microscope lose some of their kinetic energy due to inelastic scattering processes within the specimen. This energy-loss is denoted by ΔE . The inelastic interaction can lead to an excitation of an electron from the occupied states of the specimen into unoccupied states of the solid and is therefore regarded as the primary excitation process (cf. Figure 4.2). Whether the excitation takes place between a core-state and the conduction band or within the conduction band, the excitations are called interband or intraband transitions, respectively. An energy-dispersive plot of the recorded electrons in the detector leads to a so-called electron energy-loss spectrum (EELS). In Figure 4.3 an EEL spectrum of bulk SrTiO_3 is plotted as an example. It consists of the so-called *zero-loss peak*, which contains all elastically scattered electrons together with electrons which have lost energy in the range of 0 – 0.2 eV due to phonon excitations. However, due to the limited energy resolution of the spectrometer, phonon peaks in general remain unresolved with state-of-the-art EEL-spectrometers for TEM. The energy range up to around 60 eV includes all

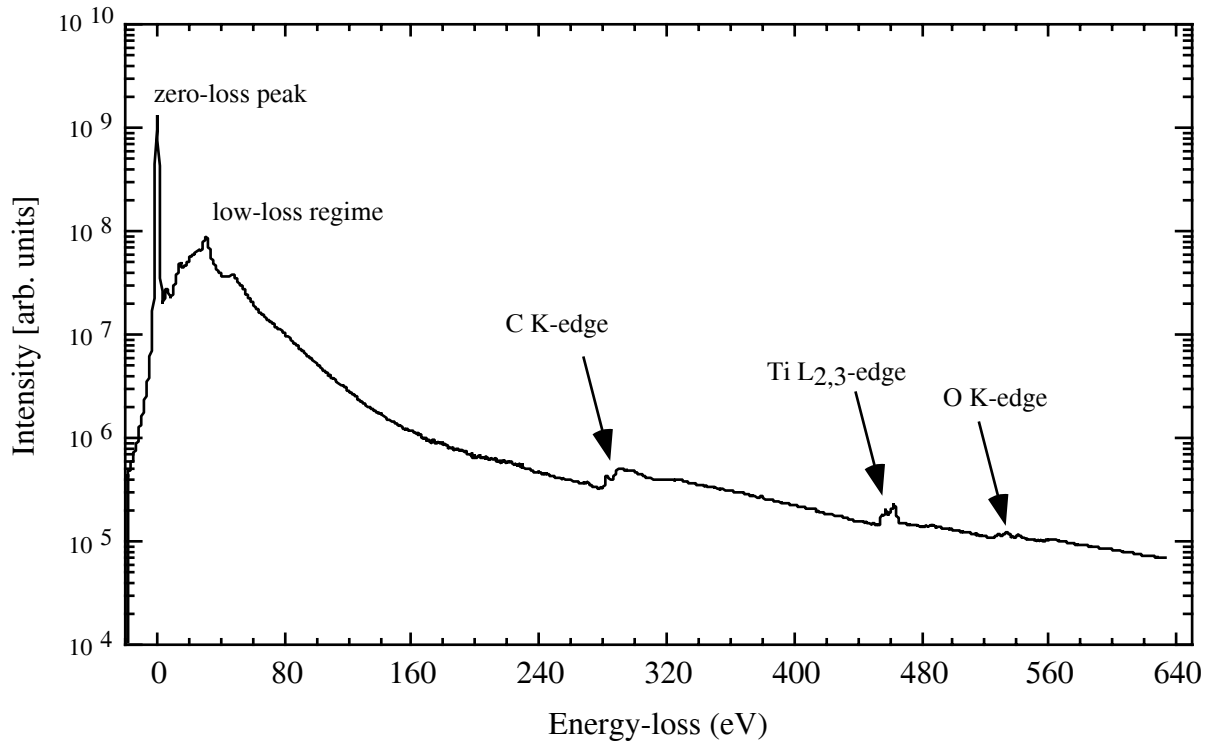


Figure 4.3: Electron energy-loss spectrum (EELS) of bulk SrTiO_3 . The spectrum was obtained by splicing two different spectra, each recorded with an energy dispersion of 0.3eV/channel in a different energy range. All spectra were recorded using the new CCD-detector. The resulting spectrum is plotted on a logarithmic intensity scale.

intraband transitions as well as all collective electron-gas excitations, the so-called plasmon losses. This energy regime is referred to as the *low-loss* regime. Approaching higher energy-losses *absorption edges* are found which are due to excitations of core electrons into the unoccupied states above the Fermi level, as it is sketched in Figure 4.2. These edges exhibit some fine-structures. The electron energy-loss near-edge fine structures (ELNES) within the first 30 eV beyond the edge onset are in the main focus of this work. The ELNES is sensitive to the local arrangement of the excited atoms and can be used to measure the unoccupied local densities of states, as will be shown later. In addition, the ELNES is often used to identify unknown phases of materials by fingerprinting techniques (see e.g. [Brydson, 1991] and [Egerton, 1996]). The extended energy-loss fine structures (EXELFS) can be used to obtain radial distribution functions of the corresponding atoms [Egerton, 1996]. In a different approach, the ELNES and EXELFS features can also be interpreted as originating from an interference pattern of multiple and single elastical scattering of the photoelectrons and the outgoing photoelectron, respectively, which were emitted due to the inelastic excitation process (see section 4.2.3).

Secondary effects take place by the relaxation of the excited core-electrons (see Figure 4.2b). The recombination processes of the excited electron state lead to either an emission

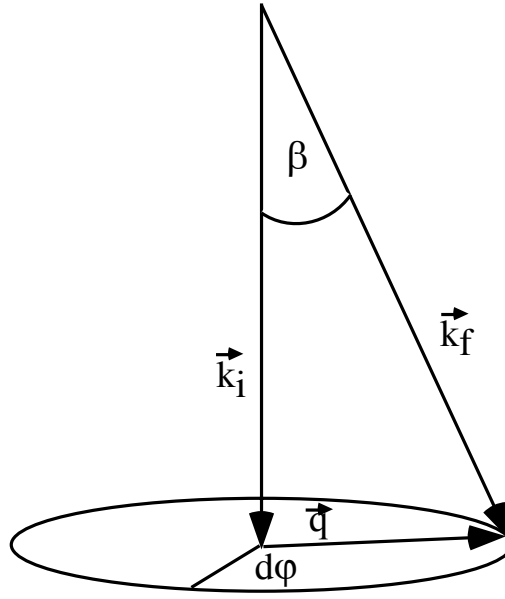


Figure 4.4: Scattering geometry with respect to equation 4.8. β is the collecting semi-angle, given by the collecting aperture and \vec{k}_i and \vec{k}_f are the wave vectors of the primary and the scattered electron wave, respectively.

of a characteristic X-ray photon or to the emission of an Auger electron. Both can be used for an additional analysis by either energy-dispersive X-ray spectroscopy (EDXS) or Auger electron spectroscopy (AES). In the present study, EDXS was used to investigate the presence of impurity atoms in the analysed specimens. The essential difference between EELS and EDXS is the atom weight sensitivity. Leapman and Hunt [Leapman, 1982] have shown that for elements with atomic numbers lower than 21 a quantitative EELS analysis is favourable compared to quantitative EDXS because of a higher sensitivity, and vice-versa. However, EDXS also does not contain any information about the local electronic structure of the material.

In the scattering theory, using atomic units, the number of electrons S scattered in a solid angle $d\Omega$ with an infinitesimal energy-loss of dE is given by

$$\frac{d^2 S}{dE d\Omega} = I_0 \cdot N \cdot V \cdot \frac{d^2 \sigma}{dE d\Omega}. \quad (4.8)$$

In equation 4.8, N is the number of atoms inside the illuminated volume V of the specimen, I_0 is the total beam current and $\frac{d^2 \sigma}{dE d\Omega}$ is the double differential cross-section [Platzman, 1973] [Egerton, 1996] [Reimer, 1994]. The solid angle $d\Omega$ is defined by the collecting semi-angle β in the experiment (cf. Figure 4.4).

As one can infer from equation 4.8, the double differential cross-section is the essential quantity for inelastic electron scattering, which is measured by EELS. Platzman and Wolff [Platzman, 1973] have shown that the double differential cross-section is proportional to the

imaginary part of the negative reciprocal dielectric function $\epsilon(\vec{q}, \omega)$:

$$\frac{d^2\sigma}{dEd\Omega} \propto \text{Im} \left(\frac{-1}{\epsilon(\vec{q}, \omega)} \right). \quad (4.9)$$

Therein, the energy-loss function $\text{Im} \left(\frac{-1}{\epsilon(\vec{q}, \omega)} \right)$ is given by the real part ϵ_1 and the imaginary part ϵ_2 of the complex dielectric function ϵ , following

$$\text{Im} \left(\frac{-1}{\epsilon(\vec{q}, \omega)} \right) = \frac{\epsilon_2}{\epsilon_1^2 + \epsilon_2^2}. \quad (4.10)$$

\vec{q} and $\omega = E/\hbar$ are the scattering vector and the angular frequency, respectively. The energy-loss function provides a complete description of the response of the specimen on the penetration of the fast electrons.

For high energy-losses, i.e., outside the low-loss regime, the energy-loss function is dominated by excitations which are highly localized near the atomic nuclei. In addition, ϵ_2 becomes small whereas ϵ_1 tends to unity. Therefore, in the one-electron picture² the energy-loss function can be written as a transition matrix element $\langle f | \exp(i\vec{q}\vec{r}) | i \rangle$ multiplied by a density of states term $\sum_{i,j} \delta(E_f - E_i - \Delta E)$. Finally, the double differential cross-section can be formulated following

$$\frac{d^2\sigma}{dEd\Omega} \propto \sum_{i,j} |\langle f | \exp(i\vec{q}\vec{r}) | i \rangle|^2 \delta(E_f - E_i - \Delta E). \quad (4.11)$$

Therein, $|i\rangle$ and $|f\rangle$ denote the initial and the final state of the atomic wave-functions, respectively, and E_i and E_f are the corresponding energies of these states. ΔE again denotes the energy-loss due to the inelastic scattering. Equation 4.11 was provided by Bethe [Bethe, 1930] and is valid in the approximation that the electron wavelength is small compared with the size of the scattering elements (Born approximation).

The densities of states term in equation 4.11 is given by the occupied and the unoccupied states in the bandstructure. However, the occupied states near the atomic nuclei only have a small dispersion in energy (cf. Figure 4.5). Therefore, only the energy distribution of the unoccupied states determines the fine structures in the EELS data. In addition, this shows that the observed spectra resulting from deep lying initial states are highly localized at the atomic sites. However, the low but non-zero dispersion of the initial states leads to an energy broadening of the occupied densities of states and therefore also to a broadening of the edge onset measured for the EELS absorption edges. An additional energy broadening of the observed spectra is due to overall life-time effects of both the excited state and the unoccupied state in the bandstructure. Hébert et al. [Hébert, 2000] provided a model for these life-time broadenings which increase linearly with increasing energy-loss above the edge-onset. Therefore, at the edge-onset the energy resolution is determined by the instrumental energy

²In the one-electron picture the interaction of the electrons of the solid state are described in the mean-field approximation, i.e. one electron inside an effective potential formed by the remaining atoms together with the atomic nuclei.

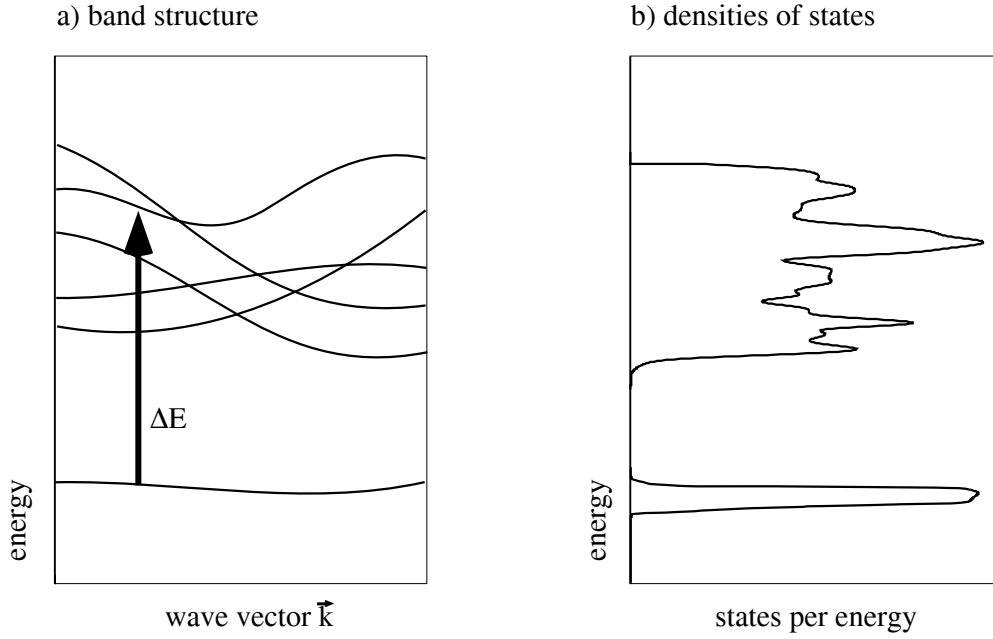


Figure 4.5: Schematic visualization of the combination of the band structure and the density of states. ΔE denotes the energy-loss occurred in EELS due to the transition from an occupied state into an unoccupied state. The transition is marked with an arrow inside the bandstructure.

resolution (cf. section 4.1.1) and the small but non-zero dispersion of the initial state, whereas for higher energy-losses, life-time broadening effects become more and more important.

The matrix element $\langle f | \exp(i\vec{q}\vec{r}) | i \rangle$ in equation 4.11 describes the spatial and the energetical overlap of the initial and the final *atomic* wave-function. For small scattering angles \vec{q} , or more generally, for $|\vec{q}\vec{r}| \ll 1$, the exponential function within the matrix element can be described by a Taylor expansion:

$$\exp(i\vec{q}\vec{r}) = 1 + i\vec{q}\vec{r} + \text{higher order terms.} \quad (4.12)$$

Performing the integration of the matrix elements, $\langle i | f \rangle$ is zero for basis vectors $|i\rangle$ and $|f\rangle$ which are orthogonal to each other, while the second term in equation 4.12 remains. All higher order terms can be neglected if the condition $|\vec{q}\vec{r}| \ll 1$ is fulfilled inside the maximum interaction volume in the specimen. To proof the fulfillment of this condition, the maximum length of the scattering vector \vec{q} is approximated by the collection semi-angle β by

$$q \approx k_0 \cdot \beta. \quad (4.13)$$

The maximum radius $|\vec{r}_m|$ of the interaction volume can be approximated by using the hydrogen model [Egerton, 1996]:

$$|\vec{r}_m| \approx \frac{a_0}{Z^*}, \quad (4.14)$$

where $a_0 = 0.0529 \text{ nm}$ is the Bohr radius and Z^* is the effective charge of the nucleus. In the case of K-shell excitations (K-edges), the second 1s-electron screens the nucleus and a

modified effective charge of $Z^* = Z - 0.3$ has to be considered. For L-shell excitations (L-edges), the effective charge is given by $Z^* = Z - 4.15$ [Egerton, 1996]. For L-shell excitations the nucleus is screened by the 2 $1s$ -electrons and by the remaining electrons from the $2s$ and $2p$ levels. For the EELS measurements performed in this work, collection semi-angles of 6.5 mrad were used, corresponding to the 2 mm PEELS entrance aperture. A calculation of the $|\vec{q} \cdot \vec{r}|$ -values results in 0.076, 0.033 and 0.017 for the O K-, the Ti $L_{2,3}$ - and the $\text{Sr}_{2,3}$ -edges, respectively. Therefore, for all measured edges the dipole selection rule is expected to be fulfilled. This allows a comparison of the O-K edges to only the p -projected local densities of states (PDOS), and the $L_{2,3}$ -edges are interpreted in terms of the corresponding mixed s - and d -projected LDOS. In addition, for anisotropic materials a non-even scaling of the LDOS corresponding to different magnetic quantum numbers has to be carried out. In the present study, these effects were neglected since SrTiO_3 has an isotropic structure. Also for the interfacial densities of states, these effects were not considered although the isotropy is of course disturbed in the interfacial region.

However, it has to be mentioned that prior to the comparison of the experimental spectra to the theoretical local PDOS, all experimental spectra were background subtracted using a power-law function B in the form $B = AE^{-r}$ [Egerton, 1996]. In addition, the spectra were corrected for channel-to-channel gain variations [Egerton, 1996].

The double differential cross-section (equations 4.9 and 4.11) can be described either in a dielectric formalism (4.9) or in the Bethe formalism (4.11). The dielectric formalism is limited to the low-loss part of the EEL-spectrum, whereas the Bethe formalism is only valid for energy-losses higher than the plasmon energies. Therefore, equation 4.9 was used to analyse data acquired in the low-loss regime. As will be shown in section 6.1, the local complex dielectric function of the investigated material can be determined by a Kramers-Kronig analysis of the low-loss data. On the other hand, equation 4.11 was used for a detailed ELNES analysis in direct comparison to the local symmetry projected densities of states, calculated by different theoretical approaches (cf. section 4.2).

4.1.3 Spatial Difference Technique

In section 3.2 it was mentioned that there exist several different methods to experimentally obtain high spatially resolved ELNES data. In the present study, the spatial difference technique was used to measure interface specific ELNES data of the different metal/ceramic interfaces. Other methods such as atomic column resolved EELS and the line scan method were not applied for stability reasons of both the VG STEM and the specimen itself. Strong spatial drift of several nanometers due to charging effects of the specimen as well as magnetic interaction effects of the thin Ni films with the electron beam made it impossible to either acquire linescans or single spectra using the spot mode (cf. Figure 4.6). In the measurements performed in this study, ELNES spectra were acquired while scanning the beam across areas between $3 \times 4 \text{ nm}^2$ and $1 \times 10 \text{ nm}^2$ in size. This acquisition mode has the advantage that during spectrum acquisition an image of the specimen is available, which can be used for a manual spatial drift correction during acquisition times.

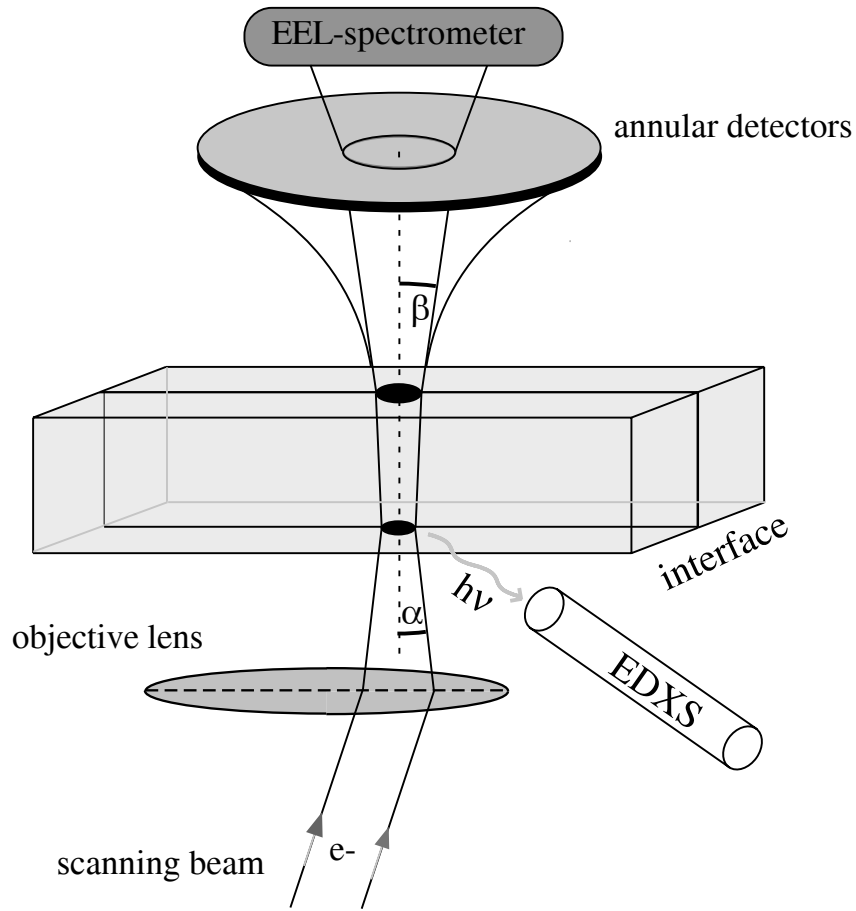


Figure 4.6: Schematic drawing of the electron beams for spectroscopy at high spatial resolution in a VG HB501 UX dedicated STEM using the spot-mode.

To perform the spatial-difference technique, the interface was tilted edge-on, i.e. the electron beam was parallel to the interfacial plane. To avoid possible extra ELNES intensities due to channeling of the beam electrons along a low-indexed zone-axis, a specimen tilt of $3^\circ - 5^\circ$ away from the zone-axis orientation along a $\langle 100 \rangle$ Kikuchi line assured that the interface remained in the edge-on orientation. A set of three ELNES spectra was acquired: one spectrum with the beam scanning an area including the interface and one spectrum in each of the adjacent bulk materials. Figure 4.7 shows an atomistic structure model of a coherent heterophase interface together with the three different scanning areas. Considering that at each time only one electron is penetrating the specimen [Reimer, 1997] and therefore the ELNES signals recorded in the detector are formed incoherently, the measured signal from the region containing the interface S_{ir} is regarded to be a simple superposition of the interface specific ELNES signal $S_{interface}$ and the two bulk signals $S_{bulk,1}$ and $S_{bulk,2}$. Thus, the interface specific component of the ELNES can be extracted from the measured spectra using

$$S_{interface} = S_{ir} - \mu \cdot S_{bulk,1} - \nu \cdot S_{bulk,2}. \quad (4.15)$$

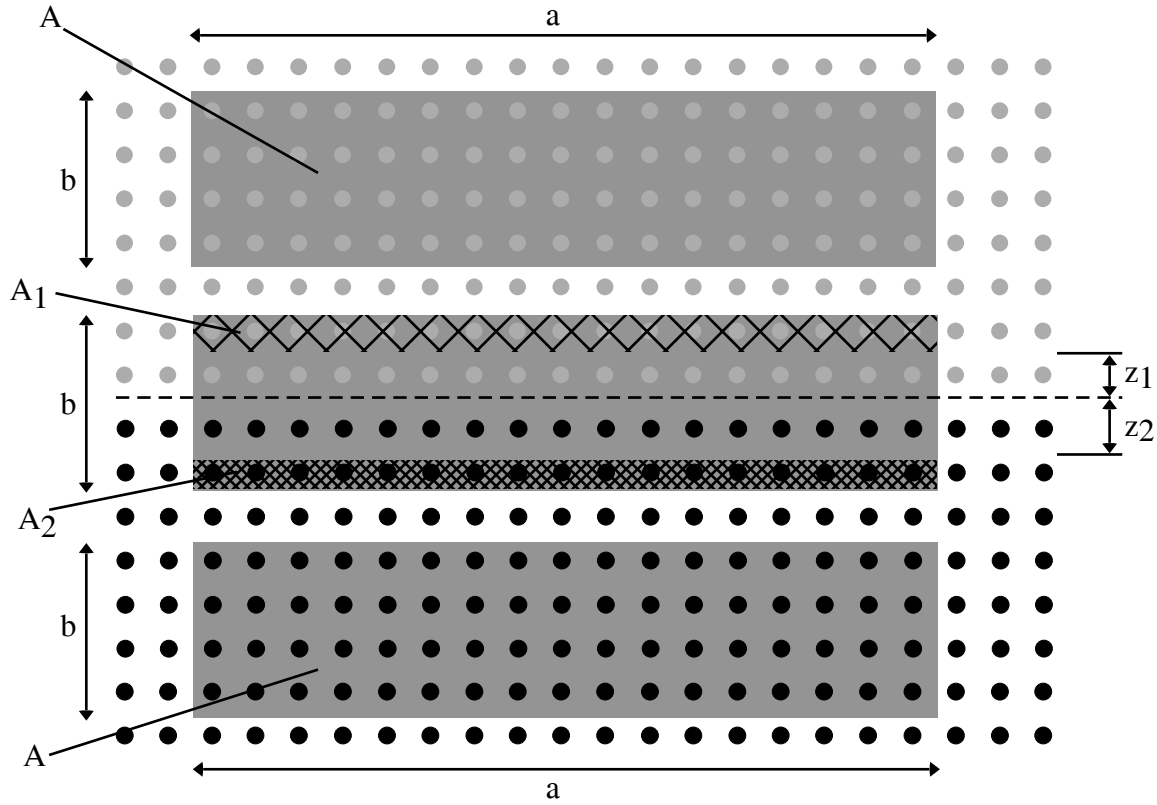


Figure 4.7: Atomistic structure model of the coherent interface. The three scanning areas used for the acquisition of the ELNES spectra are included in addition.

μ and ν are scaling factors obeying the conditions

$$0 \leq \mu, \nu \leq 1 \quad \text{and} \quad 0 \leq \mu + \nu \leq 1. \quad (4.16)$$

A scaling of the spectra is necessary due to the different numbers of bulk atoms irradiated during the acquisition of the bulk spectra and the spectrum from the interface region [Müllejans, 1995].

The spatial difference method is based on assumptions which have been thoroughly discussed in the scientific community. In general, it should be possible to proof the validity of the spatial difference technique by a combination with *ab-initio* band structure calculations of the unoccupied local densities of states. This comparison is one of the topics in section 7.3.2.

The critical point in the extraction of the interface specific ELNES component is the determination of the scaling factors μ and ν [Muller, 1999]. Bruley [Bruley, 1993], who first introduced the spatial-difference method for ELNES investigations, determined the scaling factors by trial-and-error methods. To attain the proper factors, critical guidelines have to be followed, which were already discussed in section 3.2.

In this work a more quantitative determination of the scaling factors was used to extract the interface specific ELNES from the measured data, which was originally developed for

homophase interfaces [Kienzle, 1999]. Scheu and co-workers [Scheu, 2000] have shown that under the assumption of constant thickness throughout one acquired data set, values of the scaling factors μ and ν can be calculated from geometrical considerations of the area ratios A_1/A and A_2/A if the interface is located within the centre of the scanned area (cf. Figure 4.7):

$$\mu = \frac{A_1}{A} = \frac{a(\frac{b}{2} - z_1)}{ab} = \frac{1}{2} \left(1 - \frac{z_1}{b/2} \right) \quad \text{and} \quad (4.17)$$

$$\nu = \frac{A_2}{A} = \frac{a(\frac{b}{2} - z_2)}{ab} = \frac{1}{2} \left(1 - \frac{z_2}{b/2} \right). \quad (4.18)$$

a and b denote the dimensions of the scanned areas parallel and perpendicular to the interface, respectively. z_1 and z_2 are the spatial extents of the interface specific bandstructures in real space for the two bulk materials. The values are measured with respect to a line which divides the distance between the two half-crystals into two equal parts [Scheu, 2000]. In general, z_1 and z_2 have different values corresponding to the materials properties. In a different attempt, one can also count the number of atomic columns present in the corresponding scanning areas and relate the interfacial number of columns to the number of pure bulk columns.

If the interface is not positioned exactly in the centre of the scanned area, e.g. in the case of spatial drift, equations 4.17 and 4.18 have to be replaced by [Scheu, 2000]

$$\mu = \frac{I_{tot}^{cont}}{I_{bulk,1}^{cont}} \left(1 - \frac{z_1}{b/2} \right) \quad \text{and} \quad (4.19)$$

$$\nu = \frac{I_{tot}^{cont}}{I_{bulk,2}^{cont}} \left(1 - \frac{z_2}{b/2} \right). \quad (4.20)$$

I_{tot}^{cont} is the "continuum intensity" of the signal far beyond the edge onset acquired in the region containing the interface, and $I_{bulk,1}^{cont}$ and $I_{bulk,2}^{cont}$ are the corresponding bulk continuum intensities. The continuum intensities are insensitive to the bonding and thus give the number of the irradiated atoms independent of any bonding effects [Scheu, 2000].

Figure 4.8 shows a schematic drawing of the spatial-difference technique. Possible artifacts in the difference spectrum due to a sub-channel drift of the PEELS detector as described by Müllejans and Bruley [Müllejans, 1995] are in general avoided by ELNES acquisitions of several different TEM specimens, multiple specimen areas, and by using different dispersions. Unless stated otherwise, the spatial difference technique was always applied to background subtracted and channel to channel gain-corrected EEL-spectra [Egerton, 1996]. In the present study, all interface specific ELNES spectra were determined using equations 4.19 and 4.20. The continuum intensities were measured by integrating signals from energy windows of approximately 60 eV above the edge onsets. The width of the energy windows was in the range of 10 – 30 eV. The calculated scaling factors were then used as starting values for the calculation of the interface specific ELNES. However, a variation of the scaling factors showed that for all ionization edges investigated in this study, the finally used values of μ and ν were within 10% – 15% of the originally calculated values.

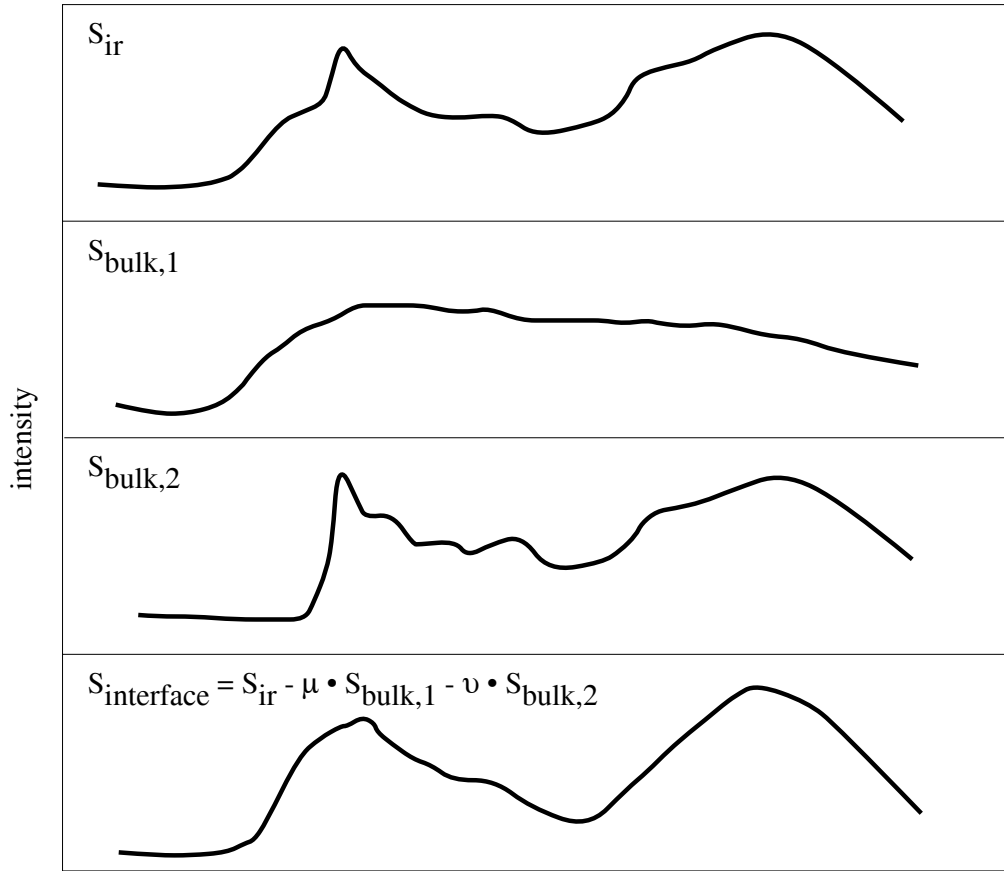


Figure 4.8: Schematic drawing of the spatial-difference technique after [Müllejans, 1995]. From the spectrum S_{ir} measured in the interfacial region the two adjacent bulk spectra $S_{bulk,1}$ and $S_{bulk,2}$ are removed using the previously calculated scaling-factors μ and ν .

4.2 Computational Details

The ELNES and VEELS investigations presented in this work were performed in combination with *ab-initio* band structure calculations. "*Ab-initio*" means that no material-specific properties except the atomic numbers are used for the calculations. In addition, no material-dependent approximations are used. The calculations are based on the LDFT. In the following only a concise overview of the LDFT will be given. Detailed information can be found in [Kohn, 1983], [Callaway, 1984] or [Jones, 1989].

In addition, some theoretical ELNES results were also obtained by using a full multiple scattering (MS) approach. This theoretical concept is described in section 4.2.3.

4.2.1 Local Density Functional Theory

The starting point for the description of a system consisting of N electrons interacting with each other in an external potential, e.g. formed by the atomic nuclei, is given by Schrödinger's equation:

$$\hat{H}|\Psi^e\rangle|\Psi^n\rangle = E|\Psi^e\rangle|\Psi^n\rangle. \quad (4.21)$$

In this equation, $|\Psi^e\rangle$ and $|\Psi^n\rangle$ denote the many-body wave function of the electrons and the atomic nuclei, respectively. In equation 4.21, the Born–Oppenheimer-approximation is already made. This approximation is based on the fact that the electron mass is much smaller than the masses of the atomic nuclei. Therefore, the electrons can react instantaneously on a movement of the nuclei because of their higher mobility and remain in their ground state all the time. Hence, in the Born–Oppenheimer-approximation the total many-body wave function of the complete system $|\Psi\rangle$ can be separated into

$$|\Psi\rangle = |\Psi^e\rangle \cdot |\Psi^n\rangle. \quad (4.22)$$

This separation of the wave functions makes it possible for the Schrödinger equation to be solved separately for $|\Psi^e\rangle$ and $|\Psi^n\rangle$. $|\Psi^e\rangle$ is the total N -electron wavefunction with the coordinates \vec{r}_i with $(i = 1, \dots, N)$. For a correct account of the Fermi statistics of the electrons, $|\Psi^e\rangle$ has to be anti-symmetric.

In Schrödinger's equation for the electronic system

$$\hat{H}|\Psi^e\rangle = E|\Psi^e\rangle \quad (4.23)$$

the eigenvalue E is the total energy of the electronic system. The Hamiltonian \hat{H} for a system of N electrons is given by

$$\hat{H} = \sum_{i=1}^N \left\{ -\frac{\hbar}{2m} \nabla_{\vec{r}_i}^2 + V_{ext}(\vec{r}_i) \right\} + \frac{1}{2} \sum_{\substack{i,j=1 \\ (i \neq j)}}^N V_{e-e}(|\vec{r}_i - \vec{r}_j|). \quad (4.24)$$

The external potential V_{ext} is due to the Coulomb interaction between the electrons and the atomic nuclei. The potential V_{e-e} describes the interaction of the electrons with each other. $-\frac{\hbar}{2m} \nabla_{\vec{r}_i}^2$ is the kinetic energy term of one electron at the site \vec{r}_i . The dynamics of nuclei in the adiabatic potential of the electron gas is not considered in the present work. The LDFT is one approach to calculate the ground state of a general electron system, based on equations 4.23 and 4.24. Hohenberg and Kohn [Hohenberg, 1964] provided two theorems to calculate the ground state.

The first theorem is that the properties of the ground state of a many-electron system are functionals of the electron density. Therefore, it is sufficient to calculate only the electron density of the ground state $n(\vec{r})$, i.e., a scalar function in three dimensions. The total electron wave-function $|\Psi^e\rangle$ is not needed. The total energy E of the ground state is then given by

$$E[n(\vec{r})] = F[n(\vec{r})] + \int V_{ext}(\vec{r}) n(\vec{r}) d^3 \vec{r} \quad (4.25)$$

with an universal, but unknown functional $F[n(\vec{r})]$. The second theorem is that the density functional of the total energy fulfills a variational principle. This means that for the external potential V_{ext} and the ground state electron density n_0 , the density functional $E[n]$ has a minimum and is equal to the ground-state energy E_0 :

$$\begin{aligned} E[n] &\geq E_0 = \langle \Psi^e | \hat{H} | \Psi^e \rangle \\ E[n_0] &= E_0 \end{aligned} \quad (4.26)$$

Levy [Levy, 1979] [Levy, 1982] provided a general proof of these two theorems for all kinds of anti-symmetric electron wave functions and for degenerated and non-degenerated ground states. Therefore, the two theorems of Hohenberg and Kohn [Hohenberg, 1964] provide a universal calculation scheme for all ground state properties of an inhomogeneous electron gas. Other ground state properties of the electron gas $\langle \Psi_0 | \hat{X} | \Psi_0 \rangle$, like e.g. elastic constants, can also be calculated by a density functional $X[n_0]$. However, for a real calculation of the ground state energy E_0 and the electron density $n_0(\vec{r})$, the universal but unknown functional $F[n(\vec{r})]$ has to be determined. Kohn and Sham [Kohn, 1965] used a functional of the following form:

$$F[n] = \frac{e^2}{2} \iint \frac{n(\vec{r})n(\vec{r}')}{|\vec{r} - \vec{r}'|} d^3\vec{r} d^3\vec{r}' + T[n] + E_x[n] + E_c[n]. \quad (4.27)$$

The first part of equation 4.27 describes the classical electro-static interaction between the electrons and can be calculated precisely. The terms $T[n]$, $E_x[n]$, and $E_c[n]$ denote the kinetic energy, the exchange energy and the correlation energy of the interacting electrons, respectively. The energy contributions $E_x[n]$ and $E_c[n]$ account for the exchange interaction between electrons of opposite spins according to Pauli's principle and for further many-body correlation effects between electrons of the same and opposite spins. Hartree-Fock calculations as well as many-body calculations have shown that the sum of the exchange and the correlation energies have an amount of approximately 10% of the total energy.

The electron density is calculated by a set of N orthogonal functions, following

$$n(\vec{r}) = \sum_{i=1}^N |\Phi_i(\vec{r})|^2. \quad (4.28)$$

The system of interacting electrons is mapped on a system of non-interacting electrons, which have the same density as the real system. Then, the kinetic energy of the electrons $T^{KS}[n]$ can be calculated from

$$T^{KS}[n] = \langle \Phi^e | \hat{T} | \Phi^e \rangle \quad \text{with} \quad \hat{T} = -\frac{\hbar^2}{2m} \sum_{i=1}^N \nabla_i^2 \quad (4.29)$$

and the rather small difference $T[n] - T^{KS}[n]$ can be approximated together with E_x and E_c . The unknown functional $F[n]$ is finally determined in the Kohn-Sham scheme by:

$$F[n] = \frac{e^2}{2} \iint \frac{n(\vec{r})n(\vec{r}')}{|\vec{r} - \vec{r}'|} d^3\vec{r} d^3\vec{r}' + T^{KS}[n] + \underbrace{T[n] - T^{KS}[n] + E_x[n] + E_c[n]}_{=: E_{xc}[n]}. \quad (4.30)$$

$E_{xc}[n]$ is defined as the exchange-correlation-energy, which describes the many-body interactions beyond the classical electrostatics and the single-particle kinetic energy. The non-interacting electrons occupy successively the one-electron states, which are solutions of the following set of equations:

$$-\frac{\hbar^2}{2m}\nabla\Phi_i(\vec{r}) + V_{eff}(\vec{r})\Phi_i(\vec{r}) = \epsilon_i\Phi_i(\vec{r}), \quad (4.31)$$

where V_{eff} is given by the external potential V_{ext} , the electrostatic Hartree potential, and the exchange-correlation-potential V_{xc}

$$V_{eff}(\vec{r}) = V_{ext}(\vec{r}) + e^2 \int \frac{n(\vec{r}')}{|\vec{r} - \vec{r}'|} d^3\vec{r}' + V_{xc}(\vec{r}). \quad (4.32)$$

The exchange-correlation potential is given by the functional derivative of the exchange-correlation functional $E_{xc}[n]$ following

$$V_{xc}(\vec{r}) = \frac{\delta E_{xc}}{\delta n(\vec{r})}. \quad (4.33)$$

So far, the functional $E_{xc}[n]$ is still unknown. In the local density approximation (LDA), one uses the exchange-correlation energy per electron $\epsilon_{xc}(n)$ of a homogeneous electron gas of the electron density n . In case of the inhomogeneous electron gas, for each \vec{r} and $n(\vec{r})$ the local exchange-correlation energy is approximated by the corresponding value of $\epsilon_{xc}(n(\vec{r}))$ of the homogeneous electron gas.

$$E_{xc}^{LDA}[n] = \int n(\vec{r})\epsilon_{xc}(n(\vec{r}))d^3\vec{r}. \quad (4.34)$$

For the homogeneous electron gas $\epsilon_{xc}(n)$ can be calculated with an arbitrary high level of numerical accuracy, and then parametrised by an analytical interpolation formula.

Using e.g. the atomic electron density as a starting point, the total energy and the electron density of the ground state can be calculated by solving self-consistently the equations 4.28, 4.31 and 4.32, which are called the Kohn–Sham equations.

4.2.2 The Mixed-Basis Pseudopotential Program

The program code for LDFT calculations used in this work to calculate electron densities of states was provided by Elsässer [Elsässer, 1990] and Meyer [Meyer, 1998]. In the following, the numerical methods supplemented in the program for the calculation of the DOS are described.

Band structure calculations are performed by solving the Kohn–Sham equations (equations 4.28, 4.31 and 4.32) for supercells of crystal structures with periodic boundary conditions. A starting point thereby is a superposition of electron densities of free atoms. In a periodic potential, like a crystal potential, the wave-functions of the crystal electrons can be represented by a superposition of free-electron wave functions (plane waves):

$$\Psi_c(\vec{r}) = \sum_{\vec{G}} c_G^k \exp[i(\vec{k} + \vec{G})\vec{r}]. \quad (4.35)$$

The sum runs over all vectors \vec{G} of the reciprocal lattice of the crystal. The coefficients c_G^k result as eigenstates from the solution of Schrödinger's equation 4.31 in matrix representation with respect to the basis of plane waves. Since the dimension of the eigenvalue problem is infinite, one has to consider an incomplete set of plane waves to reduce the numerical effort of the calculations. Therefore, only plane waves with kinetic energies smaller than E_{max} are considered in the calculations, i.e.

$$|\vec{k} + \vec{G}|^2 \leq E_{max} . \quad (4.36)$$

In practice, the value of E_{max} was successively increased until the calculated results converged and this value was assumed to be the solution for a complete basis set. In the present study, maximum kinetic energies of $E_{max} = 345 \text{ eV}$ were used. To reduce the number of plane waves in the basis drastically, the program code uses a mixed-basis of plane waves and localized functions. Thus, the advantage of using a mixed-basis set with localized functions is that the corresponding electron wave-functions need not to be approximated only by a set of plane-waves. Electrons which are close to the atomic nuclei do not participate in the bonding of the crystal. Besides that, close to the nuclei there are strong variations of the electron density.

The interaction between the core electrons and the valence electrons close to the nucleus is subject to Pauli's principle, which leads to a separation of the valence electrons from the core electrons into naturally orthogonal eigenstates. Following the rule, that the eigenvalues and the eigenfunctions of the valence states remain the same outside the core region, the electron potential inside the core region can have an arbitrary shape. These potentials are then called pseudopotentials. The pseudopotentials can be created in such a way, that the wave functions of the valence electrons $\Phi(\vec{r})$ have a smooth shape approaching the atomic nucleus. This finally leads to the fact that only rather few Fourier components have to be used in the calculation. In the present study, local norm-conserving pseudopotentials were used [Hamann, 1979] which were obtained by all-electron free-atom calculations (cf. Table 4.1). In fact, reference configurations different from the free-atom ground-state configurations were used for the pseudopotentials [Ochs, 2000]. This method for creating pseudopotentials was proposed by Vanderbilt [Vanderbilt, 1985].

By the excitation of a core electron, e.g., a 1s electron, an electron hole is created in the corresponding inner-shell. In this case, the electro-static screening of the nucleus is disturbed and therefore the effective potential (cf. equation 4.32) is changed. This leads to a modification of the local band structure and finally to a modified ELNES [Pantelidis, 1985]. This effect is called 'core-hole effect'. The influence of the core-hole effect on the experimentally observed ELNES will be described in detail in section 6.5. In the LDFT calculations, the core-hole effect can be accounted for by the use of a pseudopotential including a real core-hole or by using a pseudopotential of the element with the next higher atomic number ($Z + 1$ approximation). In this work, the latter technique is used. This means that, for example, one oxygen atom was replaced in the supercell by one fluorine atom. Therefore, the theoretical modelling of the core-hole effect is the same as the simulation of a substitutional atomic defect in the crystal structure [Fujikawa, 1983] [Elsässer, 2001] [Köstlmeier, 2001].

Table 4.1: Free atom ground-state electron configuration and reference-state electron configuration of Ti, V, Sr, Y, O, F, and Pd for the pseudopotential construction. In addition, the projection radii used for the calculation of the site projected densities of states are listed together with the charge included in the corresponding sphere volumes.

element	ground state	reference state	projection radius for local DOS	charge in projection sphere
Ti	[Ar]3d ² 4s ²	([Ne]3s ² 3p ⁶ 3d ⁰) ⁴⁺	81 pm	+4.0
V	[Ar]3d ³ 4s ²	([Ne]3s ² 3p ⁶ 3d ⁰) ⁵⁺	81 pm	+3.9
Sr	[Kr]5s ²	([Ar]4s ² 4p ⁶ 4d ⁰) ²⁺	138 pm	+2.0
Y	[Kr]4d ¹ 5s ²	([Ar]4s ² 4p ⁶ 4d ⁰) ³⁺	138 pm	+2.5
O	[He]2s ² 2p ⁴	[He]2s ² 2p ^{3.5} 3d ^{0.5}	150 pm	+2.0
F	[He]2s ² 2p ⁵	[He]2s ² 2p ^{4.5} 3d ^{0.5}	150 pm	-1.9
Pd	[Kr]4d ¹⁰	[Kr]4d ^{9.5} 5s ^{0.25} 5p ^{0.25}		

After reaching the convergence criteria in the self-consistency loop of the Kohn–Sham equations 4.28, 4.31, and 4.32, the total density of states $D(\epsilon)$ were calculated from the eigenvalues $\epsilon_{n,k}$ of the system by a Brillouin-zone integration using a discrete mesh of \vec{k} -points [Moreno, 1992]:

$$D(\epsilon) = \sum_n \int_{1^{st} BZ} \delta(\epsilon - \epsilon_{nk}) d^3 \vec{k}. \quad (4.37)$$

Site projections of the density of states (LDOS) were done within spheres surrounding the corresponding atomic sites. The radii of these spheres were chosen in such a way that the projection spheres of Sr, Ti and O contain the formal charges +2, +4 and −2, respectively. The radii used for the calculation of the Pd/SrTiO₃ system are listed in Table 4.1. The valence-electron charges included in the projection volumes are also given in Table 4.1.

For a more quantitative comparison of the calculated PDOS and the measured ELNES, the PDOS were convoluted with the experimental energy broadening of the electron beam. Unless stated otherwise, all calculated PDOS presented in this work consider an energy broadening of 0.8 eV, which corresponds to a standard setup of the STEM.

A reliable calculation of the atomistic and the electronic structure of crystal defects, such as grain boundaries or metal/ceramic interfaces, requires a large number of atoms inside the supercells. Since the supercell sizes are limited to approximately 100 atoms due to the performance of state-of-the-art workstations (DECalpha with typically 500Mhz CPU and 2GB RAM), only defects with a small periodicity can be calculated. In the case of metal/ceramic interfaces, this means that with the currently available workstations only coherent interfaces can be considered for these reasons. In this study, the supercells of the metal/SrTiO₃ interfaces contained 30 atoms [Ochs, 2000] [Ochs, 2001], whereas supercells for core-hole calculations of bulk SrTiO₃ contained up to 120 atoms.

It should be emphasized that in this approach no transition probabilities for the core-

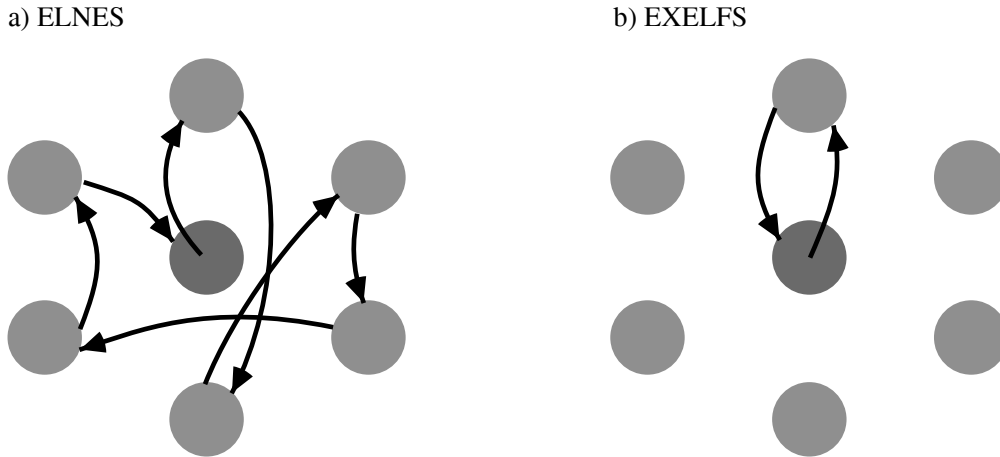


Figure 4.9: Visualization of the multiple scattering approach. The near-edge fine structures (ELNES) can be described by a multiple elastic scattering of a photo-electron. The extended fine structure (EXELFS) can be assigned to a single elastic scattering event.

electron excitations are considered, i.e., ELNES data are only compared to the calculated densities of unoccupied states. The transition probabilities are assumed to be slowly varying functions of energy in the observed energy ranges. Hence, in the present study only peak energies and no peak intensities are compared quantitatively. The reasonably good agreement of calculated and measured peak intensities for the O K-edges can be considered as an *a priori* justification of the neglect of energy-dependent transition probabilities.

4.2.3 Multiple Scattering Approach

A different concept for describing the ELNES is the multiple scattering (MS) approach. Within this theoretical model, the primary electron beam excites a so-called absorbing atom, which leads to the emission of a photoelectron. The emitted photoelectron is then multiply elastically scattered by the surrounding atomic cluster, as it is sketched in Figure 4.9. The fine structures of the EELS absorption edges are finally created by an interference effect of spherical elementary waves of the multiply elastically scattered photoelectron at the site of the absorbing atom. Figure 4.10 shows that for kinetic energies of the photoelectron below ≈ 50 eV, multiple elastic scattering is dominating due to the large inelastic mean free path Λ_i [Egerton, 1996], whereas for energies above 50 eV the probability for inelastic scattering is increased by a smaller value for Λ_i . Therefore, the fine structures above 50 eV beyond the edge onset can be described by a single elastic scattering of the excited photoelectron (cf. Figure 4.9).

The MS calculations, often also referred to as cluster calculations, are performed in real space. An atomic arrangement has to be specified for which the full multiple scattering calculation is intended to be done. In this so-called cluster, one atom, which is considered to

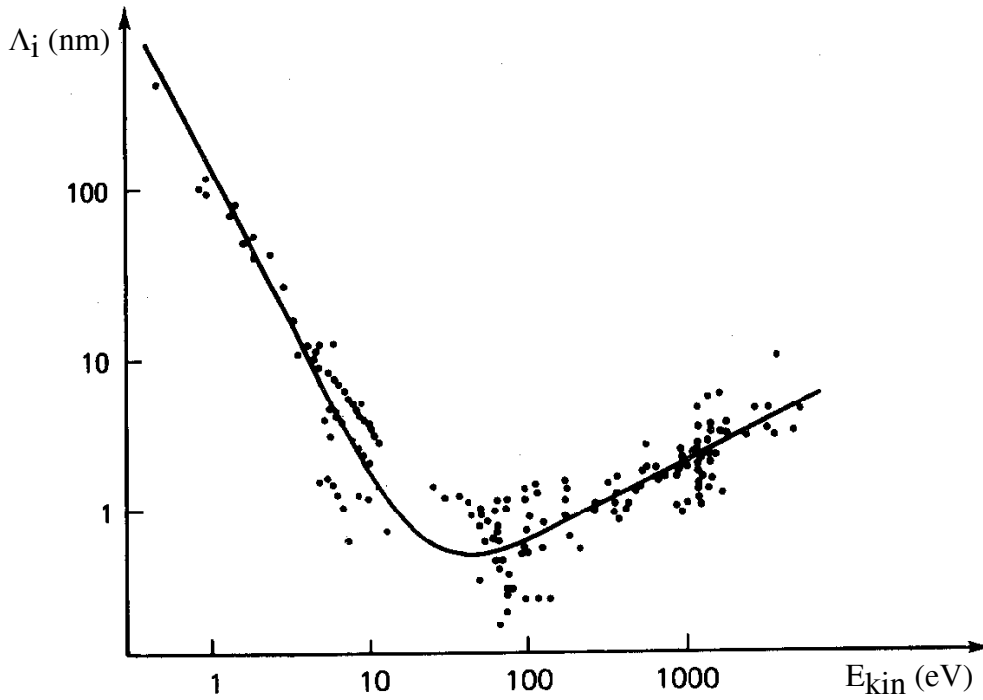


Figure 4.10: Inelastic mean-free path Λ_i as a function of the kinetic energy E_{kin} of an emitted photo-electron. The data were measured and afterwards fitted by Seah and Dench [Seah, 1979].

be the absorbing or excited atom, has to be chosen. In the limit of an infinitely large cluster, the MS theory is equivalent to the so-called *KKR band structure theory* of Korringa, Kohn and Rostocker ([Korringa, 1947] and [Kohn, 1954]). In the notation of the multiple scattering theory, the local density of states $LDOS(E)$ is written in the following form [Durham, 1982]:

$$LDOS(E) = 1 - \text{Im} \left(\frac{\tau_{LL}(E) - it_L^0(E)}{\sin^2 \delta_l(E)} \right). \quad (4.38)$$

t_L^0 is, apart from some constants, the partial scattering amplitude on the site of the central atom for the total angular momentum $L = (l, m)$. τ_{LL} are elements of the scattering path operator [Gyorffy, 1973]. This operator contains all parts of the incoming elastically scattered wave-functions with respect to the absorbing atom. $\delta_l(E)$ are the phase shifts of the scattered partial wave-functions as a function of the energy-loss E .

In this work, the commercially available program code FEFF8.10 was used to perform multiple scattering calculations of bulk SrTiO_3 . Detailed descriptions of FEFF8.10 and earlier versions are published in [Rehr, 1990], [Ankudinov, 1998] and [Rehr, 2000]. The code uses a self-consistent field real space multiple scattering approach [Zhang, 1989] [Ankudinov, 1998] for clusters of atoms. The calculations are based on an all-electron relativistic Green function formalism. However, the crystal potential is approximated by a muffin-tin-potential. This potential consists of atomic potentials for free atoms inside spheres with a distinct radius.

Outside the atomic spheres the potential is regarded to be constant. The radii of the atomic spheres are chosen in such a way that the spheres touch each other in between the atoms [Ankudinov, 1998]. The crystal potential is finally calculated self-consistently by a successive modification of the effective potentials inside the muffin-tin spheres.

For a comparison to experimental data, the calculated spectra were also broadened in energy using Gaussians with a FWHM of 0.8 eV, as in the LDFT calculations. The atomic cluster size was chosen in such a way that the calculated ELNES converges, or only minor differences appear in the ELNES by further increasing the cluster size, which are below the experimental detection limits. Core-hole effects were considered using the $Z+1$ approximation as described in the previous section. Apart from that, also a so-called Z^* approximation was used. In this approximation an already excited atom potential is used for the absorbing atom, i.e., a potential including an electron hole in the initial state together with an additional electron in the deepest unoccupied state. The results for these calculations of bulk SrTiO_3 will be shown and discussed in section 6.5.

The disadvantage of the multiple scattering approach compared to the LDFT is, that on one hand no *ab initio* self-consistent full crystal potential is calculated and hence no relaxed atomistic structure calculations are obtainable. The latter is essential to investigate the atomistic and the electronic structure of defects. In addition, since no full potential for the crystal is calculated, no other materials properties like, for example, elastic constants, etc., are accessible. However, for an already relaxed atomistic structure model, e.g., obtained by LDFT calculations, large cluster sizes can be used for the ELNES calculation with rather small computation times.

Chapter 5

Specimen Preparation

In this chapter, the specimen preparation is described in detail. The interfaces were prepared using the molecular-beam epitaxy (section 5.1). Afterwards, the interfaces were cross-sectionally prepared for the TEM investigations as described in section 5.2.

5.1 Molecular Beam Epitaxy

For this study, all metal/ceramic interfaces were prepared using MBE. The MBE method is based on the thermal evaporation of the metal and the deposition onto the solid ceramic substrate. On the substrate surface, the metal atoms condensate and are adsorbed on specific nucleation sites. Additional surface diffusion may occur, depending on the substrate temperature during the growth process. The metal atoms in the gas phase remain uncharged during the whole process and are not accelerated in any direction.

The MBE growth experiments were done using UHV conditions with pressures of typically $5 \cdot 10^{-9}$ Pa. Under these conditions, Richter [Richter, 2000] found that a storage of the readily prepared substrate surfaces becomes possible for a couple of days without absorption of any contamination layers [Richter, 2000]. The metal atoms were transferred into the gas-phase using effusion-cells or electron beam evaporators. The use of effusion cells has the advantage of enabling high evaporation temperatures up to 1500°C as well as high stabilities of the deposition rates [Richter, 2000]. For an *in-situ* analysis and observation of the growth behaviour, RHEED, AES, XPS, AFM, and STM facilities are attached to the MBE system.

In the present study, undoped commercially prepared (100)-oriented single crystalline SrTiO_3 substrates (Crystal GmbH, Berlin, Germany) of $10\text{ mm} \times 10\text{ mm} \times 0.5\text{ mm}$ in size were used as ceramic substrates. The miscut of the (100) surfaces was below 0.1° . The substrate surfaces were prepared following the routes of Kawasaki et al. [Kawasaki, 1994] and Polli et al. [Polli, 1999] to obtain predominantly TiO_2 terminated SrTiO_3 surfaces. Prior to ultrasonic etching of the crystals in a NH_4F -buffered HF solution, the as-received crystals were ultrasonically soaked in distilled water for approximately 10 minutes. After the etching process, the crystals were annealed at 1100°C in pure O_2 (purity: 99.9%, pressure: $6 \cdot 10^4$ Pa) for one hour. This procedure leads to a compensation for oxygen vacancies due to the etching

process. Afterwards, the SrTiO_3 substrates were mounted onto the MBE specimen holders and were then annealed at 850°C for one hour in UHV to remove any contamination or carbon impurities. Following this routine, AES measurements did not show any impurities like C or Ca, and AFM measurements showed atomically flat surfaces exhibiting steps in the substrate surface of a height of one unit cell [Polli, 1999].

Pd, Ni and Cr films with different nominal thicknesses were deposited by MBE onto the (100) SrTiO_3 surfaces using different substrate temperatures. In Table 5.1 the nominal thicknesses and the substrate temperatures for the different metal-depositions are listed in detail. Pd was evaporated with a thermal effusion cell, whereas Ni and Cr were electron beam evaporated. With respect to the EELS/ELNES and HRTEM investigations, substrate temperatures and nominal thicknesses were chosen in such a way that an epitaxial orientation relationship between the metal film and the ceramic substrate occurs [Richter, 2000] [Polli, 1998].

Table 5.1: Processing parameters such as substrate temperature $T_{\text{substrate}}$ during the MBE growth and nominal film thickness t of the deposited metal films.

	Pd	Ni	Cr
$T_{\text{substrate}} (^\circ\text{C})$	650	650	65
$t \text{ (nm)}$	35	50	35

5.2 TEM-Specimen Preparation

For TEM investigations the metal/ceramic interfaces have to be prepared in cross-section with a specimen thickness such that the material is transparent for the electron beam in the TEM. Typical specimen thicknesses which have to be achieved are below 100 nm. However, in EELS experiments with specimen thicknesses above ~ 50 nm, inelastic plural scattering can occur [Egerton, 1996] which has to be removed after the acquisition. To avoid this processing step, which introduces noise, ELNES analyses were facilitated by using specimen thicknesses below ~ 50 nm.

A high quality TEM sample is characterized by both an optimum specimen thickness and an undisturbed crystal structure compared to a solid macroscopic piece of the material. The TEM specimen preparation is always a compromise between these two conditions. Several different techniques are available to fulfill these conditions to different amounts: electrolytical thinning and polishing, chemical etching, tripod grinding, mechanical cleavage, ion-thinning techniques, ion-beam cutting techniques, etc.. Which of these techniques is preferable strongly depends on the properties of the material. In the case of metal/ceramic interfaces, two materials are present with very different mechanical and chemical properties. In most cases, ceramics are non-conductive and brittle, whereas metals possess high electronic conductivity and can easily be plastically deformed. Due to the differences in the mechanical properties for metals and ceramics, interfaces between these two classes of materials are sensitive to mechanical grinding processes. For this reason, ion-thinning was applied

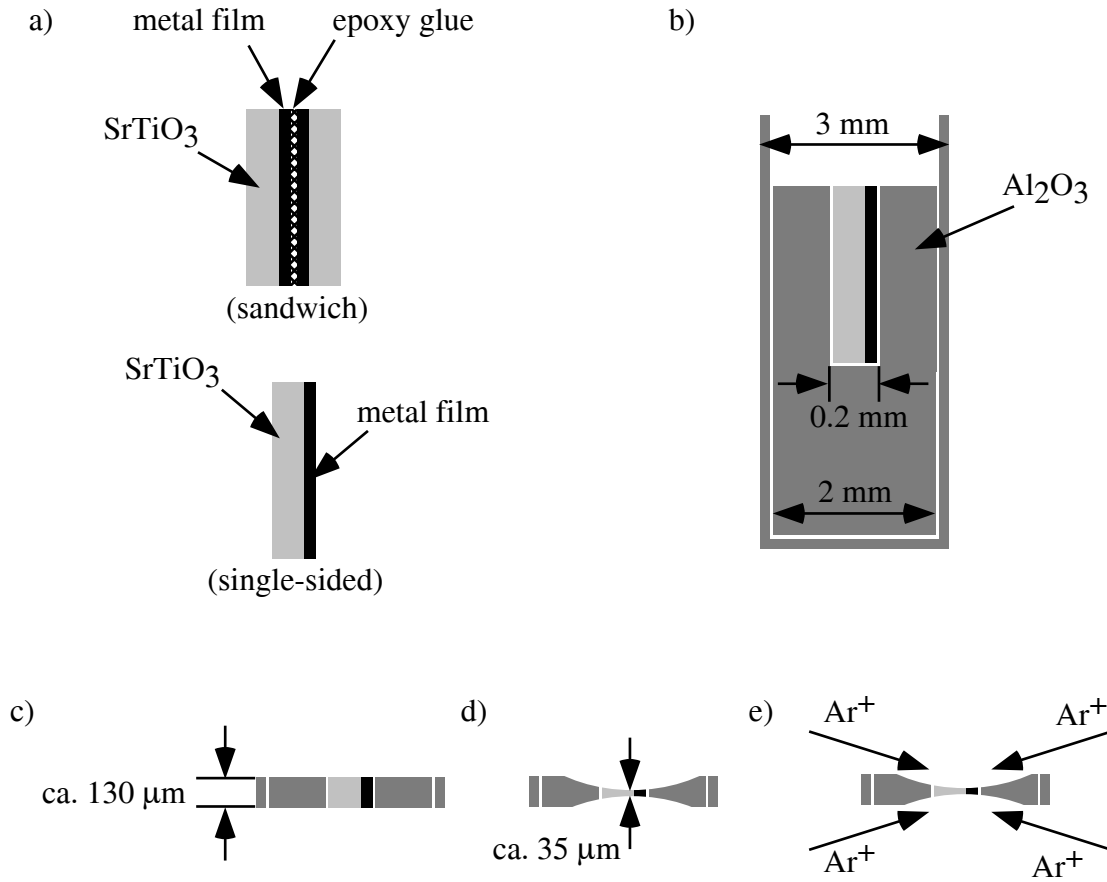


Figure 5.1: Schematic drawing of the cross-sectional TEM preparation: a) preparation of a sandwich or a single-sided sample; b) embedding into a polycrystalline Al_2O_3 tube; c) sawing and mechanical grinding of disks with a thickness of approximately $130\text{ }\mu\text{m}$; d) dimpling to a thickness of approximately $35\text{ }\mu\text{m}$ from both sides and final polishing; e) ion-milling until electron transparency is achieved.

for sample thicknesses below $35\text{ }\mu\text{m}$. For this technique the processing parameters such as the ion-beam energy, the illumination angle and the geometry play an important role and control the quality of the specimen. However, before ion-thinning, the material has to be mechanically thinned. The preparation techniques used in this work are based on methods developed by Strecker and co-workers [Strecker, 1993]. In a first step, the $10\text{ mm}\times 10\text{ mm}\times 0.5\text{ mm}$ -sized crystals prepared by MBE are cut into small strips of 2 mm width along the (100) or (110) plane. Afterwards, these strips were glued together with the metal film of one strip facing the metal film of the other strip (cf. Figure 5.1a).

For this process a highly dispersed epoxy-glue (M-Bond610) is used in order to form a thin gap of glue. This sandwich is then glued inside a poly-crystalline Al_2O_3 slit of 2 mm

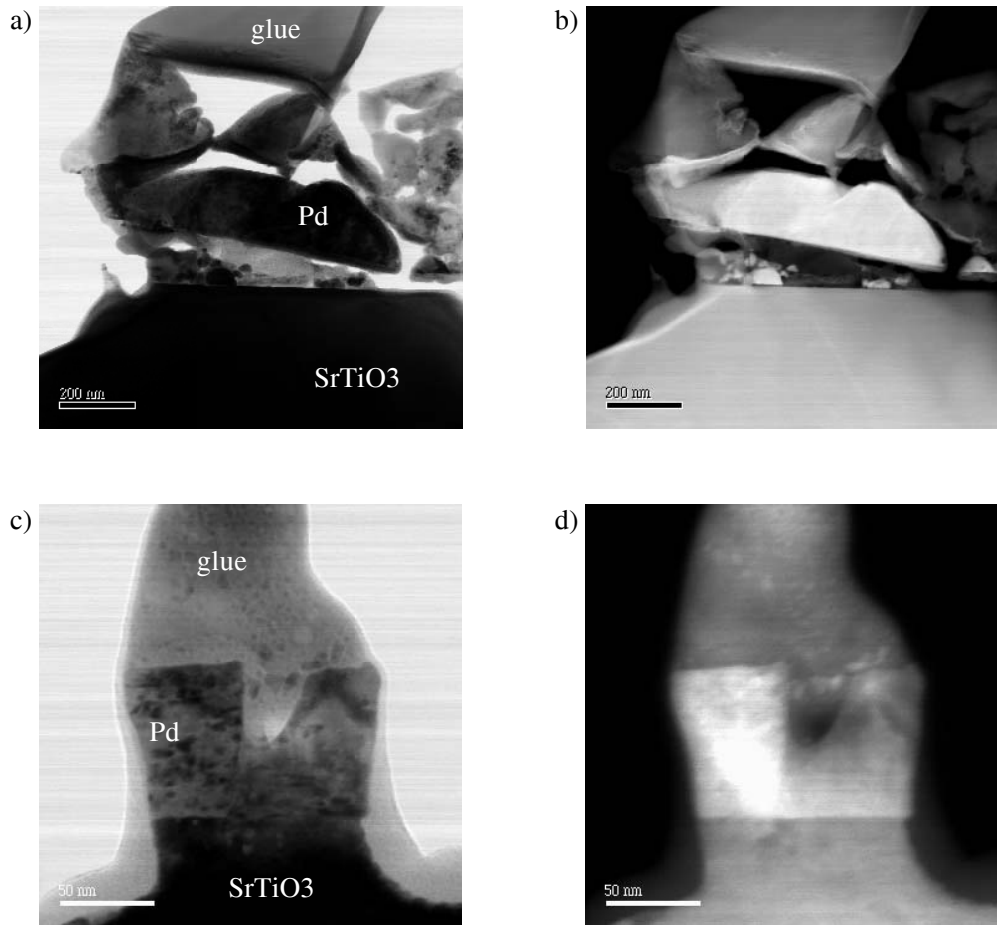


Figure 5.2: BF ((a) & (c)) and HAADF ((b) & (d)) images of a Pd/SrTiO₃ interface. The images a) and b) originate from a sample for which the conventional sandwich technique was used. The sample shown in c) and d) is a single-sided specimen ion-thinned from both directions.

length and 200 μm in width after mechanical grinding and polishing of the SrTiO₃. The slit itself is glued inside a circular tube of 3 mm diameter, as is sketched in Figure 5.1b. The outer diameter of 3 mm of the tube is the final lateral size of the TEM specimen. The epoxy-glue M-Bond AE15 used for inserting the sandwich into the alumina tube is characterized by a higher final stiffness than the previously used M-Bond610, but it is not that highly dispersed. After hardening of the epoxy-glue, the tube is cut into disks of approximately 500 μm thickness, using a wire-saw. The wire was running parallel to the interface plane avoiding cracks inside the materials. The disks were then mechanically grinded to be plan-parallel and polished to a thickness of approximately 100 μm to 130 μm (cf. Figure 5.1c). Afterwards the specimens were dimpled from both sides to a thickness of approximately 35 μm . Smaller thicknesses have led to extended crack-formation during the dimpling process.

Due to high shear stresses during the sandwich formation, the metal film can be disconnected from the substrate, leading to a destruction of the metal/ceramic interface. In fact,

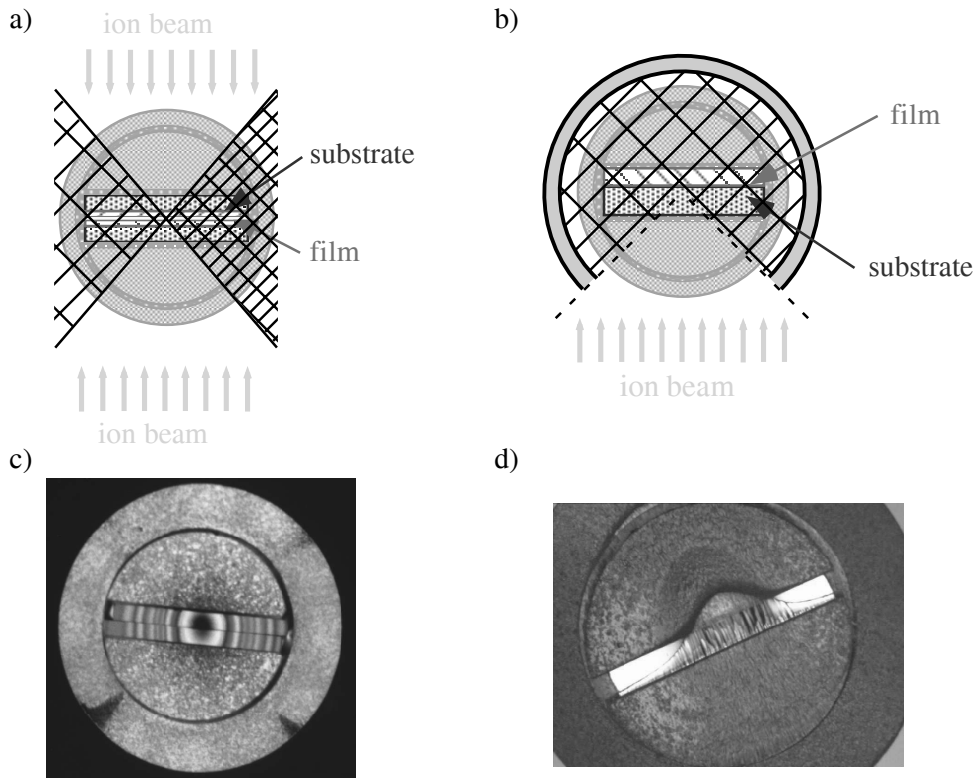


Figure 5.3: Ion beam thinning of TEM samples from a) two directions and b) from one direction. c) and d) show light-microscope images of the corresponding TEM samples.

this effect was observed for Pd/SrTiO₃ interfaces, as is shown in Figure 5.2a & b. Therefore, the sandwich formation was avoided for these interfaces and only "single-sided" crystals were embedded into the alumina tubes (cf. Figure 5.1a). In addition, contamination effects in the electron microscope, especially in the STEM, appeared to be stronger for the sandwich specimens due to the glue used during preparation.

Finally, ion-thinning of the specimens was performed from both sides using high-energy Ar⁺-ions until a hole in the specimen could be observed by simultaneous observation using light microscopy. At the edge of the hole, the specimen is transparent for the electron beam in the TEM. For the ion-thinning process two different machines are used: a modified Gatan PIPS¹ and a modified Gatan DUOMILL600². The modifications of the machines from the standard setup consist of TV-monitoring during processing, a focussed ion-beam, a cooling stage, and an oil-free vacuum for the PIPS. All modifications were performed by Strecker et al. [Strecker, 2001a]. In addition, special specimen holders made of graphite were used for both types of ion-thinning machines [Strecker, 2001a]. Ion-thinning with the PIPS was performed with ion-beam energies of 3.4 keV under illumination angles of 6° with respect to the specimen surface. In the DUOMILL600, ion-beam energies of 5 keV and illumination

¹Precision Ion Polishing System, Model-691, Gatan, Inc.

²Dual Ion Mill, Model 600, Gatan, Inc.

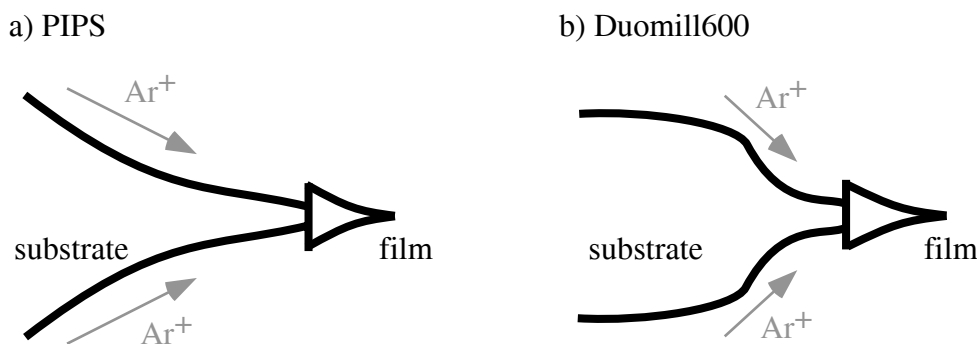


Figure 5.4: Schematic drawing of the ion-milling process of the metal/ceramic interfaces using a) a Gatan PIPS under 6° and b) a Gatan DUOMILL under 12° . The mentioned procedures have their advantages in analytical TEM and HRTEM, respectively, for bending effects and specimen thickness.

angles of 12° were used. After perforation, the specimens were further ion-thinned for 5 minutes at 2.0 keV in the PIPS or at 3.5 keV in the DUOMILL600 to remove any surface damage effects. The Cr/SrTiO₃ specimens were additionally cooled with liquid nitrogen to avoid any chemical reactions due to heating effects during the ion-beam thinning.

Two different ion beam geometries were used for the single-sided specimens: one-directional thinning and two-directional thinning. Both methods are sketched in Figure 5.3.

In the one-directional thinning, the Ar^+ -ion bombardment was performed from both sides of the specimen but with the ion-beam coming from the back-side of the ceramic substrate approaching the interfacial area (cf. Figure 5.3b). In the two-directional thinning mode, the ion-beam approaches the interface also from the side of the metal, as is displayed in Figure 5.3a. The latter technique showed strong damage effects on the metal films due to the ion-thinning process (cf. Figure 5.2c & d). Therefore, only the one-directional ion-thinning technique was used to prepare the TEM samples. It could be observed that samples prepared by the PIPS exhibited large areas with a small thickness (Figure 5.4), but also with strong bending effects (Figure 5.5). Using the DUOMILL600, only small thin areas could be obtained because with the larger illumination angles of the Ar^+ -ions the fraction of bent specimen areas was small for these specimens. These results are shown in Figure 5.4. However, for the TEM preparation of metal/SrTiO₃ interfaces, the use of the Gatan PIPS is preferred for EELS investigations, because large areas with small thicknesses are obtained. For HRTEM investigations a suppression of bending is crucial for high quality images, and therefore the Gatan DUOMILL is preferable.

Ion-thinning of the specimens also leads to amorphization effects on the surfaces. So far it is not clear if these disordered structures are due to amorphization effects of the specimen material or due to contamination effects within the ion-milling process. However, systematic HRTEM and XPS investigations have recently shown that disordered layers on the specimen surfaces can be significantly decreased by ion-polishing the TEM specimens for 30 min. using ion-beam energies of 500 eV or less [Strecker, 2001b].

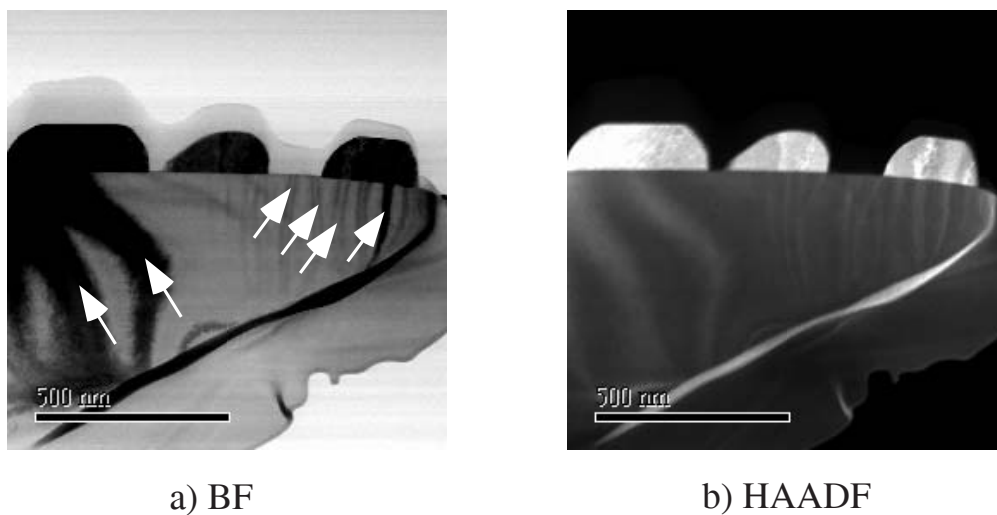


Figure 5.5: STEM a) BF and b) HAADF images of the same area showing strong bending effects of the specimen. The arrows mark bending contours in the BF image.

Chapter 6

Bulk SrTiO_3

Two different types of investigations were performed: the analysis of the valence electron structure by low energy-loss electron spectroscopy (section 6.1) and the analysis of the ELNES by experiment (section 6.3) and theory (section 6.4).

6.1 VEELS-Investigations

As was shown in section 4.1.2, EEL spectra contain information about the valence electronic structure of the investigated material for energy-losses below approximately 50 eV. From spectra recorded in this energy range, the interband transition strength and all optical properties can be calculated in terms of the complex dielectric function extracted from the acquired data [Egerton, 1996]. So-called low-loss spectra were acquired for 0.14 wt% Fe-doped and for undoped bulk SrTiO_3 to analyse the valence electronic structure of the material in terms of interband transitions between the occupied valence bands and the unoccupied conduction bands. Spectra were recorded using an energy dispersion of 0.1 eV/channel for energy-losses up to approximately 90 eV. Since the signal-to-noise ratio is large in the low-loss regime, the extraction voltage of the FEG was reduced in order to achieve a higher energy resolution (cf. section 4.1.1). The FWHM of the zero-loss peak was then found to be in the range of 0.5 eV-0.6 eV. Acquisition times were chosen in such a way that the highest intensity in the spectra, i.e. the zero-loss peak, reached about 95% of the 16 bit detector level, corresponding to about 60000 counts. Acquisition times between 0.1 sec and 0.5 sec per read-out were used, and an integration of five spectra was used to increase counting statistics. For the zero energy calibration, the center of the zero-loss peak was fitted by a Lorentzian. Subsequently, the spectra were corrected for multiple scattering events by Fourier-log deconvolution (see Figure 6.1) [Egerton, 1996]. During this procedure the wings of the zero-loss peak were fitted separately with an asymmetric Pearson VII line-shape [Dorneich, 1998]. The fitting was performed over the intensity range up to 50% of the height of the zero-loss peak. For energies below 3.4 eV, which is close to the optical band gap energy of SrTiO_3 (3.2 eV [Cardona, 1965], 3.1 eV [Waser, 1990]), no transitions are expected and therefore the intensity in the single-scattering deconvoluted spectrum (SSD) is set to zero in this region, as can be inferred from

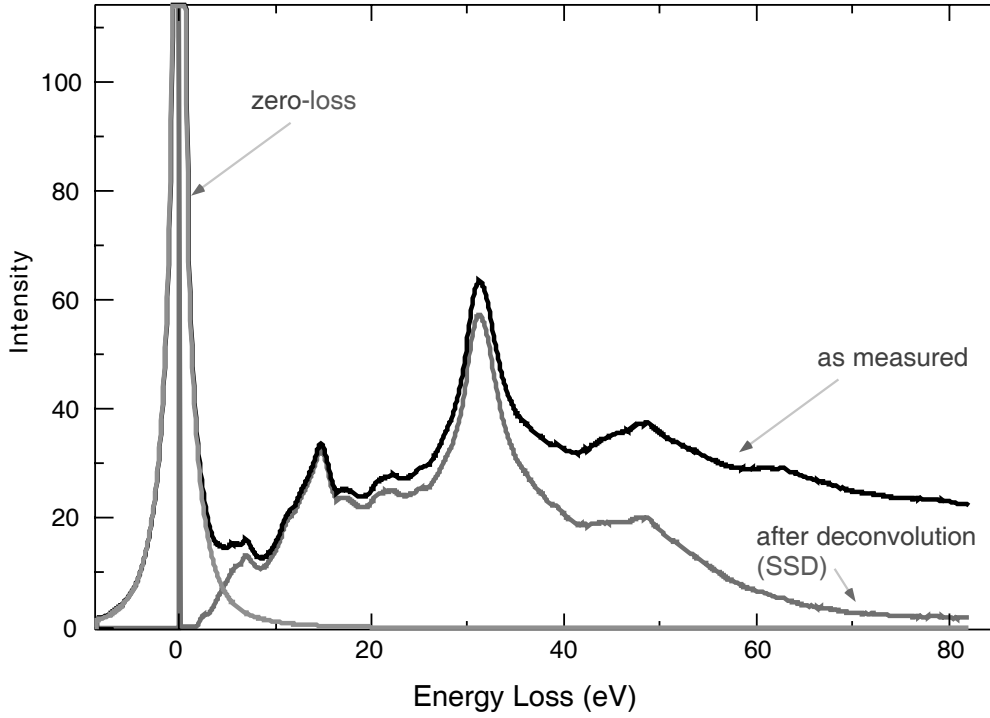


Figure 6.1: Valence electron energy-loss spectrum of bulk SrTiO_3 : the extracted zero-loss peak and the corresponding single-scattering spectrum after Fourier-log deconvolution (SSD). The relative specimen thickness was $t/\Lambda_i = 2.245$. Λ_i denotes the inelastic mean free path.

Figure 6.1. A similar procedure was followed in a previous study of SrTiO_3 low-loss spectra by Ryen et al. [Ryen, 1999]. Influences of a variation of these cut-off energies within ± 0.3 eV were found to be negligible. The resulting energy-loss function ELF is proportional to the imaginary part of the negative reciprocal complex dielectric function, as it was shown in section 4.1.2. Therefore, by a Kramers–Kronig transformation [Kramers, 1927] [Kronig, 1926] of the energy-loss function, the complex dielectric function $\epsilon = \epsilon_1 + i\epsilon_2$ can be calculated. For a more accurate Kramers–Kronig transformation, the spectra were extrapolated up to an energy-loss of 1000 eV, using a power-law description similar to the background modelling in core-loss EELS [Egerton, 1996]. From the complex dielectric function, the so-called interband transition strength J_{cv} is calculated according to

$$J_{cv}(E) = J_{cv1}(E) + iJ_{cv2}(E) = \frac{m_0^2}{e^2\hbar^2} \frac{E^2}{8\pi^2} i(\epsilon_2(E) + i\epsilon_1(E)), \quad (6.1)$$

where m_0 is the electron mass, e its charge, and E the energy. In equation 6.1, $J_{cv1} = \text{Re}J_{cv}$ corresponds to the joint density of states. For a correct scaling of $J_{cv}(E)$, the oscillator strength, or f-sum rule [Egerton, 1996] [Smith, 1985], was used with the refractive index $n = 2.37$ as determined by spectroscopic ellipsometry [van Benthem, 2001a]. The f-sum rule

evaluated for J_{cv1} is given by

$$n_{eff}(E)|_{J_{cv1}} = \frac{4\nu_f}{m_0} \int_0^E \frac{J_{cv1}(E')}{E'} dE'. \quad (6.2)$$

ν_f is a characteristic volume of material, in the present study corresponding to one chemical formula unit of SrTiO_3 , which has a volume of 59.55 \AA^3 . The analysis of the spectra was done with the electronic structure tools [ESTools], including the VEELS, CONCOR, and KKEELS programs.

Besides the VEELS measurements, spectroscopic ellipsometry and vacuum ultraviolet (VUV) spectroscopy experiments of the same bulk crystals were performed. These measurements were done by R. H. French (DuPont, Inc., Wilmington, Delaware, USA).

6.1.1 VUV Spectroscopy and Spectroscopic Ellipsometry

Figure 6.2 shows the complex index of refraction ($\hat{n} = n + ik$) determined by spectroscopic ellipsometry in comparison to data from Palik's *Handbook of Optical Constants* [Palik, 1991]. The real part n of the investigated samples of SrTiO_3 is $n = 2.37$ in the range of visible light. In the literature, values are reported from 2.20 to 2.66, due to variations in the composition or due to lattice strains of the SrTiO_3 specimens [Ryen, 1999]. Direct and indirect band gap energies were determined by linear fits to the optical absorption coefficient $\alpha = 4\pi k \lambda^{-1}$, which was calculated from the spectroscopic ellipsometrically determined extinction coefficient plotted in Figure 6.2. In this formula, k denotes the wave vector and λ the wavelength. The band gap energies can vary depending on the range of absorption coefficients used in the linear fit [Mattheiss, 1972]. A direct band gap energy of 3.75 eV was determined for Fe-doped SrTiO_3 as the intercept of a linear fit line to a plot of $\alpha^2 E^2$ versus energy E for the absorption coefficient in the range of $120000 \text{ cm}^{-1} < \alpha < 300000 \text{ cm}^{-1}$. An indirect band gap energy of 3.25 eV was determined as the intercept of the linear fit line to a plot of $\sqrt{\alpha}$ versus energy for the absorption coefficient in the range of $2000 \text{ cm}^{-1} < \alpha < 45000 \text{ cm}^{-1}$.

By the Kramers–Kronig dispersion analysis the interband transition strength J_{cv} is determined from both the VEELS data and the VUV spectroscopy data. In Figure 6.3 the real part of $J_{cv}(E)$ is extracted from two independent measurements of each experiment. In Figure 6.3a, the interband transition strength, as calculated from the complex index of refraction determined from spectroscopic ellipsometry and from the VUV data, is plotted for energies up to 15 eV, together with the results from VEELS measurements. The ellipsometry spectra as well as the VUV spectra in Figure 6.3a show well-resolved peaks labeled A_2 (4.9 eV/4.8 eV) and A_4 (6.3 eV) and two corresponding shoulders labeled A_1 (4.2 eV) and A_3 (5.4 eV/5.3 eV). At energies between 7.0 eV and 15.0 eV, i.e., beyond the energy range of ellipsometry, the VUV spectroscopy data show three clearly resolved peaks at 9.1 eV, 9.9 eV, and 11.9 eV, labeled B_1 , B_2 and C , respectively. In addition, two weaker features labeled D_1 at 12.9 eV and D_2 at 13.7 eV, are observable. Although absolute intensities can vary in different experimental spectra determined by one technique (cf. peaks A_i and B_i), the overall line-shapes are the same, reflecting identical sets of interband transitions. At higher energies

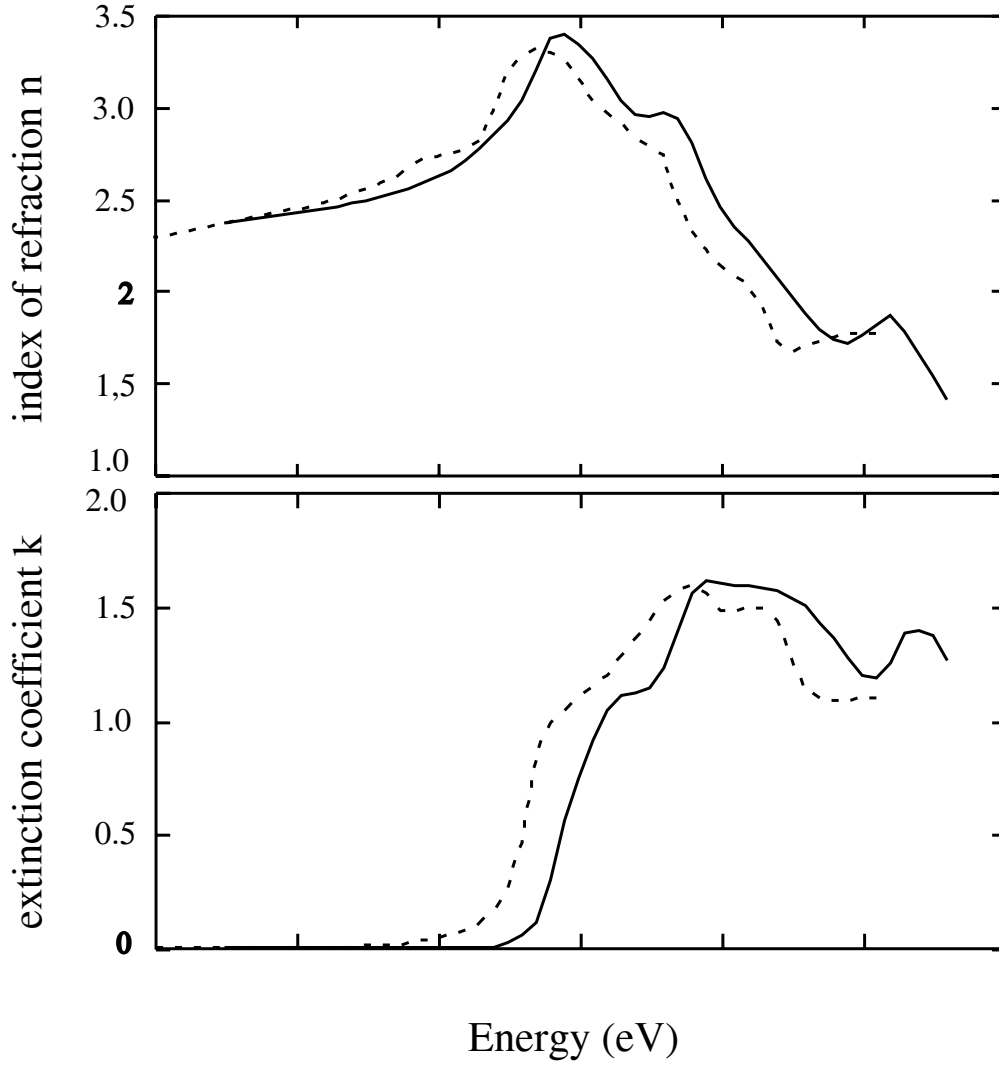


Figure 6.2: Complex index of refraction $\hat{n} = n + ik$, for bulk SrTiO_3 extracted from spectroscopic ellipsometry experiments. For comparison, data from [Palik, 1991] are included (dashed line-shapes).

(cf. Figure 6.3b) the VUV spectra exhibit transitions at 16.4 eV (E_1), 19.2 eV (E_2), 21.7 eV (E_3), 24.2 eV (E_4), 126.4 eV (F_1), and 24.4 eV (F_2). Above 32 eV the signal-to-noise ratio in the VUV measurements is diminishing due to low absolute levels of the reflected signal, which makes peak identifications unreliable in this energy range.

The determined peak energies extracted from the results obtained by the different experimental techniques are listed in Table 6.1. From the VUV data the oscillator strength f-sum rule can be determined, which gives information about how many valence electrons are involved in transitions up to a specific energy. The results of these calculations for the same independent experiments are given in Figure 6.4. The energy-loss functions calculated from the VUV spectroscopy data are plotted in Figure 6.5.

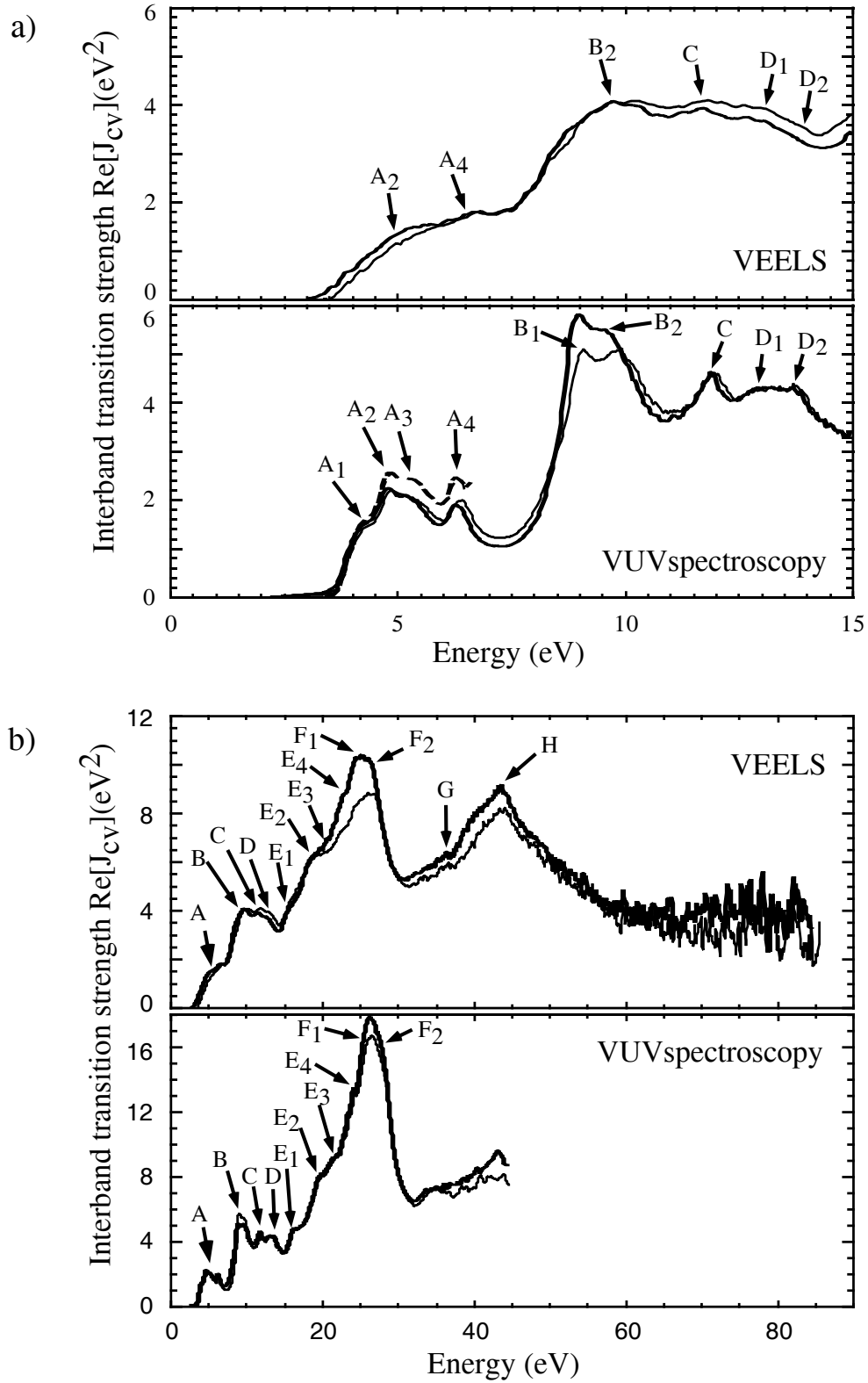


Figure 6.3: $\text{Re}[J_{cv}] = J_{cv1}$ of bulk SrTiO_3 from VEELS and VUV spectroscopy. a) Energy range up to 15 eV. The results obtained by spectroscopic ellipsometry are added as dashed lines. b) Complete energy range obtainable by VEELS and VUV spectroscopy. For all graphs two independent measurements are shown.

Table 6.1: Interband transition energies in eV for bulk SrTiO_3 as determined from spectroscopic ellipsometry, VUV spectroscopy (VUVS), VEELS, and local density functional theory (LDFT). Transitions are labeled as in Figure 6.3, with p denoting a peak and s a shoulder. Experimentally determined transition energies reported by Bäuerle et al. [Bäuerle, 1978] are listed for comparison.

Transition	Assignment	Type	Ellipsometry	VUVS	VEELS	LDFT	[Bäuerle, 1978]
<i>Transitions from the O-2p upper valence band</i>							
A_1	O-2p \rightarrow Ti-3d t_{2g}	s	4.2	4.2			4.0
A_2	O-2p \rightarrow Ti-3d t_{2g}	p	4.9	4.8	5.0	5.1	4.86
A_3	O-2p \rightarrow Ti-3d t_{2g}	s	5.4	5.3			5.5
A_4	O-2p \rightarrow Ti-3d t_{2g}	p	6.3	6.3	6.4	6.7	6.52
B_1	O-2p \rightarrow Ti-3d e_g	p		9.1			9.2
B_2	O-2p \rightarrow Ti-3d e_g	p		9.9	9.7	9.7	10.2
C	O-2p \rightarrow (Ti-3d e_g , Sr-4d t_{2g})	p		11.9	11.8	11.8	12.0
D_1	O-2p \rightarrow Sr-4d t_{2g}	s		12.9	12.7		13.0 – 13.8
D_2	O-2p \rightarrow Sr-4d e_g	s		13.7	13.2	13.1	13.0 – 13.8
<i>Transitions predominantly from the O-2s, Sr-4p lower valence band</i>							
E_1	Sr-4p \rightarrow Ti-3d t_{2g}	s		16.4	16.1	16.7	16.4
E_2	Sr-4p \rightarrow Ti-3d e_g	s		19.7	18.7	20.0	19.6
E_3	Sr-4p \rightarrow Sr-4d t_{2g}	s		21.7	21.7		
E_4	Sr-4p \rightarrow Sr-4d e_g	s		24.2	23.6		
F_1	O-2s \rightarrow (Ti-3d, Sr-4d)	s		26.4	26.1		
F_2	O-2s \rightarrow (Ti-3d, Sr-4d)	s		27.4	27.3		
<i>Transitions predominantly from the Sr-4s, Ti-3p shallow core level</i>							
G	Sr N ₁ -edge Sr-4s \rightarrow O-2p	s			37.5		
H	Ti M _{2,3} -edge Ti-3p \rightarrow (Ti-3d, Ti-4s, Sr-4d)	p			45.5		

6.1.2 VEELS-Results

In Figure 6.5 the ELF's from two independent measurements at different specimen areas are plotted. The zero-loss peak is already subtracted. The interband transition strengths J_{cv1} obtained from the energy-loss functions by the Kramers–Kronig transformations were already shown in Figure 6.3. In the low energy region below 15 eV (Figure 6.3a) only the peaks labeled A_2 , A_4 , B_2 , and C as well as two shoulders at the positions of peaks D_1 and D_2 are observable. At higher energies (cf. Figure 6.3b) the features E_i and F_i were resolved at similar energies as in the VUV spectra (cf. Table 6.1). Two additional features labeled G and H can be observed at 37.5 eV and 45.5 eV, respectively, which were not detectable by VUV spectroscopy.

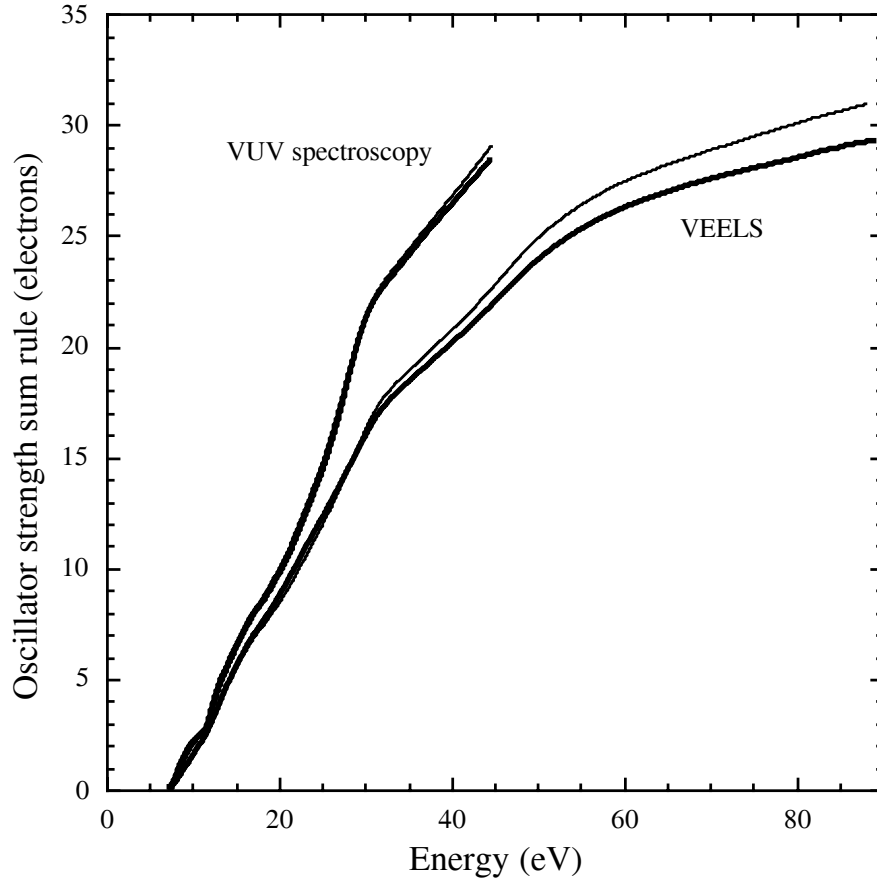


Figure 6.4: f-sum rule from EELS and VUV spectroscopy.

6.1.3 Band structure calculations

The interband transition strength J_{cv1} corresponds to transitions from occupied valence states of the material to unoccupied conduction states. By comparing of the experimentally observed transition energies, i.e., the peak energies in Figure 6.3, with the band structure and the densities of states, assignments of orbital origins of these interband transitions can be made. Therefore, *ab initio* band structure calculations were performed (see section 4.2.1) to calculate the site projected DOS and the total densities of states for bulk SrTiO_3 . Within the calculations, the cubic unit cell of the perovskite structure was used, which contains one Sr, one Ti and three O atoms. The densities of states were obtained from the Kohn–Sham eigenstates on a cubic mesh of $8 \times 8 \times 8$ k -points in the first Brillouin zone. The energy E_F (Fermi energy) of the highest occupied one-electron state at the valence band edge is taken as the energy zero. Figure 6.6 shows the site projected densities of states for O, Ti, and Sr atoms. The occupied bands from which interband transitions originate are the Ti-3s levels at -56 eV, Ti-3p and Sr-4s levels at -33 eV, the Sr-4p levels at -14.7 eV, and the O-2s and O-2p levels at -16.6 eV and at -5.0 eV to -0.5 eV, respectively. The most prominent unoccupied energy bands in the conduction band are composed of Ti-3d t_{2g} ($+1.0$ eV to $+4.5$ eV), Ti-3d

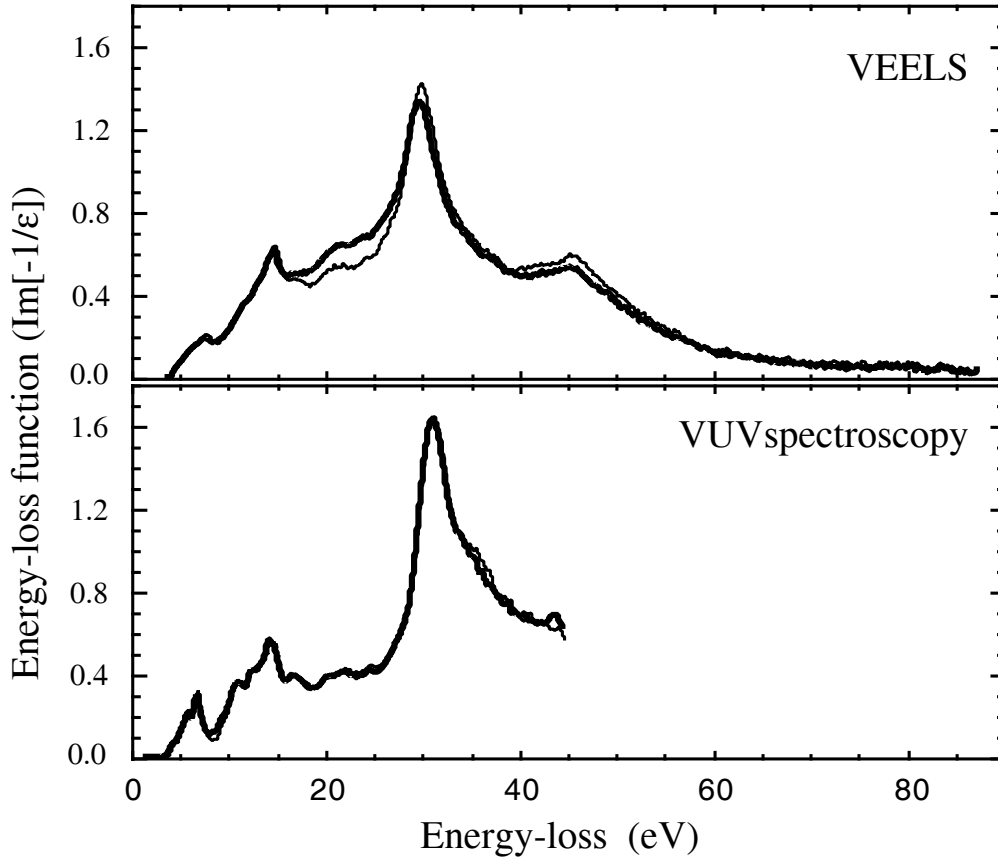


Figure 6.5: Energy-loss functions from VEELS in comparison to VUV spectroscopy up to an energy-loss of 85 eV.

Table 6.2: Indirect and direct band gap energies in eV determined from spectroscopic ellipsometry and from LDA band structure calculations.

Band gap	Ellipsometry	LDA band structure
direct	3.75	1.89 ($R \rightarrow \Gamma$)
indirect	3.25	2.22 ($\Gamma \rightarrow \Gamma$)

e_g (+4.5 eV to +9.0 eV), and Sr-4d levels (+5.0 eV to +12.0 eV) as well as various empty O-2p levels. The indirect and the direct band gap energies of SrTiO_3 determined from the band structure calculations are 1.89 eV and 2.22 eV, respectively, which underestimates the experimentally determined values listed in Table 6.2 by about 1.5 eV. This effect of underestimating band gap energies is well-known for calculations performed in the LDA [Cappellini, 2000].

However, these results are in good agreement with theoretical LDA results from Cappellini et al. [Cappellini, 2000], who calculated values of 2.24 eV and 1.90 eV for the direct and the indirect band gap, respectively. In the following discussion of the VEELS investigations

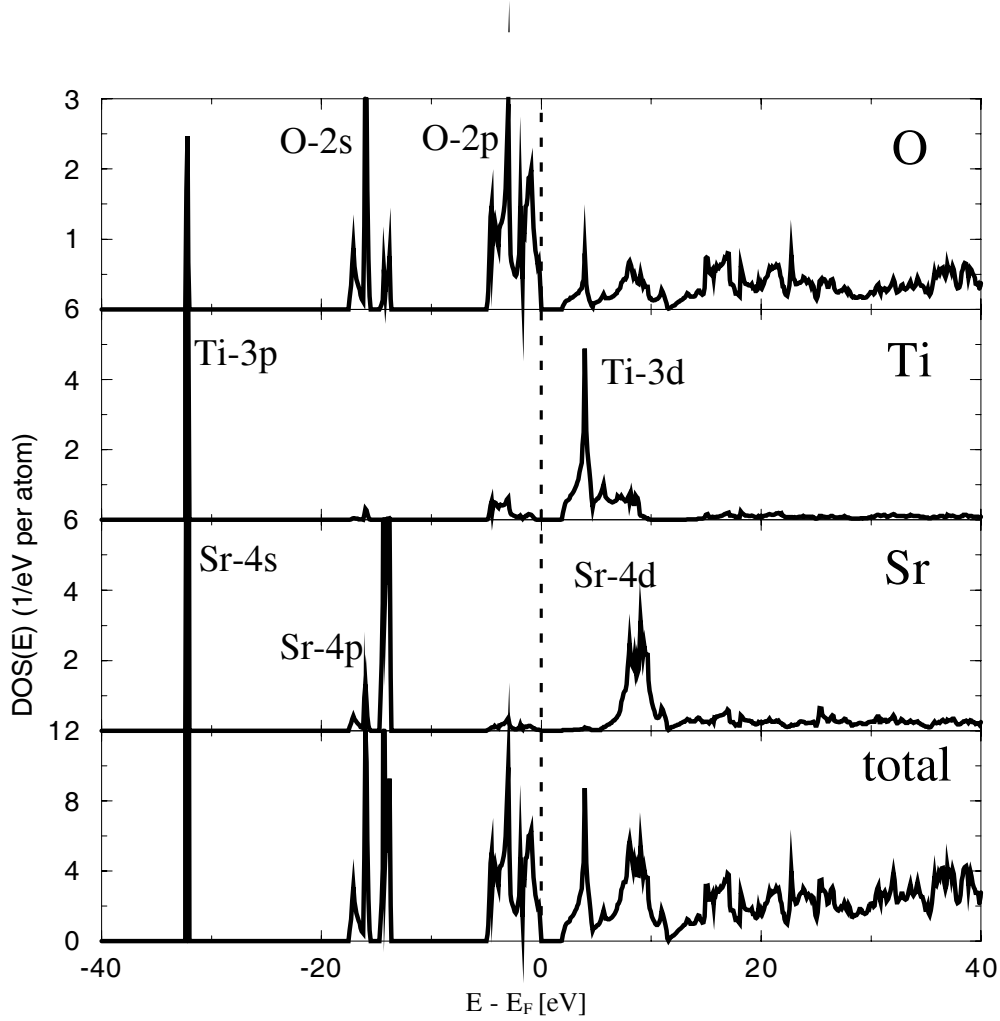


Figure 6.6: Calculated total density of states (DOS) for SrTiO_3 and site projected DOS for oxygen, titanium, and strontium, respectively.

in section 6.2, the unoccupied densities of states are shifted *ad hoc* by 1.5 eV towards higher energies by a "scissors" operation to compensate for this systematic error in the LDA.

6.2 Discussion of the VEELS Data

In this section, assignments of the spectral features in the interband transition strength, which are tabulated in Table 6.1, are developed in the context of distinct interband transitions from occupied valence bands and shallow core levels to the unoccupied conduction bands using atomic-orbital and symmetry characters in the corresponding energy bands. On this basis, a schematic energy level diagram can be developed. The results of the different experimental techniques are then compared. Since the transition energies extracted from VUV spectroscopy

and VEELS differ in several spectral features, the transition energies extracted from the optical results are used whenever possible for the assignments since the energy resolution of the VUV spectra is higher than that of the VEELS data. However, VEELS spectra do not show any additional spectral features compared to the VUV data, so that Cerenkov radiation does not play an important role in the present study.

6.2.1 UV optical Constants and Band Gaps

The UV optical constants n and k reported in Figure 6.2 show features comparable to those reported by Palik [Palik, 1991], but the transition energies found here exhibit a shift to higher energies. Frye et al. [Frye, 2001] have observed a similar shift of features in the UV optical constants towards higher energies due to prior thermal treatment of the SrTiO_3 crystals. The band gap energies fitted by Frye et al. to Palik's data give direct and indirect band gap energies of 3.52 eV and 3.28 eV, while their results show direct band gap energies ranging from 3.58 eV to 3.90 eV and indirect band gap energies from 3.00 eV to 3.77 eV. The direct and indirect gap energies found in this work of 3.75 eV and 3.25 eV, respectively (cf. Table 6.2), fall within the range seen by Frye et al. [Frye, 2001] for SrTiO_3 .

6.2.2 Valence Electron Counts in SrTiO_3

When utilizing the oscillator strength or f-sum rule (equation 6.2) to count the electrons involved in interband transitions, it is important to understand the expected number of valence electrons in the material. For SrTiO_3 the upper valence band (UVB) has 18 electrons in total originating from three oxygen atoms per unit cell, each with six 2p electrons. The lower valence band (LVB) is filled with 12 electrons in total, composed of three oxygen atoms with six O-2s and six 4p electrons of one Sr atom. The highest core level contains eight electrons arising from two Sr-4s and six Ti-3p electrons. The next lower core level consists of two electrons arising from Ti-3s electrons. Altogether, this adds up to 40 electrons, which can be expected to result from the f-sum rule evaluated up to 85 eV. This has been done in the current work from the VEELS data and the result was already shown in Figure 6.4. According to the measurements, only 30 electrons have undergone interband transitions with energies up to 85 eV.

This discrepancy of 10 electrons to the expected electron count is mainly due to the observed energy range extending only up to 85 eV. Valence electrons need not be involved only in transitions in the observed energy range. For an accurate calculation, one has to consider an infinite energy range. Therefore, the measured sum rule is expected to underestimate the theoretical value. For an integration of equation 6.2 to infinite energies, the slopes in Figure 6.4 will become flat at high energies [Shiles, 1980], which is not the case for the present experimental results. This effect is even stronger for the VUV spectroscopy data, since here the observed energy range extends only up to 45 eV.

6.2.3 Transitions from the Upper Valence Band (*A*, *B*, *C*, and *D*)

In Figure 6.3a the J_{cv1} peaks labeled A_1 to A_4 below 7 eV originate from transitions of O-2p electrons into Ti-3d t_{2g} conduction bands, while transitions B_1 and B_2 correspond to O-2p to Ti-3d e_g excitations. Peak C at 11.9 eV has a mixed character of O-2p \rightarrow Ti-3d e_g and O-2p \rightarrow Sr-4d t_{2g} transitions, whereas the two shoulders D_1 and D_2 at 12.9 eV and 13.7 eV are due to O-2p \rightarrow Sr-4d t_{2g} and e_g transitions, respectively. Further transitions can be extracted from the calculated total density of states than those visible in the experimental spectra plotted in Figure 6.3a, since the effect of the experimental energy resolution causes some broadening of the transition peaks in the J_{cv1} spectra.

6.2.4 Transitions from the Lower Valence Band (*E* and *F*)

At transition energies of 16.4 eV (E_1) and 19.7 eV (E_2), the interband transition strengths determined by VEELS and VUV spectroscopy exhibit two shoulders, which are due to Sr-4p to Ti-3d t_{2g} and e_g transitions, respectively. A spin-orbit splitting of the Sr-4p levels by 0.6 eV, which would occur as splitting of the peaks E_1 and E_2 , could not be resolved with any of the applied experimental techniques due to strong overlapping effects with other spectral features (cf. Figure 6.3b). Since the occupied O-sp and Sr-4p levels are separated by 10–13 eV and peaks C and E_3 differ by approximately 10 eV, the weak spectral features labeled E_3 at 21.7 eV and E_4 at 24.2 eV can be assigned to Sr-4p to Ti-3d t_{2g} and e_g transitions, respectively. Peaks F_1 and F_2 correspond to O-2s to Ti-3d and Sr-4d transitions, respectively. Since the initial states of these transitions are at different atomic sites than the final states, such transitions do not violate selection rules for dipole transitions. However, the broad spectral feature supporting peak E_2 to F_2 is predominantly due to collective electron gas excitations in SrTiO₃.

6.2.5 Shallow Core Level transitions (*G* and *H*)

Peaks G and H appearing in the J_{cv1} VEEL-spectra in Figure 6.3b at 37.5 eV and 45.5 eV, respectively, could not be resolved by VUV spectroscopy. These features are due to shallow core level excitations. Although peak G at 37.5 eV is a weak spectral feature, which is not clearly resolved, it is most likely due to a Sr-4s \rightarrow O-2p transition, which is called a Sr N₁-edge in the core-EELS notation [Egerton, 1996] [Ahn, 1983]. Also an assignment to a Ti-3p \rightarrow O-2p transition is possible. Peak H can be identified with the Ti-M_{2,3}-edge [Egerton, 1996], which arises from transitions from the Ti-3p to the Ti-4s, Ti-3d and Sr-4d levels. The energetic shift of 1.5 eV of peak H towards lower energies in comparison to the Ti M_{2,3}-edge in metallic titanium [Ahn, 1983] [Egerton, 1996] is due to the oxidation state of Ti in SrTiO₃, which was also observed in bulk TiO₂ [Ahn, 1983].

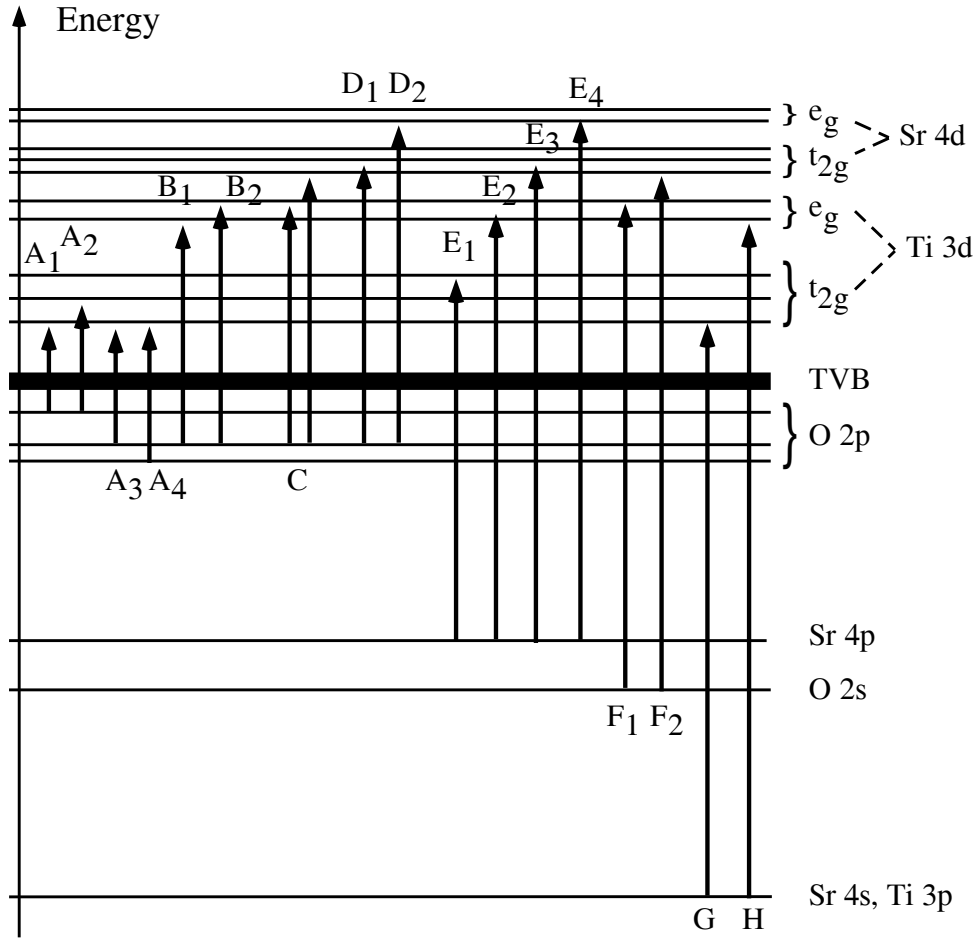


Figure 6.7: Schematic energy level diagram for bulk SrTiO_3 . The transitions from the valence band into the unoccupied conduction bands are plotted based on the assignments listed in Table 6.1. Energies are taken from the densities of states calculations and are calibrated with respect to the energy zero at the top of the valence band.

6.2.6 Schematic Energy Level Description

From the assignments of the different transition energies (cf. Table 6.1) extracted from the J_{cv1} spectra in Figure 6.3, to distinct transition processes, a schematic energy level diagram is constructed, which is plotted in Figure 6.7.

6.2.7 Comparison to Results from the Literature

In a previous study Bäuerle and co-workers [Bäuerle, 1978] examined the band structure of SrTiO_3 by VUV spectroscopy experiments and compared these results to band structure calculations by Mattheiss [Mattheiss, 1972]. Bäuerle also provided a schematic energy level diagram, but only assigned transitions from the O-2p to Ti-3d levels. For comparison, the results of Bäuerle et al. are also given in Table 6.1 and correspond to the transitions A_1 to

E_2 found in this work within tolerances of ± 0.3 eV. Ryen et al. [Ryen, 1999] showed that the interband transition strength determined by valence electron energy-loss spectroscopy is sensitive to local stresses in SrTiO_3 . LDA calculations of SrTiO_3 band structures and dielectric properties have been done by several authors ([Mattheiss, 1972], [Louie, 1975], [Xu, 1990], [de Groot, 1993], [Mo, 1999], and [Cappellini, 2000]) and are in agreement with the LDA results presented in this study [van Benthem, 2001a].

6.2.8 Comparison of VEELS and VUV Spectroscopy

Spectroscopic ellipsometry as well as vacuum ultraviolet and valence electron energy-loss spectroscopy are able to measure the interband transition strength of the investigated material through either Fresnel analysis (for ellipsometry) or Kramers–Kronig dispersion analysis on the experimental data. By the Kramers–Kronig analysis, all VEELS data can be used to determine any of the complex optical properties with high spatial resolution available in the STEM, as could be shown for a $\Sigma = 11$ grain boundary in $\alpha\text{-Al}_2\text{O}_3$ [Mülleijans, 1996] and for a near $\Sigma = 13$ grain boundary in SrTiO_3 [van Benthem, 2001a]. In the same way, the single scattering energy-loss function $\propto \text{Im}(-1/\epsilon)$ can be calculated from the optical spectra (cf. Figure 6.5). The peak energies in the J_{cv1} spectra obtained by VEELS and VUV spectroscopy are the same within ± 0.2 eV and reproduce results from previous VUV spectroscopy investigations [Bäuerle, 1978].

The optical spectroscopy methods are sensitive in the low energy region below 15 eV since the optical reflectivity provides high intensities in this regime. The VEELS data are susceptible to artifacts due to the need of fitting and subtracting the zero-loss peak. Above 15 eV, where the optical signals become weak, VEELS is superior, provided that the single scattering deconvolution is done appropriately. The Kramers–Kronig analysis performed on VEELS data is much more reliable than for optical spectra because the energy data region is much larger for VEELS, depending on the used value for the energy dispersion. This becomes important if core-edges appear at transition energies that are higher than those accessible in optical spectroscopy.

As mentioned earlier, there are differences in the transition energies extracted from VUV spectra and from VEELS. Averaging the differences in peak energies given in Table 6.1, the transition energies are reproduced by both experimental methods within an accuracy of ± 0.15 eV and ± 0.4 eV for peaks and for shoulders, respectively. Although the energy resolution in VUV spectroscopy measurements is better by a factor of 3 than in energy-loss spectroscopy, VEELS experiments using the CCD PEELS detector showed an increased experimental energy resolution, resulting in more pronounced spectral features in the VEELS data.

VUV spectroscopy and VEELS measurements of 0.14 wt% Fe-doped and undoped SrTiO_3 showed exactly the same results in the ELF's and the J_{cv1} spectra. Therefore, the electronic structure of SrTiO_3 seems to be unchanged by this amount of Fe-doping in the resolution limits of VUV spectroscopy and VEELS.

6.3 EELS-Ionization Edges

Electron energy-loss near-edge structures were measured for the Ti $L_{2,3}$ -, the O K-, and the Sr $L_{2,3}$ -edges. The edge onsets of the different edges in bulk SrTiO_3 were determined by a calculation of the second derivative of the spectra. The results are listed in Table 6.3. Energies were calibrated with respect to the C K-edge, whose π^* -peak energy is known to occur at 284.0 eV. Another method used for calibration was to acquire the zero-loss peak and the edge, which is intended to be calibrated, within a short time interval of 10 – 20 sec. During this time energy drifts are negligible and therefore the energy of the edge onset for this measurement is then given by the voltage applied to the drift-tube of the spectrometer. Throughout this study the edge onset is defined as the energy, where the second derivative of the edge onset becomes zero.

Table 6.3: Edge onset energies of the Ti $L_{2,3}$ -, the O K-, and the Sr $L_{2,3}$ -edges. Uncertainties are ± 0.2 eV for the Ti $L_{2,3}$ -edges and the O K-edge and ± 0.6 eV for the Sr $L_{2,3}$ -edges.

	Ti $L_{2,3}$	O K	Sr $L_{2,3}$
Edge onset	455.2 eV	528.4 eV	1940 eV

The Ti $L_{2,3}$ -edge and the O K-edge were measured with energy dispersions of 0.1 eV/channel or 0.2 eV/channel. With this latter setup, both edges could be acquired within one measurement. The Sr $L_{2,3}$ -edge was acquired using a dispersion of 0.3 eV/channel. By increasing the dispersion, the signal-to-noise ratio in the spectra can be improved, which is essential for these large energy-losses where the differential cross sections become small. In all ELNES measurements care was taken not to acquire spectra in a low-index zone-axis orientation in order to avoid artificial ELNES shapes from electron channeling effects [Loane, 1988] [Egerton, 1996].

Figure 6.8 shows the Ti $L_{2,3}$ -edge of bulk SrTiO_3 . The spectrum was recorded using the PDA at an energy dispersion of 0.2 eV/channel. The spectrum shown has the background subtracted and is corrected for channel-to-channel gain variations. The Ti L_3 - and the Ti L_2 -edge (peaks A_i and B_i , respectively) are formed by electron excitations from the Ti-2p $_{3/2}$ and Ti-2p $_{1/2}$ levels to unoccupied d-states in the SrTiO_3 conduction band, respectively [Egerton, 1996]. Each of these transitions leads to a so-called white-line related to the unoccupied Ti-3d states. Both lines exhibit the same ELNES since they originate from the same unoccupied densities of states. Therefore, a ratio of integrated peak-intensities can give information about the electron distribution in the Ti-2p levels [Leapman, 1982]. The ELNES of the Ti $L_{2,3}$ -edges in SrTiO_3 show a splitting by 2.4 eV [Cox, 1995] of each of the white-lines into two peaks (A_1 and A_2 , B_1 and B_2). This peak splitting is called the *crystal field splitting* and represents the energetic separation of the Ti-3d t_{2g} and Ti-3d e_g states. The Ti atoms in SrTiO_3 are octahedrally coordinated by six oxygen atoms. These oxygen

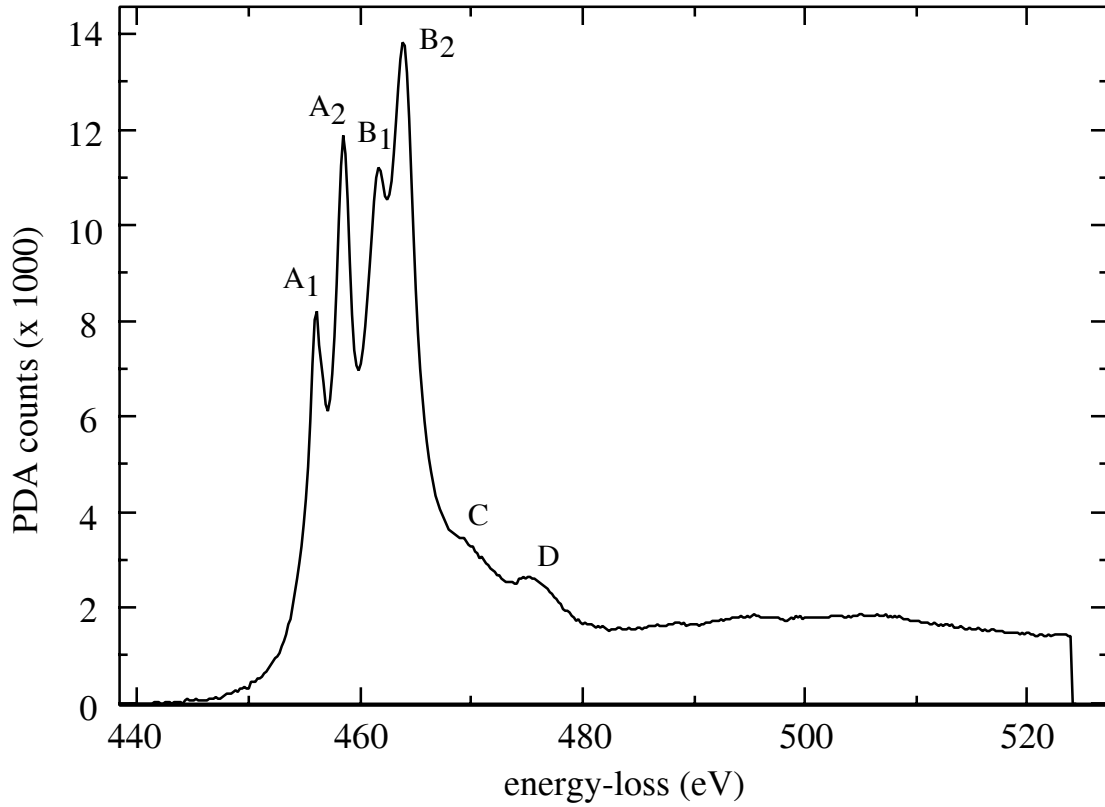


Figure 6.8: EEL-spectrum showing the Ti $L_{2,3}$ -edge in bulk SrTiO_3 . The spectrum is already background subtracted and corrected for channel to channel detector gain variations.

atoms form an electrostatic field at the Ti site, which leads to the observed breakdown of the Ti-3d degeneracy. At energy-losses of $\Delta E = 469 \text{ eV}$ and $\Delta E = 476 \text{ eV}$, two additional features labeled *C* and *D*, respectively, appear in the ELNES line shape of the Ti $L_{2,3}$ -edges.

In Figure 6.9 the ELNES of the O K-edge measured in bulk SrTiO_3 is plotted. Assuming that the dipole selection rule is valid, this absorption edge is formed by transitions from the oxygen 1s-level to the unoccupied p-states of the conduction band. The K-edge consists of five pronounced peaks labeled *A*, *B₂*, *C*, *D₂*, and *E*. In addition, on both wings, peak *B₂* shows significant shoulders labeled *B₁* and *B₃*. In the following, peaks *B_i* are often referred to by using the synonym *B*, which always denotes the complete line shape formed by all three peaks *B_i*. Peak *D₂* possesses an additional feature *D₁* on its low-energy wing. A broad peak labeled *E* is observable between energy-losses of 560 eV and 570 eV. As it was already discussed by Brydson et al. [Brydson, 1991] and de Groot et al. [de Groot, 1993], the first approximately 5 eV beyond the edge onset of the O K-edge, i.e., peaks *A* and *B*, are formed by unoccupied states related to a strong O-2p to Ti-3d hybridization [de Groot, 1989] [Brydson, 1992]. In the range of 5 eV to 30 eV above the edge onset, hybridizations of the O-2p levels with Sr-4s and Sr-4p states dominate the ELNES line-shape [de Groot, 1993]. The influence of crystal field splittings within the SrTiO_3 structure and a detailed analysis of the O K-ELNES in

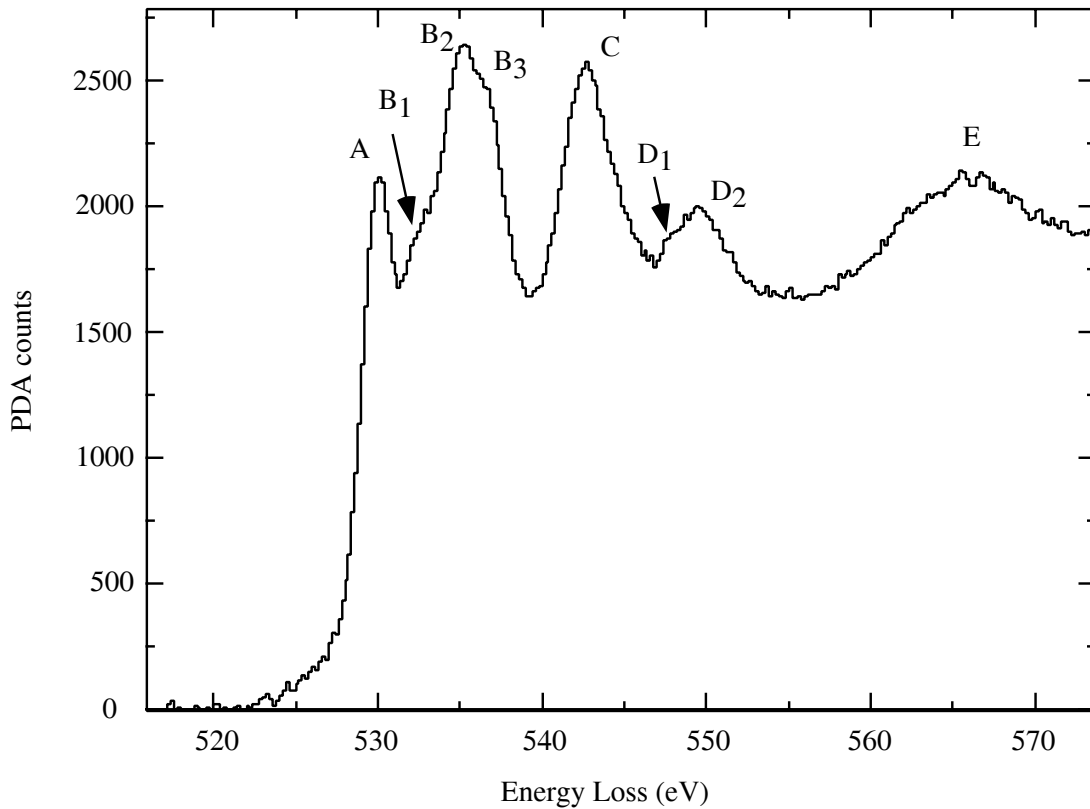


Figure 6.9: EEL-spectrum of the O K-edge in bulk SrTiO_3 . The spectrum is already background subtracted and was corrected for channel-to-channel gain variations.

terms of the local band structure are given in section 6.5. The experimental spectrum is compared to the calculated symmetry projected local densities of states.

A typically measured Sr $L_{2,3}$ -edge spectrum for bulk SrTiO_3 after background subtraction and gain correction is plotted as a function of energy-loss in Figure 6.10. The spectra were acquired using the CCD-based UHV Enfina PEELS detector with an energy dispersion of 0.3 eV/channel. Due to the significantly smaller sensitivity of the PDA detector, it was impossible to acquire the Sr $L_{2,3}$ -edges in a quality comparable to the titanium or oxygen edges by the PDA detector (compare appendix B). The Sr $L_{2,3}$ -edges are formed by electron transitions from the $\text{Sr-}2p_{\frac{1}{2}}$ and the $\text{Sr-}2p_{\frac{3}{2}}$ states into unoccupied Sr-4s and Sr-4d states in the conduction band. The Sr $L_{2,3}$ -edges also show two white-lines (peaks A and B), similar to the Ti L-edges, whereas no peak splitting of the white lines could be observed in SrTiO_3 . At energy-losses of approximately 1955 eV and 2020 eV, two weak features labeled A' and B' appear in the Sr $L_{2,3}$ -ELNES, which are not clearly resolved due to the low signal-to-noise ratio. The different widths of peaks A and B in Figure 6.10 originate from the low counting statistics and are not due to differences in the unoccupied densities of states or due to differences in the life-time broadening. With higher counting statistics they should exhibit exactly identical ELNES line-shapes.

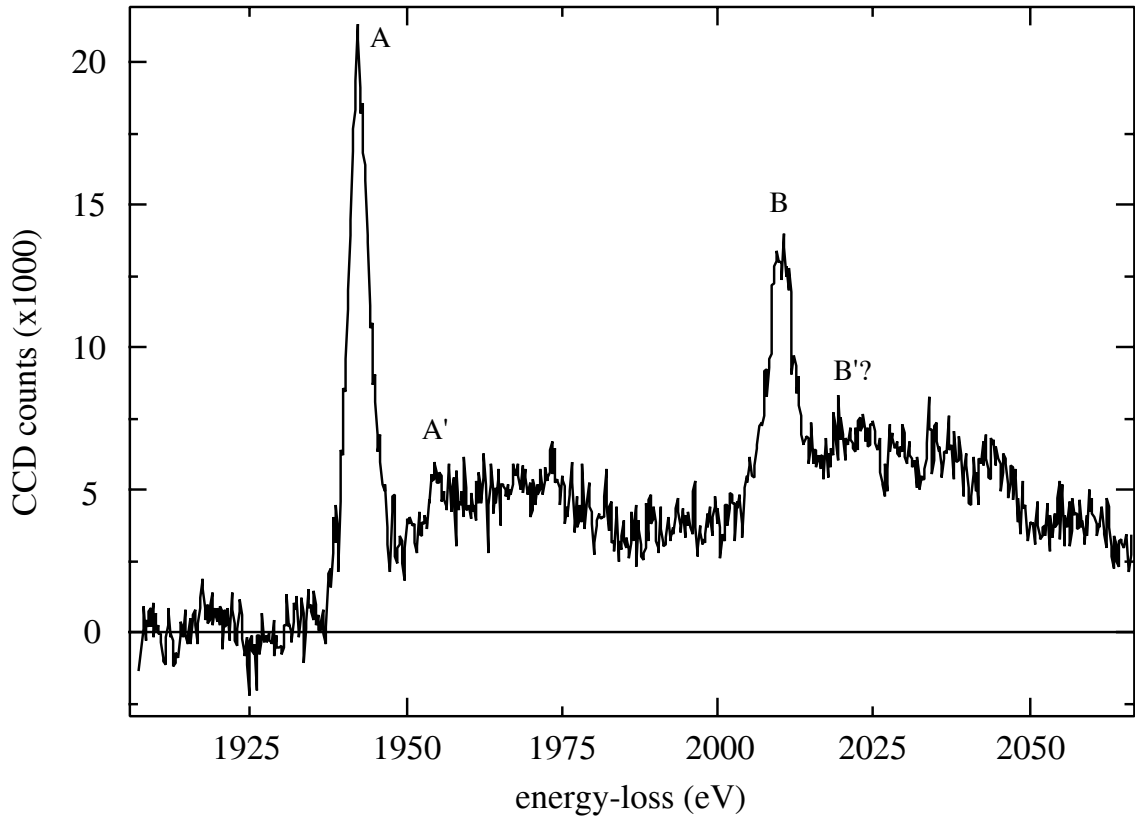


Figure 6.10: Sr $L_{2,3}$ -edges in bulk SrTiO_3 , acquired with the CCD-based UHV Enfina system. The spectrum is background subtracted and channel to channel gain corrected.

6.4 Core-hole-Effects in SrTiO_3

For a detailed understanding of the ELNES line shapes of the Ti $L_{2,3}$ -, the O K-, and the Sr $L_{2,3}$ -edges, calculations of the unoccupied local densities of states were performed using the LDFT based program code described in section 4.2.2. In addition, the FEFF8.10 code was used for ELNES calculations based on a full multiple scattering approach. As was shown by several authors, core-hole effects play an important role in analysing ELNES line shapes of K- and L-edges [Pantelides, 1975] [Fujikawa, 1983] [Brydson, 1991] [Rez, 1991] [Sawatzky, 1991] [Tanaka, 1996] [Elsässer, 2001] [Köstlmeier, 2001] [Nufer, 2001a] [Ogasawara, 2001]. The influence of electron-hole pairs, which are created by the inelastic scattering process, was investigated theoretically by applying different approaches. By doing this, simulations of these effects helped to achieve a detailed understanding of the core-hole effect in SrTiO_3 . Based on this knowledge, a reliable interpretation of the ELNES line shapes becomes possible. For the simulations, the core-hole was modeled by the so-called $Z+1$ and the Z^* approximations (cf. section 4.1.2).

6.4.1 LDFT-based Calculations

The cubic supercells of $(\text{SrTiO}_3)_n$ used for the LDFT calculations comprised n SrTiO_3 formula units with $n = 1, 2, 4, 8$, and 16 (cf. Table 6.4). For all supercell sizes up to $n = 8$, three calculations were performed using the following supercells in the $Z + 1$ approximation: $(\text{SrTiO}_3)_n$, $\text{Sr}_n\text{Ti}_n\text{O}_{3n-1}\text{F}$, and $\text{Sr}_n\text{Ti}_{n-1}\text{VO}_{3n}$. The $\text{Sr}_n\text{Ti}_n\text{O}_{3n-1}\text{F}$ supercell was also calculated for $n = 16$. To investigate the core-hole effect on the $\text{Sr } L_{2,3}$ -edge, a $\text{Sr}_7\text{YTi}_8\text{O}_{24}$ supercell was used for the calculations. By these calculations, the effect of the $Z + 1$ approximation on total energies and projected densities of states can be studied systematically.

Table 6.4: Supercell size $(\text{SrTiO}_3)_n$ and Bravais-lattice type, minimum distance d of neighbouring $Z + 1$ centers in units of the cubic lattice parameter of SrTiO_3 , and total energy differences ($\Delta E_{SCF}(\text{O})$ and $\Delta E_{SCF}(\text{Ti})$) between the bulk supercell and the corresponding $Z + 1$ supercells for O and Ti, respectively. The values of ΔE_{SCF} are referred to the $(\text{SrTiO}_3)_{16}$ supercell. *sc*, *fcc*, and *bcc* denote simple cubic, face-centered cubic, and body-centered cubic Bravais-lattice types of the supercells, respectively.

n	Bravais lattice	d/a	$\Delta E_{SCF}(\text{O})$ (eV)	$\Delta E_{SCF}(\text{Ti})$ (eV)
16	<i>fcc</i>	$2\sqrt{2}$	0.0	0.0
8	<i>sc</i>	2	-0.02	> -0.01
4	<i>bcc</i>	$\sqrt{3}$	-0.08	-0.01
2	<i>fcc</i>	$\sqrt{2}$	-0.30	-0.13
1	<i>sc</i>	1	-0.65	-0.26

To judge the reliability of the supercell size, two different criteria were considered: first, the convergence of the total energy differences $\Delta E_{SCF}(\text{O})$ and $\Delta E_{SCF}(\text{Ti})$ between the unperturbed $(\text{SrTiO}_3)_n$ cell and the cell containing the corresponding $Z + 1$ centre; and second, the convergence of the spectral shape of the site and symmetry projected unoccupied DOS in each supercell. In addition, the calculated PDOS is compared to the experimentally observed ELNES data.

In Table 6.4 the differences in the total energies ΔE_{SCF} between the unperturbed and the $Z + 1$ supercells are listed for the O sites ($\Delta E_{SCF}(\text{O})$) and for Ti sites ($\Delta E_{SCF}(\text{Ti})$), referred to the total energy of the $(\text{SrTiO}_3)_{16}$ supercell. If the supercells are too small, adjacent $Z + 1$ centres interact and lead to a non-negligible contribution to this energy difference. In the limit of infinitely large supercells, ΔE_{SCF} must converge to the actual excitation energy, i.e., to the absolute energy of the edge onset. This argument, however, only holds in the framework of an all-electron theory. In this work, pseudopotentials are used and therefore the total energies ΔE_{SCF} are calculated only from the valence electrons. For that reason, the focus of Table 6.4 is only on the convergence of the total energies with respect to the supercell size rather than on absolute energies.

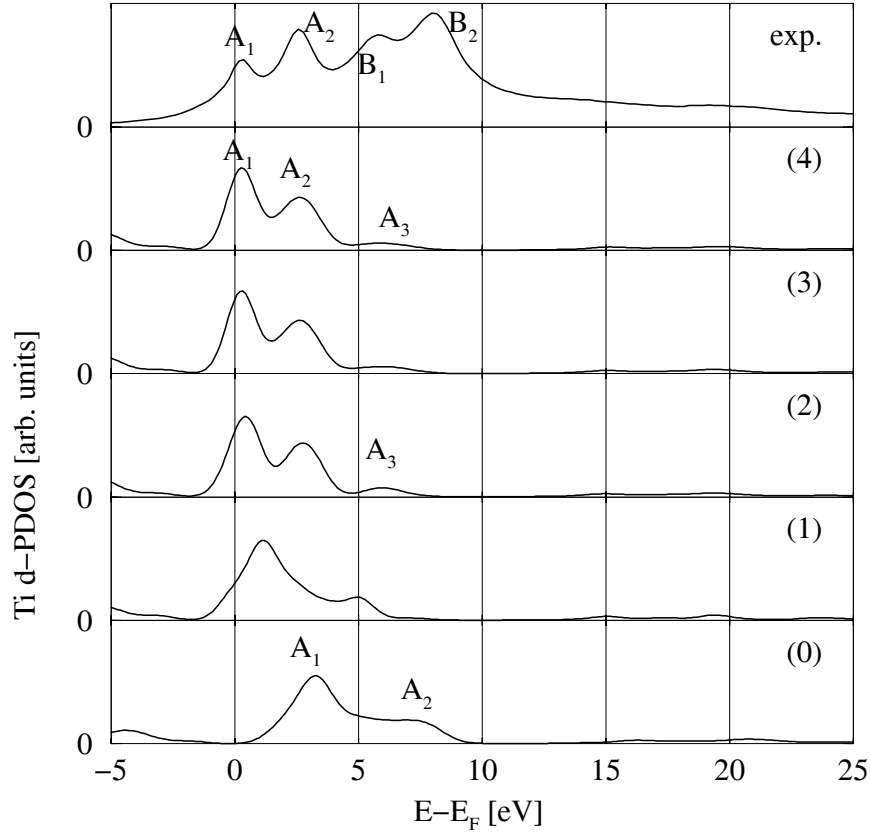


Figure 6.11: Projected densities of states for the central excited Ti^* (Ti/V) atom in projection on $l = 1$ ($\text{L}_{2,3}$ -edges, d-PDOS). The PDOS (0) at the bottom are calculated for Ti in bulk SrTiO_3 without core-hole, the others for V in $\text{Sr}_n\text{Ti}_{n-1}\text{VO}_{3n}$ supercells. From (1) to (4) the supercell sizes and shapes change: $n = 1$ (sc), $n = 2$ (fcc), $n = 4$ (bcc), and $n = 8$ (sc). For comparison, the experimental Ti $\text{L}_{2,3}$ -edge is plotted topmost.

The data in Table 6.4 show that the smallest SrTiO_3 unit cell contains a significant interaction between adjacent $Z + 1$ centers. For $n = 4$, the F–F interaction energy drops below 0.1 eV, which equals the experimental energy dispersion per channel, whereas the V–V interaction energy is by one order of magnitude smaller than the experimental energy dispersion. However, for $n = 8$, which corresponds to a simple cubic supercell consisting of $2 \times 2 \times 2$ SrTiO_3 cubes, the interaction energies are -0.02 eV and below -0.01 eV for O and Ti core-holes, respectively. Therefore, for the purpose of a comparison to experimental data, supercell sizes with $n = 8$ are used throughout the analysis of the core-hole effects in SrTiO_3 . For this supercell size total energies are regarded to be converged at least in the framework of the experimental energy dispersion and energy resolution limits.

O obeying the dipole selection rules, the Ti $\text{L}_{2,3}$ -edges are regarded to be formed by local unoccupied 3d- and 3s-states of the conduction bands. However, in the first 10 eV above the Fermi level, the s-PDOS is small and flat compared to the d-PDOS. Therefore, the Ti $\text{L}_{2,3}$ -edges are considered to be determined only by the local unoccupied d-PDOS. In Figure 6.11

the calculated V d-PDOS and the Ti d-PDOS are plotted for the different supercell sizes. It is sufficient to compare the local unoccupied d-PDOS to one of both edges, for example, with the L_3 -edge. A comparison to the L_2 -edge in general is also possible, although the interpretation is not that straightforward due to the overlap with the L_3 -edge. The calculated Ti d-PDOS of the smallest SrTiO_3 supercell ($n = 1$, curve (0) in Figure 6.11) differs markedly from the experimentally observed line shape, since only one sharp peak A_1 and a broad shoulder A_2 at higher energies are present. The exchange of the Ti atom by a V atom in the $n = 1$ supercell leads to a transformation of the broad shoulder A_2 into a small peak in spectrum (1). With increasing size of the calculated supercell, the V d-PDOS shifts in energy towards the Fermi level and peak A_2 becomes more pronounced. The d-PDOS line shape seems to be already converged to its final shape for the supercell with $n = 4$ (curve (3)). This behaviour could already be estimated from the convergence of the corresponding total energies in Table 6.4. Starting with $n = 4$, an additional peak labeled A_3 appears at 7 eV above the Fermi level (cf. Figure 6.11).

The calculated line shapes (3) and (4) are in good agreement to the experimental Ti L_3 -edge as far as peak energies are concerned. The crystal field splitting of 2.4 eV is provided by both theory and experiment, whereas the d-PDOS calculated without consideration of a core-hole does not show this peak splitting. In Figure 6.12 the converged V d-PDOS is plotted together with the experimental Ti $L_{2,3}$ -edge. In addition, V-3d t_{2g} and V-3d e_g densities of states are plotted for a more detailed analysis. One can clearly observe a sharpening of both states due to the core-hole effect. The e_g states form the peak labeled A_2 , which is experimentally observed.

Assuming the validity of the dipole selection rule for the O K-edge, this absorption edge is analysed in terms of the site projected unoccupied densities of oxygen p-states (O p-PDOS). The p-PDOS for oxygen and fluorine are plotted with increasing cell size from the bottom to the top in Figure 6.13. As indicated, the lowermost curve (0) is the p-PDOS of oxygen in unperturbed SrTiO_3 , which is identical for all sizes of $(\text{SrTiO}_3)_n$ supercells without the core-hole approximation, i.e. for $1 \leq n \leq 16$. The experimental O K-edge was calibrated with its edge onset on the calculated Fermi level. Curve (0) has a line-shape showing similarities to the experimental spectrum, as far as the number and the energies of peaks occurring in the ELNES are concerned. However, the experimental spectrum shows an additional significant shoulder B_1 between the first peak A and the second peak B_2 and a shoulder B_3 on the high energy wing of B_2 . Focussing on curves (1) to (5), the line-shapes converge in spectrum (4), which corresponds to a supercell size denoted by $n = 8$. Differences between curves (4) and (5) appear not to be significant or resolvable by the experiment. The converged p-PDOS (4) shows asymmetric line shapes for the features B and peak C , similar to the experimental spectrum. Peak A in the p-PDOS has lower intensity compared to the calculation of the undisturbed supercell. However, after incorporation of a core-hole, the shoulder B_1 between peaks A and B_2 is not observable in the F p-PDOS (see Figure 6.13). In Figure 6.14, curve (4) ($n = 8$) is again plotted in comparison to the experimental spectrum. For a more detailed analysis, the calculated p-PDOS is split into amounts originating from oxygen p_x , p_y , and p_z orbitals. In the calculated $2 \times 2 \times 2$ supercell, F–Ti bonds are oriented along the x -axis. As

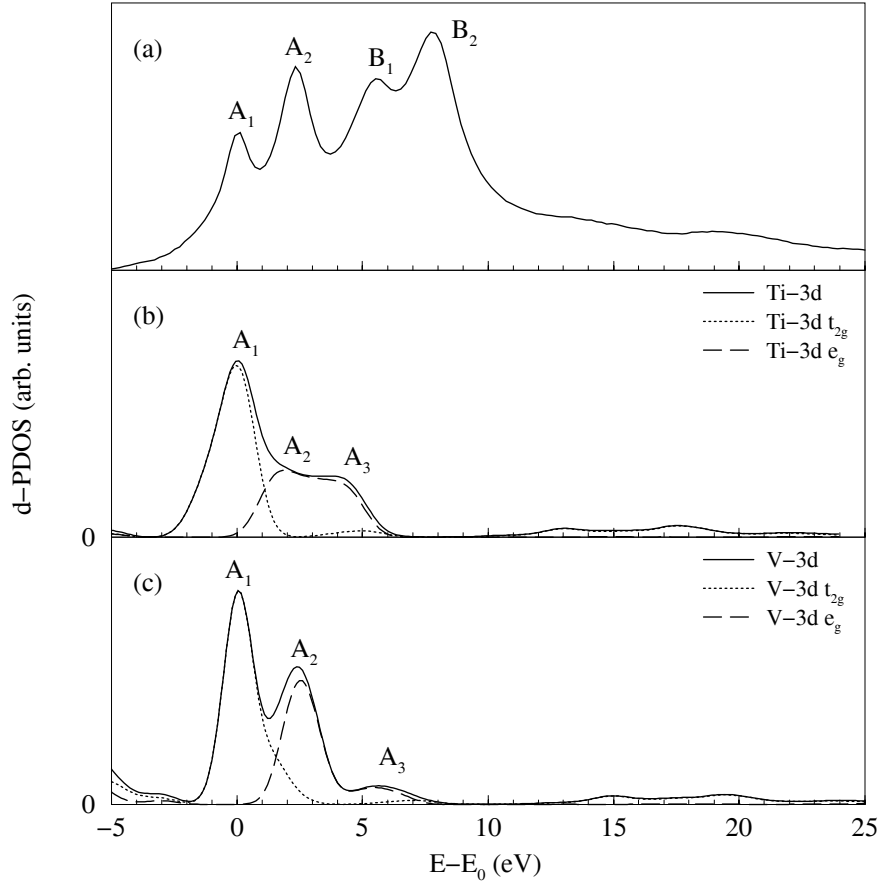


Figure 6.12: Core-hole effect on the Ti d-PDOS in bulk SrTiO_3 : a) experimental ELNES, b) unoccupied d-PDOS for titanium, and c) unoccupied d-PDOS for vanadium ($Z + 1$ approximation). The first peak of all spectra was calibrated to a relative energy of $E_0 = 0$ eV.

one can infer from Figure 6.14, the p_y and p_z projected DOS show the same line shapes, but differ from the p_x -PDOS. Especially at the energetic position of peak B_1 , the F p_x -PDOS provides some extra intensity compared to the O p -PDOS. This effect is rather small and is therefore not observable in the total p -PDOS, in which the different p_m -PDOS are summed by equal amounts.

In a $2 \times 2 \times 2$ supercell of SrTiO_3 , one Sr atom was exchanged with an Y atom to simulate the core-hole effects on the Sr $L_{2,3}$ -edges. Convergence calculations with respect to the size of the supercell were not performed for this system, based on the results for O and Ti where this supercell size was sufficiently large. This is also assumed for the exchange of a Sr atom by a Y atom. The results of the calculations for the Sr-3d and the Y-3d states are plotted together with the experimental Sr L_3 -edge in Figure 6.15.

As one can infer from Figures 6.15b and 6.15c, the substitution of one Sr atom by one Y atom leads to an overall increase in intensity of the unoccupied t_{2g} -PDOS and a sharpening

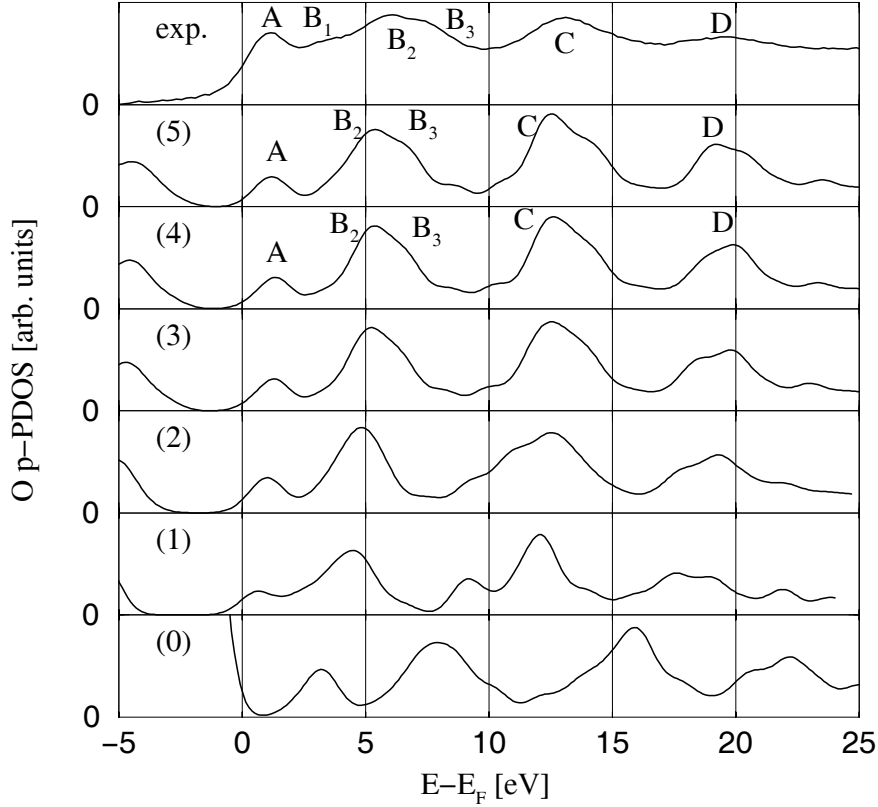


Figure 6.13: Projected densities of states for the central excited O^* (O/F) atom in projection on $l = 1$ (K-edge, p-PDOS). The PDOS (0) at the bottom are calculated for O in bulk SrTiO_3 without consideration of a core-hole, the others for F in the $\text{Sr}_n\text{Ti}_n\text{O}_{3n-1}\text{F}$ supercells. From (1) to (5) the supercell sizes and shapes change: $n = 1$ (sc), $n = 2$ (fcc), $n = 4$ (bcc), $n = 8$ (sc), and $n = 16$ (fcc). For comparison the experimental O K-edge is plotted topmost. E_F denotes the Fermi level.

of the unoccupied e_g -states in energy. However, the calculated line shapes for both supercells, i.e., with and without considering the core-hole effect, show the same level of agreement with the experimental Sr L_3 -edge in Figure 6.15a. Differences in the Y d-PDOS compared to the Sr d-PDOS are beyond the experimental resolution limits.

6.4.2 Multiple Scattering-based Calculations

Additionally to the above mentioned LDFT bandstructure calculations, ELNES simulations using the FEFF8.10 code in the full multiple scattering approach were also performed (see section 4.2.3). Atomic clusters of bulk SrTiO_3 including 114 atoms were considered for the full multiple scattering calculation, corresponding to a cluster radius of 0.72 nm. The cluster radius is $\sim 6\%$ larger than the diagonal dimension of the $2 \times 2 \times 2$ supercell. The crystal muffin-tin potential was calculated self-consistently within a cluster radius of 3.0 nm. Test

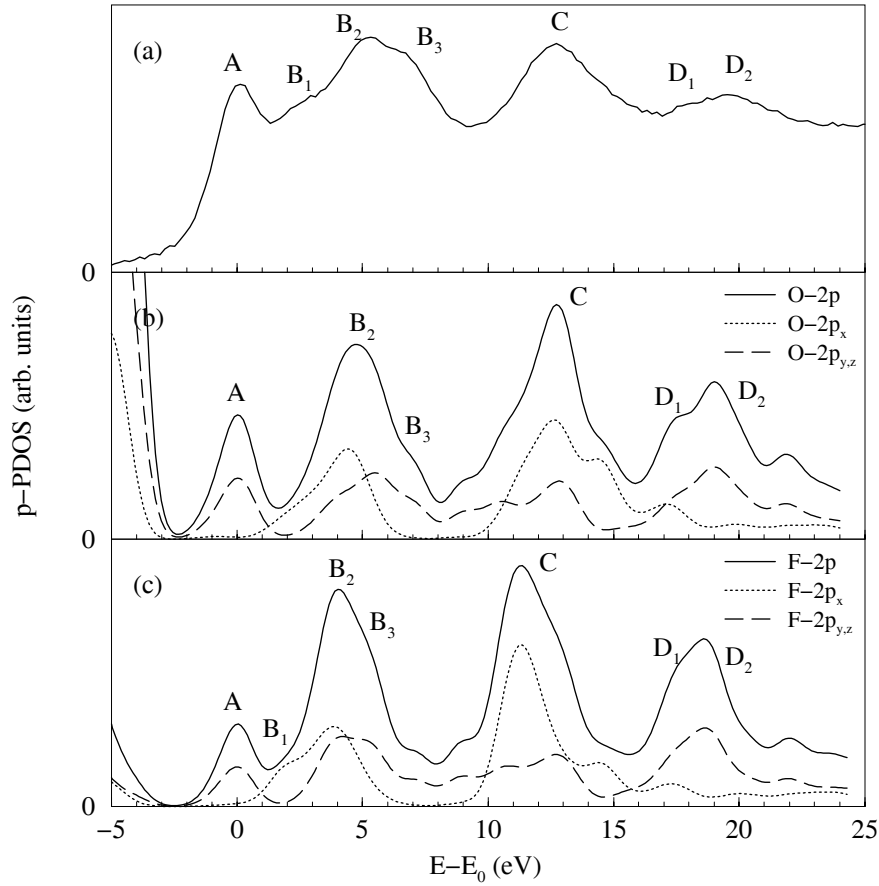


Figure 6.14: Core-hole effect on the O p-PDOS in bulk SrTiO_3 : a) experimental ELNES, b) unoccupied p-PDOS for oxygen, and c) unoccupied p-PDOS for fluor ($Z+1$ approximation). The first peak of all spectra were calibrated to a relative energy of $E_0 = 0 \text{ eV}$.

calculations did not show any significant change in the final ELNES line shapes after further increasing the atomic cluster in which the self-consistent potential calculation is performed. The core-hole was approximated by the $Z+1$ approximation (F for O, V for Ti, or Y for Sr), or by the Z^* approximation. In the latter approach a 1s electron of the corresponding atom is moved into the deepest unoccupied state in the atomic potential.

In Figure 6.16 the results of the multiple scattering calculations for the Ti L_3 -edge are plotted together with the experimental Ti $L_{2,3}$ -edges for comparison. All spectra were calibrated with respect to peak A to a relative energy-loss of $E_0 = 0 \text{ eV}$. The resulting ELNES from the calculations without core-hole incorporation (Figure 6.16) shows three significant spectral features labeled A_1 , A_2 , and A_3 , whereas A_1 also has a pre-peak A' on its left wing and a shoulder A'' on its right wing. The energetic peak position of peak A_2 coincides with the one of peak A_2 from the experimental spectrum. A_3 is not observable in the experimental data due to the overlap with the Ti L_2 -edge. From Figure 6.16a and 6.16b one can infer that

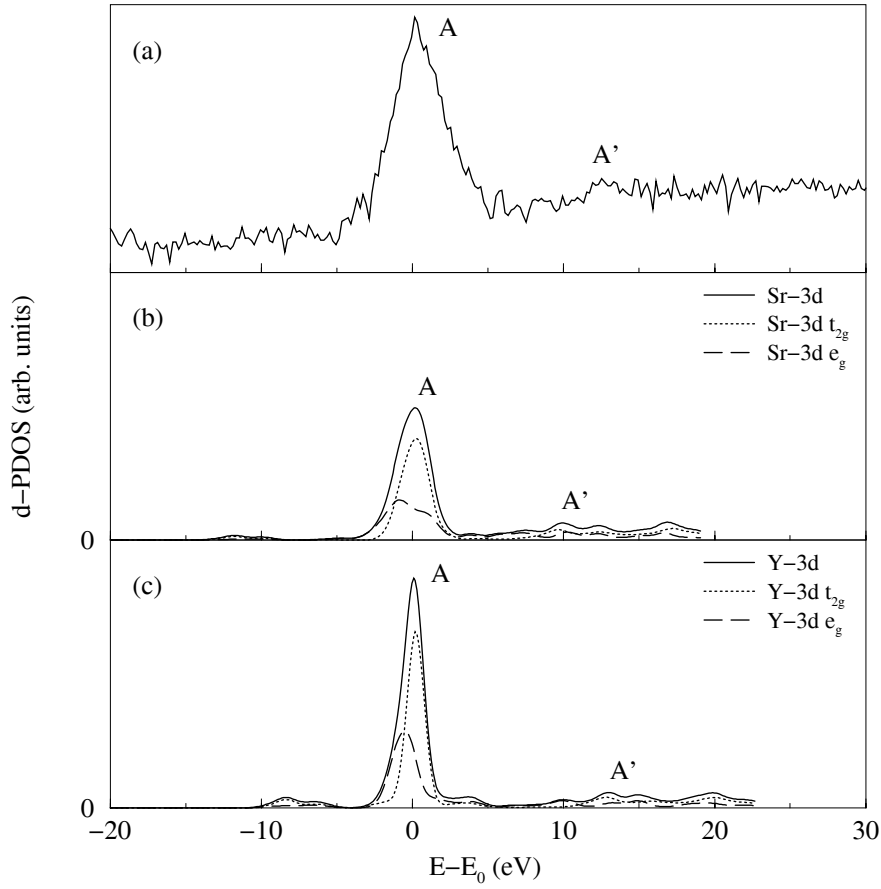


Figure 6.15: Core-hole effect on the Sr d-PDOS in bulk SrTiO_3 : a) experimental ELNES, b) unoccupied d-PDOS for strontium, and c) unoccupied d-PDOS for yttrium ($Z + 1$ approximation). The first peak of all spectra was calibrated to a relative energy of $E_0 = 0$ eV.

the $Z + 1$ and the Z^* approximations both produce nearly the same ELNES results for the Ti $L_{2,3}$ -edges. The incorporation of the core-hole effect results in two strong ELNES peaks labeled A_1 and A_2 , which are similar in height, and a third feature A_3 at a relative energy-loss of $E_0 = 5.0$ eV. A_1 and A_2 exhibit a peak splitting of 1.9 eV. The pre-peak A'_1 occurs as a shoulder in the core-hole calculations, whereas A''_1 on the high energy wing is not observed for an incorporated core-hole. However, the pre-edge feature A'_1 is not observable in the experiment.

The MS calculations for the O K-edge are plotted in Figure 6.17. Again, all spectra were calibrated with respect to peak A of the ELNES to a relative energy-loss of $E_0 = 0$ eV. Without the incorporation of the core-hole effect, the MS calculation produces a line shape consisting of 3 clearly resolved peaks labeled A, B, and C, together with a broad spectral feature labeled D (Figure 6.18a). After calibration peaks B and C in the non-core-hole calculation appear at energies which are 0.5 eV – 1.0 eV smaller than in the experiment.

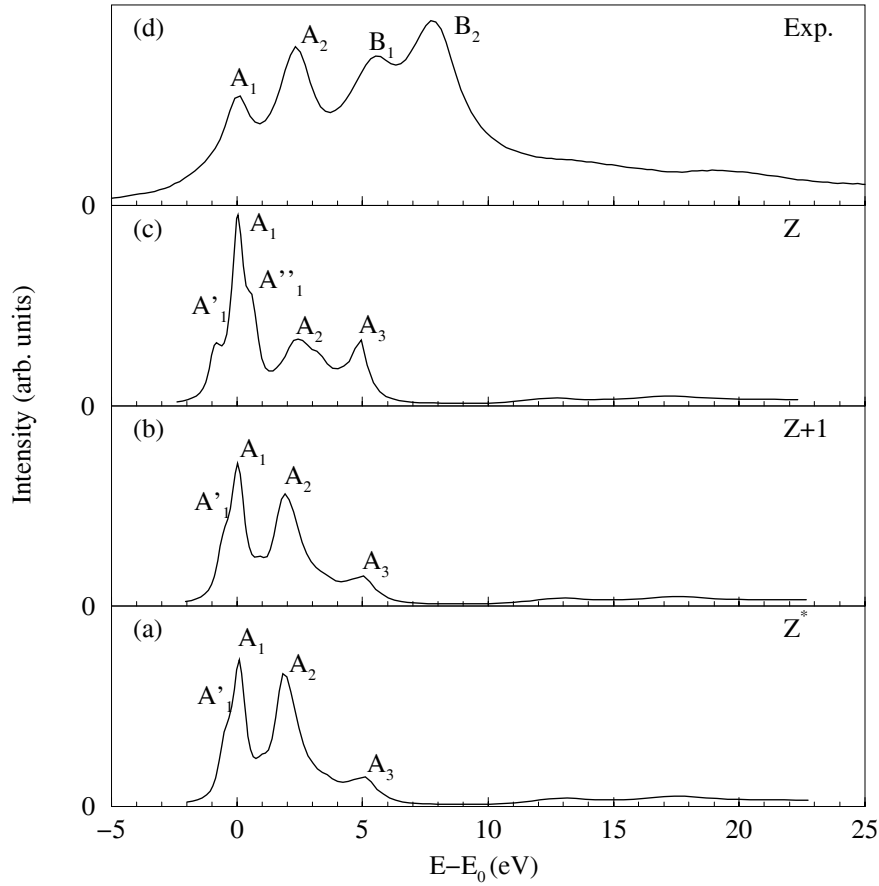


Figure 6.16: Results of FEFF-code calculations for the Ti $L_{2,3}$ -edge with different core-hole approximations.

The energy of peak D in the calculation is by about 3 eV smaller when compared to the experimental spectrum. The incorporation of the core-hole effect by the $Z + 1$ and Z^* approximations again produces nearly the same line shapes for the O K-edge. The peak positions of peaks A , B , C , and D remain the same with or without consideration of the core-hole effects. The inclusion of the core-hole effect leads to an asymmetric line shape of peak B , resulting in a shoulder B_2 at a relative energy-loss of 5.5 eV, which fits to the shoulder B_2 in the experimental data. However, a spectral feature at the position of B_1 can again not be observed in any of the MS calculations of the O K-edge.

Figure 6.18 shows the MS results for the Sr L_3 -edge in SrTiO_3 . All calculations of the different supercells show nearly the same line shapes of one pronounced peak labeled A together with a small feature labeled A' . Without incorporating the core-hole effect, A' appears at a relative energy of 9 eV, whereas the simulations of the core-hole effects shift this feature by 3.5 eV towards higher energies. However, all three calculated ELNES data reproduce the experimental spectrum of the Sr L_3 -edge.

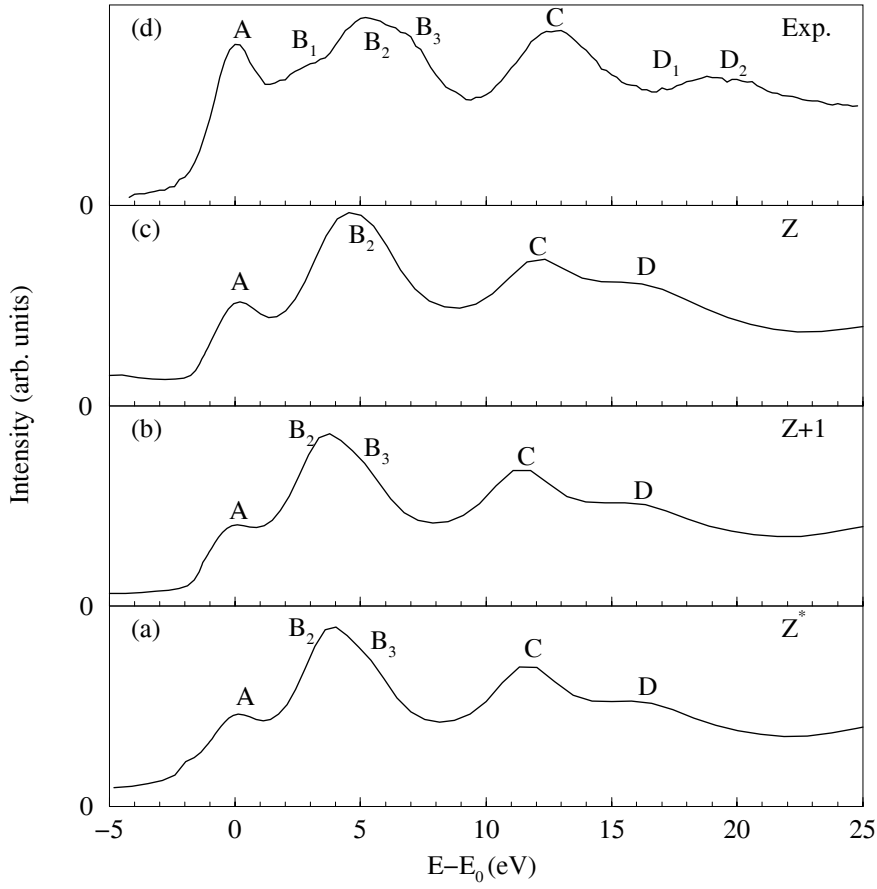


Figure 6.17: Results of FEFF-code calculations for O K-edge with different core-hole approximations.

6.5 Discussion of the Core-hole-Effects

A comparison of the experimental absorption edges to the local symmetry projected densities of states provides a detailed understanding of the core-hole effects on the experimental ELNES line shapes. The consideration of final state effects such as the core-hole effect is reported to be crucial for a detailed quantitative analysis of the near-edge structures in electron energy-loss spectra [Pantelides, 1975] [Brydson, 1991] [Tanaka, 1996] [Elsässer, 2001] [Köstlmeier, 2001] [Nufer, 2001a] [Ogasawara, 2001]. The more localized the initial state of the transition, the more important is the consideration of core-hole effects in the PDOS calculations due to a decreased screening of the electron hole by the remaining core electrons. Therefore, core-hole effects are regarded to be most important for the analysis of K-edges and L-edges [Brydson, 1991] [Elsässer, 2001] [Köstlmeier, 2001] [Nufer, 2001a]. Significant features in experimental data are the high intensities at the onset of the edges, which are attributed to the core-hole effect [Tanaka, 1996]. For the O K- and the Mg K-edges [Elsässer, 2001], as well as for the O K-edge in $\alpha\text{-Al}_2\text{O}_3$ [Nufer, 2001a], detailed analyses of the core-hole effect were performed by LDFT investigations. The authors found a significant

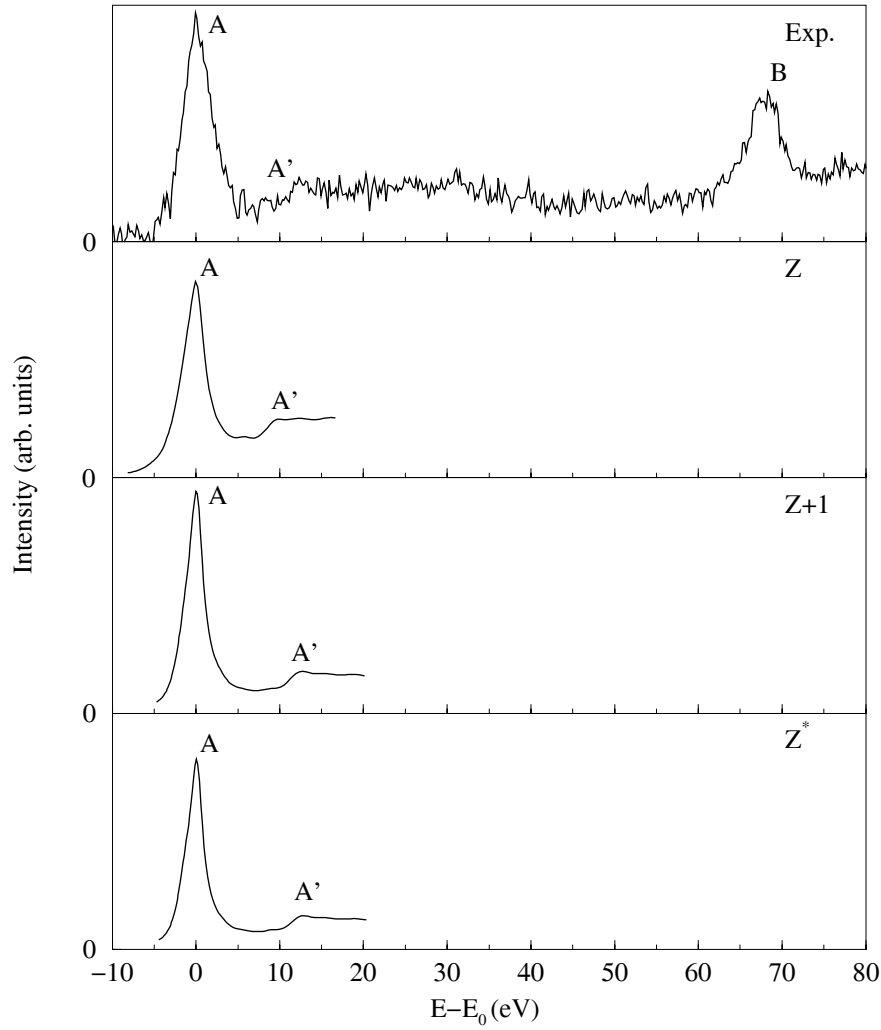


Figure 6.18: Results of FEFF-code calculations for the Sr $L_{2,3}$ -edge with different core-hole approximations.

increase in intensity of the PDOS near the Fermi level, i.e. at the edge onset, due to the incorporation of a core-hole.

As shown in section 6.4, the V d-PDOS exhibits significant differences from the Ti d-PDOS (cf. Figure 6.12). The experimentally resolved crystal field splitting of 2.4 eV cannot be observed in the Ti-3d densities of states, in which the t_{2g} states form a sharp peak at the edge onset, whereas the e_g states form a broad spectral shape consisting of the peaks A_2 and A_3 . The energetic separation of peaks A_1 and A_2 is 1.9 eV. In the $Z + 1$ calculation, the V d-PDOS in Figure 6.12 exhibits two strong peaks labeled A_1 and A_2 separated by 2.4 eV, and a third minor peak labeled A_3 at a relative energy-loss of 5.6 eV. For a detailed analysis of the core-hole effect on the Ti $L_{2,3}$ -edge, a contour map of the Ti valence electron screening clouds around the core hole was calculated along the $(0\bar{1}1)$ plane and is plotted in Figure 6.19. The valence-electron density of the unperturbed $\text{Sr}_8\text{Ti}_8\text{O}_{24}$ cell (Figure 6.19b)

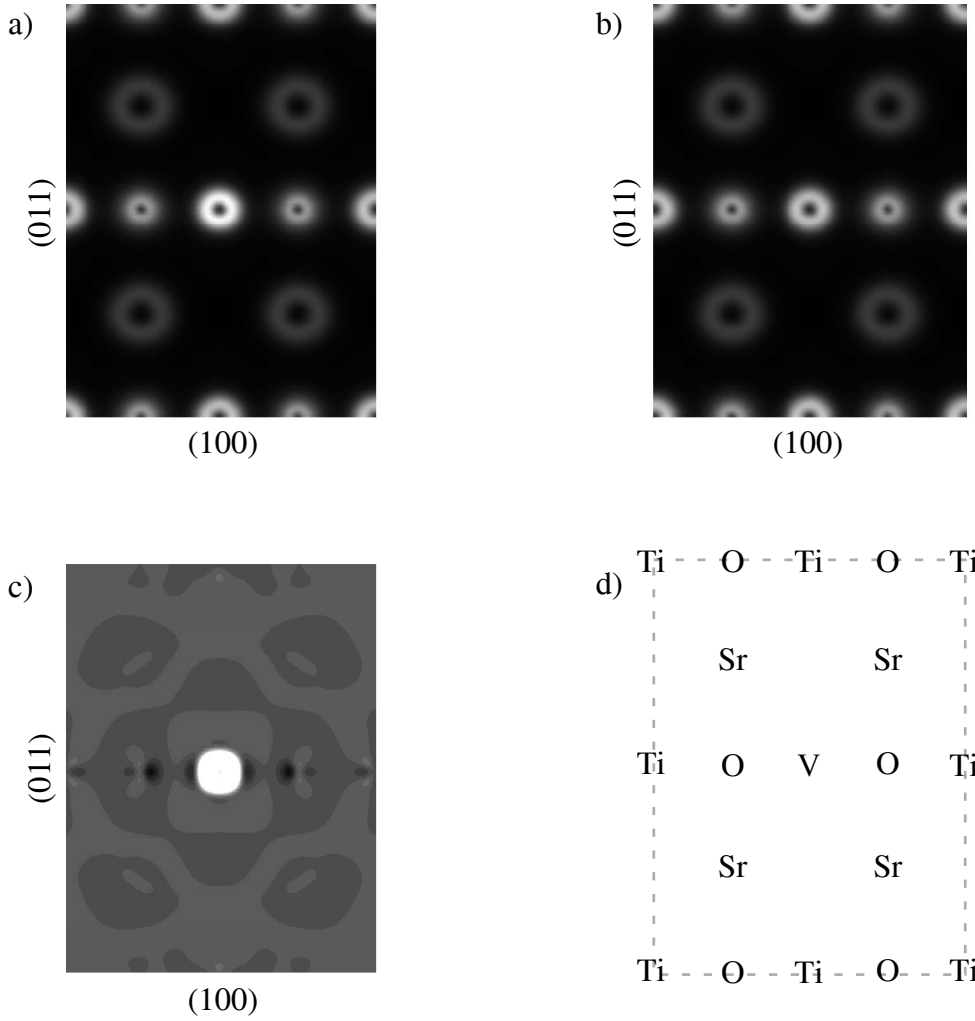


Figure 6.19: Charge distribution plots in SrTiO_3 a) for SrVO_3 to simulate the core-hole effect for the Ti $L_{2,3}$ -edge in the $Z+1$ approximation, b) for pure SrTiO_3 , and c) the difference of a) and b). In d) the atom arrangement in the charge distribution maps is plotted.

was subtracted from that of the corresponding $Z + 1$ cell $\text{Sr}_8\text{Ti}_7\text{VO}_{24}$ (Figure 6.19a). Bright contours denote electron enrichment, dark contours electron depletion. Contours range from -0.025 electrons/ Bohr^3 to 0.055 electrons/ Bohr^3 with a spacing of 0.005 electrons/ Bohr^3 . In Figure 6.19d the atom arrangement in the $(0\bar{1}1)$ plane is sketched in addition. It can be observed that along the Ti–O–V–O–Ti line in the (100) direction, charge is removed from areas between the V atom and the O atoms. Thus, an electron depletion occurs in the V-3d e_g states, which are oriented along the $\langle 100 \rangle$ -axis. This amount of charge is concentrated at the site of the excited atom by the formation of the core-hole (bright contrast in Figure 6.19c). At the same time, electrons are removed from the O p_x -states and are pushed into the p_y and p_z orbitals. No significant change of the charge screening cloud along the $\langle 011 \rangle$ direction can

be observed. For this reason, the V-3d e_g densities of states remain nearly unchanged by the core-hole effect. However, the t_{2g} states, i.e., peak A_1 in Figure 6.12, become sharper. The surrounding Sr atoms are also influenced by the core-hole. A charge accumulation close to the Sr site in the Sr–Ti direction is noticeable.

Similar observations of the spectral line shapes can be done by analysing the results from the multiple scattering calculations in Figure 6.16. Also in this approach, the incorporation of a core-hole leads to the formation of two pronounced peaks A_1 and A_2 , while peak A_3 is damped compared to the other peaks. However, the separation in energy of peaks A_1 and A_2 is only 1.9 eV. Without considering the core-hole effect, these peaks are separated by 2.5 eV, while A_2 shows a decreased intensity comparable to A_3 . Differences between the two different core-hole approximations do not occur. Therefore, also in the multiple scattering approach, the core-hole approximations tend to represent the overall spectral line shape correctly, whereas the energy axis is compressed with respect to the experimental and the LDFT data. This effect was also observed for the O K-edge and may be an effect of the energy-dependent exchange correlation potential [Brydson, 1991].

For SrTiO_3 the O K-edge shows a decrease of the first spectral peak A due to the incorporation of the core-hole effect. This is in contrast to previous investigations of the core-hole effects in, for example, MgO [Elsässer, 2001] and $\alpha\text{-Al}_2\text{O}_3$ [Nufer, 2001a]. In addition, peak B_1 becomes more pronounced due to an increased unoccupied density of the p_x -states at a relative energy-loss of 2 eV.

For a more detailed analysis of the core-hole effect on the O K-edge, a contour map of the O valence electron screening clouds around the core hole was calculated on the $(0\bar{1}1)$ plane and is plotted in Figure 6.20. The valence-electron density of the unperturbed $\text{Sr}_8\text{Ti}_8\text{O}_{24}$ cell (Figure 6.20b) was subtracted from those of the corresponding $Z+1$ cell $\text{Sr}_8\text{Ti}_8\text{O}_{23}\text{F}$ (Figure 6.20a). Contours are chosen in the same limits as in Figure 6.19. In Figure 6.20d the atom arrangement in the $(0\bar{1}1)$ plane is sketched in addition.

Figure 6.20c shows a strong increase in the charge distribution at the F site (O with core-hole) due to the more attractive potential compared to the oxygen. An electron depletion between the F atom and the neighbouring Ti atoms, i.e., along the x direction within the supercell, can be observed. This corresponds to an increased unoccupied density of F p_x -states, which is shown in Figure 6.14 and leads to the formation of the peak labeled B_1 and a more pronounced peak B_3 in the O K-ELNES. An electron enrichment is observed in the Ti d-orbitals between Ti and F. To summarise these observations, peaks B_1 and B_2 can be regarded as spectral features originating from the core-hole effect with respect to the O-2 p_x to Ti-3d e_g hybridization. Along the $\langle 011 \rangle$ -direction a small increase in the electron density can be observed between the F and the neighbouring Sr atoms, leading to the modified p_y and p_z line shapes of peak C in Figure 6.14. An interaction of the core-hole with other atoms inside the supercell could not be observed, since no other significant localized features occur in the valence electron screening clouds. In summary, the core-hole created by an O-1s electron excitation has no rotational symmetry, i.e. it is anisotropic due to the high amount of covalent bonding between O and Ti in SrTiO_3 , and it is highly localized only within the nearest neighbouring atoms. The weighting of peaks B_2 and B_3 , as well as the asymmetry

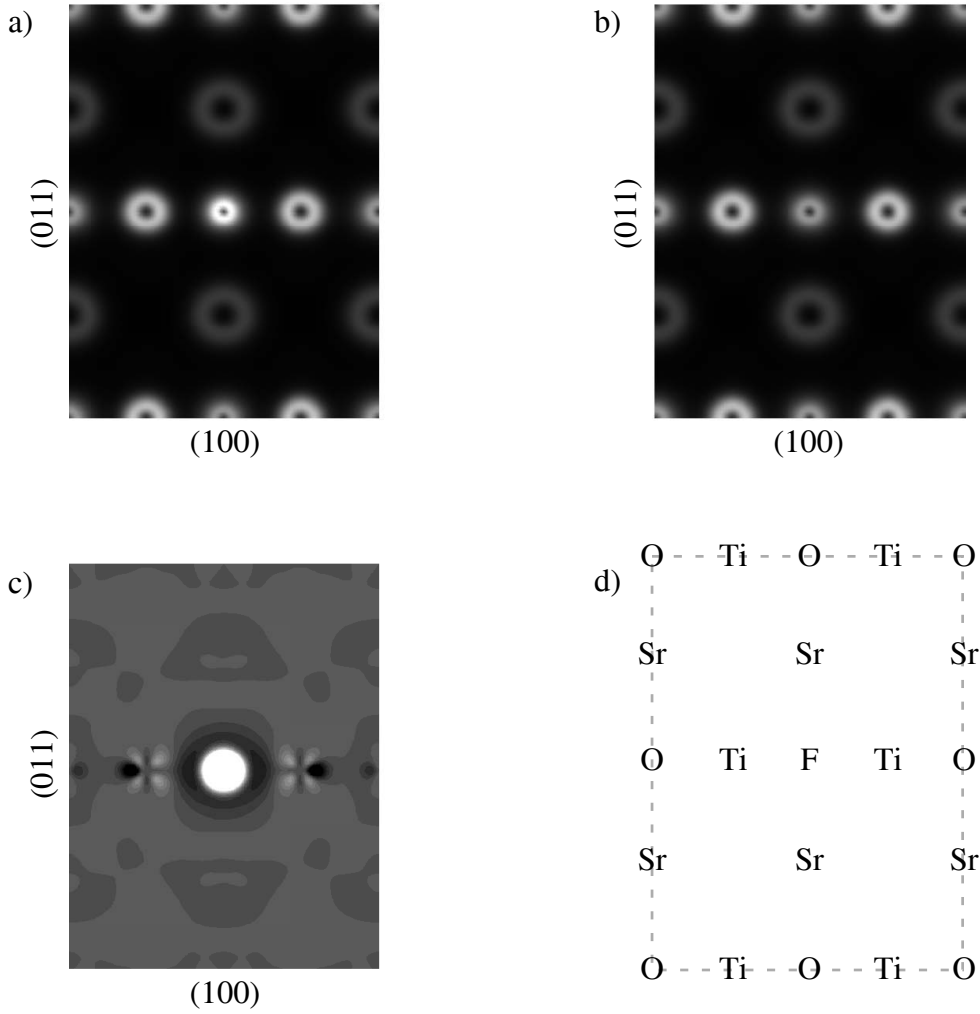


Figure 6.20: Charge distribution plots in SrTiO_3 a) for SrTiO_2F to simulate the core-hole effect for the O K-edge in the $Z+1$ approximation, b) for pure SrTiO_3 , and c) the difference of a) and b). In d) the atom arrangement in the charge distribution maps is plotted.

of peak C in the experimental spectrum, is well reproduced by the calculations if the $Z + 1$ approximation is used. However, a simple addition of the different p-projected DOS does not lead to a satisfying fit of the experimental O K-edge, since peak B_1 in the p_x -PDOS is then superimposed by the wings of peak B_2 . This behaviour is consistent with the results from the multiple scattering calculations in Figure 6.17, which could not reproduce peak B_1 . For smaller energy broadenings, peak B_1 was not observable in the calculated data. Wallis and Browning [Wallis, 1997] also performed MS calculations of the O K-edge of bulk SrTiO_3 , using the FEFF6 program code [Rehr, 1990]. Their results show a clearly resolved peak at an energy-loss of ~ 1 eV below the position of peak B_1 observed in this work. Furthermore, the overall line shape of the MS calculated O K-ELNES is different as far as peak energies are

concerned, compared to both experiment [Wallis, 1997] and the results obtained in this work. Wallis and Browning report that these effects are due to a failure of the muffin-tin potential to accurately represent the true crystal potential [Wallis, 1997]. In a later paper from the same group, Moltaji and co-workers [Moltaji, 2000] report MS calculations of the O K-edge in bulk SrTiO₃ which disagree to the results of Wallis and Browning [Wallis, 1997], but show similar ELNES line shapes compared to the present study and to previous investigations [de Groot, 1989] [Brydson, 1992] [de Groot, 1993] [Tanaka, 1997].

For the analysis of the O K-edge in SrTiO₃ the $Z + 1$ approximation is useful to interpret the ELNES but does not completely reproduce all spectral features. However, transition matrix elements were considered in the LDFT calculations and therefore absolute and also relative peak intensities have to be discussed carefully.

The calculated d-PDOS line shapes for Sr and for Y in Figure 6.15 do not show any significant differences in the first 9 eV beyond peak A. For relative energy-losses higher than 9 eV the small peak A' is shifted to higher energies in the Y d-PDOS, originating from a shift of the t_{2g} states due to the Sr-O interaction. In addition, the inclusion of the core-hole effect (Y d-PDOS) leads to a sharpening of both the t_{2g} and the e_g states. However, the Sr d-PDOS and the Y d-PDOS both provide the same level of accuracy in reproducing the experimental spectrum, since for peak A' the signal-to-noise ratio is small. Comparable results are provided by the FEFF-code calculations of the Sr L₃-edge in Figure 6.18. In this approach, the two different core-hole approximations provide the same ELNES as the calculation without any core-hole, except from a 3.5 eV shift of peak A' towards higher energies. Thus, for the analysis of the Sr L_{2,3}-ELNES, it is not necessary to incorporate any core-hole approximation into the calculations. The level of agreement between theory and experiment is reasonably good for the Sr L_{2,3}-edge.

In conclusion, for the interpretation of the Ti L_{2,3}-edge in SrTiO₃, the incorporation of core-hole effects into the ELNES calculations is crucial. By the $Z + 1$ approximation within the LDFT calculations, it is possible to reproduce the 2.4 eV crystal field splitting of the Ti-3d t_{2g} and e_g states. In relaxed bulk SrTiO₃ only a splitting of 1.7 eV is present, as the O p-PDOS in Figure 6.14 shows. However, the observed ELNES line shape is only a quantum mechanical effect due to the interaction between the sample and the measuring process, which leads to modified unoccupied local densities of states. As it could be shown by the analysis of the valence electron screening clouds, the core-hole effect is highly localized and affects the unoccupied densities of states of the Ti-O hybridized orbitals. An even better reproducibility of the peak energies and the relative peak intensities could recently be achieved by incorporating so-called multiplet effects into the calculations for simulating configuration interactions within the material [Ogasawara, 2001].

For the O K-edge in SrTiO₃, the core-hole effects were found to play an important role. The experimentally well-resolved peak B₁ only occurs in the core-hole calculations, originating from the Ti-O nearest neighbour bonding. In addition, the asymmetric line shapes for peaks B and C are reproduced more clearly in the core-hole approximations. However, the level of agreement is not as high as for the Ti L_{2,3}-edges. Thus, the $Z + 1$ approximation can be used to interpret the O K-ELNES in terms of bondings in bulk SrTiO₃, but this approximation

of the core-hole effect seems not sufficient to obtain high levels of agreement between theory and experiment for the O K-edge in SrTiO_3 .

The LDFT-based calculations and the FEFF-code calculations have not shown a significant influence of the core-hole effect on the ELNES line shape of the Sr $L_{2,3}$ absorption edges within the currently available energy resolution limits. However, the appearance of a core-hole effect for this absorption edge cannot be completely neglected.

Due to the results for bulk SrTiO_3 , for the analysis of the electronic structure of the metal/ceramic interfaces in the following chapters, the core-hole effect has to be considered in the calculations of the Ti d-PDOS and the O p-PDOS for a quantitative comparison to the experimental spectra.

Chapter 7

The Pd/SrTiO₃ Interface

In this chapter, experimental and theoretical results obtained at the Pd/SrTiO₃ interface are reported. These results are then discussed in detail. In section 7.3.2, the experimental interfacial ELNES components are compared to LDFT calculated densities of states. On this basis, the bonding behaviour across the interface between the Pd film and the SrTiO₃ substrate surface is analysed and discussed.

7.1 Experimental Results

As mentioned earlier, several different experimental techniques were used to investigate the morphology as well as the atomistic and electronic structure of the Pd/SrTiO₃ interface. As substrate material, both undoped and Fe-doped single-crystalline SrTiO₃ were used. In the following two sections the experimental results from diffraction and imaging studies as well as from the EELS studies are presented.

7.1.1 Diffraction and Imaging Studies

Prior and during the deposition of 35 nm thick Pd films on top of the (100)SrTiO₃ surface, *in situ* RHEED measurements of the samples were performed inside the MBE chamber by Richter [Richter, 2000]. Film thicknesses were determined from the deposition rates and deposition times. Related to the growth mode, these film thicknesses can only be understood as nominal thicknesses and not as absolute ones. Figure 7.1a shows RHEED patterns prior to the Pd deposition (denoted by 0 nm film thickness) and after the deposition of nominal film thicknesses of 0.2 nm and 1.5 nm. With increasing thickness of the Pd film, the substrate diffraction spots are damped and superimposed by non-elongated diffraction spots, which have to be ascribed to the Pd film formation. The RHEED patterns exhibit diffraction patterns similar to those of transmission electron diffraction patterns, indicating an island formation on the substrate surface. In addition, the appearance of single diffraction spots in these patterns reflect an epitaxial growth of the islands on the substrate surface. After a Pd deposition of 0.2 nm additional diffraction spots appear. This effect is most probably

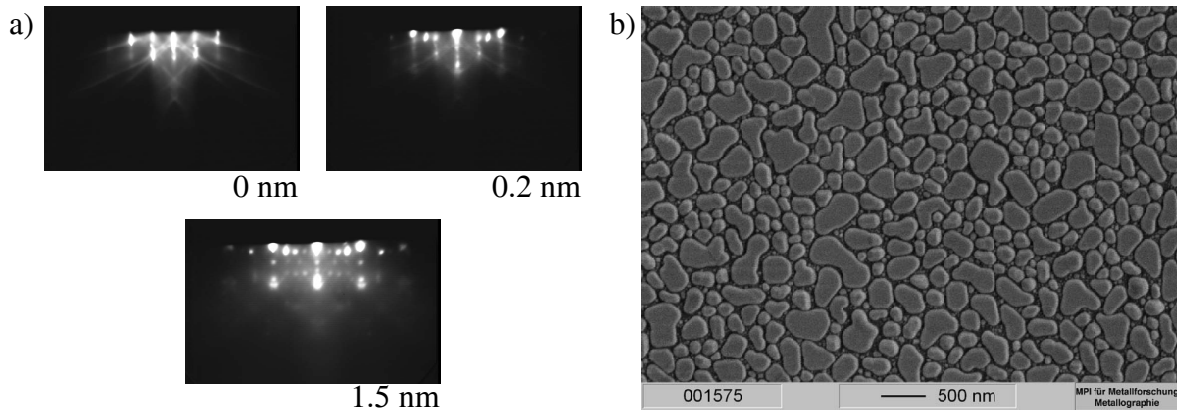


Figure 7.1: a) *In situ* RHEED patterns of Pd/SrTiO₃ in the (001) azimuth after deposition of nominally 0nm, 0.2nm, and 1.5nm Pd on the (100)SrTiO₃ surface at a temperature of 600°C [Richter, 2000]. b) SEM image of the readily as-deposited Pd film.

due to a long range ordering of the islands on the substrate surface. A more detailed quantitative analysis of the RHEED patterns is given by Richter [Richter, 2000] and Wagner et al. [Wagner, 2001b].

After the MBE growth experiments, the samples were investigated by scanning electron microscopy (SEM). Figure 7.1b shows a SEM top-view image of the Pd/SrTiO₃ sample, that is, the illuminating electron beam is parallel to the surface normal of the (100) oriented substrate. In accordance with results by Richter [Richter, 2000] and Wagner [Wagner, 2001b] the SEM micrograph clearly exhibits islands of Pd on top of the substrate surface.

The orientation relationship between the Pd film and the SrTiO₃ substrate was investigated by X-ray reflection diffractometry (XRD)¹. For the investigated specimens grown at 650°C, θ -2 θ -scans show reflections of the {100} type for SrTiO₃ and of the {200} and {400} type coinciding for both, Pd and SrTiO₃. In addition, the Fe-doped specimens also show the {111} and {220} lines for Pd. These observations indicate an epitaxial orientation relationship between the Pd film and both pure and Fe-doped substrates. The (100) planes of the Pd film are found to be parallel to the (100)SrTiO₃ surface. However, for the Fe-doped substrate, some islands exist where the {111} or {220} planes are parallel to the substrate surface.

After the cross-sectional TEM preparation of the samples, conventional TEM and selected area diffraction experiments were performed on the Pd/SrTiO₃ interface. Figure 7.2a shows a typical CTEM micrograph of the interface, where Pd islands can be observed. Some of the islands show facets along the {110} planes. The island thickness was in the range of 70 nm–90 nm. For some larger islands, twin formation in the Pd film was observed. Figure 7.2b shows a SAD micrograph acquired in the $\langle 100 \rangle_{STO}$ zone-axis orientation. The diffraction

¹The XRD measurements were performed by Dr. Lamparter and co-workers at the ZWE Röntgenbeugung, which is gratefully acknowledged.

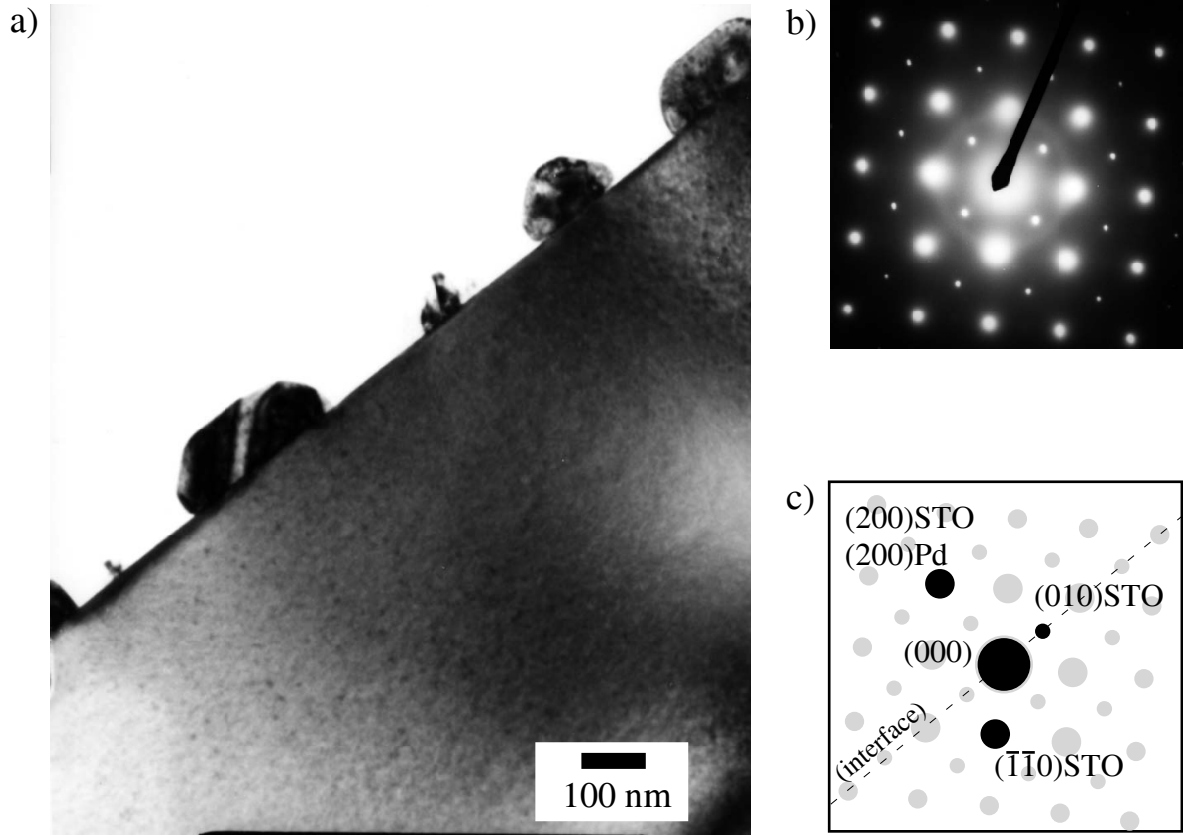


Figure 7.2: Conventional TEM investigations of the Pd/SrTiO₃ interface, indicating a) Pd island formation on the (100)SrTiO₃ surface. b) reveals selected area diffraction patterns used to determine the orientation relationship (c) between the Pd film and the substrate.

pattern exhibits a superposition of the $\langle 100 \rangle$ zone-axis patterns for both bulk SrTiO₃ and *fcc* Pd, indicating that the $[100]$ directions are parallel in both crystals. A more detailed analysis showed that the $(200)_{STO}$ diffraction spots coincide with the $(200)_{Pd}$ spots (cf. Figure 7.2c). Due to the small lattice mismatch of $m = 0.4\%$ between Pd and SrTiO₃, the separation of the diffraction spots was not resolvable in the experiment. This coincidence shows that the $\{100\}$ planes in Pd are parallel to the (100) surface of the substrate, reflecting a cube-on-cube orientation relationship, which can be described by

$$100_{Pd} \parallel 100_{STO}. \quad (7.1)$$

Other epitaxial orientation relationships could not be observed by TEM. This result was already obtained by Richter in a parallel study [Richter, 2000]. All experiments described below were performed on interfaces which are characterised by the cube-on-cube orientation relationship given in equation 7.1.

Assuming that pure oxygen columns do not lead to a contrast variation in HRTEM micrographs of bulk SrTiO₃, in the $\langle 110 \rangle$ zone-axis orientation only pure Sr columns and

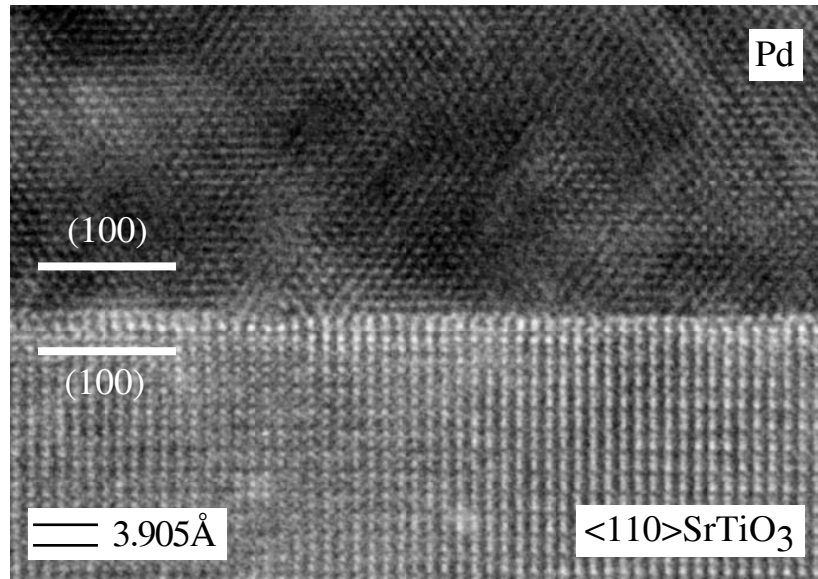


Figure 7.3: HRTEM micrograph of the Pd/SrTiO₃ interface in $\langle 110 \rangle$ zone-axis orientation.

mixed TiO-columns are present. By the different scattering strengths of Sr and Ti atoms, it is in general possible to distinguish metal/SrTiO₃ interfaces with a TiO₂ and SrO termination of the substrate by a qualitative analysis of the intensity distribution of the interfacial HRTEM spot pattern [Strecker, 2001b]. Figure 7.3 shows a HRTEM micrograph of the Pd/SrTiO₃ interface in $\langle 110 \rangle$ zone-axis orientation. The micrograph shows that the interface is coherent. The interface is abrupt over large areas and no reaction layer or reaction phase could be observed between the film and the substrate. In some regions steps of one unit cell in height occur at the interface, corresponding to steps in the substrate surface prior to the MBE growth. This step formation is due to the preparation process of the surface [Kawasaki, 1994] and was also observed by Richter [Richter, 2000] and Polli [Polli, 1999] by STM measurements of the (100)SrTiO₃ surface. Diffuse contrasts appear in the HRTEM micrograph resulting in a not sufficiently well resolved pattern so that no information about the substrate termination could be extracted.

To determine the terminating layer of the (100)SrTiO₃ surface Z-contrast imaging was performed in the $\langle 100 \rangle$ zone-axis orientation using a JEOL JEM2010F TEM² operating at 200 keV accelerating voltage. The objective lens of this microscope has a high resolution pole piece with a C_s -value of $C_s = 0.5$ mm and is designed for a side-entry specimen holder [Šturm, 2001]. For the acquisition of the Z-contrast images, the JEOL HAADF EM-24015BU detector was used. The detector is placed between the projective lens system and the viewing screen. In the applied setup, this detector records electrons which are scattered into angles between 100 mrad and 200 mrad [Šturm, 2001]. The specimen tilt and the correction for the

²These experiments were done at the Jožef Stefan Institut in Ljubljana, Slovenia. The cooperation of M. Čeh and S. Šturm is gratefully acknowledged.

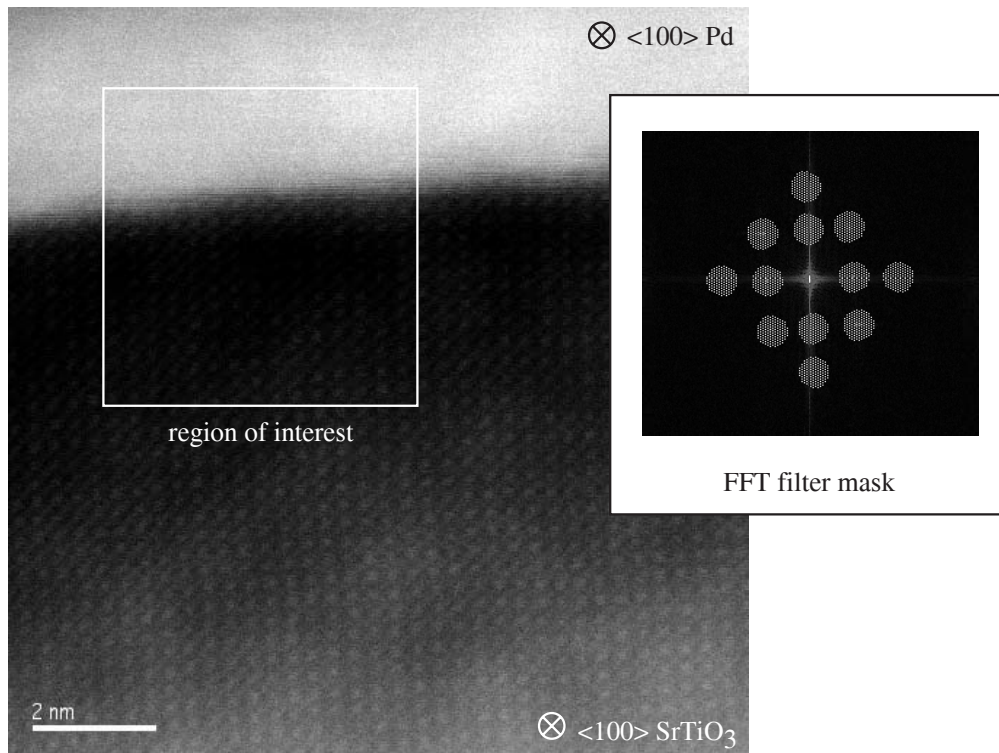


Figure 7.4: HAADF micrograph (Z-contrast image) of the Pd/SrTiO₃ interface in $\langle 100 \rangle$ zone-axis orientation (a). In b) a Fourier transform of the indicated area is shown, which was used for applying a noise reduction by the indicated digital filter mask.

astigmatism were done using the ronchigram technique described by James and Browning [James, 1999]. A HAADF micrograph, which could be obtained from the Pd/SrTiO₃ is shown in Figure 7.4a. Changes in contrast can be observed at the metal/ceramic interface. Approaching the interface in the bulk SrTiO₃, the intensity decreases, leading to an even stronger jump in contrast directly at the interface. Because of the low signal-to-noise ratio in the SrTiO₃ region and to compensate the highly localized step in the overall contrast, digital image filtering was used. The filtering included a fast Fourier transformation (FFT) of the image. Afterwards, a filter mask was generated as illustrated in Figure 7.4b. Outside the shaded regions, the intensity in the FFT image was set to zero, whereas inside the intensities remain unchanged. At the borders of the filter mask, intensities are smoothed in an area of 6 pixels to each side. After an inverse FFT the intensities were transformed into the RGB color code for better visualization. The final image, extracted from the region of interest marked in Figure 7.4a, is shown in Figure 7.5a and represents a HAADF micrograph of the Pd/SrTiO₃ interface. A periodic spot pattern is observable with well resolved Sr columns. In between four adjacent Sr columns, in some areas of the image, some extra intensity spots are visible (see, for example, the region marked A in Figure 7.5), which often show a non-centric position in the framework of the 4 Sr columns. These contrasts indicate most probably mixed Ti-O-columns. The use of modified filter masks provided that these effects do not originate

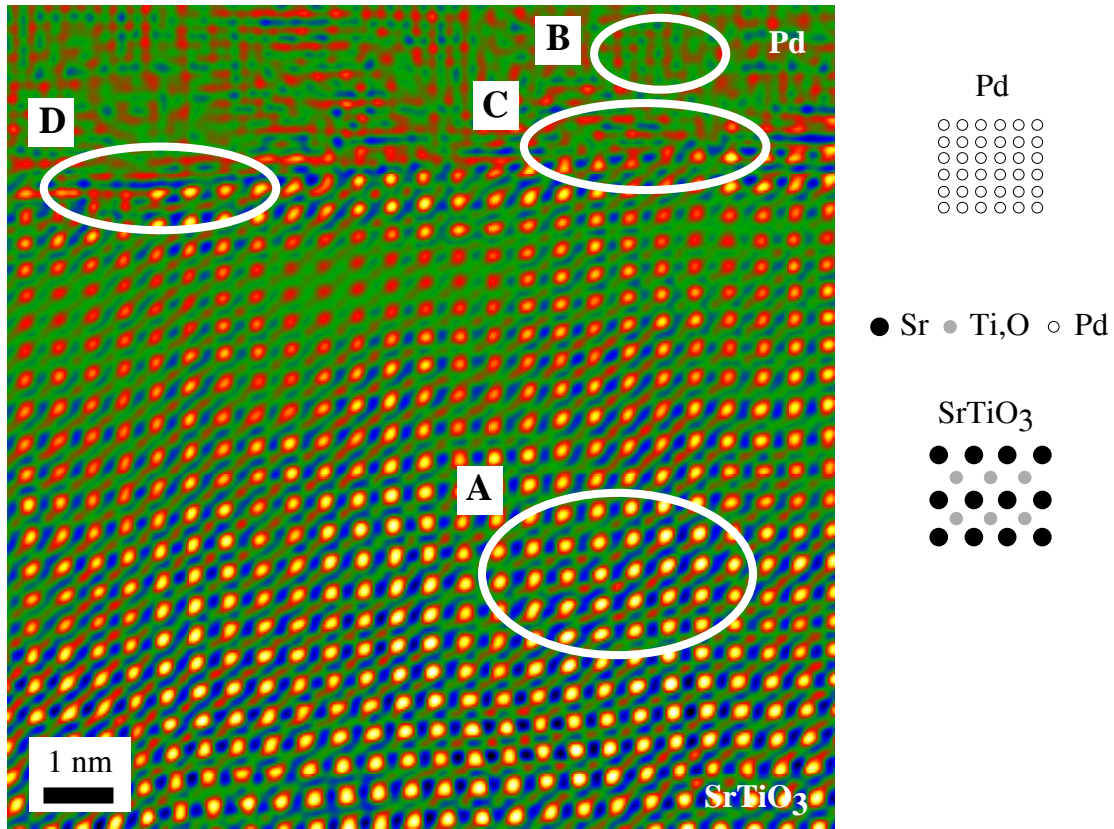


Figure 7.5: HAADF micrograph of the Pd/SrTiO₃ interface in $\langle 100 \rangle$ zone-axis orientation after applying a noise reduction filter. The grey values are color coded in the RGB scheme.

from the FFT-filtering process. Inside the Pd film the spot pattern shows predominantly a periodic intensity pattern indicating columns of the Pd film in $\langle 100 \rangle$ zone-axis orientation (cf. region B Figure 7.4b). In the interfacial region the interface is not clearly resolved. In some regions, a TiO₂ termination seems to be present (C), whereas in other regions (D) a SrO termination may be prominent. In some interfacial areas a slight mis-tilt of the specimen is observable through some blurred contrast of the atomic columns.

7.1.2 EELS Results

ELNES spectra of the Ti L_{2,3}-edge, the O K-edge, and the Sr L_{2,3} were measured in regions containing the interface and in regions in the adjacent bulk materials. The interface specific ELNES components were extracted by the spatial difference method described in section 3.2. The size of the scanning window was $2 \times 20 \text{ nm}^2$, while acquisition times between $10 \times 5 \text{ sec.}$ and $10 \times 8 \text{ sec.}$ were used. For the acquisition of the Ti L_{2,3}-edges and the O K-edges, dispersions of 0.1 eV/channels and 0.2 eV/channel were used. As one can infer from Figure 7.6a, the Ti L_{2,3}-edge at an energy-loss of 455.2 eV overlaps with the Pd M_{4,5}-edge, whose edge onset is

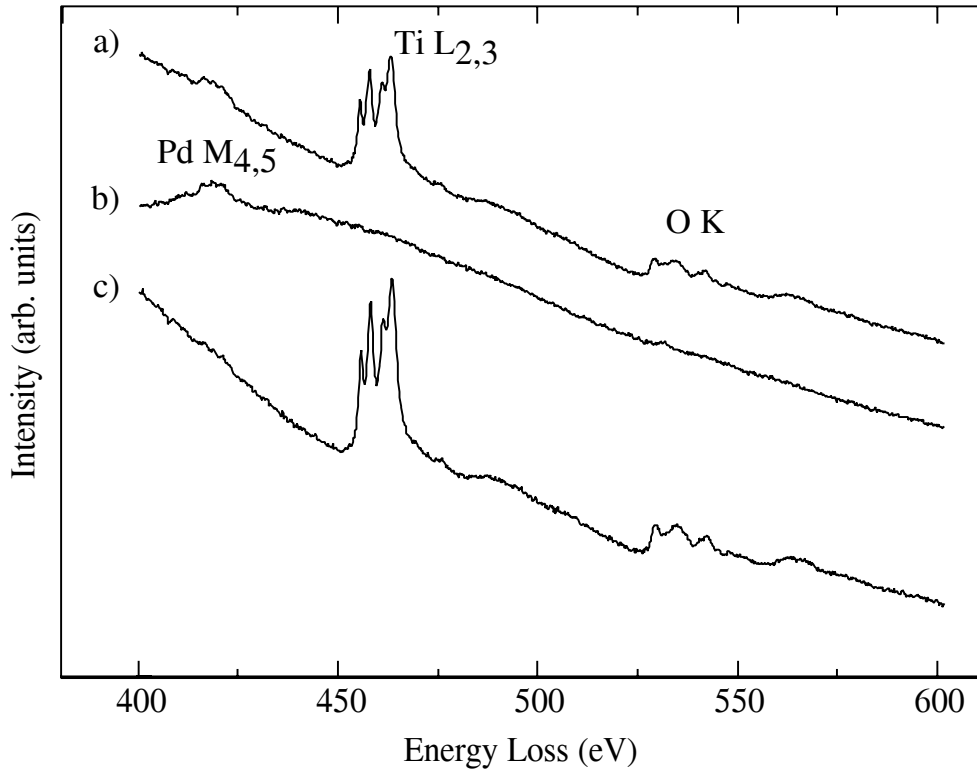


Figure 7.6: Overlap of the Pd $M_{4,5}$ - and the Ti $L_{2,3}$ -edges at the Pd/SrTiO₃ interface a). The line shape in b) shows the Pd $M_{4,5}$ -edges in the Pd film. The Pd signal was removed from a) by the spatial difference technique in order to model a smooth pre-edge background for the Ti $L_{2,3}$ -edge (c).

at 335 eV [Egerton, 1996]. This edge overlap causes problems in the pre-edge background for the ELNES-analysis of the Ti $L_{2,3}$ -edge. However, the Pd $M_{4,5}$ -edge exhibits no pronounced near-edge fine structures (cf. Figure 7.6b). For this reason, these edges were not considered for a detailed ELNES analysis in this work. To extract the interface specific ELNES of the Ti $L_{2,3}$ -edge, the spatial difference technique was split into two separate steps. First, the as-acquired spectrum from the Pd film (Figure 7.6b) was gradually subtracted from the as-acquired spectrum from the region containing the interface (spectrum a) in Figure 7.6). The calculated scaling factor of $\mu = 0.42$ for the spatial difference technique was slightly modified to $\mu' = 0.40$ to model a smooth pre-edge background of the Ti $L_{2,3}$ -edge, as is shown in Figure 7.6c. The background fit for both the interfacial spectrum and the bulk spectrum was performed within identical energy intervals. After background subtraction, the spatial difference technique was applied a second time to subtract the amount of bulk SrTiO₃ intensity, using a scaling factor of $\nu = 0.23$. The resulting interface specific component of the Ti $L_{2,3}$ -edges is plotted in Figure 7.7c.

From Figure 7.7c one can see that the interface-specific component of the Ti $L_{2,3}$ -edges shows a reduced crystal field splitting of 2.0 ± 0.2 eV, compared to 2.4 eV in bulk SrTiO₃.

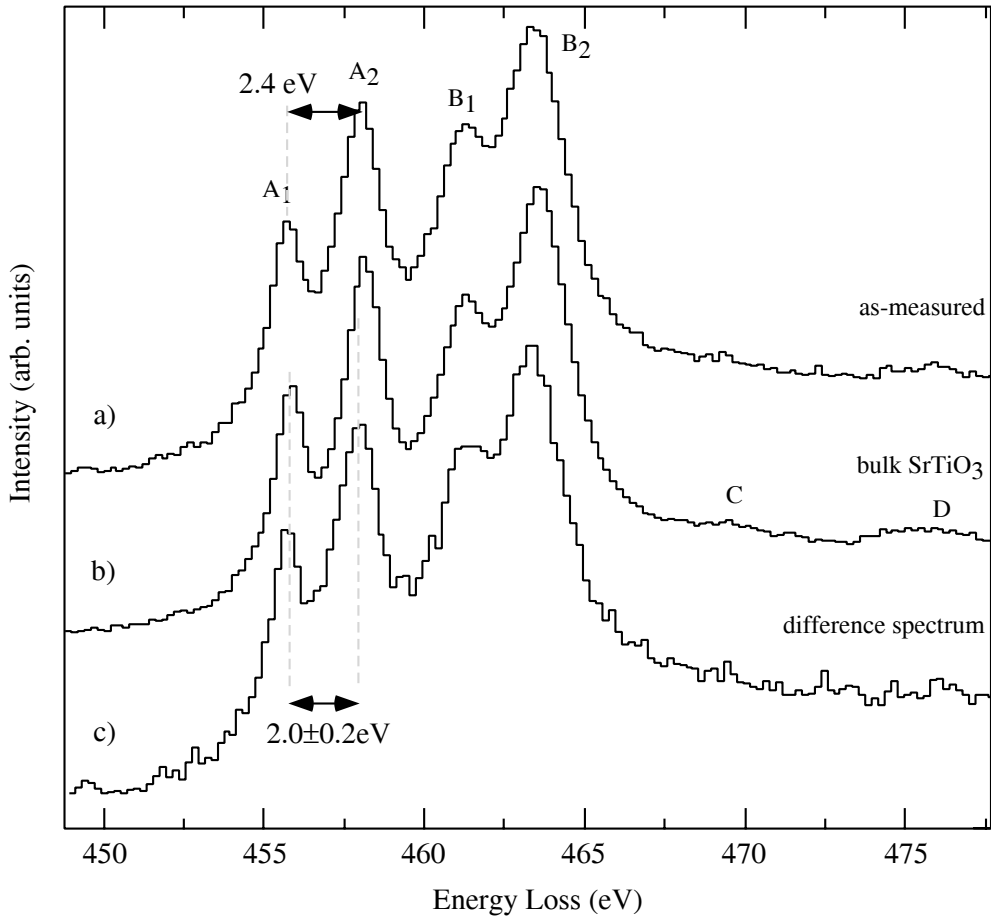


Figure 7.7: Experimental results for the Ti $L_{2,3}$ -edge at the Pd/SrTiO₃ interface. a) is the difference spectrum after removing the Pd $M_{4,5}$ -edge; b) is the Ti $L_{2,3}$ -edge of bulk SrTiO₃; c) is the interface-specific component of the Ti $L_{2,3}$ -edge.

This reduction was found throughout all acquired spectra. A small shift of 0.2 eV of the edge onsets towards lower energy-losses could also be observed. The resulting difference spectrum 7.7c appeared not to be dependent on any sub-channel drift, since EELS measurements using dispersions of 0.05 eV/channel and 0.1 eV/channel gave exactly the same line shapes.

By using an energy dispersion of 0.2 eV/channel, the simultaneous acquisition of both the Ti $L_{2,3}$ -edges and the O K-edge is possible. In Figure 7.8 the set of O K-edges measured for the Pd/SrTiO₃ interface is plotted as a function of the absolute energy-loss. The spectra were extracted from the same set of data as the Ti $L_{2,3}$ -edge shown in Figure 7.7. Spectrum 7.8c is the extracted interface-specific O K-ELNES. Since the signal-to-noise ratio of the interfacial ELNES component is low, the spectrum was smoothed by a 1.0 eV-wide top-hat function. The result after smoothing is shown in Figure 7.8d. The difference spectrum exhibits a similar line shape as the O K-ELNES for bulk SrTiO₃ (cf. spectrum b), and the existence of the clearly resolved peaks labeled A , B_2 , and C , which are also characteristic for bulk SrTiO₃. The peaks labeled B_1 and B_3 are present at the interface but they are not clearly resolved due

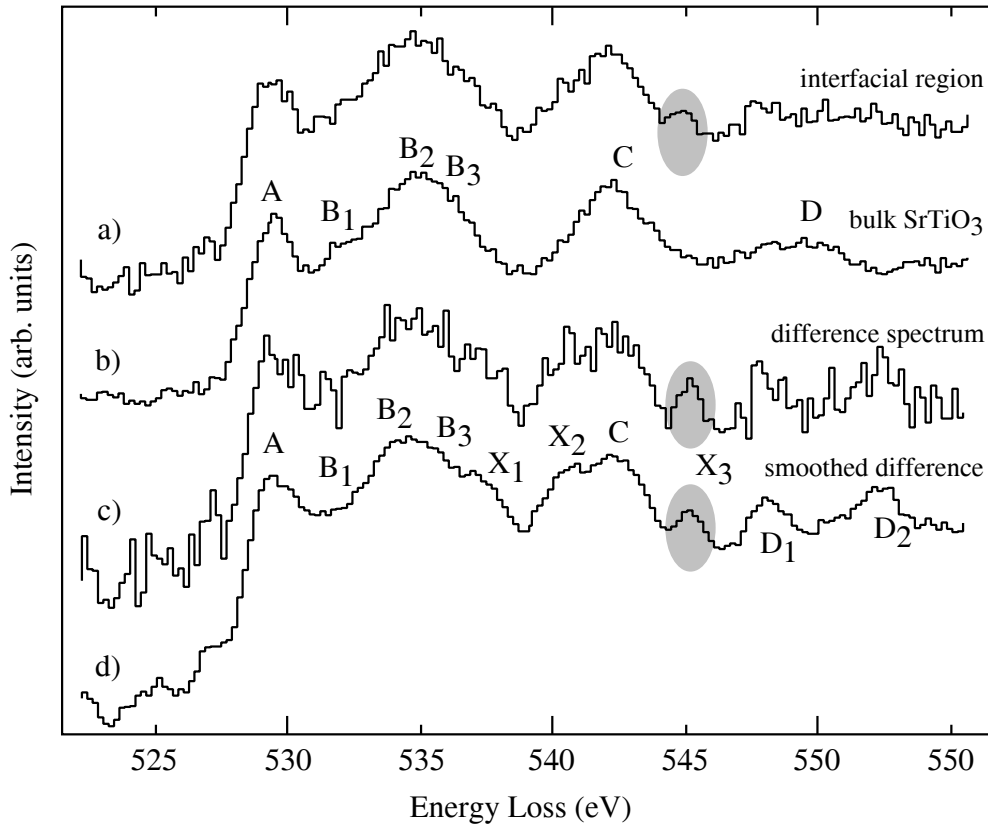


Figure 7.8: Experimental results for the O K-edge at the Pd/SrTiO₃ interface. a) is the as-measured O K-edge from a region containing the interface after background subtraction; b) is the O K-edge of bulk SrTiO₃, and c) is the corresponding difference spectrum. The difference spectrum was smoothed with a top-hat function of 1.0eV in width, resulting in spectrum d).

to the limited signal-to-noise ratio. Since peak *D* in the bulk ELNES is broad in energy and low in intensity, its possible presence in the difference spectrum cannot be resolved. As can be inferred from Figures 7.8c and 7.8d, the interface specific ELNES component shows three significant extra spectral features at the interface compared to the bulk line shape, namely the peaks *X*₁, *X*₂, and *X*₃. In addition, two weak features labeled *D*₁ and *D*₂ are observable at the interface. The most significant interface specific spectral feature is peak *X*₃, formed by 9 channels in the energy-loss. In the bulk O K-ELNES only a minimum in the line shape appears at this energy position. Peaks *X*₁ and *X*₂ appear rather like shoulders in the original line shape than as pronounced peaks. However, both are significant in spectrum 7.8c.

Muller stated that energy drifts during the measurements, e.g., by high voltage instabilities of the microscope, can lead to artificial features in the difference spectrum [Muller, 1999]. To exclude the influence of such effects, the spatial difference technique using the previously determined scaling factor of $\mu = 0.23$ was applied for two bulk SrTiO₃ O K-edges, which were shifted by -0.1 eV, -0.2 eV, -0.3 eV and -0.4 eV with respect to each other. These shifts

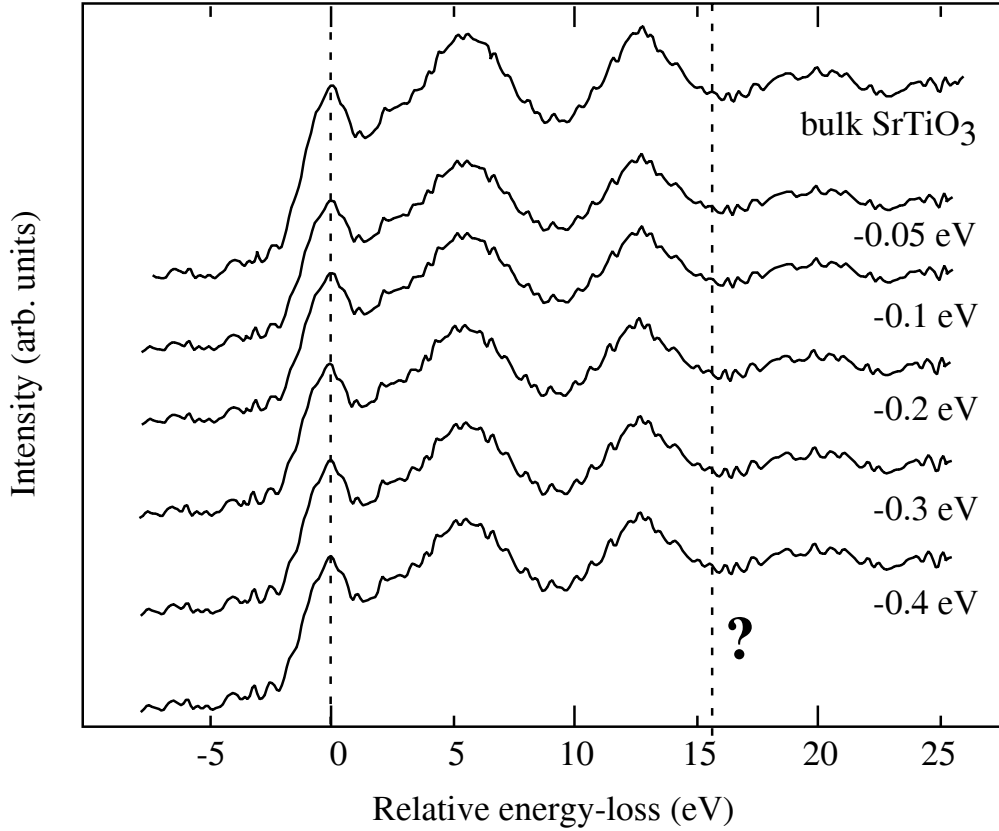


Figure 7.9: Spatial difference technique applied for two identical bulk SrTiO₃ O K-edges, whereas one of the spectra is shifted in energy by 0.05 eV, 0.1 eV, 0.2 eV, 0.3 eV, and 0.4 eV towards lower energies with respect to the original spectrum. A scaling factor of 0.23 was used as in Figure 7.8. For a better comparison, all spectra were afterwards aligned to the same edge onset energy.

simulate possible high-voltage instabilities of the microscope and also effects of sub-channel drifts. As one can infer from Figure 7.9, energy drifts between 0.1 eV and 0.4 eV do not lead to any artificial spectral features in the O K-edge. Since the spectrum was acquired with a dispersion of 0.2 eV/channel, this observation also holds for the so-called sub-channel drift [Muller, 1999]. Therefore, peaks X_1 , X_2 and X_3 in Figure 7.8 are real interface specific ELNES features rather than artificial peaks.

Figure 7.10 shows the experimental ELNES results for the Sr L_{2,3}-edge of the Pd/SrTiO₃ interface. An energy dispersion of 0.2 eV/channel was used, while the beam was scanning over an area of $2 \times 20 \text{ nm}^2$. Although the spectrum in Figure 7.10, which originates from a region containing the interface, clearly exhibits the Sr L_{2,3} white-lines, the interface specific component c) does not show any intensity in this energy region above the noise level. The scaling factor used for the spatial difference technique was calculated to be $\nu = 0.48$. Some low frequency modulations in the background of the difference spectrum as well as spikes at 1927 eV and 2025 eV are effects due to an insufficient correction of channel-to-channel gain

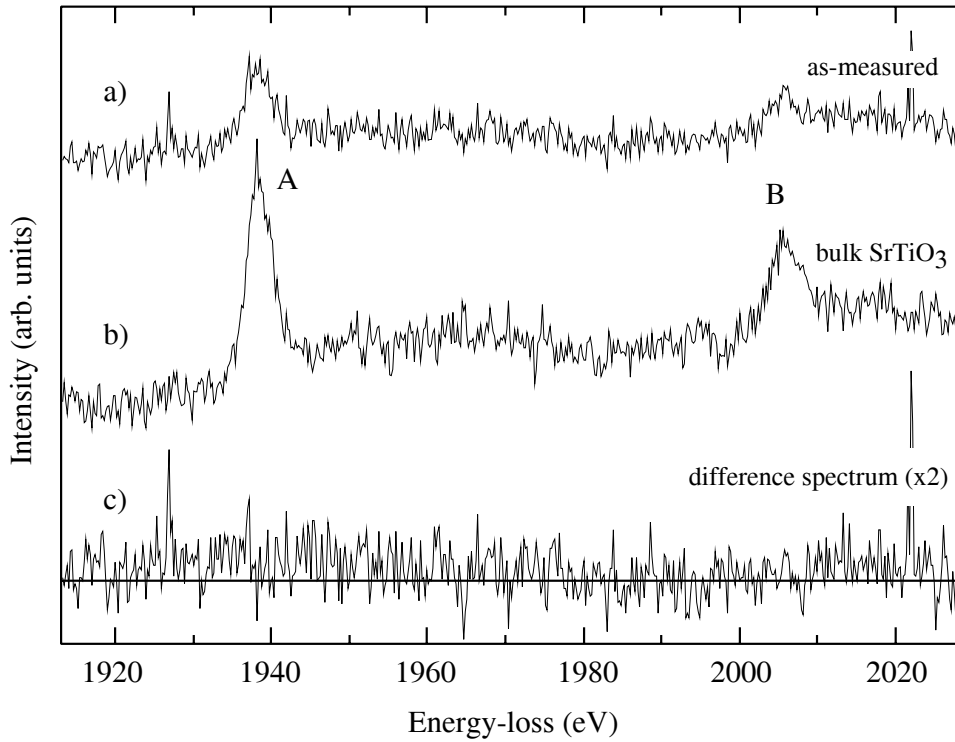


Figure 7.10: Experimental results for the Sr $L_{2,3}$ -edge at the Pd/SrTiO₃ interface. a) represents the edges measured from a region containing the interface after background subtraction; b) is the Sr $L_{2,3}$ -edge of bulk SrTiO₃, and c) is the corresponding difference spectrum, magnified by a factor of 2.

variations.

7.2 Computational Results

For the Pd/SrTiO₃ interface, LDFT-based *ab initio* band structure calculations of the local occupied and the local unoccupied densities of states were performed. For these calculations relaxed atomistic structure models of the interface are required. In a previous study, Ochs theoretically developed an atomistic structure model of the Pd/SrTiO₃ interface by calculating the total energy for different atomic configurations [Ochs, 2000] [Ochs, 2001]. He considered models for different surface terminations and different adsorption sites for Pd. The different atomic configurations were then optimised until the interatomic forces became zero and the total energy of the system reached a minimum value [Ochs, 2000] [Ochs, 2001].

On the TiO₂ terminated substrate, the atoms of a *fcc* Pd film can adsorb either above O atoms, denoted by Pd|O, or above Ti atoms and hollow sites to equal proportions, denoted by Pd|Ti [Ochs, 2000]. The hollow sites are surrounded by four oxygen atoms. For both configurations Ochs and co-workers found that an adsorption of Pd atoms above the O atoms of the terminating layer is energetically favoured. Besides that, they observed that

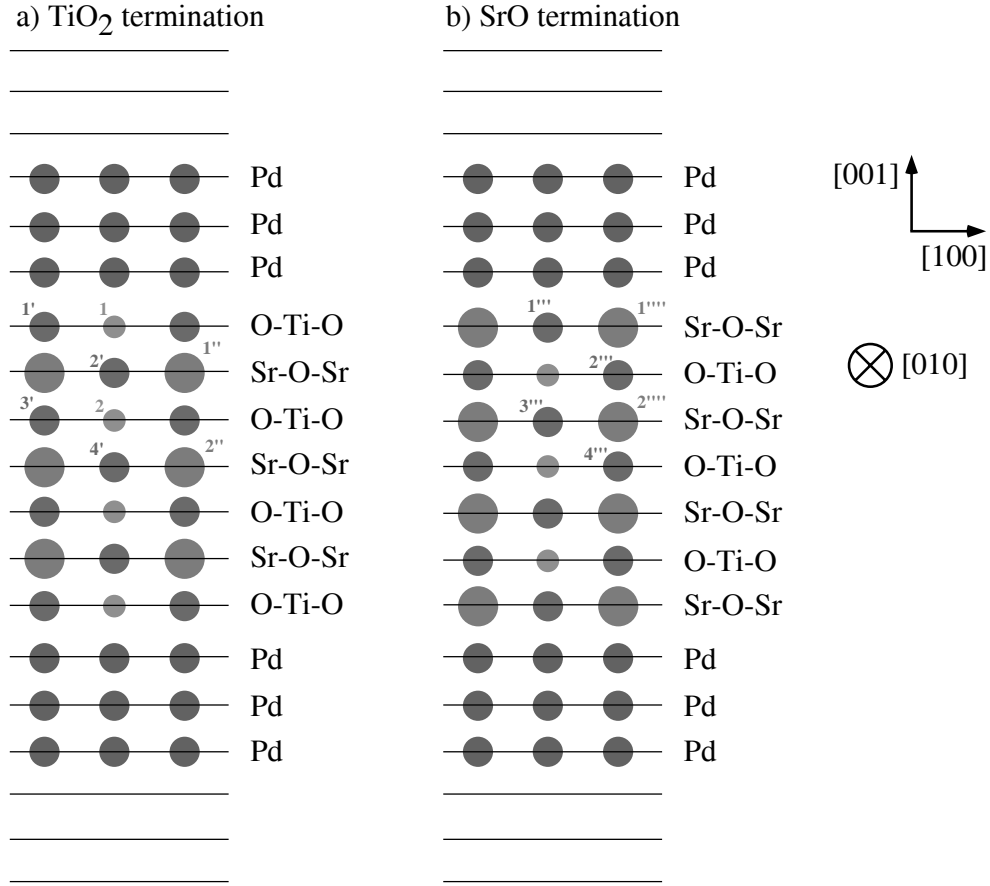


Figure 7.11: Supercell geometries of a) the TiO₂ terminated and b) the SrO terminated Pd/(100)SrTiO₃ interface. The cells are projected onto an [010]-plane.

the work of separation as well as the interatomic distances in the supercells are converged for a coverage of 3 Pd layers on top of the TiO₂ terminated (100)SrTiO₃ surface [Ochs, 2000] [Ochs, 2001].

For the SrO terminated substrate, the nucleation of *fcc* Pd is possible either above Sr and O atoms (Pd|Sr,O) or above hollow sites (Pd|◇). Each hollow site is surrounded by two Sr and two O atoms. After a full relaxation of the atomistic structure, the (Pd|Sr,O) configuration was found to be energetically favoured compared to (Pd|◇) as far as separation energies are concerned.

Comparing the relaxed atomistic structure models for both terminations, an adsorption of Pd above the O atoms of the TiO₂ terminated (100)SrTiO₃ surface is energetically favoured compared to the (Pd|Sr,O) configuration on the SrO terminated surface. However, the Pd–O interaction was found to be stronger for the SrO termination while a significant repulsion of Sr and Pd was observable [Ochs, 2000]. This makes this configuration unfavoured compared to the TiO₂ terminated interfacial structure [Ochs, 2000].

Ochs and co-workers constructed supercells for the Pd/SrTiO₃ interface consisting of

seven planes of SrTiO_3 , 2×3 planes of Pd and another 2×3 vacuum layers. In the supercell the SrTiO_3 is described by seven alternating TiO_2 and SrO planes. The topmost substrate plane is followed by three planes of Pd. The supercell was built up in such a way that it contains two interfaces to achieve inversion symmetry throughout the cell, which reduces computation times. Three additional vacuum layers are inserted on the top and the bottom side of the supercell to avoid any interaction of the metal films with the neighbouring cells due to the periodic boundary conditions. The supercell geometries of the TiO_2 termination and the SrO termination of the substrate surface are shown in Figure 7.11a and 7.11b, respectively. These supercells were used for the calculation of the local symmetry projected densities of states. Ochs and co-workers found that no interaction of the two interfaces across the vacuum region within the constructed supercells occurred [Ochs, 2001].

For a theoretical analysis of the local symmetry projected unoccupied DOS at the interface, and later for a comparison with the experimentally determined Ti $L_{2,3}$ -edges, one V atom was substituted for one Ti atom for the different sites labeled 1 and 2 in Figure 7.11 to consider core-hole effects. In the following, the sites 1 and 2 are referred to as the interfacial Ti site and a bulk-like Ti site, respectively. Calculations of the Ti d-PDOS and V d-PDOS were only performed for the TiO_2 terminated Pd/ SrTiO_3 interface. For an SrO termination, no interfacial Ti d-PDOS is present due to their high localisation near the sites of the nuclei. In Figure 7.12 the results of the calculations are plotted together with a bulk SrTiO_3 V d-PDOS calculation, which was already shown in Figure 7.7 and discussed in section 6.5. The interfacial and the bulk-like V d-PDOS exhibit nearly identical line shapes consisting of a prominent peak A_1 , formed by V-d t_{2g} states, and two less pronounced peaks A_2 and A_3 originating from V-d e_g states. The only significant difference is the separation of peaks A_1 and A_2 of 1.1 eV for the interfacial site and 1.5 eV for the bulk-like site, which is significantly smaller than the splitting in pure SrTiO_3 (cf. Figure 7.12c). Comparing the bulk-like V d-PDOS to the line shape in Figure 7.12c, one can observe significant differences.

In the case of the TiO_2 terminated Pd/ SrTiO_3 interface, O atoms occupy four inequivalent sites in the corresponding supercell (positions 1', 2', 3', and 4' in Figure 7.11a). The local O p-PDOS projected for these sites are plotted in Figure 7.13. For the sites 2', 3', and 4', the p-PDOS exhibit nearly the same line shapes. Differences are based on numerical uncertainties rather than on physical reasons. However, for site 1', i.e., the interfacial oxygen site, the local p-PDOS shows a different line shape. The peaks B_2 , C , and D_1 are significantly reduced in intensity. For this reason, the shoulders of B_2 and C become more pronounced. An additional feature labeled X_1 is observable for site 1' while for the feature labeled X_2 no interface-specific line shape can be observed in this plot. At an energy of 18.5 eV above the Fermi level E_F , a pronounced peak X_3 appears at the interface. The fact that the spectral features labeled X_1 and X_3 only appear in the site projection for the interfacial oxygen atom (site 1'), shows that the corresponding unoccupied states in the conduction bands are highly localized at the interface. The next nearest oxygen site 2' already shows a bulk-like local unoccupied p-PDOS. In Figure 7.14 the calculated results for the O p-PDOS are plotted in comparison to the F p-PDOS, representing the $Z + 1$ approximation for the core-hole effects. Here, only the projections for the sites 1' and 4' are plotted together with the O and F p-

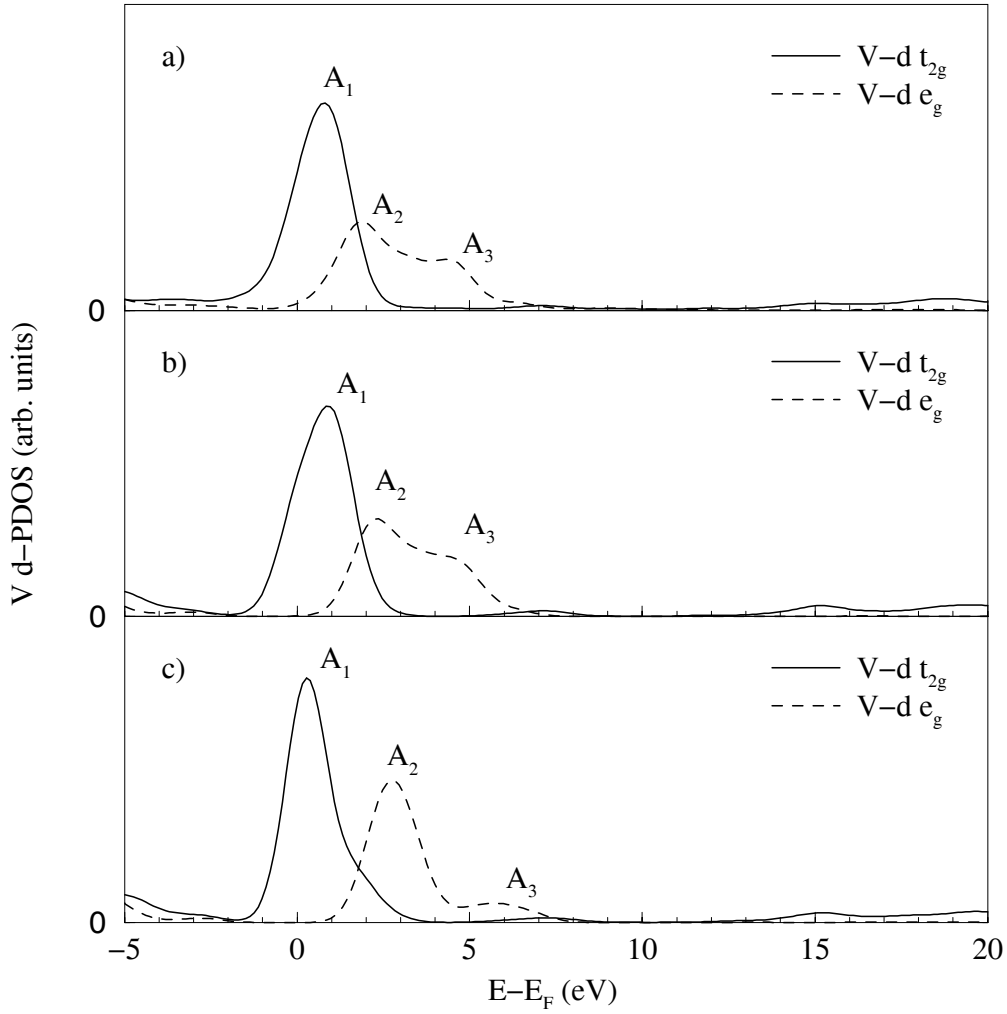


Figure 7.12: . Calculated V d-PDOS for a) the Pd/SrTiO₃ interface (site 1 in Figure 7.11), and b) for site 2 in the Pd/SrTiO₃ supercell with a TiO₂ terminated substrate. For comparison, in c) the corresponding V d-PDOS calculated in a pure bulk supercell is plotted.

PDOS spectra for pure bulk SrTiO₃ from Figure 6.14b and 6.14c. In Figure 7.14, peak *A* of all spectra was set to 0 eV for an easier comparison of the spectra. As can clearly be inferred from Figure 7.14a, the F p-PDOS and the O p-PDOS show almost the same line shapes. Differences in the F p-PDOS compared to the O p-PDOS occur as a damping of peak *A*, a more pronounced peak *B*₁ and a shift of the peaks in regions 3, 4 and 5 by 0.5 eV towards higher energies.

Comparing the interfacial p-PDOS spectra in Figure 7.14a to the spectra calculated in a pure bulk supercell (cf. Figure 7.14c) for both F and O, one can clearly observe that peaks *X*₁ and *X*₃ are not observable in bulk SrTiO₃, while the situation for peak *X*₂ is different. In comparison to Figure 7.14, the presence of peak *X*₂ at the interface might originate from

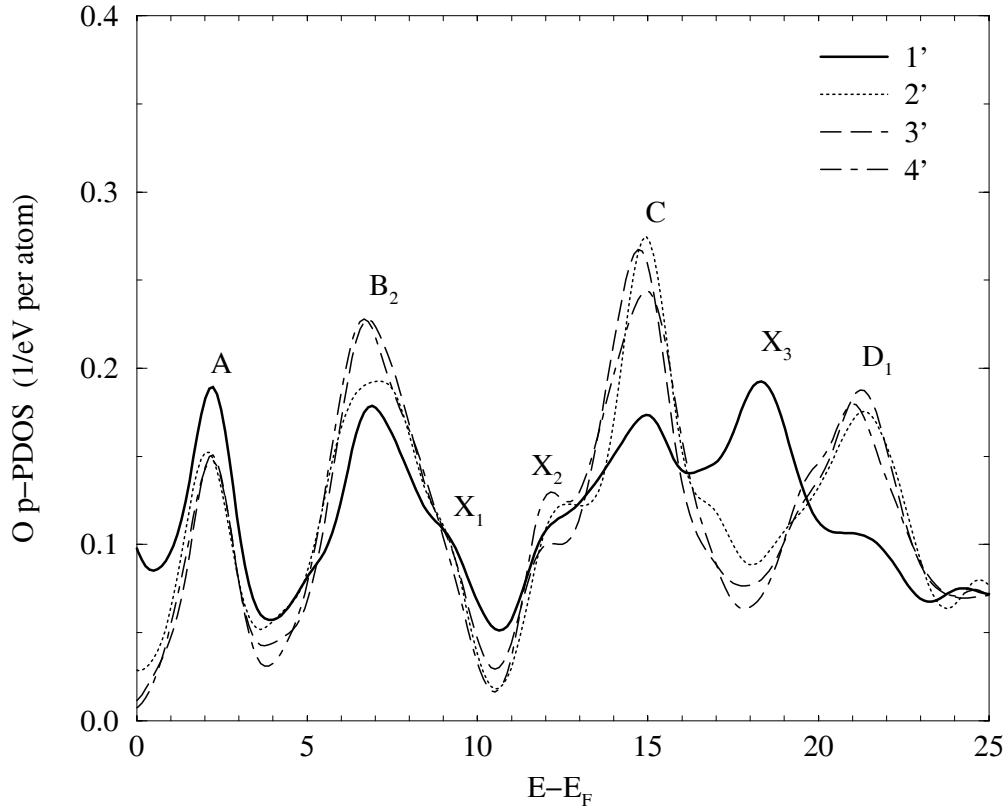


Figure 7.13: Local O p-PDOS projected for different sites in the atomistic structure of the TiO₂ terminated Pd/SrTiO₃ interface. The sites 1', 2', 3', and 4' correspond to the sites defined in Figure 7.11.

supercell effects, since in this energy regime a pronounced peak appears in the F p-PDOS projected for site 4'.

For a more detailed analysis of the interfacial peaks X_2 and X_3 in the real space, distribution maps of the unoccupied densities of states were calculated for five different energy windows defined in Figure 7.14a for the (020)-plane in the corresponding supercell. The definition of energy windows was performed such, that regions 1 and 3 contain only the peaks X_1 and X_3 , respectively, whereas the other regions contain the neighbouring spectral features, which are predominantly formed by bulk SrTiO₃ unoccupied states. The results of this calculation for the different energy windows are shown in Figure 7.15. The atomic arrangement in the (020)-plane is also shown. Since the contour maps are plotted for a (020) plane throughout the supercell, only Ti and O atoms are visible, whereas Sr atoms are not present in the chosen plane. Intensities are coded by different greylevels and range from 0.025 electrons/Bohr³ to 0.125 electrons/Bohr³ with a step width of 0.005 electrons/Bohr³. All five regions show a predominantly homogeneous intensity distribution throughout the whole supercell. In regions 1 and 2 extra intensities appear at the Ti sites of the interface. These features originate from the appearance of peak X_2 and from the broadening of peak

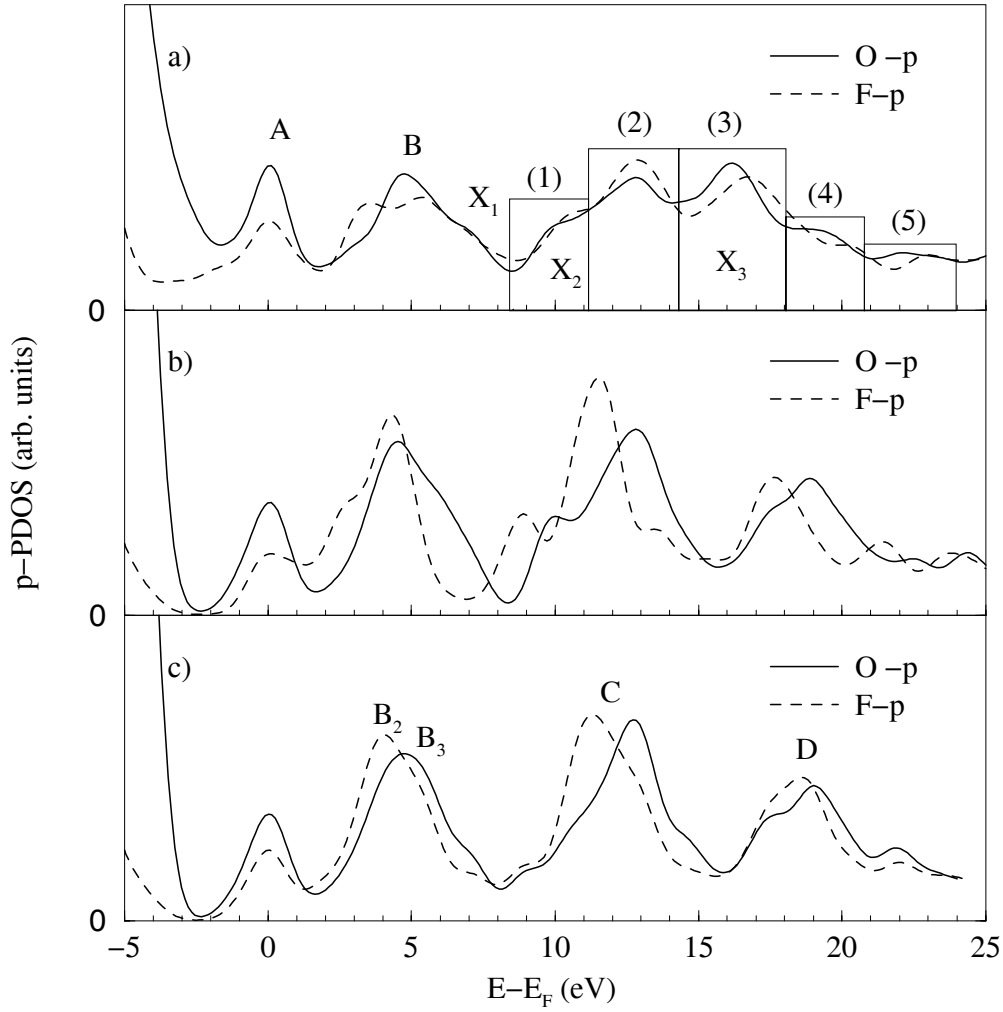


Figure 7.14: Calculated O and F p-PDOS for a) the Pd/SrTiO₃ interface, and b) for bulk SrTiO₃ in the same supercell with a TiO₂ terminated substrate, corresponding to the sites 1' and 4' in Figure 7.11a, respectively. For comparison, in c) the corresponding O and F p-PDOS calculated in a pure bulk are shown. In this graph, the first peak of all spectra were calibrated to a reference energy E_0 , which is not identical to the Fermi energy.

C at the interface, as can be concluded from Figure 7.14. In region 3 some significant extra intensity is observable above the interfacial Ti site in between two Pd atoms from the first metal layer. In addition, some extra intensity is visible for the O atom in the second bulk layer (with respect to the interface) and in between the oxygen atoms from the first and the second bulk layer. Since observed energy window 3 includes the interfacial O p-PDOS peak X_3 , which is absent in the bulk p-PDOS, the corresponding unoccupied state is highly localized at the Pd/(100)SrTiO₃ interface. In regions 4 and 5 only a homogeneous intensity distribution is observable, indicating no interface-specific features in the unoccupied densities of states.

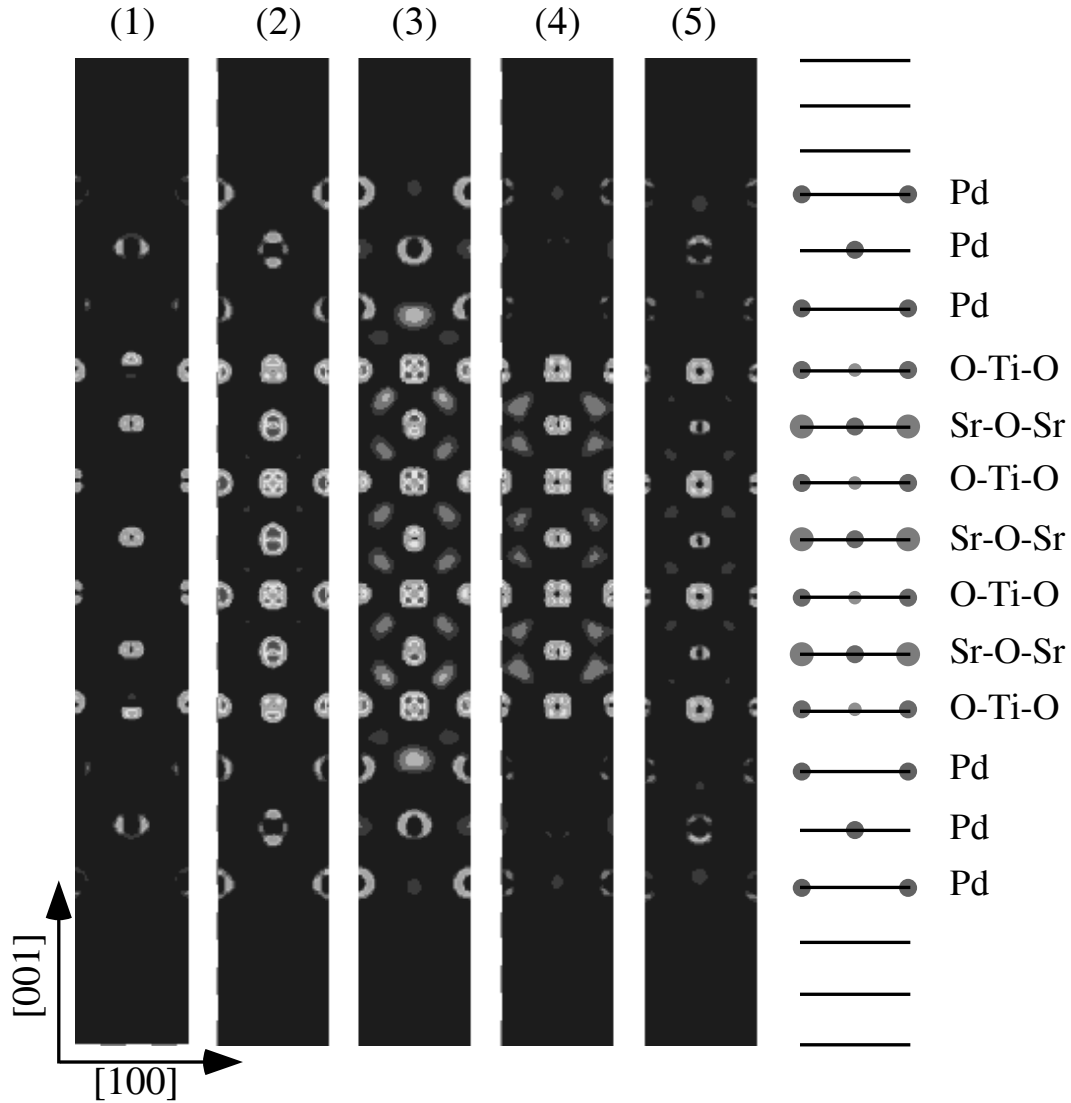


Figure 7.15: Spatial distribution of the local unoccupied O p-PDOS in a $[020]$ plane of the supercell for five different energy regimes defined in Figure 7.14. Intensities are coded with grey levels, ranging from 0.025 electrons/Bohr³ to 0.125 electrons/Bohr³ in 11 steps.

So far, it is not clear whether the appearance of the interfacial peaks X_1 , X_2 , and X_3 is only a surface effect of bulk SrTiO₃ or an interface effect due to the Pd/SrTiO₃ contact. Therefore, in a further calculation the Pd atoms were removed from the supercell, forming a (100)SrTiO₃ free surface. The atomistic structure of the free surface was again relaxed with respect to the total energy of the system [Ochs, 2000]. In Figure 7.16 the O p-PDOS from Figure 7.14 are plotted as solid lines in comparison to the results from the calculations of the free surface supercell. The site projections for the free surface model were performed for the same sites as in the interface calculation (cf. 1' and 4' in Figure 7.11a). The O p-PDOS

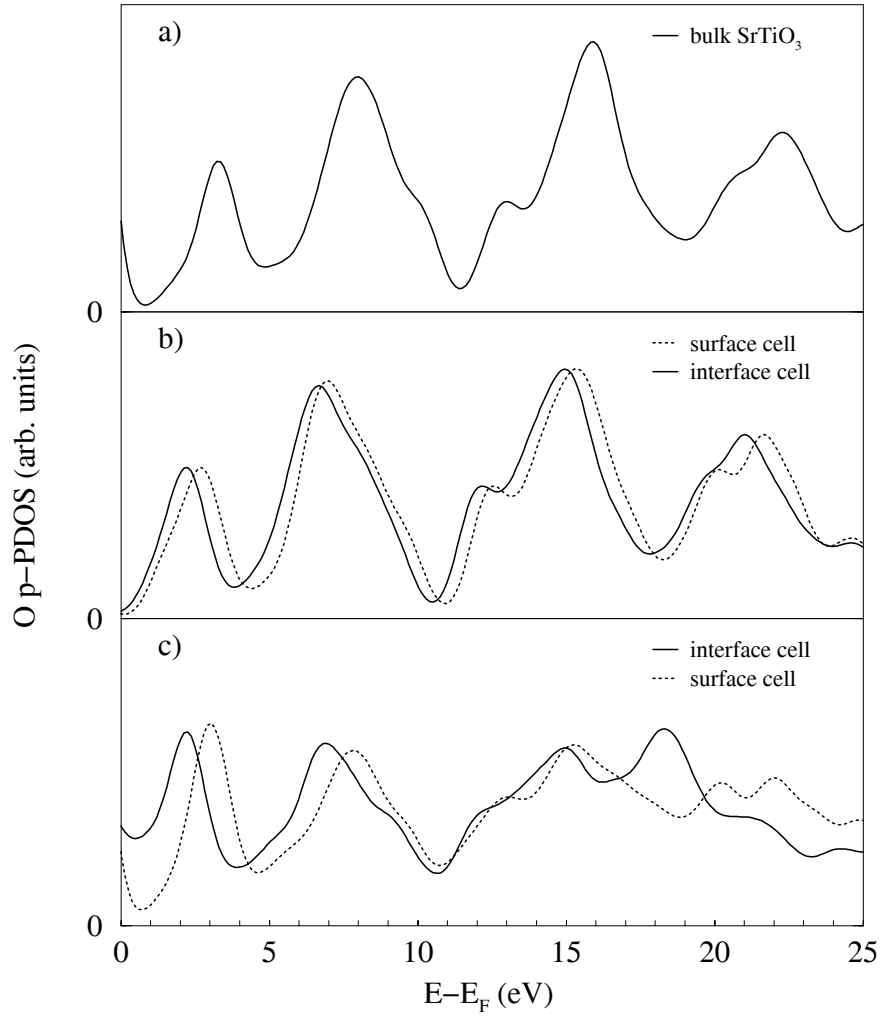


Figure 7.16: Calculated O p-PDOS for a) bulk SrTiO₃, for b) bulk SrTiO₃ within the supercells for the Pd/SrTiO₃ interface and for the free (100)SrTiO₃ surface, and c) for the O sites at the interface and at the free surface.

in Figure 7.16a was calculated using a bulk supercell of exactly the same size and the same scaling of the k -point mesh as in the free surface and the interface calculations. For this reason, differences between this line shape and the bulk SrTiO₃ line shape in Figure 7.14c are due to size effects of the bulk SrTiO₃ supercell. Comparing the results for bulk SrTiO₃ from the different supercells in Figure 7.16a and 7.16b, no significant influence of the missing Pd film is observable on the O p-PDOS, apart from a 0.5 eV shift of the Fermi level towards lower energies. Focussing on the results for the interfacial and for the surface O site, a 0.9 eV shift of the Fermi level towards lower energies is observable for the surface-cell calculation. In the calculation of the O p-PDOS of the free surface, the peaks labeled X_1 and X_2 in the interfacial p-PDOS are observable, while peak X_3 is only present at the Pd/SrTiO₃ interface. At approximately 20.1 eV and 21.0 eV, two peaks appear in the surface-cell calculation, which

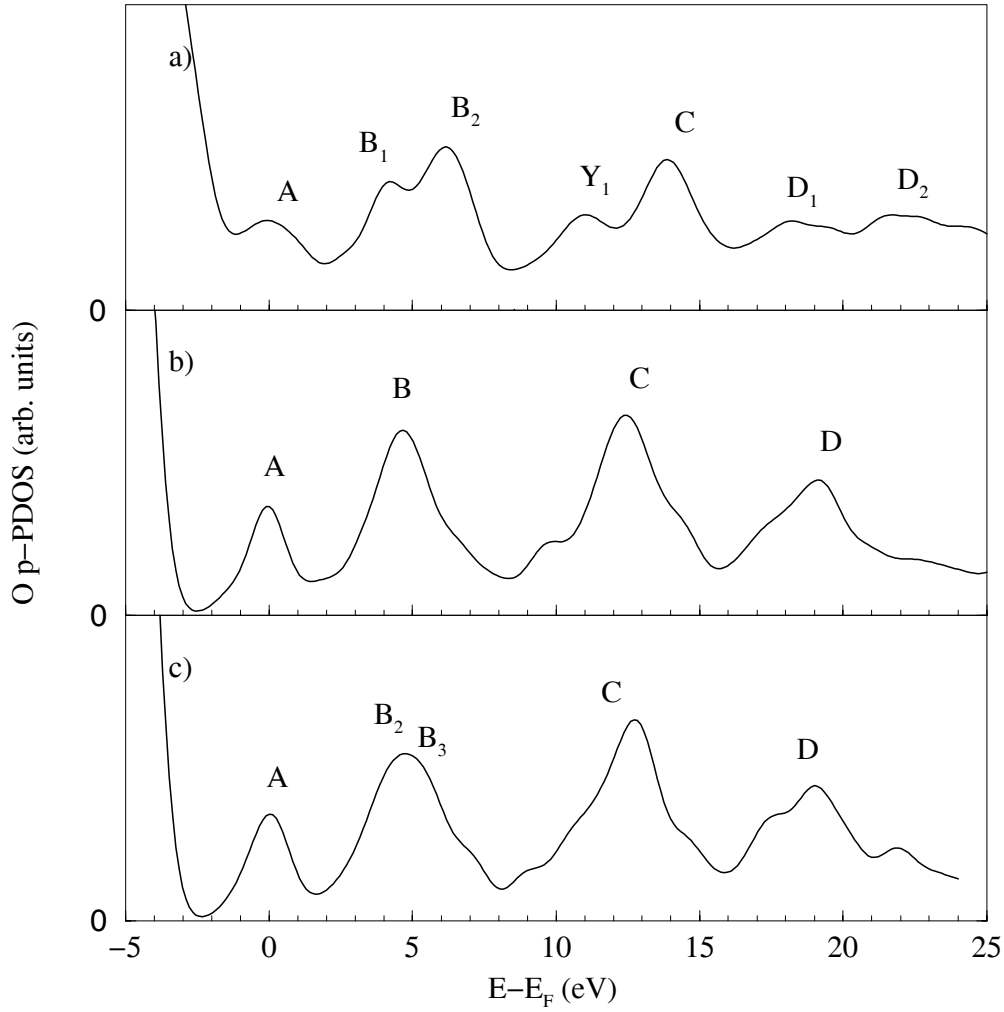


Figure 7.17: Calculated O p-PDOS for a) the Pd/SrTiO₃ interface, and b) for bulk SrTiO₃ in the same supercell with a SrO terminated substrate, corresponding to the sites 1''' and 4''' in Figure 7.11b, respectively. For comparison, in c) the corresponding O p-PDOS calculated in a pure bulk are shown. In this graph, peak A of all spectra were calibrated to a reference energy E_0 , which is not identical to the Fermi energy.

are not present at the Pd/SrTiO₃ interface.

Calculations of the O p-PDOS were also performed for the SrO terminated Pd/SrTiO₃ interface using the supercell shown in Figure 7.11b. The corresponding results for the sites 1''' and 4''' are plotted in Figure 7.17 together with the O p-PDOS of bulk SrTiO₃. The interfacial O-pDOS exhibits peaks at 4.1 eV and 6.2 eV, labeled B_1 and B_2 , respectively. At 11.0 eV an interfacial peak labeled Y_1 is observable while peak C occurs at 13.8 eV. Above 17 eV two broad features labeled D_1 and D_2 are visible. In summary, the overall line shape of the interfacial O p-PDOS is different compared to the p-PDOS calculated for the bulk-like site 4''' (Figure 7.17b) and bulk SrTiO₃ (Figure 7.17c).

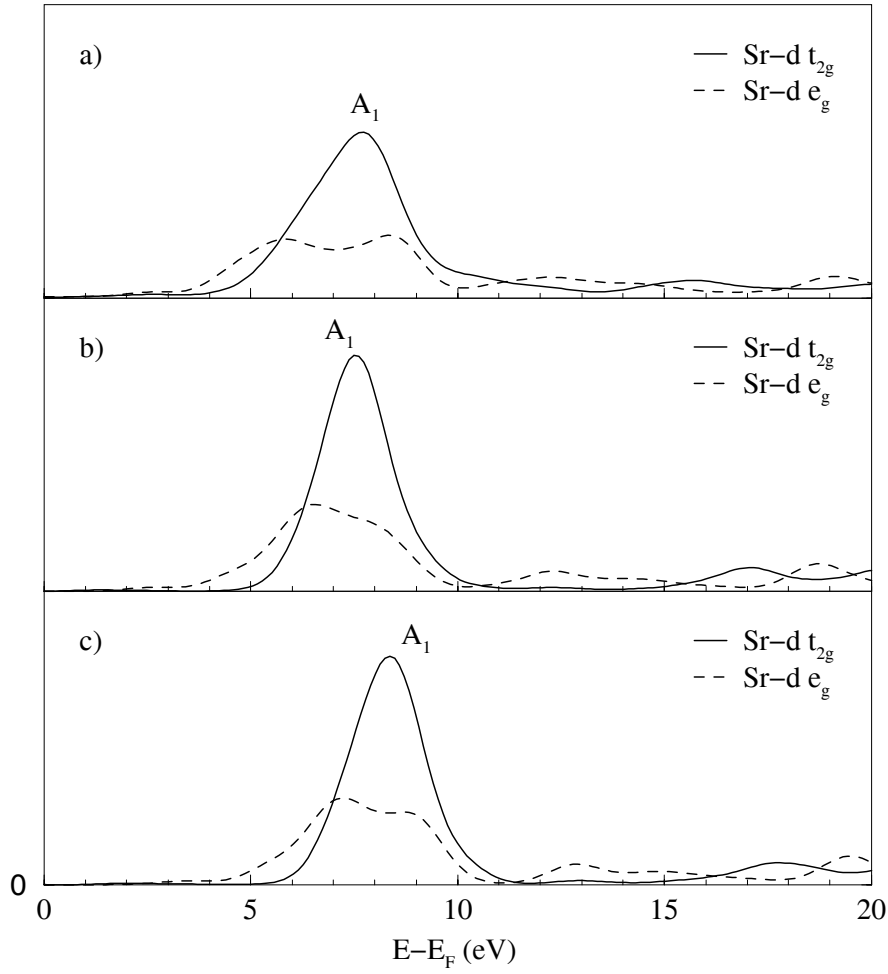


Figure 7.18: Calculated Sr d-PDOS for a) the Pd/SrTiO₃ interface, and b) for bulk SrTiO₃ in the same supercell with a TiO₂ terminated substrate, corresponding to the sites 1'' and 2'' in Figure 7.11a, respectively. For comparison, in c) the corresponding Sr d-PDOS calculated in a pure bulk supercell of the same size is plotted. The results for the SrO terminated Pd/SrTiO₃ are plotted in d) for the interfacial layer and in e) for a bulk-like layer, originating from projections for the sites 1''' and 2''' in Figure 7.11.

For an analysis of the experimental Sr L_{2,3}-edges, the Sr d-PDOS was calculated only for SrO terminated Pd/SrTiO₃ interface. For the TiO₂ termination, the amount of the Sr d-PDOS present at the interface is significantly small and is therefore unimportant. The calculated results for the Sr d-PDOS for the sites 1''' and 2''' are plotted in Figure 7.18a and 7.18b, respectively. In addition, the Sr d-PDOS for bulk SrTiO₃ is plotted for comparison in Figure 7.18c. Core-hole effects were not considered in these calculations, as they are not important for a comparison to experimental Sr L_{2,3}-edges (cf. section 6.4). For the SrO terminated interface, the e_g states at the position 1''' show a relatively large splitting compared to the position 2'''. The t_{2g} PDOS is significantly broadened at the interface with

a non-symmetric peak shape (cf. Figure 7.18a). However, the overall summation of the d-PDOS leads to a broadening of the white line at the interface. In addition, two weak shoulders appear due to the Sr-3d e_g states.

7.3 Discussion

In the following the results obtained for the Pd/SrTiO₃ interface are discussed in detail. One part of this discussion is dedicated to the comparison between experiment and theory concerning the ELNES investigations (section 7.3.2). In the second part, the bonding between the film and the substrate is analysed in terms of the calculated occupied densities of states.

7.3.1 Interface Structure

During the film growth *in situ* RHEED patterns for different nominal film thicknesses showed diffraction patterns similar to those of transmission diffraction studies (cf. Figure 7.1a), indicating a 3-dimensional growth mechanism of Pd on the (100)SrTiO₃ surface at a temperature of 650°C. These observations could be further confirmed by SEM and CTEM investigations (Figures 7.1b and 7.2a, respectively) after the growth process. The formation of islands demonstrates that it is energetically favoured to form free Pd surfaces compared to the formation of a Pd/SrTiO₃ interface. During the growth process, Pd atoms hitting the substrate surface undergo short range surface diffusion processes to form clusters of atoms at different nucleation sites. The nucleation density thereby depends on the substrate temperature, the deposition rate, the substrate surface structure, etc. [Richter, 2000].

The cube-on-cube epitaxy is the dominant orientation relationship between the Pd film and the (100)SrTiO₃ surface, although Fe dopants in the substrate material seem to lead to a modified film morphology. However, more detailed investigations of this effect were not performed in the present work.

A coherent and abrupt interface structure was observed by qualitative HRTEM studies. The absence of an extended reaction layer at the interface indicates that no solid state reaction appeared between the Pd film and the SrTiO₃ substrate. Diffuse contrasts in the HRTEM micrograph most likely originate from the TEM specimen preparation and are caused by some beam damage and contamination effects during the ion-milling process. Due to this contrast which also appears in the interface region, the contrast pattern in the HRTEM is not sufficiently well resolved to extract information about the substrate termination from the intensity distribution. Furthermore, the inhomogeneous contrast pattern makes a quantitative HRTEM study using image simulations impossible.

To summarize these facts, at this point a weak bonding strength between the Pd film and the SrTiO₃ can be concluded. This was also already observed during the TEM specimen preparation (cf. Figure 5.2). Only with further developed preparation methods, including less mechanical treatments of the TEM samples, investigations of the Pd/SrTiO₃ interface became possible. Recent developments in TEM specimen preparation cover low-voltage ion-

milling processes for polishing TEM samples after ion-thinning. After an additional low-voltage ion-milling process, HRTEM micrographs of bulk SrTiO₃ exhibit an homogeneous intensity distribution over large specimen areas. Hence, a quantitative HRTEM study of the Pd/SrTiO₃ interface will become possible [Tchernychova, 2001].

In the HAADF micrographs a strong change in contrast can be observed at this metal/ceramic interface due to the large difference in the atomic numbers for Pd and for the atoms forming SrTiO₃. Therefore, a compromise has to be achieved between the use of relatively small acquisition times to avoid too bright intensities for the Pd, and longer acquisition times to account for a sufficient signal-to-noise ratio in the SrTiO₃ area. In addition, specimen drift during longer acquisition times have to be considered. Non-centric positions of Ti,O-columns in between four adjacent Sr columns are instability effects of the scanning generator of the microscope rather than effects of the applied filter technique.

From the intensity point of view, Sr columns can easily be distinguished from mixed Ti-O columns due to the Z^2 -dependence of the intensity distribution in HAADF patterns. Also inside the Pd film the spot pattern shows a geometry as it was expected for a *fcc* crystal structure in $\langle 100 \rangle$ zone-axis orientation (cf. Figures 7.4b). Although an abrupt interface can be observed, more detailed information on the atomistic structure, especially on the determining layer of the substrate surface, cannot be extracted. In some interfacial areas a slight mis-tilt of the specimen is observable through some blurred contrasts of the atomic columns, corresponding to a non-edge-on orientation of the interface. Contamination effects during acquisition times strongly affect the quality of the final HAADF micrographs. Even a very low amount of contamination, which would not be observable in conventional HRTEM experiments, leads to a blurring of contrasts in the HAADF images. These contamination effects originate from the glue used during the TEM specimen preparation.

Summing it up, the terminating layer of the substrate could not be determined due to artificial distortions of the HAADF patterns discussed above. Further development of the TEM specimen preparation and a higher stability of the used TEM should lead to more quantitative HAADF investigations in the near future. A simultaneous EELS measurement during the Z-contrast imaging was impossible since the electron beam current was significantly reduced to improve the spatial resolution for the imaging conditions. For this reason, signal-to-noise ratios appeared to be too low for a reliable EELS or ELNES measurement of any of the previously discussed ionization edges.

7.3.2 ELNES-Analysis: Experiment and Theory

The ELNES measurements of the Ti L_{2,3}-edges and the O K-edge show significantly different line shapes for the interface specific ELNES component and for bulk SrTiO₃ in both theory and experiment. A comparison of the results of the experimental Ti L₃-edge and the calculated V d-PDOS is given in Figure 7.19. Focussing only on one of the two L-edges, e.g., on the L₃-edge, the experimental data and the calculated data show the peaks A_1 and A_2 . The same would also hold for the peaks B_1 and B_2 of the Ti L₂ when they are compared to the V d-pDOS. The calculated peaks A_3 and B_3 are not observable in the experiment

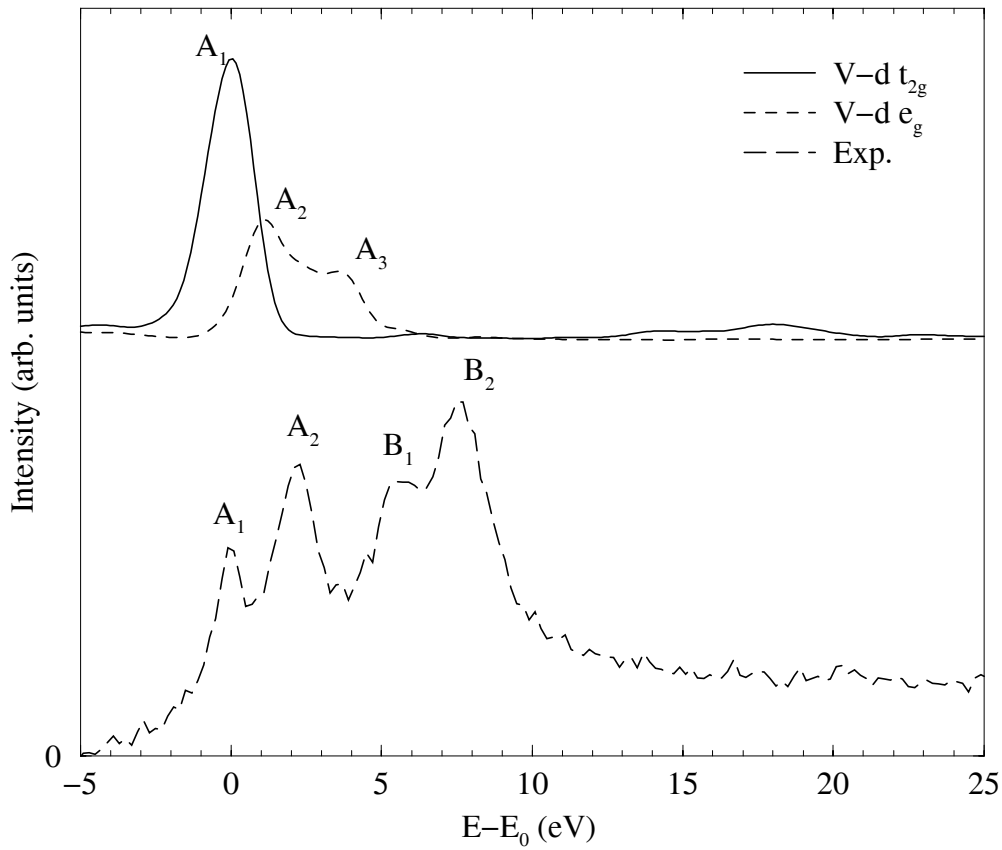


Figure 7.19: Interfacial V d-PDOS in comparison to the experimentally determined interface specific ELNES of the Ti $L_{2,3}$ -edges.

due to the overlap of the L_3 and the L_2 edges. The peak intensities are not comparable since in the calculations the transition matrix elements as well as configuration interactions [Ogasawara, 2001] were not included.

In the experimental interface specific ELNES component of the Ti $L_{2,3}$ -edges, a reduced crystal field splitting of peaks A_1 and A_2 of 2.0 ± 0.2 eV is observable. In the calculated V d-PDOS, the separation of peaks A_1 and A_2 of 2.4 eV in bulk SrTiO_3 is reduced to 1.1 eV for the interfacial Ti layer, which does not correspond to the experimental observations. The bulk-like V d-PDOS also does not reproduce the pure bulk crystal field splitting but shows a peak separation of 1.5 eV.

The discrepancies in the crystal field splitting between theory and experiment can have several reasons: a slightly modified atomistic structure in the experiment, i.e. a different nearest neighbour environment for Ti at the interface; an unreliable application of the spatial difference technique; an oxidation of the Pd layer; or an incorrect core-hole approximation at the interface. Among these, an unreliable application of the spatial difference technique can be excluded. A variation of the applied scaling factors in the spatial difference technique resulted in differences in relative peak intensities but not in a variation of the crystal field

splitting for the Ti L_{2,3}-edge. An oxidation in the volume of the Pd film could not be observed since within the Pd film no O K-edge was detectable. In addition, no experimental evidence could be found for a different atomistic structure of the interface by HRTEM or HAADF analysis. A further discussion of this point would be possible e.g. by quantitative HRTEM study of the Pd/(100)SrTiO₃ interface. Uncertainties in the calculated data can be found in the $Z + 1$ approximation of the core-hole effects at the interface. The validity of this approximation was shown to be valid in bulk SrTiO₃. However, this can be different especially at a metal/insulator interface. An electron-hole pair can easily be screened in the adjacent metal film, whereas the response in the insulating ceramic is completely different. Thus, a straightforward interpretation of the core-hole effects on the Ti L_{2,3}-edges, formed by unoccupied Ti-3d states, is not possible and the simple $Z + 1$ approximation becomes questionable.

However, both experiment and theory show a significant reduction of the crystal field splitting at the interface, showing that the octahedral coordination of Ti in the bulk material is disturbed at the interface. This is clearly the case since one O atom of the surrounding O octahedron is removed and replaced by a hollow site within the Pd film, as can be inferred from Figure 7.11. A reduction of Ti, i.e., a change in the formal oxidation state, could be resolved by experiment by a 0.2 ± 0.1 eV chemical shift of the Ti L_{2,3}-edges towards lower energy-losses. For a reduction of Ti from the nominal oxidation state +4 to +3, Leapman and co-workers observed a chemical shift of 0.4 eV [Leapman, 1982].

In Figure 7.20 the experimentally determined interface specific O K-ELNES (7.20a) is plotted in comparison to the interfacial O p-PDOS for both the TiO₂ (7.20b) and the SrO (7.20b) terminated (100)SrTiO₃ surface. The calculated O p-PDOS for the two different terminations show different line shapes. In contrast to the TiO₂ termination, the O-pDOS for the SrO termination exhibits a double peak between 3 eV and 8 eV above the Fermi level, labeled B_1 and B_2 , respectively. Approaching higher energies, the O p-PDOS exhibits the peaks Y_1 and C , which are clearly separated. No coincidence in the O p-PDOS for peak X_3 can be found for the two different terminations. Above $E_0 + 16$ eV two peaks are observable for both terminations (D_1 and D_2), which differ in their peak energies. Comparing the calculated p-PDOS in Figure 7.20 to the experimentally determined O K-edge, one can observe an agreement between the line shapes 7.20a and 7.20b, especially focussing on peak X_3 , while line shape 7.20c does not agree with the experimental data. Therefore, the analysis of the interface specific O K-edge demonstrates the presence of a TiO₂ terminated Pd/SrTiO₃ interface since no experimental ELNES line shape similar to calculated O p-PDOS for an SrO termination could be observed in any interfacial area. In summation, this ELNES analysis is in agreement with the theoretical interface model of the lowest total energy. So far no experimental evidence for a successful preparation of a TiO₂ terminated (100)SrTiO₃ surface [Kawasaki, 1994] has been proven by any TEM investigation in the literature.

The comparison of the calculated unoccupied O p-PDOS for the Pd/SrTiO₃ interface and for the free (100) surface of SrTiO₃ showed that the peaks X_1 and X_2 correspond to highly localized states induced by the (100) surface of SrTiO₃, whereas peak X_3 is induced by the interface formation. However, the origin for peak X_3 in the O K-ELNES is still an

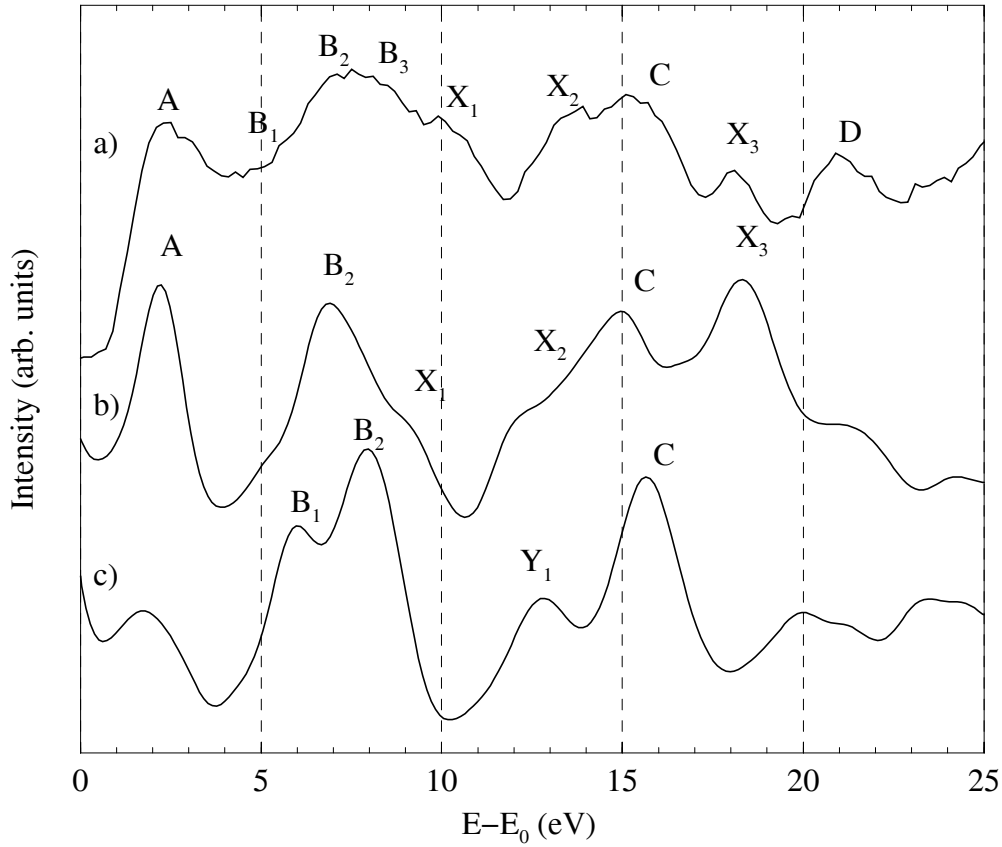


Figure 7.20: O p-PDOS from the interfacial layer for both the TiO₂ (b) and the SrO (c) terminated Pd/SrTiO₃ interface, in comparison to the experimental interface specific ELNES component of the O K-edge (a).

open question. Therefore, the calculated interfacial O p-PDOS is analysed in more detail in terms of the p_x -, p_y -, and p_z -projected local unoccupied DOS, which are shown in Figure 7.21. The vertical line denotes the energy position at which the interface specific peak X₃ appears. In contrast to bulk SrTiO₃, the interfacial p_z -PDOS shows no pronounced feature between 12 eV and 21 eV above the Fermi level E_F . Especially at $E_F + 18.5$ eV, the intensity remains unchanged. While in bulk SrTiO₃ only one sharp peak at 7.0 eV is observable in the p_z -PDOS, which corresponds to peak B₂, a broadened asymmetric feature with its maximum intensity at 8.5 eV appears. Apart from that, the p_z -PDOS also provides some extra intensity directly across the Fermi level, especially for peak A.

In the p_x -PDOS the peak at 21 eV in the bulk is shifted downwards in energy to 17.8 eV, forming a plateau together with a nearly unchanged peak at 14.5 eV. At lower energies, the broad bulk peak at 12.0 eV (peak B₃) is replaced by a sharper peak at the position of peak B₂ with some extra intensity in the regime of peak B₁. In addition, the contribution of the p_y -PDOS to peak A in bulk SrTiO₃ is completely removed at the interface. The latter reflects an increased hybridization between the Ti-3d t_{2g} and the O p_y states by the decreased density

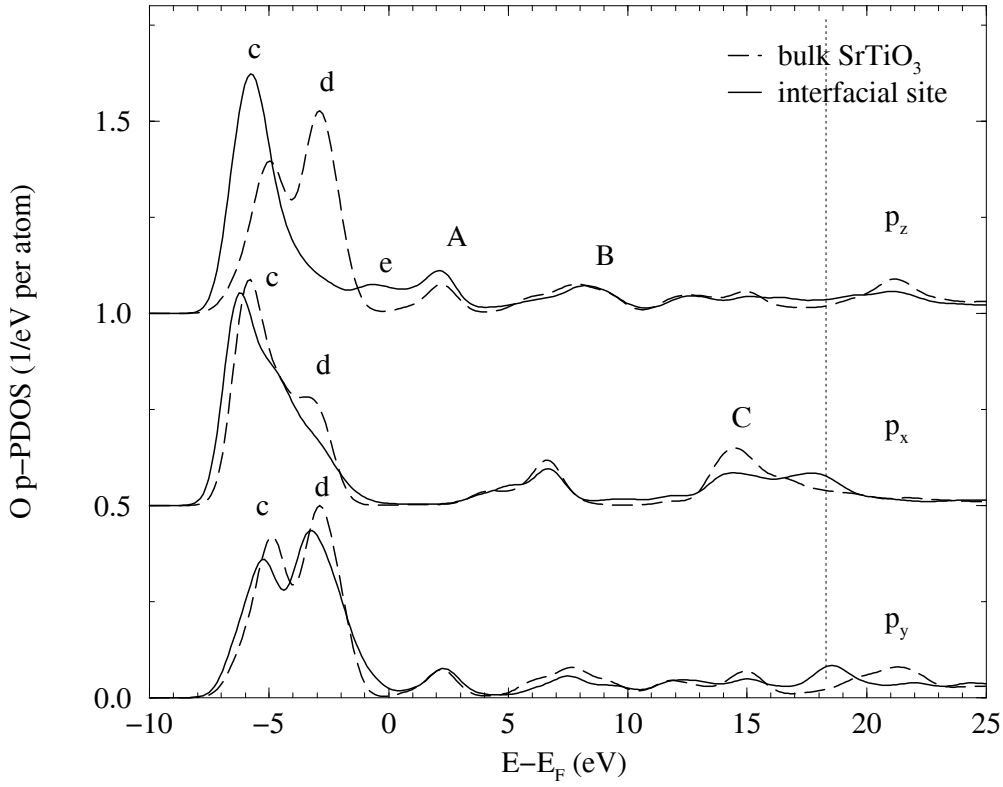


Figure 7.21: Local O p-PDOS for the interfacial sites (solid lines) and a bulk-like site (dashed line) within a TiO_2 plane. The line shapes correspond to the p_z , p_x , and p_y projected densities of states.

of *unoccupied* states and therefore an increased interaction of the O atoms and the Ti atoms at the interface.

The bulk p_y -PDOS remains nearly unchanged at the interface except from a peak at 21 eV moving downwards in energy to 18.6 eV.

In conclusion, from Figure 7.21 it can be inferred that the interface specific peak X_3 in the O K-edge is formed predominantly by the unoccupied p_x - and p_y -states, whereas the p_z states do not contribute to this peak. This behaviour can be interpreted as a change of the crystal field for the O site at the interface. In bulk SrTiO_3 , oxygen atoms are coordinated by two Ti atoms in, for example, the x -direction and by four Sr atoms in the $(y + z)$ -direction, as is sketched in Figure 7.22. This schematic viewgraph provides an explanation of the origin of peak X_3 : It is an effect of the changed crystal field at the interfacial O sites. The coordinating atoms form a crystal field at the O site, leading to the well-known local band structure in SrTiO_3 [Mo, 1999] [van Benthem, 2001b]. For the free (100) surface of SrTiO_3 , two Sr atoms are removed and therefore also the crystal field at the O site is changed. Placing a Pd atom above the O atom leads again to change in the local band structure and thus to a modified crystal field at this site.

For the Sr $L_{2,3}$ -edges no experimental interface specific ELNES component could be

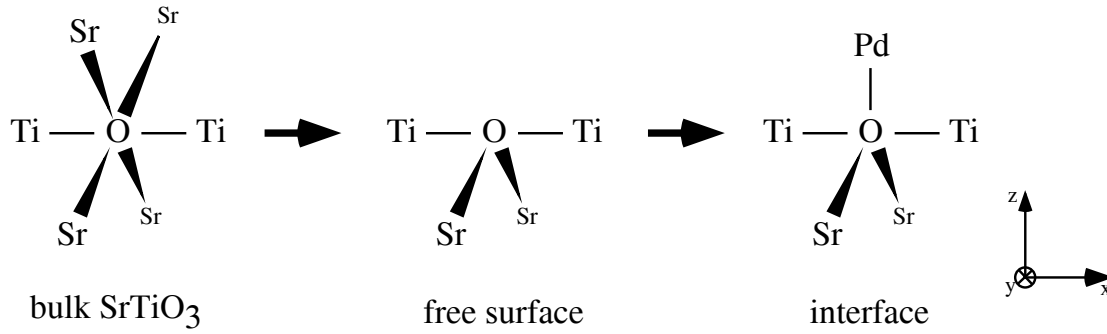


Figure 7.22: Nearest neighbours for O at the TiO_2 terminated $\text{Pd}/(100)\text{SrTiO}_3$ interface. A scheme is sketched for the formation of the interface via the free (100) surface of bulk SrTiO_3 .

determined. The calculated results in Figure 7.18 only show weak differences between the bulk and the interfacial Sr d-PDOS. Due to the resolution limits in the experiment, none of these differences would occur in the currently available experimental data. Therefore, no information about the terminating layer of the SrTiO_3 could be obtained in terms of the Sr $L_{2,3}$ -edges. In the case of a TiO_2 termination, one would however not expect any interface specific component in the local Sr d-PDOS, especially if one assumes a high localisation of the unoccupied interfacial Sr d-PDOS only at the interfacial Sr sites, similar to the O p-PDOS in Figure 7.13.

Summing it up, the experimentally observed interface specific ELNES data agree with the LDFT calculations of the corresponding site and symmetry projected unoccupied densities of states for the $\text{Pd}/(100)\text{SrTiO}_3$ interface model with the lowest total energy. For the Ti $L_{2,3}$ -edges, trends in the crystal field splittings observed in the experiment can be reproduced by the theory using a $Z + 1$ approximation accounting for core-hole effects. The level of agreement is limited due to the one-electron description and due to an insufficient approximation of the core-hole effect by the $Z + 1$ approach at the interfacial site. For the O K-edge, a higher level of agreement could be achieved between theory and experiment. Independent from some core-hole effects, three ELNES peaks (X_1 , X_2 and X_3) could be observed at the Pd/SrTiO_3 interface by both experiment and theory. A theoretical analysis of these peaks showed that the features X_1 and X_2 correspond to unoccupied states induced by the SrTiO_3 surface rather than by the interface formation. The origins of the peak labeled X_3 are the change of the crystal field around the oxygen site at the interface, i.e., an effect of the interface formation. By a calculation of the interfacial O p-PDOS for both possible terminations of the (100) SrTiO_3 surface, a comparison of theoretical and experimental data showed the presence of TiO_2 terminated substrates at the Pd/SrTiO_3 interface. This again corresponds to the configuration of the lowest total energy in a previous theoretical study [Ochs, 2000] [Ochs, 2001]. For the Sr $L_{2,3}$ -edges, no interface specific ELNES component could be observed. The calculations of the local Sr d-PDOS did not show significant differences in the line shapes for the different Sr sites throughout the supercell, at least not within

the experimental resolution limits. Therefore, the Sr L_{2,3}-edges could not be used for the investigation of the substrate termination at the Pd/SrTiO₃ interface.

The present study is an indirect proof of the validity of the theoretical model since only the unoccupied band structure in terms of the densities of states was investigated. Direct evidence can only be given by, for instance, a quantitative HRTEM study of the Pd/SrTiO₃ interface [Tchernychova, 2001], including HRTEM simulations. On the other hand, assuming the validity of the theoretically determined atomistic structure model, the synergy of theory and experiment demonstrates the validity of the spatial difference technique to extract the interface specific ELNES components from spectra recorded only in the interfacial region.

7.3.3 Bonding Analysis

Due to the validity of the theoretically obtained atomistic structure model of the Pd/SrTiO₃ interface, the bonding between the film and the substrate can be analysed in terms of the calculated occupied densities of the valence states, which were calculated simultaneously with the unoccupied DOS. No core-hole effects need to be considered in this analysis since only intrinsic material properties are important while the experimental influences need not to be considered.

In the following discussion the z -axis is considered to be parallel to the normal of the interfacial plane, while the (x, y) -plane denotes the interfacial plane itself. In Figure 7.23 the densities of occupied d -states are plotted for the interfacial Ti site and for a bulk-like Ti site within the same supercell (sites 1 and 2 in Figure 7.11). The d -states are plotted with respect to their different components related to the different magnetic quantum numbers.

In bulk SrTiO₃ all three t_{2g} -PDOS, i.e., the d_{xy} -, the d_{xz} -, and the d_{yz} -PDOS, show similar line shapes for the occupied states. In the d_{xy} -PDOS, two peaks at -5 eV (a) and at -3.2 eV (b) arise, whereas the degenerated d_{xz} and d_{yz} states show a peak and a shoulder in their PDOS at exactly the same positions. In all three PDOS the band gap of the bulk insulator SrTiO₃ is visible. The interfacial d_{xy} -PDOS is broadened leading to a decrease in intensity of peak a . In addition, peaks a and b are shifted in energy to -5.3 eV and -3.7 eV, respectively. The remaining t_{2g} states (d_{xz} and d_{yz}) are degenerated at the interface. Peak a is shifted to -6 eV and the shoulder b becomes a pronounced peak at -3.2 eV. In addition, a significant increase in intensity labeled b' is observable in the band gap region. The e_g states show different line shapes in their PDOS. In bulk SrTiO₃ the $d_{x^2-y^2}$ -PDOS shows a peak a at -5.8 eV and a smaller peak b at -2.9 eV. At the interface, peak a is shifted to -6.2 eV while peak b remains at the same position. The overall line shape is broadened by a small amount compared to the bulk PDOS. The d_{z^2} PDOS in the bulk also shows two peaks a and b at -5.8 eV and -2.9 eV, respectively. Approaching the interface, peak a is shifted to -5.4 eV and the peak labeled b remains as a shoulder of a . At the interface, the whole shape of a and b is broadened leading to a significant broadening and decrease in intensity of peak a . The width of the band gap region is thereby significantly decreased, as one can infer from Figure 7.23.

The increase of the occupied Ti-PDOS in the band gap region at the interface displays

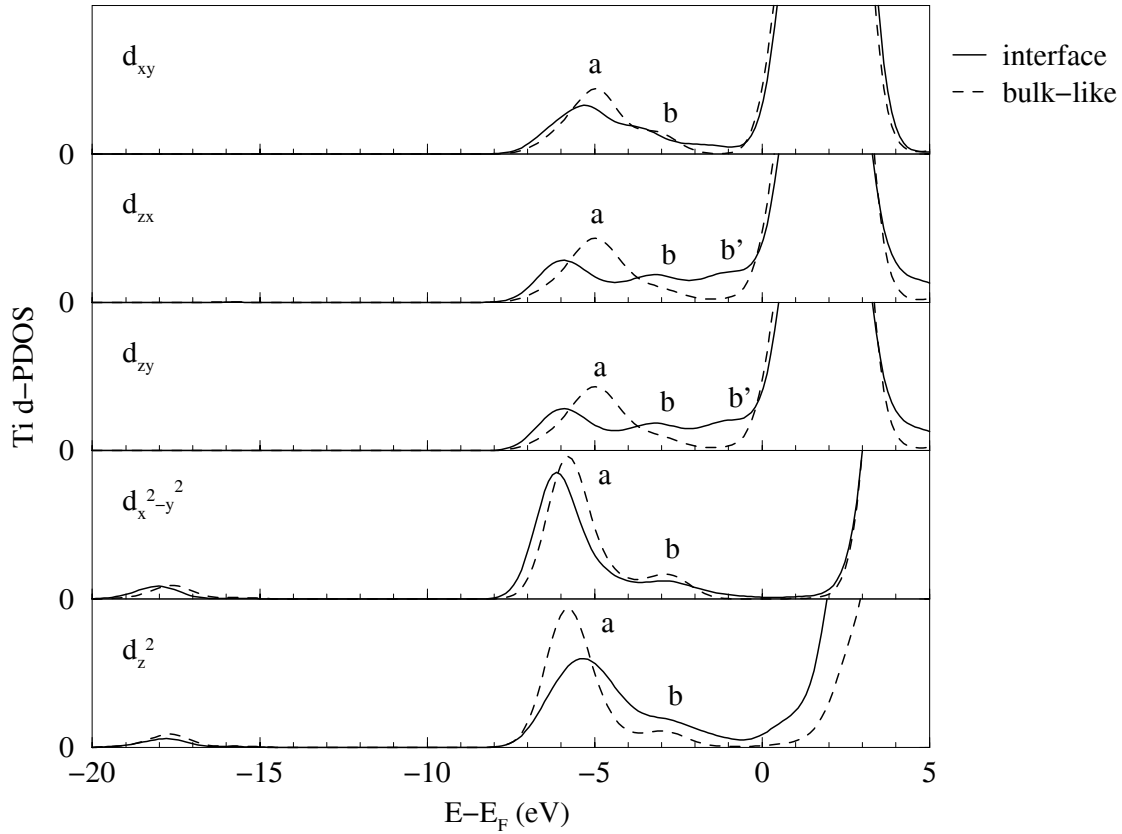


Figure 7.23: Occupied local Ti d-PDOS for the interfacial site and a bulk-like site within the SrTiO₃ substrate.

the appearance of occupied states induced by the contact of the insulating SrTiO₃ substrate to the metallic Pd film. The appearance of these effects are well-known in the literature and are referred to as so-called metal-induced gap states (MIGS) [Sutton, 1995]. A more detailed analysis of the MIGS appearing at the Pd/SrTiO₃ interface is given later in this section.

Considering the local energy of the occupied bands E_{band}^{local} defined in equation 7.2, conclusions could be drawn on the bonding strength of the suggested atom in the direction along the spatial extent of the observed orbital.

$$E_{band}^{local} = \int_{-\infty}^{E_F} LDOS(E) \cdot E dE \quad (7.2)$$

$LDOS(E)$ denotes the local densities of states. The local band energy is directly connected to the first moment of the momentum theorem of Cyrot-Lackmann [Cyrot-Lackmann, 1967] [Ducastelle, 1970], which is the average energy measured with respect to the center of the band. As can be inferred from Figure 7.23, the first moment decreases for the occupied Ti-3d_{x²-y²}, whereas it increases for the Ti-3d_{z²}-states at the interface. This behaviour corresponds to a bond strength which is higher for bondings formed by the d_{x²-y²} orbitals, and which is lower for d_{z²} orbital bonding. The latter is a reasonable result since one O atom is

missing as one of the bonding partners for Ti atoms at the interface and therefore a decreased bonding strength results along the z -direction, that is, normal to the interface plane.

O atoms are the nearest neighbours of Ti atoms in both bulk SrTiO₃ and for the Pd/SrTiO₃ interface. The occupied O-2p PDOS for p_z -, p_x -, and p_y -states are plotted in Figure 7.21. In bulk SrTiO₃ the occupied p_z -PDOS consists of two pronounced peaks at -5.0 eV labeled c and at -2.9 eV labeled d . For the interfacial site, only peak c appears at -5.8 eV, which is slightly broadened compared to peak c in the bulk. Peak d is no longer observable. In addition, the PDOS intensity is significantly increased in the band gap region of bulk SrTiO₃ by a peak labeled e at -0.6 eV, which reflects the appearance of MIGS also at the O site. The first moment of the O $2p_z$ -PDOS is shifted to lower energies of approximately 1.5 eV. This behaviour clearly reflects a change of bonding of the interfacial O atoms. However, it is not clear whether this is due to one Ti atom missing as a bonding partner for O, or if this effect is due to a direct bonding of O atoms to Pd atoms.

The O p_x -PDOS in bulk SrTiO₃ consists of two peaks c and d at -5.9 eV and -3.4 eV, respectively (cf. Figure 7.21). For the interfacial site only peak c remains at -6.6 eV, which shows a strong asymmetry. On its high energy wing, peak d splits into two weak shoulders appearing at -4.8 eV and -3.2 eV. The first moment of the p_x -states is therefore shifted to lower energies.

In the present geometry, the O p_y -states in bulk SrTiO₃ are degenerate with the p_z states and therefore show exactly the same line shape in the local PDOS. For the interfacial site, peaks c and d shift by 0.6 eV towards lower energies. In addition not only a decrease of the first moment, but also an increase of the second moment, or a peak broadening, can be observed from Figure 7.21.

In Figure 7.24 the occupied d-PDOS for Pd are plotted for the interfacial Pd site and for a bulk-like Pd site within the metal film. The occupied Pd d_{xy} -PDOS is formed by a shoulder f and two peaks g and h at -3.9 eV, -2.5 eV, and -0.2 eV, respectively. For the interfacial Pd site no significant change in the line shape occurs, except from an increase in intensity of peak f and a slightly decreased first moment for the d_{xy} -PDOS. This indicates a weakly increased bonding strength of the Pd atoms within the plane parallel to the interface. For the occupied d_{xz} -PDOS an asymmetric peak h at -1.3 eV can be observed in Figure 7.24. At the interface, this peak is significantly shifted by 1.1 eV towards lower energies showing a pronounced shoulder labeled g' at -4.3 eV. Due to the changes of the first moment of the d_{xz} -PDOS a bonding of Pd atoms with interfacial Ti atoms of the substrate is observable. For the interfacial d_{yz} -PDOS, peak h remains unshifted compared to the metal film, while at the interface two additional shoulders g and g' at its low energy wing appear at -4.8 eV and -2.8 eV, respectively. The first moment of the d_{yz} -PDOS remains nearly unchanged at the interface compared to metallic Pd film. Also in this case a decrease of the first moment is observed, which is smaller than the decrease for the d_{xz} -PDOS. This is caused by the fact that in the present geometry the next nearest neighbours of Pd are two Ti atoms along the $\pm x$ directions, whereas in the $\pm y$ directions no Ti atom is present. The $d_{x^2-y^2}$ -PDOS for Pd shows two peaks labeled g and h for both, the interfacial site and the bulk-like Pd site. In the Pd film these peaks occur at -2.8 eV and -0.9 eV, respectively, whereas for the

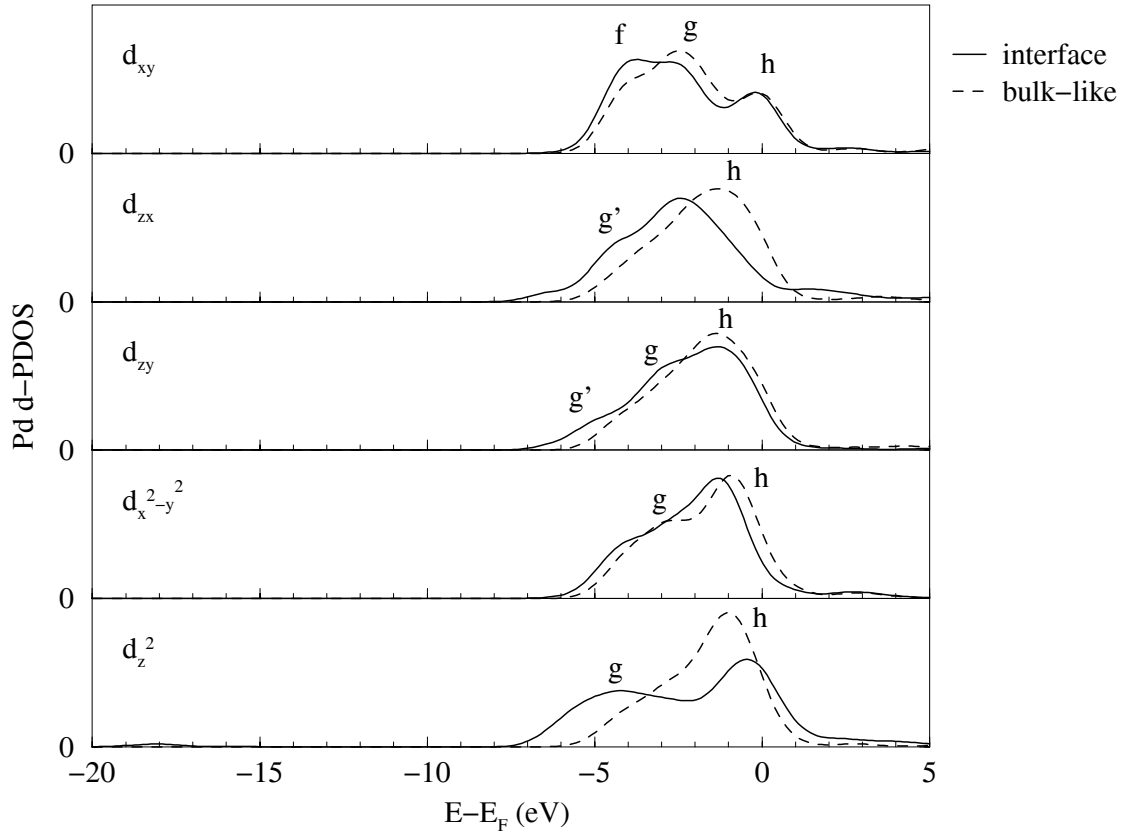


Figure 7.24: Occupied local Pd d-PDOS for the interfacial site and a bulk-like site in the Pd film.

interfacial site, peak h is shifted by 0.4 eV towards lower energies, while peak g is slightly reduced in intensity and shifted to -3.7 eV. Therefore, the first moment is decreased while a small increase of the second moment is present. This again reflects an increased bonding strength within the planes parallel to the interfacial plane. The d_{z^2} -PDOS in the metallic Pd film consists of a broad asymmetric peak labeled h with its maximum at -1.0 eV. At the interfacial site, the d_{z^2} -PDOS splits into two peaks g and h at -4.2 eV and -0.4 eV, respectively. Due to this strong broadening of the occupied d_{z^2} -PDOS the bond energy is significantly decreased while the second moment is increased. Therefore, it can be stated that the Pd- d_{z^2} orbitals form strong bonds along the z -axis.

For the analysis of the bonding characteristics across a metal/ceramic interface, different types of interactions have to be considered, such as the van-der-Waals interaction, the ionic bonding, and the covalent bonding. Finnis showed that van-der-Waals interactions do not play an important role for the adhesion of a metal film on a ceramic substrate [Finnis, 1996]. For an ionic substrate the bonding between the metal and the ceramic substrate can be described by the formation of an image charge as a response of the metal electron cloud on the ions in the substrate surface leading to ionic bonds. This concept was introduced

by Stoneham [Stoneham, 1983] and is described in detail by Finnis [Finnis, 1996]. In the case of the Pd/SrTiO₃ interface, it was shown by Ochs that the image charge description for the bonding across this interface is not sufficient, due to the high amount of covalent bonding in SrTiO₃ [Ochs, 2000]. Thus, the bonding characteristic between the Pd film and the (100)SrTiO₃ surface is described in terms of covalent bonding. Therefore, hybridization between different atomic orbitals is analysed in terms of the site and symmetry projected occupied local densities of states. For those energies, for which the local occupied PDOS of two different atomic sites overlap, a hybridization of the corresponding atomic orbitals occurs. Of course this is only true if the two corresponding atomic orbitals overlap in real space. Based on the observations for the first and the second moment, in the following the bonding between the Pd film and the SrTiO₃ surface is analysed.

Focussing on the energy shifts of peaks *c* and *a* in the O *p_z*- and the Ti *d_{z²}*-PDOS, respectively, a decrease of the overlap can be observed reflecting a decreased hybridization between these two atomic orbitals. The appearance of peak *g* in the Pd *d_{z²}*-PDOS leads to the formation of a O-*p_z*-Pd-*d_{z²}* hybridization, corresponding to a σ bonding between O and Pd. Parallel to this effect, an increased overlap of the O *p_x*-PDOS with the Ti *d_{x²-y²}*-PDOS can be observed, reflecting an increased bonding between O and Ti within the interfacial plane. The decreased first moment of the O *p_y*-PDOS also reflects this behaviour in the current configuration. In the TiO₂ terminated (100)SrTiO₃ surface two different oxygen positions exist, which are crystallographically equivalent. The difference between these two O sites are in the direction of the O-Ti-O bonding, which can be along the *x*- or along the *y*-axis. Therefore, the observations for the *p_x*-PDOS are also valid for the *p_y*-PDOS of the different O sites. Also for Pd a small increase in the bonding strength is observed within the plane parallel to the interfacial plane, due to the absence of one Pd atom along the *z* direction by the interface formation.

Focussing on peak *b'* in the Ti *d_{zx}*-PDOS, an overlap with the Pd *d_{zx}*-PDOS can be observed in the energy regime between -2.0 eV and the Fermi level. Due to the geometry, this effect does not appear in the *y*-direction. However, for a different Pd site, it can be observed for the *d_{zy}*-PDOS of Ti and Pd and not in the *d_{zx}*-PDOS. This overlap shows a hybridization of Ti *d_{zx}*-orbitals with Pd *d_{zx}*-orbitals (or Ti *d_{zy}* with Pd *d_{zy}*). Therefore, an intermetallic bonding between Pd and the next nearest neighbouring Ti atoms is observed, similar to investigations of Heumann [Heumann, 1957], Wood [Wood, 1958] and of Mizuno and Tanaka [Mizuno, 1998] [Tanaka, 1998] for Fe/TiO₂ and Cu/MgO. The intermetallic interaction between Ti and Pd across the Pd/SrTiO₃ interface can be seen in real space by plotting the change of the valence charge density due to the interface formation in comparison to the pure bulk materials. Such a plot is shown in Figure 7.25 for the Pd/SrTiO₃ interface for a [010] TiO₂-plane in the used supercell, but in this case only for one layer of Pd on top of the (100)SrTiO₃ surface. The plot shows a significant increase of the valence charge density between the Pd atoms and the Ti atoms of the substrate surface, indicating an intermetallic bonding between the film and the substrate [Classen, 2001b].

The overlap of the Ti *d*-, the Pd *d*-, and the O *p*-PDOS in the region between -5 eV and the Fermi level indicates the formation of MIGS, as was mentioned earlier. These gap states

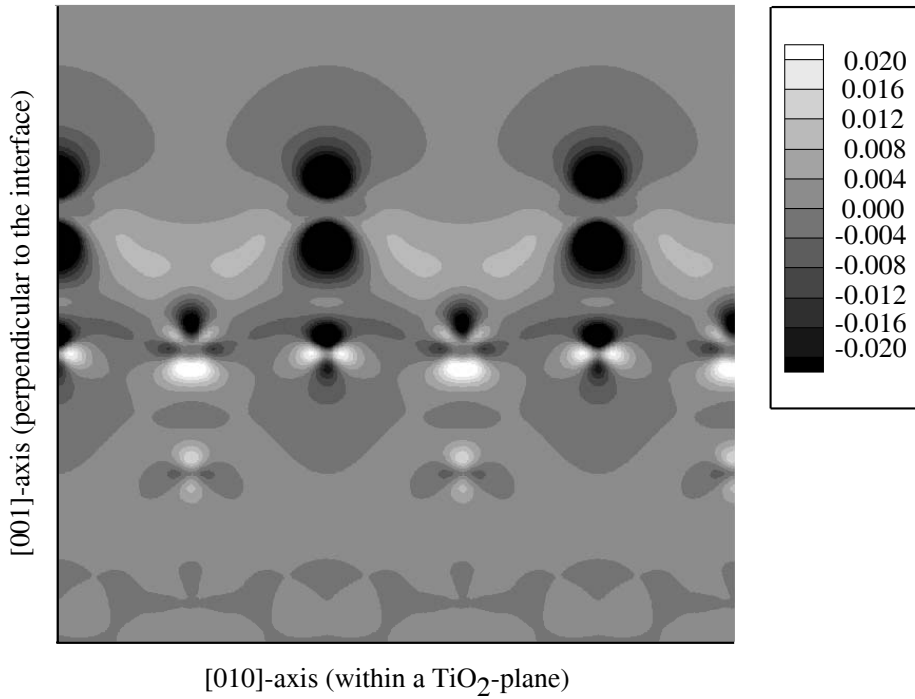


Figure 7.25: Changes in the charge distribution in a (020)-plane of the used supercell for the Pd/SrTiO₃ interface in comparison to the single bulk materials. The intensity is color coded in the RGB scheme for 10 different levels. The minimum and maximum intensity in the Figure correspond to -0.020 electrons/bohr³ and $+0.020$ electrons/bohr³. This plot is from T. Classen [Classen, 2001b].

appear by the contact of a metal and an insulating or semiconducting material. Bloch states in the metal coinciding with the band gap of a ceramic exponentially decay into the ceramic material [Heine, 1965] [Sutton, 1995]. For an analysis, the site projected local total densities of states (LDOS) for the interfacial sites of Pd, O, and Ti are plotted in Figures 7.26a, 7.26b, and 7.26c, respectively. For each site, the LDOS is plotted for energy broadenings of 0.8 eV and 0.2 eV.

For the line shapes broadened by 0.8 eV, i.e., similar to the experimental energy resolution in the ELNES experiments, no pronounced peak in the band gap region of bulk SrTiO₃ can be observed. By a smaller broadening of 0.2 eV, additional features are visible in all line shapes for the three different atomic sites. A broadening of 0.2 eV is so small that the k -point sampling within the calculation strongly affects the LDOS line shapes. Peaks occurring in this LDOS plot are artificial features due to the calculation method and do not have a physical meaning in terms of occupied states. However, these "peaks" are used to define different energy intervals (cf. Figure 7.26) to calculate the corresponding charge distribution in real space throughout the supercell. Considering the calculated indirect band gap energy for SrTiO₃ of 2.22 eV, three possible candidates among the appearing peaks can be observed in the band gap region, which can be found in the energy regions marked (1), (2) and (3) in

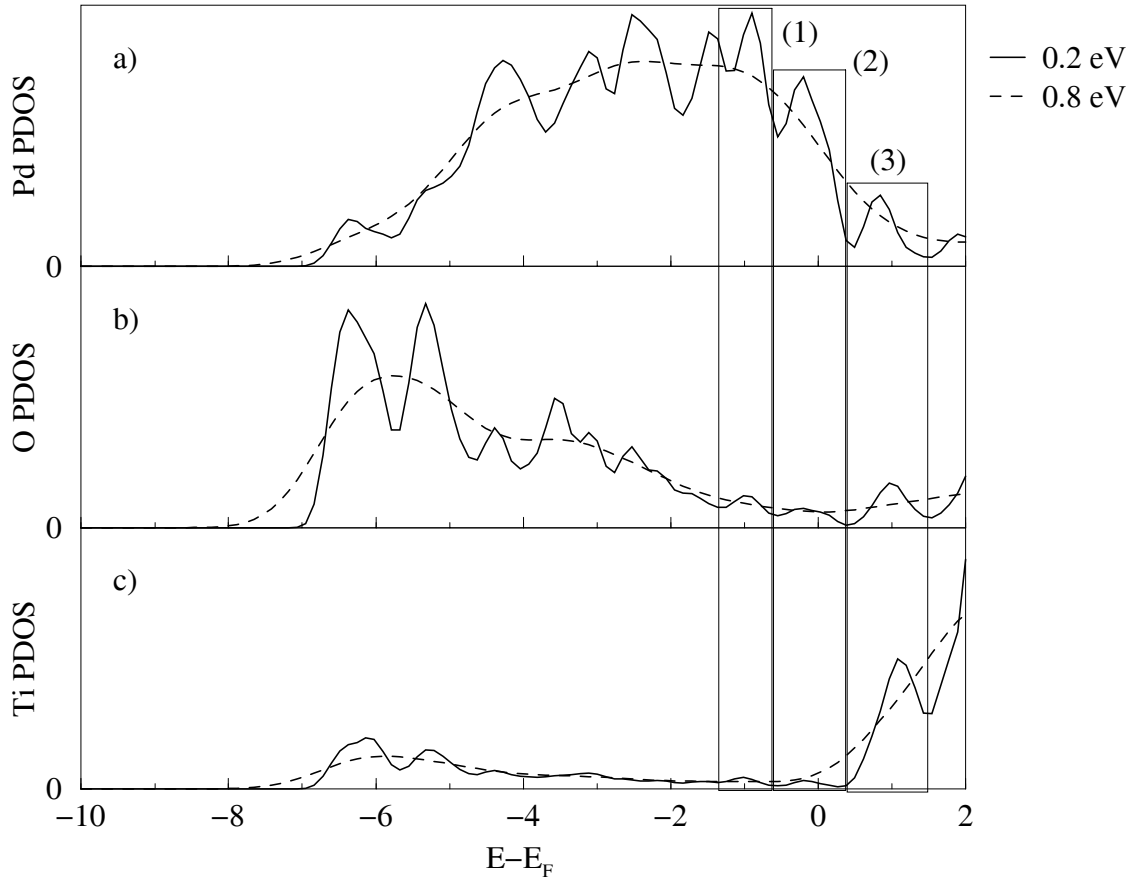


Figure 7.26: Local interfacial total PDOS in the band gap region for a) Pd, b) O, and c) Ti. Some extra interfacial intensities appear in the marked energy regions (1), (2), and (3). For all three sites the PDOS are plotted for a 0.2 eV and a 0.8 eV broadening in energy.

Figure 7.26. For the three peaks in the Pd LDOS an overlap with LDOS features from both the Ti LDOS and the O LDOS can be found. The calculated charge distributions for the different energy intervals are plotted in Figure 7.27.

As one can infer, the charge density in the regions (1) and (2) is mainly distributed in the Pd films rather than in the bulk region. However, intensities also appear at the interfacial O sites along the p_z orbitals. Furthermore, also some charge is distributed at the interfacial Ti sites along the $(x + z)$ -axes. The same holds for the $(y + z)$ -axes not visible in Figure 7.27. In addition to these observations, the overall intensity, distributed mainly inside the metal films, decays exponentially into the substrate. In the third energy interval the charge density is distributed on the Ti sites with some decay into the Pd. An increased charge density at the interface can not be observed.

In conclusion, the additional PDOS intensities in the energy intervals (1) and (2), which are located within the band gap region of bulk SrTiO₃, originate from states induced by the

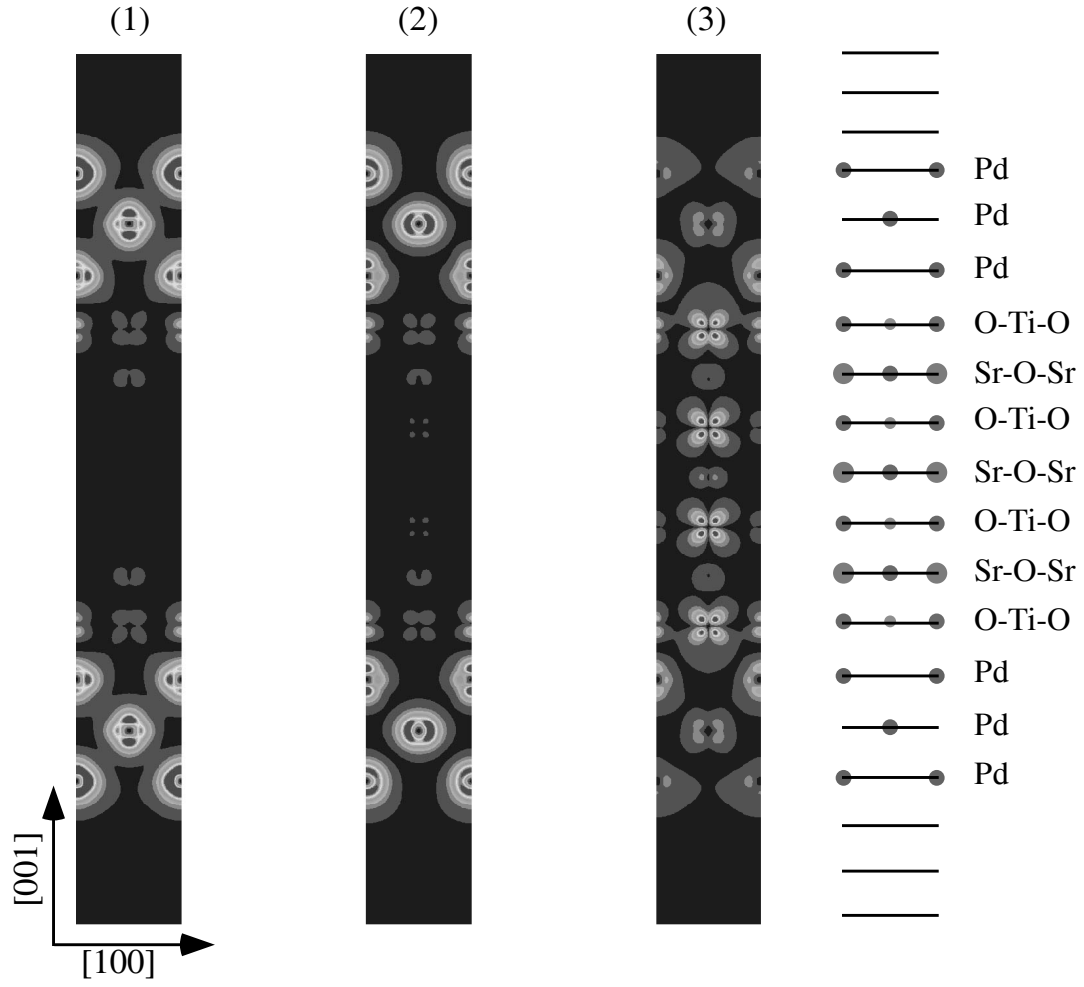


Figure 7.27: Spatial distribution of the total DOS in three different energy intervals in the band gap region. The intervals are defined in Figure 7.26.

metal/ceramic contact. These MIGS are located on both the interfacial O and the interfacial Ti sites, as it is shown in Figure 7.27. The gap states are formed by orbitals along the z -axis for O sites and along the Ti-Pd axes at the Ti sites, which was already observed by the overlap of the corresponding local PDOS.

Chapter 8

The Ni/SrTiO₃ Interface

In this chapter the experimental as well as the calculated results for the Ni/(100)SrTiO₃ interface are reported and discussed. Ni atoms have the same valence electronic structure as Pd atoms. Both metals crystallize in the *fcc* structure. Therefore, the bonding characteristics of Ni are expected to be similar to those of Pd films.

8.1 Experimental Results

8.1.1 Diffraction and Imaging Studies

Thin Ni films with a nominal thickness of 50 nm were grown by MBE on the (100) surface of undoped SrTiO₃ at a substrate temperature of 650°C. The experiments were performed under the same UHV conditions applied during Pd deposition, which were described in the previous chapters.

Figure 8.1a shows *in situ* RHEED patterns of the (100)SrTiO₃ surface after Ni deposition of nominal film thicknesses of 0.1 nm, 3.0 nm and 34.0 nm. As one can infer, the diffraction spots of the SrTiO₃ surface (cf. Figure 7.1a) are damped by the Ni diffraction pattern for a Ni coverage of 0.1 nm. Approaching higher nominal film thicknesses, the RHEED spot patterns do not change significantly. The RHEED pattern indicate Ni island formation instead of a continuous film growth. Furthermore, the cubic spot pattern reflects an epitaxial orientation relationship between the Ni islands and the substrate. From the separation of the Ni spots from the SrTiO₃ spots, a lattice mismatch of $m = -9.9\%$ between (100)Ni and (100)SrTiO₃ can be observed as well. The 3-dimensional growth mode (island growth) was also confirmed by SEM investigations of the samples after the MBE growth. A typical SEM micrograph is shown in Figure 8.1b. X-ray diffraction measurements also showed an epitaxial orientation relationship between the Ni film and the SrTiO₃ substrate. $\theta - 2\theta$ -scans exhibited a coincidence of the Ni (200)-peaks with the (200)-peaks of bulk SrTiO₃, indicating that the corresponding crystal planes of both Ni and SrTiO₃ are parallel.

Conventional TEM investigations showed Ni islands on the (100)SrTiO₃ substrate, as it can be inferred from a typical CTEM micrograph shown in Figure 8.2. Ni islands with

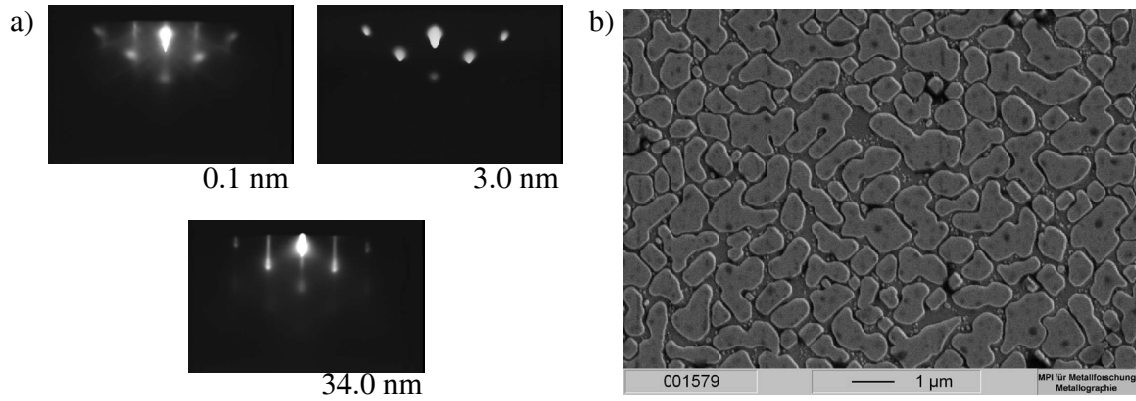


Figure 8.1: a) *In situ* RHEED patterns of Ni/SrTiO₃ in the (001) azimuth after deposition of nominally 0.1 nm, 3.0 nm, and 34.0 nm Ni on the (100)SrTiO₃ surface at a temperature of 650°C. b) SEM image of the deposited Ni film after the MBE growth.

varying lateral sizes could be observed. Large islands were formed by coalescence processes of smaller islands. These larger islands exhibit {110} facets to reduce their surface energies. The lateral size of the islands is larger than in the case of Pd (see previous chapter), which could already be inferred from a comparison of the corresponding SEM micrographs (Figures 7.1b and 8.1b). The thickness of the Ni islands ranged between 50 nm and 100 nm. From the selected area diffraction patterns of the interface in Figure 8.2b and 8.2c, it can be found that Ni is growing epitaxially with a cube-on-cube orientation relationship on the (100)SrTiO₃ surface. The [001] directions of the Ni film and the SrTiO₃ substrate as well as the {001} lattice planes of Ni and SrTiO₃ are parallel to each other, which can be written as:

$$100_{Ni} \parallel 100_{STO}. \quad (8.1)$$

This result is in agreement with the observations from RHEED and XRD mentioned above.

Figure 8.3a shows a HRTEM micrograph of the Ni/SrTiO₃ interface in $\langle 001 \rangle$ zone-axis orientation. The epitaxial orientation relationship given in 8.1 between the film and the substrate can also be observed in the HRTEM micrograph. Although no quantitative analysis of the HRTEM image was performed, one can identify an abrupt interface between the Ni film and the substrate. No reaction phase is detectable. However, the appearance of bright contrast variations directly at the interface probably indicate a chemical reaction between the film and the substrate. Due to the lattice mismatch of $m = -9.9\%$ between (100)Ni and the (100)SrTiO₃ substrate extra Ni planes are inserted every 11th column. This effect is visualized by a FFT filtering of the HRTEM micrograph in Figure 8.3b. For the FFT filter, which was already used for the HAADF image analysis described in section 7.1.1, the filter mask shown in Figure 8.3 was used. By this FFT filtering technique, all information in the vertical direction are removed from the HRTEM micrograph. In the resulting image, inserted Ni planes are marked by arrows. In between these areas, lattice planes are coherent between the film and the substrate, i.e., distorted areas due to the inserted lattice plane are highly

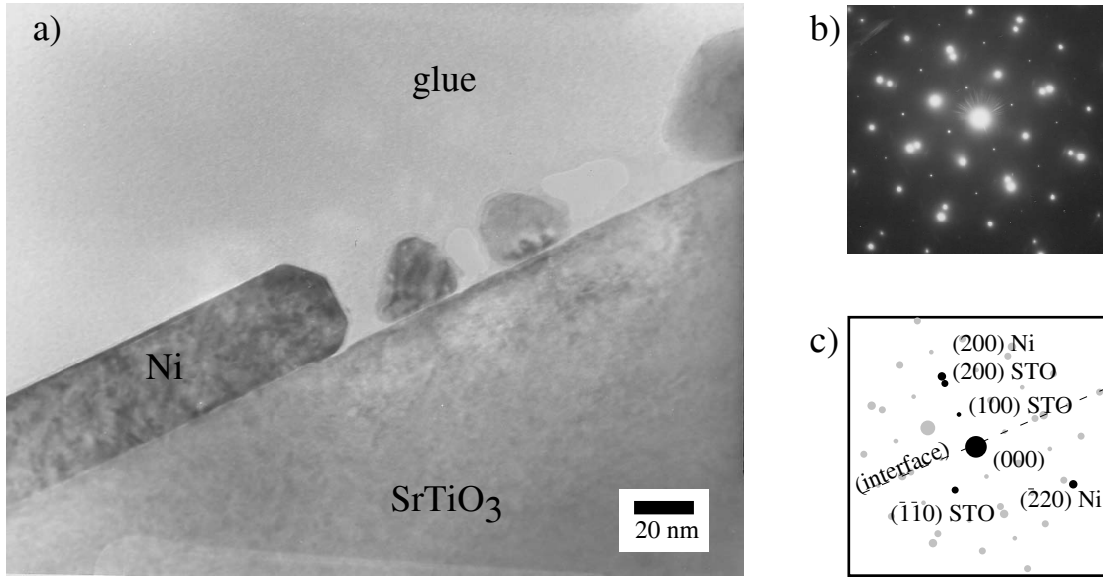


Figure 8.2: Conventional TEM investigations of the Ni/SrTiO₃ interface, showing a) a micrograph of Ni island formation on the (100)SrTiO₃ surface, and b) selected area diffraction pattern to determine the orientation relationship (c) between the Ni film and the SrTiO₃ substrate.

localized. Thus, the Ni/SrTiO₃ interface exhibits a semi-coherent interfacial structure. The lateral distance between two misfit dislocations, i.e., the inserted Ni planes, is about 1.7 nm to 1.8 nm.

8.1.2 EELS Results

For the Ni/SrTiO₃ interface the Ti L_{2,3}-edges, the O K-edge, and the Ni L_{2,3}-edges were measured in the same way as described in section 7.3.2. The edge onset of the Ni L_{2,3}-edges in pure metallic Ni appears at an energy-loss of 855 eV [Egerton, 1996]. The interface specific ELNES components were determined by the spatial difference method as described previously. Since no edge overlap in energy appears for this interface, all spectra could be background subtracted prior to the spatial difference calculations. In addition, only one scaling factor μ needed to be calculated, since none of the observed absorption edges appeared simultaneously on both materials adjacent to the interface. An interdiffusion of Ni or O across the interface could not be observed by EDXS measurements.

During the EELS experiments, scanning areas of the sizes $5 \times 50 \text{ nm}^2$ and $2 \times 20 \text{ nm}^2$ were used, so that the appearance of misfit dislocations do not play an important role for the observed ELNES line shapes. Specimen thicknesses were below 0.5 multiples of the inelastic mean-free path Λ_i in the investigated specimen areas. Hence, a Fourier-ratio deconvolution [Egerton, 1996] to correct the spectra for multiple inelastic scattering processes was not necessary.

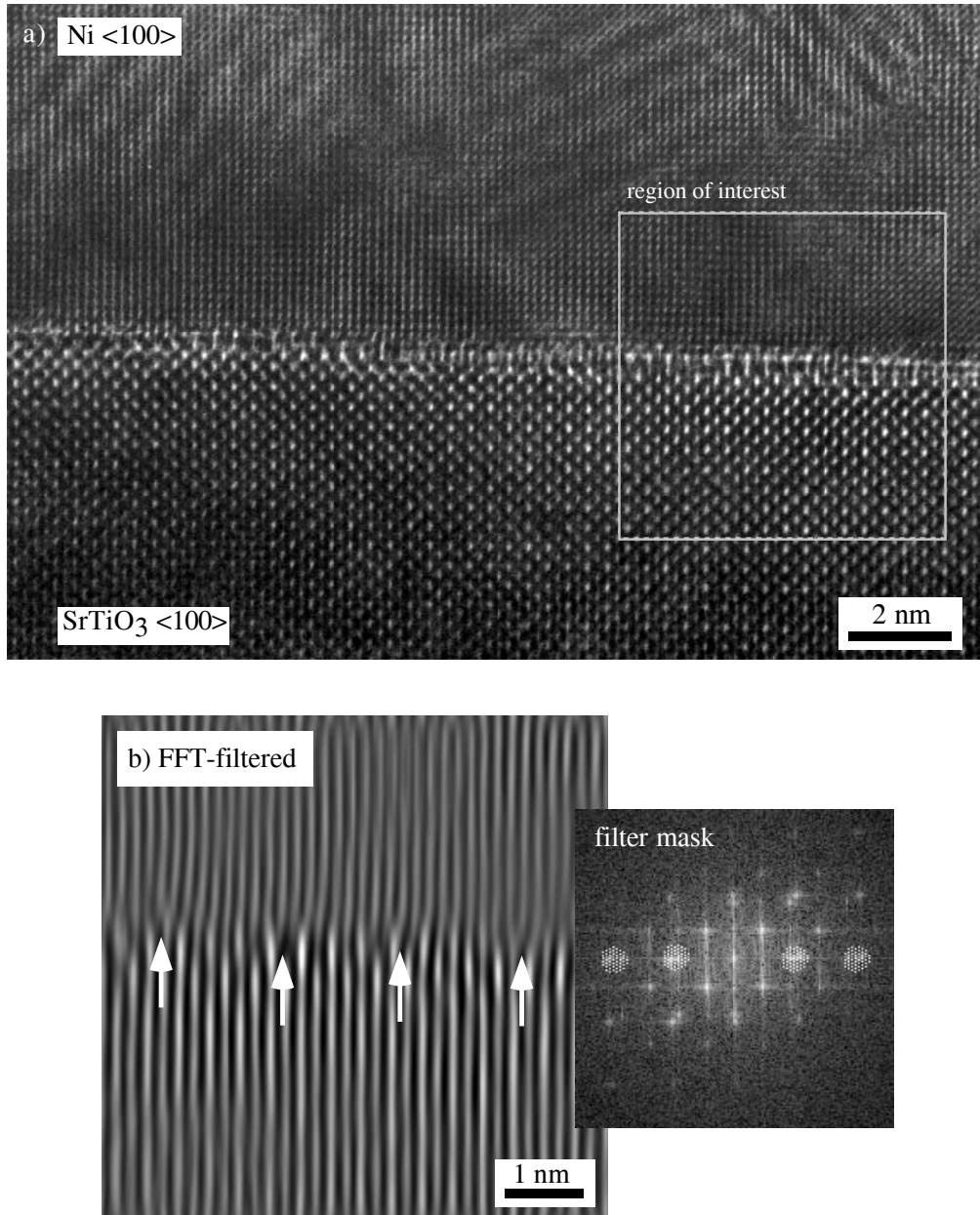


Figure 8.3: HRTEM micrograph of the Ni/SrTiO₃ interface in $\langle 100 \rangle$ zone-axis orientation. In b) the marked region of interest was Fourier-filtered in order to visualize the displacements of the lattice planes, which are perpendicular to the interface.

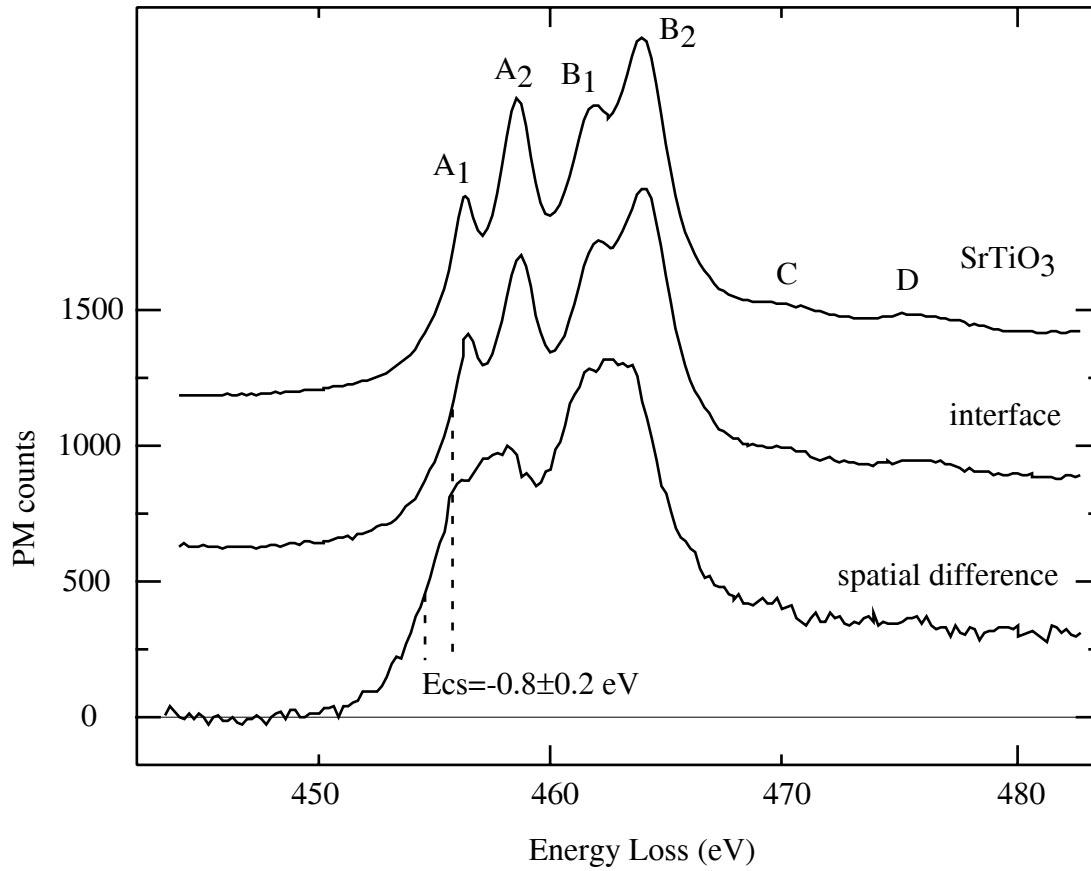


Figure 8.4: Ti $L_{2,3}$ -edges of the Ni/SrTiO₃ interfaces. Plotted are the edges measured in bulk SrTiO₃ (a) and in region containing the interface (b), together with the extracted interface specific component (c).

In Figure 8.4 three Ti $L_{2,3}$ -edges are plotted, one of bulk SrTiO₃, one recorded in a region which contains the Ni/SrTiO₃ interface, and the extracted interface specific ELNES component. The scaling factor used for the presented Ti $L_{2,3}$ -edges was $\mu = 0.18$. Peak splittings within the L-edges were determined by calculating the second derivative of the corresponding spectrum. In bulk SrTiO₃ the crystal field splitting of 2.4 eV is well resolved, while it is reduced to $1.5 \pm 0.2\text{ eV}$ for the interface specific component. Furthermore, the edge onsets of the interfacial Ti $L_{2,3}$ -edges are both shifted by $0.8 \pm 0.2\text{ eV}$ towards lower energy-losses. The spectral features labeled *C* and *D* in the bulk spectrum are not observable in the interface specific ELNES.

Figure 8.5 shows the O K-edges measured in bulk SrTiO₃, in a region containing the interface, and the interface specific ELNES component ($\mu = 0.18$), all extracted from the same set of data as the Ti $L_{2,3}$ -edges shown in Figure 8.4. The ELNES measured in a region containing the interface exhibits a line shape whose spectral features are significantly broadened compared to bulk SrTiO₃, resulting in a completely different ELNES line shape for the extracted interface specific component. The ELNES of the difference spectrum consists

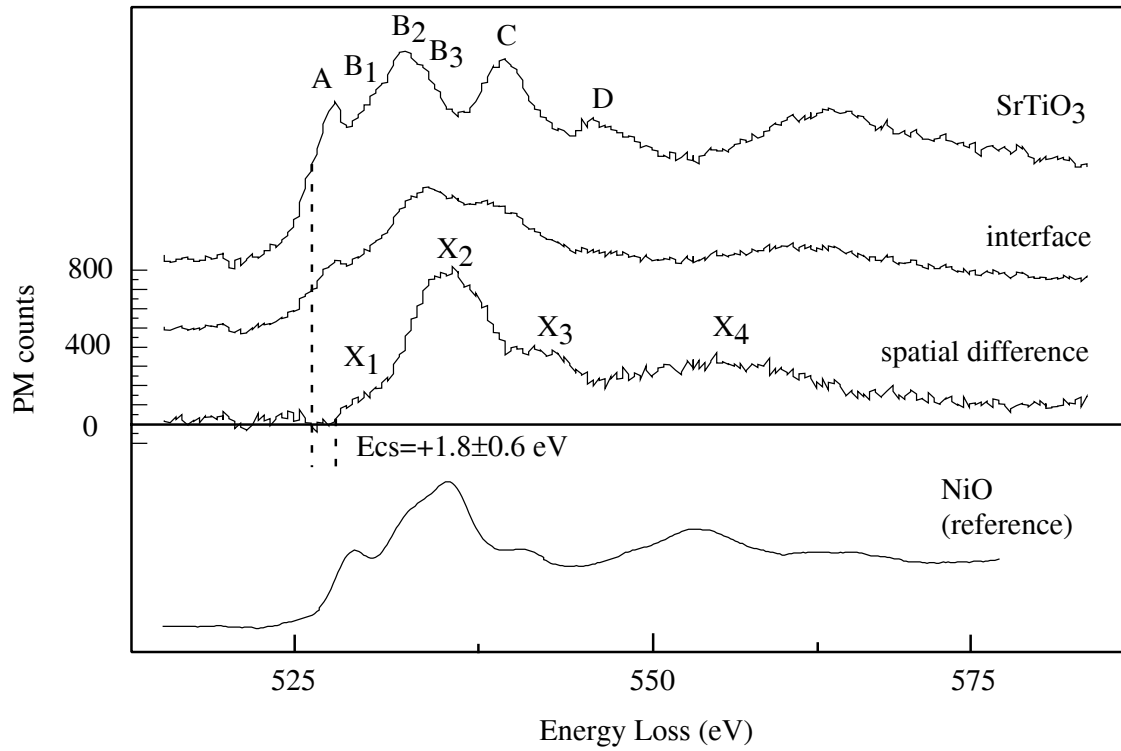


Figure 8.5: O K-edges of the Ni/SrTiO₃ interfaces. Plotted are the edges measured in bulk SrTiO₃ (a) and in a region containing the interface (b), together with the extracted interface specific component (c). A reference spectrum measured in a completely oxidized Ni film (d) is plotted in addition.

of four peaks X_1 , X_2 , X_3 , and X_4 , while X_1 appears as a broad shoulder at the edge onset. X_2 is the most intense ELNES peak, followed by a smaller peak X_3 and a broad feature labeled X_4 . Furthermore, the edge onset of the difference spectrum is shifted by 1.8 ± 0.6 eV towards higher energy-losses relative to the bulk O K-edge. As a reference, the O K-ELNES was measured in a completely oxidized Ni film under the same experimental conditions as the interface measurements. The experimental reference spectrum was calibrated on peak X_2 of the spatial difference spectrum. The extracted interface specific ELNES shows a similar line shape compared to the reference ELNES. After the calibration, the spectral features coincide in energy with the peaks X_1 and X_3 of the difference spectrum within uncertainties of ± 1.0 eV. Unlike in the interface specific ELNES component, X_1 appears as a pronounced peak in the reference ELNES.

Figure 8.6 shows the experimental EELS results for the Ni L_{2,3}-edges. All three spectra exhibit similar line shapes formed by the two white lines A and B and a small shoulder A' in between. Although the bulk ELNES and the interface specific ELNES are very similar, peak A' , which is clearly resolved within the Ni film is smeared out at the interface. Furthermore, the width of the white lines A and B , measured as the FWHM after fitting by a Lorentzian, is slightly increased in the interfacial ELNES compared to the bulk. The edge onsets of

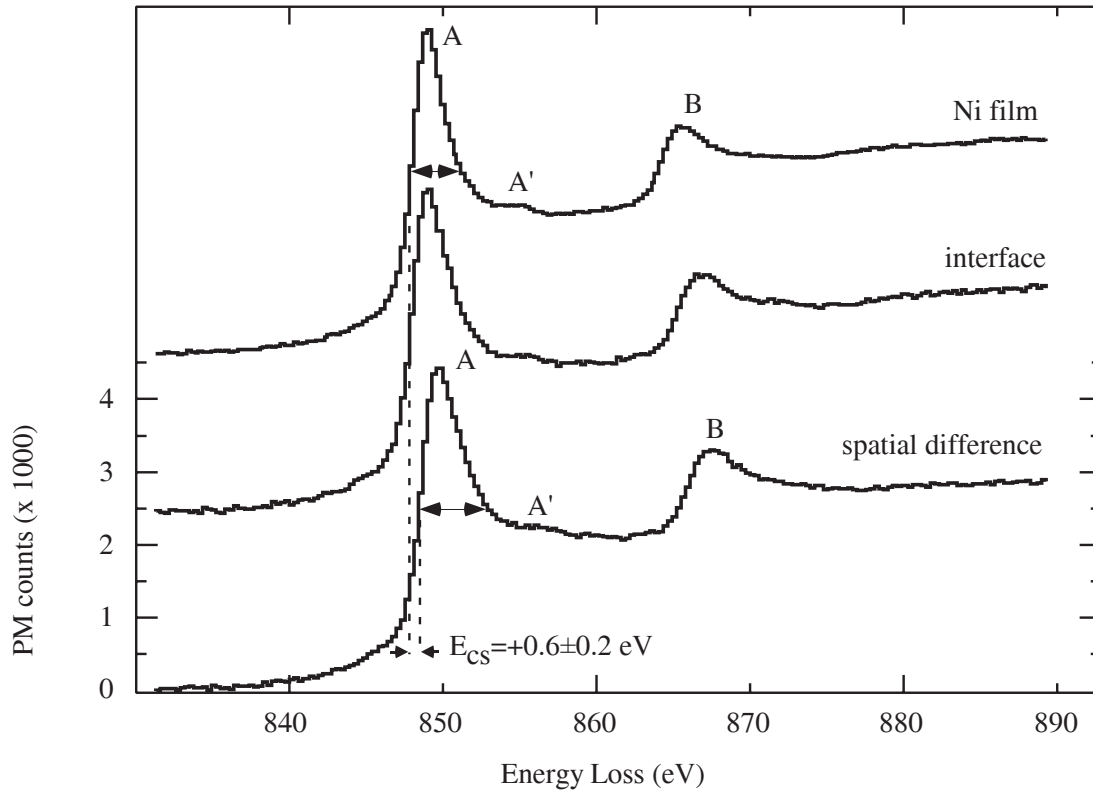


Figure 8.6: Ni $L_{2,3}$ -edges of the Ni/SrTiO₃ interfaces. Plotted are the edges measured in the nickel film (a) and in a region containing the interface (b), together with the extracted interface specific component (c).

both edges are shifted in energy by 0.6 ± 0.2 eV towards higher energy-losses. An analysis of the local integrated intensity ratios of the two white lines, the so-called L_3/L_2 intensity ratio, can give additional information about the local d-state occupancy and therefore also about the formal oxidation state of the corresponding transition metal. Since the $L_{2,3}$ -edge intensity is formed by a superposition of unoccupied s- and d-states, the intensity formed by the unoccupied s-states has to be extracted by fitting the edge intensity by the continuum intensities and extrapolating the fitted background under the white lines [Leapman, 1980] [Egerton, 1996]. The transition metal d-states are assumed to be localized only within the first 10 – 15 eV beyond the edge onset. In the literature there exist several different models to fit the continuum background of the $L_{2,3}$ -edges to finally calculate the integrated intensity ratios [Leapman, 1980] [van Aken, 1998] [Garvie, 1998]. In this work, L_3/L_2 intensity ratios were obtained by directly comparing the bulk and the difference spectra after normalization to the continuum background intensities. Then, peak intensities were integrated from energy intervals of 5 eV in width symmetrical to the peak maxima. The interfacial Ni $L_{2,3}$ -edge qualitatively shows a slightly decreased L_3/L_2 intensity ratio compared to the pure Ni film.

8.2 Computational Results

Ni atoms have a similar valence electronic structure as Pd and therefore the bonding characteristics of Ni and Pd to any other material are assumed to be similar. Both metals crystallize in the *fcc* structure. The CTEM investigations presented in section 8.1.1 have shown the same growth behaviour for Ni as for Pd on the (100)SrTiO₃ surface. For these reasons, the atomistic structure model for the Pd/SrTiO₃ interface was taken for PDOS calculations of the Ni/SrTiO₃ interface, i.e., the pseudopotentials were substituted in the calculation of the self-consistent lattice potential. In realistic calculations for the Ni/SrTiO₃ interface, the whole atomistic structure again has to be relaxed with respect to the total energy. An analysis of the forces on the different atoms present in the supercell for the Ni/SrTiO₃ interface only showed components along the *z*-axis, i.e., perpendicular to the interfacial plane. The maximum atom displacement caused by the maximum appearing force has a value of 0.24%, indicating only small stresses within the Ni/SrTiO₃ supercell. Thus, the use of the Pd/SrTiO₃ supercell from [Ochs, 2000] for band structure calculations for the Ni/SrTiO₃ interface seems to be a realistic approximation. For the Ni/SrTiO₃ interface no core-hole effects were considered in calculating the site projected PDOS, which are necessary for the interpretation of the Ti L_{2,3}-edges. However, as for the Pd/SrTiO₃ interface model, the *Z* + 1 approximation turned out not to be able to reproduce quantitatively the experimentally observed crystal field splitting. Since the atomistic structure of the Ni/SrTiO₃ interface is only approximated here, an additional approximation for the core-hole effects is regarded to be not very reliable. Therefore, only the calculated O p-PDOS for the Ni/SrTiO₃ interface is compared to the experimentally determined O K-edge.

Figure 8.7 shows the results of the O p-PDOS calculations for a) the interfacial O site, b) for a bulk-like O site within the interface supercell, and c) for an O site in bulk SrTiO₃. Similar to bulk SrTiO₃, the interfacial O p-PDOS exhibits two clearly resolved peaks *A* and *B*₂ at 2.3 eV and 7.0 eV above the Fermi level, respectively. In addition, a weak shoulder at 4.9 eV (*B*₁) appears at the interface. In the higher energy part of the interfacial O p-PDOS, the line shape is different from bulk SrTiO₃. Peaks are present in the energy regions marked in Figure 8.7a. In the first interval (1) a weak peak is observable for the interfacial site, which appears only as a shoulder in bulk SrTiO₃. In the neighbouring energy window (2) a peak is resolved in all three spectra, which is broadened at the interface compared to the more sharp feature in the bulk spectra. Within interval (3) a pronounced peak is observable again for both bulk SrTiO₃ and the interfacial O site. This feature overlaps with an additional interfacial peak appearing in interval (4). The bulk O p-PDOS line shapes do not show any peak in this energy regime. The interval labeled (5) exhibits a broad spectral feature throughout all O sites, which consists of a double peak in the bulk and a single peak at the interface.

For the discussed energy intervals marked in Figure 8.7, the spatial distribution of the corresponding unoccupied states throughout the used supercell was calculated, similar to the analysis of the O p-PDOS for the Pd/SrTiO₃. The results of these calculations are plotted in Figure 8.8 for a cut through a [010] TiO₂ plane together with the corresponding atomistic

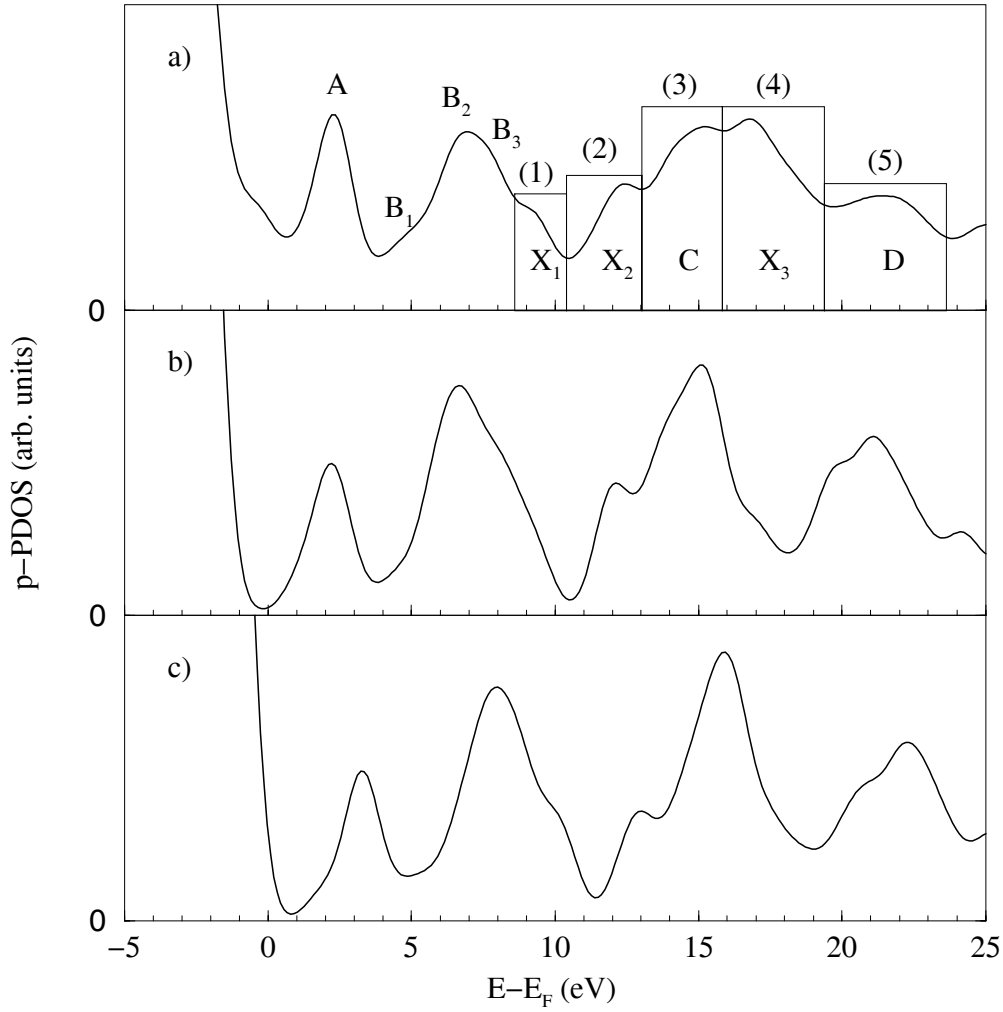


Figure 8.7: Calculated O p-PDOS for a) the Ni/SrTiO₃ interface (site 1' in Figure 7.11), and b) for site 4' in the same supercell with a TiO₂ terminated substrate. For comparison, in c) the corresponding O p-PDOS calculated in a pure bulk supercell is plotted.

structure model. For the intervals (1) and (2), the DOS distribution plots show an almost homogeneous intensity distribution throughout the supercell except from some additional intensities appearing at the interfacial Ti site. In interval (3), no localized interfacial DOS features are visible coinciding with the observations for the O p-PDOS in Figure 8.7. In interval (4), bulk SrTiO₃ intensities extend into the first Ni layer with a modified shape between the Ti sites and the Ni sites. Some additional intensity appears between the two Ni atoms in the first layer. For higher energies in the interval labeled (5), intensity is distributed homogeneously throughout the whole supercell. Therefore, in the intervals (1), (2), and (4) the DOS shows spectral features which are highly localized at or near the interfacial plane. A comparison of the calculated O p-PDOS and the experimentally determined O K-edge of

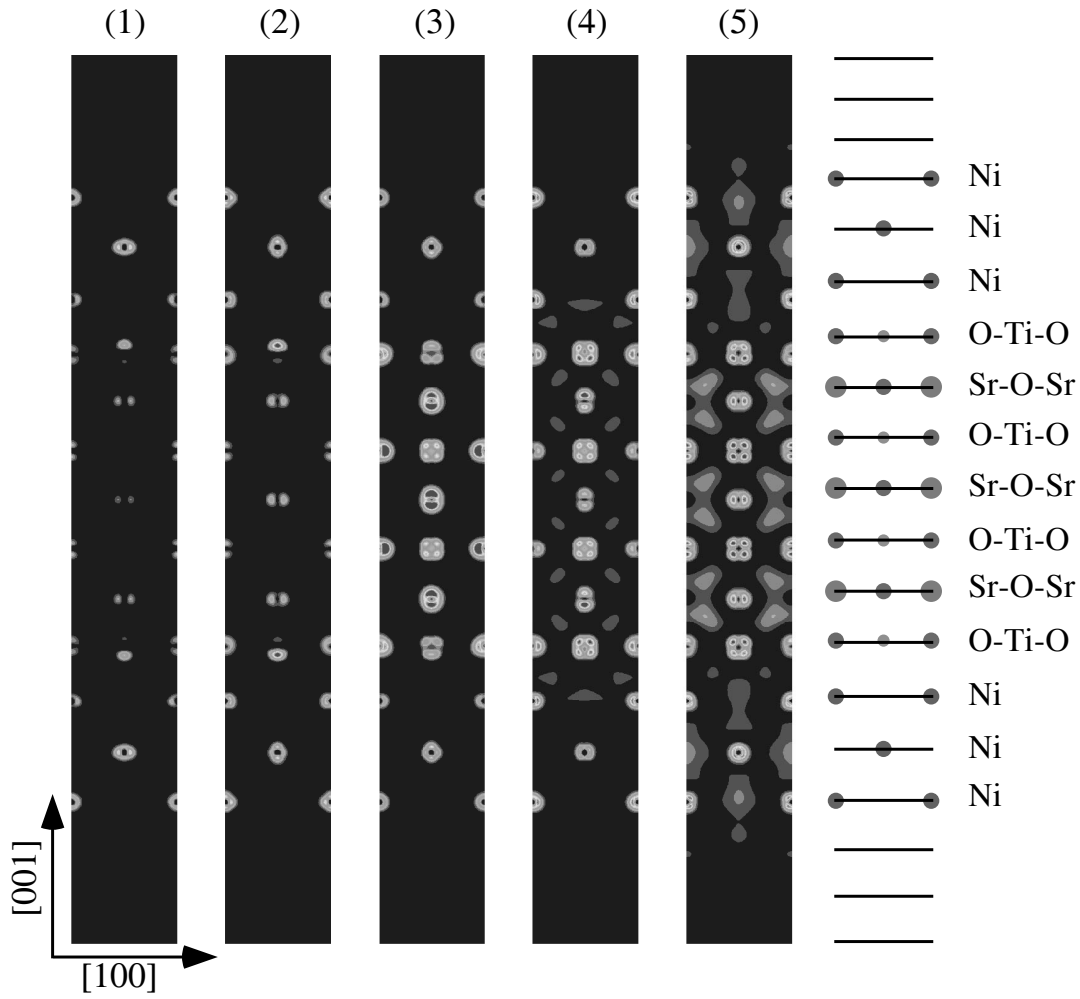


Figure 8.8: Spatial distribution of the local unoccupied O p-PDOS in a (020) plane of the supercell for five different energy regimes defined in Figure 8.7. Intensities are color coded, ranging from 0.025 electrons/Bohr³ to 0.125 electrons/Bohr³ in 11 steps.

the Ni/SrTiO₃ interface is given together with a detailed discussion in the section 8.3.2.

8.3 Discussion

For the O K-edge the experimental ELNES results are compared to theoretical results of the O p-PDOS. Based on the knowledge about the Pd/SrTiO₃ system, a model for the bonding between the Ni film and the SrTiO₃ substrate is developed.

8.3.1 Interface Structure

In situ RHEED investigations during film growth, SEM micrographs after the Ni deposition (cf. Figures 8.1a and 8.1b, respectively) as well as CTEM investigations of cross-sectional

prepared Ni/SrTiO₃ samples (cf. Figure 8.2) showed that Ni is growing 3-dimensionally as islands on the (100)SrTiO₃ surface at a substrate temperature of 650°C. These observations show that the formation of a free Ni surface is energetically preferred compared to the Ni/SrTiO₃ interface formation, as can be concluded from Young's equation 2.3. Regarding this, Ni islands also form {110}-facets in order to minimize the islands' surface energies.

The Ni film has a cube-on-cube epitaxy to the SrTiO₃ substrate. For this orientation relationship, the lattice mismatch is $m = -9.9\%$. HRTEM micrographs of the Ni/SrTiO₃ interface exhibit misfit dislocations in the Ni film. Only Ni planes close to the inserted atom plane show a curvature whereas planes with a larger distance from the inserted plane are straight. Due to the misfit dislocations, interfacial stresses caused by the lattice mismatch between the two materials are reduced. Thus, the observed Ni/SrTiO₃ has a semi-coherent interface structure (cf. section 2.1.3).

However, in the HRTEM micrographs of the interface some additional elongated bright contrasts perpendicular to the interfacial plane can be observed (cf. Figure 8.3a). Although no quantitative HRTEM investigations including image simulations were performed, these additional contrasts can be interpreted as originating from a local chemical reaction between Ni atoms and the SrTiO₃ surface. An extended reaction layer or a reaction phase at the interface could however not be observed in the experiment, which does not neglect the appearance of a 2-dimensional reaction layer in the interfacial plane of, e.g., NiO composition. Kennedy [Kennedy, 1995] and Jackson et al. [Jackson, 1998] demonstrated the formation of NiO/SrTiO₃ interfaces with a cube-on-cube orientation relationship. By XPS measurements, Kido and co-workers [Kido, 2000] observed a metallic nature of Ni for a coverage of the (100)SrTiO₃ surface by nominally 1 monolayer. Since they did not perform any bonding analysis on a microscopic scale, these results are not contrary to the formation of a 2-dimensional reaction layer.

8.3.2 ELNES-analysis: Experiment and Theory

A comparison of the experimentally determined interface specific O K-edge (cf. Figure 8.5c) with the calculated interfacial O p-PDOS (cf. Figure 8.7a) obviously shows completely different line shapes. This disagreement is not based on a lack of relaxation of the used atomistic structure model, as it could be excluded in section 8.2. The atomistic structure model is based on an abrupt interface between the (100)SrTiO₃ surface and a *fcc* Ni film, which need not to be the case for the Ni/SrTiO₃ interfaces. The experimental interface specific O K-ELNES shows a nearly identical line shape compared to the experimental reference spectrum recorded from an oxidized Ni island. For a more detailed analysis the O K-edge of bulk NiO was calculated as an additional reference using the MS approach. In this calculation, the core-hole effects were considered by the $Z + 1$ approximation. A cluster including 93 atoms was used for the multiple scattering calculation. The final result was broadened in energy using a Gaussian with an FWHM of 0.8 eV. In Figure 8.9 the experimentally determined interface specific ELNES component and the experimental reference ELNES (both from Figure 8.5) are plotted in comparison to the calculated NiO reference spectrum. All spectra shown

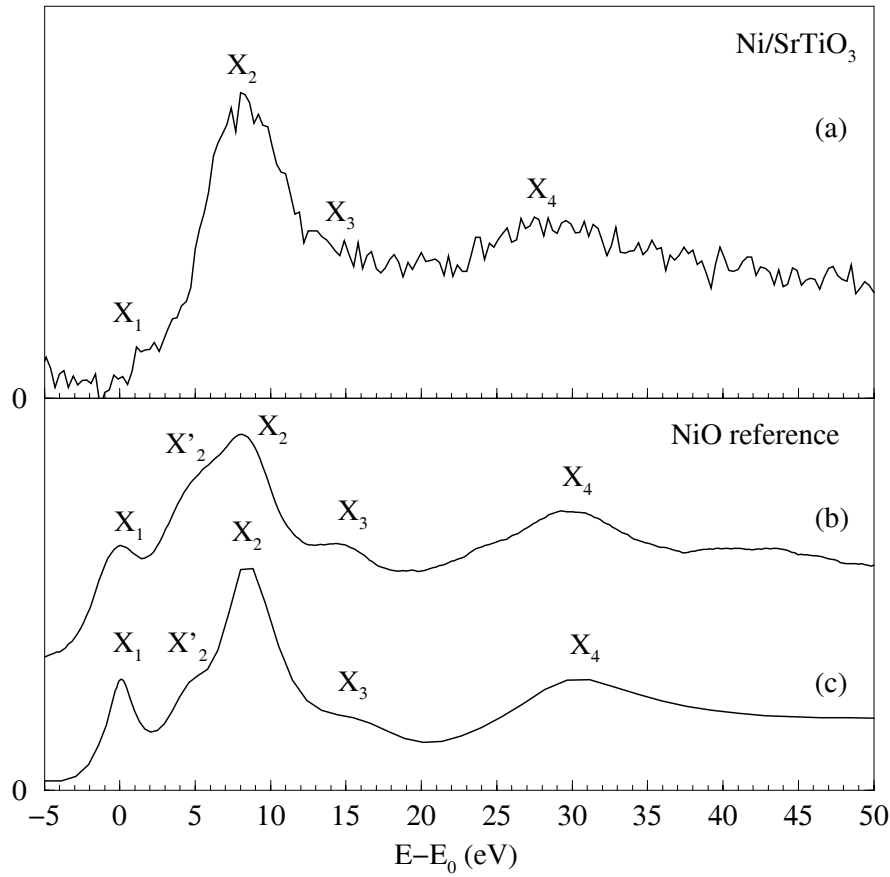


Figure 8.9: Comparison of the experimental (a) interface specific O K-ELNES component with an experimental (b) and a calculated reference spectrum (c) for bulk NiO.

in Figure 8.9 were energetically shifted to achieve a coincidence of the most intense ELNES peaks labeled X_2 , while the relative energy axis was calibrated with respect to the peaks labeled X_1 of the reference spectra. The calculated results for stoichiometric NiO (Figure 8.9c) reproduce the experimental ELNES line shape of the reference spectrum (Figure 8.9b), indicating the validity for using the experimental spectrum as a reference for NiO. Since the experimental interface specific O K-ELNES shows a nearly identical line shape compared to the experimental and theoretical references for bulk NiO (see Figure 8.9), the formation of Ni–O bonds at the interface can be concluded, which have a characteristic similar to bulk NiO. A possible description of this phenomenon can be the formation of a thin NiO layer at the Ni/SrTiO₃ interface, as it was already assumed in the discussion of the HRTEM micrographs. An oxidation of Ni would lead to a simultaneous reduction of Ti, which is indeed observed experimentally by a chemical shift of $E_{cs} = 0.8$ eV towards lower energy-losses for the interfacial Ti L_{2,3}-edges. Furthermore, the reduction of the interfacial Ti atoms also leads to a disturbed ligand field at the Ti site which can be the origin of the reduced crystal field splitting for the interfacial Ti L-edges.

For bulk NiO, Leapman and co-workers [Leapman, 1982] observed a chemical shift of the

Ni $L_{2,3}$ -edges towards lower energy-losses together with an increased L_3/L_2 -intensity ratio, both compared to bulk metallic Ni. In contrast to their observations, the presented experimental Ni $L_{2,3}$ difference spectrum shows a chemical shift towards higher energy-losses and slightly decreased L_3/L_2 -intensity ratio.

The reported methods to determine L_3/L_2 intensity ratios are based on the analysis of data originating from areas of identical specimen thicknesses and the use of exactly the same parameters for background fits and integration windows. Following these rules, the extracted absolute ratios are then only comparable to each other and cannot be used for a comparison with other data from the literature. The method used in this work is reliable since specimen thicknesses were identical in the observed specimen areas and only qualitative changes in the intensity ratios rather than quantitative data sets were determined. Systematic errors in the determination of the intensity ratios cannot be completely avoided, but they are the same for all analysed data and do therefore not lead to artificial results.

The chemical shift of the edge onset indicates an increased nominal oxidation state of Ni directly at the interface, which can only be due to an oxidation of the metal. A reduction in the nominal oxidation state of a metal would be physically meaningless. An oxidation of the Ni atoms at the interface can then be described by a hybridization of Ni-3d and O-2p orbitals. In this case, oxygen atoms surrounding Ni atoms of the first metal layer create a modified ligand field at the sites of the interfacial Ni atoms, forming an overall broadening of the Ni white lines, which is underlined by the experimental ELNES results. The decrease in the L_3/L_2 -intensity ratio is therefore caused by an overall broadening of the Ni d-PDOS due to the modified crystal field at the Ni/SrTiO₃ interface. In this argumentation, an amount of ionic bonding between the Ni film and the SrTiO₃ substrate can be neglected. From Figure 8.10 one can infer that a TiNi phase is present in the binary phase diagram for the Ni–Ti system above 630°C [Massalski, 1990], while Ti₂Ni and TiNi₃ phases exist also at lower temperatures (cf. Figure 8.10). Therefore, an intermetallic bonding between Ni and Ti across the interface is possible in general and cannot be neglected. Such a bonding may also cause some effects on the peak energies or the peak shapes of the Ni $L_{2,3}$ -edge.

In conclusion, it is assumed that a thin layer of NiO is formed at the interface which dominates the bonding between the Ni islands and the (100)SrTiO₃ surface. This thin NiO layer can be regarded as a 2-dimensional NiO phase in the interface plane. Kennedy [Kennedy, 1995] has shown the possibility of NiO growing epitaxially on the (100)SrTiO₃ surface, while Kido and co-workers [Kido, 2000] argue that one monolayer of Ni shows a metallic nature on the (100)SrTiO₃ surface. Their results from UPS measurements clearly show a broadening of the TiO₂ valence band together with a significant increase of intensity in the band gap region of bulk SrTiO₃. Therefore, an oxidation of Ni is present in their experiments although they do not comment on these effects. However, Kido et al. performed the Ni deposition at room temperature, whereas in the present study a substrate temperature of 650°C was used, for which the oxidation probability for Ni is higher.

The developed model for the bonding between thin Ni films on the (100)SrTiO₃ surface at a substrate temperature of 650°C is based on experimental observations. while for a more detailed analysis of the atomistic structure, the electronic structure and the bonding

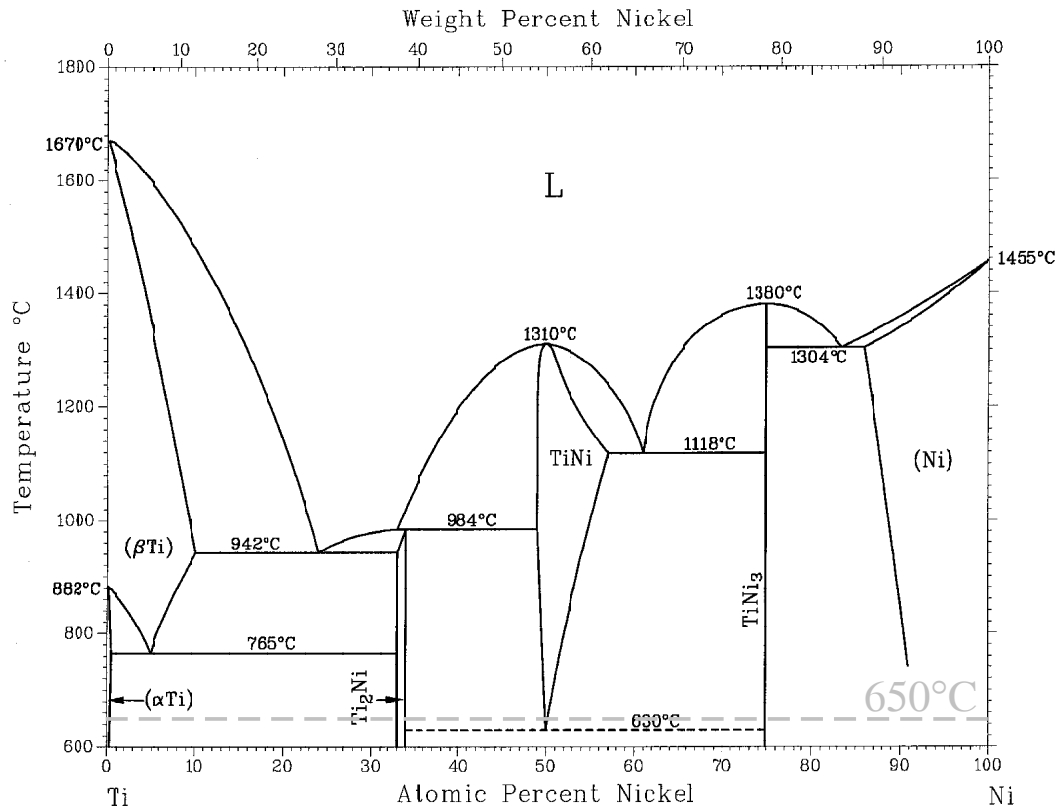


Figure 8.10: Binary phase diagram for the Ni-Ti system [Massalski, 1990].

characteristics at the Ni/SrTiO₃ interface, quantitative HRTEM studies and more intensive theoretical studies have to be performed. The latter should include the possibility of interface and interphase reactions across the Ni/SrTiO₃ contact.

Chapter 9

The Cr/SrTiO₃ Interface

As a third system, the Cr/SrTiO₃ interface was investigated experimentally by CTEM, HRTEM, and EELS/ELNES. Cr has a higher oxygen affinity than Ni and is therefore regarded as a reactive metal.

9.1 Experimental results

In contrast to Pd and Ni, Cr was deposited by MBE on the previously prepared (100)SrTiO₃ surface at a substrate temperature of $t_{\text{substrate}} = 65^\circ\text{C}$, close to room temperature. This relatively low temperature was chosen to avoid any temperature activated reactions of the first Cr layers with the substrate surface.

9.1.1 Diffraction and Imaging Studies

As it was reported for the previously described growth studies of Pd and Ni, during the Cr growth process *in situ* RHEED measurements were performed [Polli, 1998] [Fu, 2001]. Figure 9.1 shows RHEED patterns in the $\langle 110 \rangle$ azimuth after a Cr deposition of nominally 0 nm (pure (100)SrTiO₃ surface), 1.0 nm, and 21.0 nm. After depositing nominally 1.0 nm, the SrTiO₃ surface RHEED pattern is superimposed by a pattern of bright diffraction spots, which show a geometry similar to a diffraction pattern in transmission electron diffraction, indicating a 3-dimensional growth mode of the Cr film. The RHEED pattern after a Cr deposition of nominally 21.0 nm still shows a spot pattern similar to that previously described, but some additional lines appear which resemble a poly-crystalline fraction of Cr on the sample surface. Parallel STM studies by Polli [Polli, 1998] and Fu [Fu, 2001] show a significantly higher nucleation density than for Ni, and therefore also an increased island density compared to Ni and Pd [Polli, 1998] [Fu, 2001].

Figure 9.2a is a typical bright field CTEM micrograph of the Cr/SrTiO₃ interface recorded in $\langle 100 \rangle$ zone-axis orientation for bulk SrTiO₃. After a deposition of nominally 35 nm Cr on the (100) substrate surface, continuous Cr layers were observed by conventional TEM (cf. Figure 9.2a) after a cross-sectional preparation of the Cr/SrTiO₃ interface. From the selected

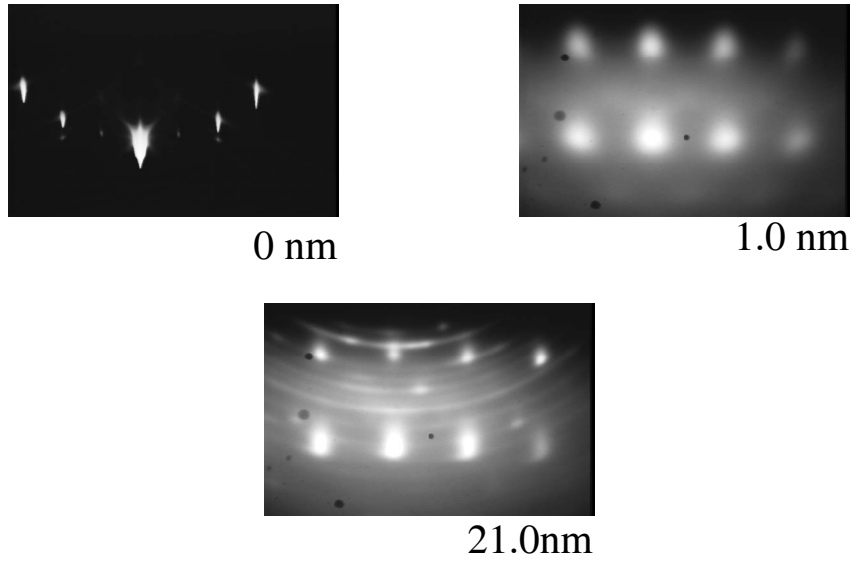


Figure 9.1: *In situ* RHEED patterns of Cr/SrTiO₃ in the (001) azimuth after deposition of nominally 0 nm, 1.0 nm, and 21.0 nm Cr on the (100)SrTiO₃ surface at a temperature of 65°C.

area diffraction pattern of the Cr/SrTiO₃ interface in Figure 9.2b and 9.2c, one can infer an epitaxial orientation relationship between the Cr film and the SrTiO₃ substrate. The Cr unit cell is rotated by 45° around the interface normal. Therefore, the $\langle 110 \rangle$ directions in Cr are parallel to the $\langle 100 \rangle$ directions of the SrTiO₃, whereas the $\{100\}$ planes of both film and substrate are parallel to each other:

$$[110](100)_{Cr} \parallel 100_{STO}. \quad (9.1)$$

This result is in agreement with previous investigations by Polli and Wagner [Polli, 1998]. Other orientation relationships, especially any poly-crystalline structures, could not be revealed from the investigated samples.

A typical HRTEM micrograph of the Cr/SrTiO₃ interface recorded in $\langle 100 \rangle$ zone-axis orientation for SrTiO₃ is shown in Figure 9.3a. One can observe the typical spot pattern of a *bcc* material in the $\langle 110 \rangle$ zone-axis orientation simultaneously with the $\langle 100 \rangle$ HRTEM spot pattern for bulk SrTiO₃, indicating the already observed orientation relationship given in 9.1. The HRTEM micrograph exhibits an abrupt interface between the Cr film and the SrTiO₃ substrate without the presence of any reaction phase at the interface. In Figure 9.3b a Fourier filtered image of a part of the HRTEM micrograph is shown to demonstrate the curvature of the lattice planes close to inserted atom planes. At the interface one can observe additionally inserted lattice planes within the SrTiO₃, which are marked by arrows in Figure 9.3b. Between the inserted planes the interface structure is almost coherent. Therefore, misfit dislocations locally compensate for strains in SrTiO₃. The distance between two misfit dislocations follows from the lattice misfit of $m = +4.3\%$, i.e., approximately every 25th lattice

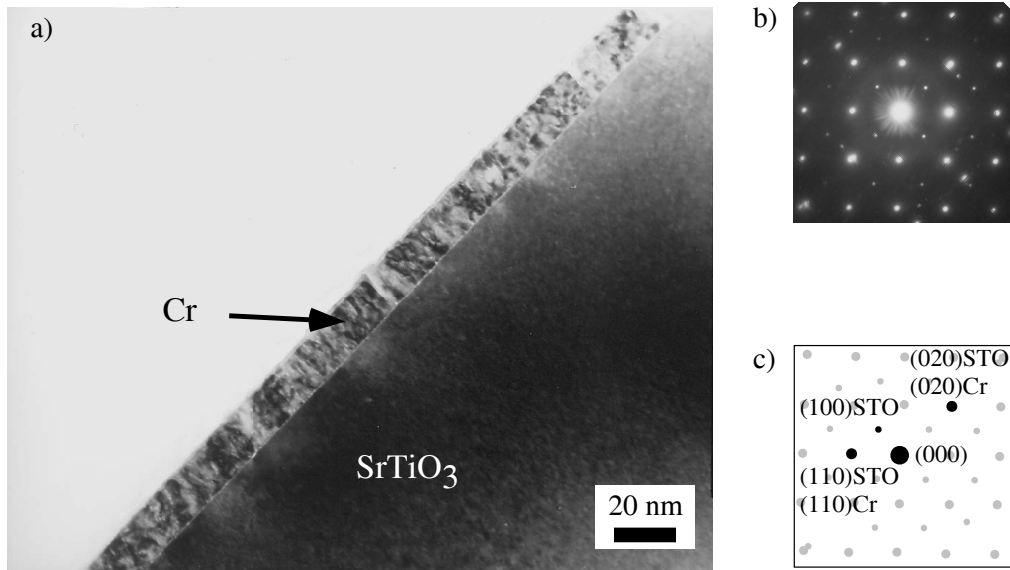


Figure 9.2: Conventional TEM investigations of the Cr/SrTiO₃ interface, showing a) a micrograph of a continuous Cr film on the (100)SrTiO₃ surface, and b) selected area diffraction patterns to determine the orientation relationship (c) between the Cr film and the SrTiO₃ substrate.

plane a misfit dislocation is present at the interface. The distance between the marked areas in Figure 9.3 corresponds to 26 – 27 lattice planes of SrTiO₃, which is close to the expected value. By analysing multiple HRTEM images, the mean value for the distance between two misfit dislocations reaches the expected value of 25. Thus, the Cr/SrTiO₃ interface possesses a semi-coherent interface structure.

9.1.2 EELS Results

ELNES measurements of the Ti L_{2,3}-, the O K-, and the Cr L_{2,3}-edges were performed following the rules described in section 4.1.2. Scanning areas of $2 \times 20 \text{ nm}^2$, $1 \times 10 \text{ nm}^2$ and $3 \times 4 \text{ nm}^2$ were used with energy dispersions of 0.1 eV/channel and 0.2 eV/channel. Since the edge onset of the Cr L₃-edge is at an energy-loss of 575 eV, the simultaneous recording of all three absorption edges becomes possible by using an energy dispersion of 0.2 eV/channel. In this energy regime, the Ti L₁-edge at an energy-loss of 564 eV overlaps with the O K-edge and causes problems for the background fit for the Cr L_{2,3}-edge. Due to the overlap of the Cr L_{2,3}-edge with the O K-edge and the Ti L₁-edge, the background intensity was fitted only in a small 5 eV-wide energy interval in front of the Cr L₃ edge onset, where the continuum intensities of the O K-edge are regarded to be constant and therefore any effects of edge overlap on the background fit can be neglected. Since only ELNES features within the first

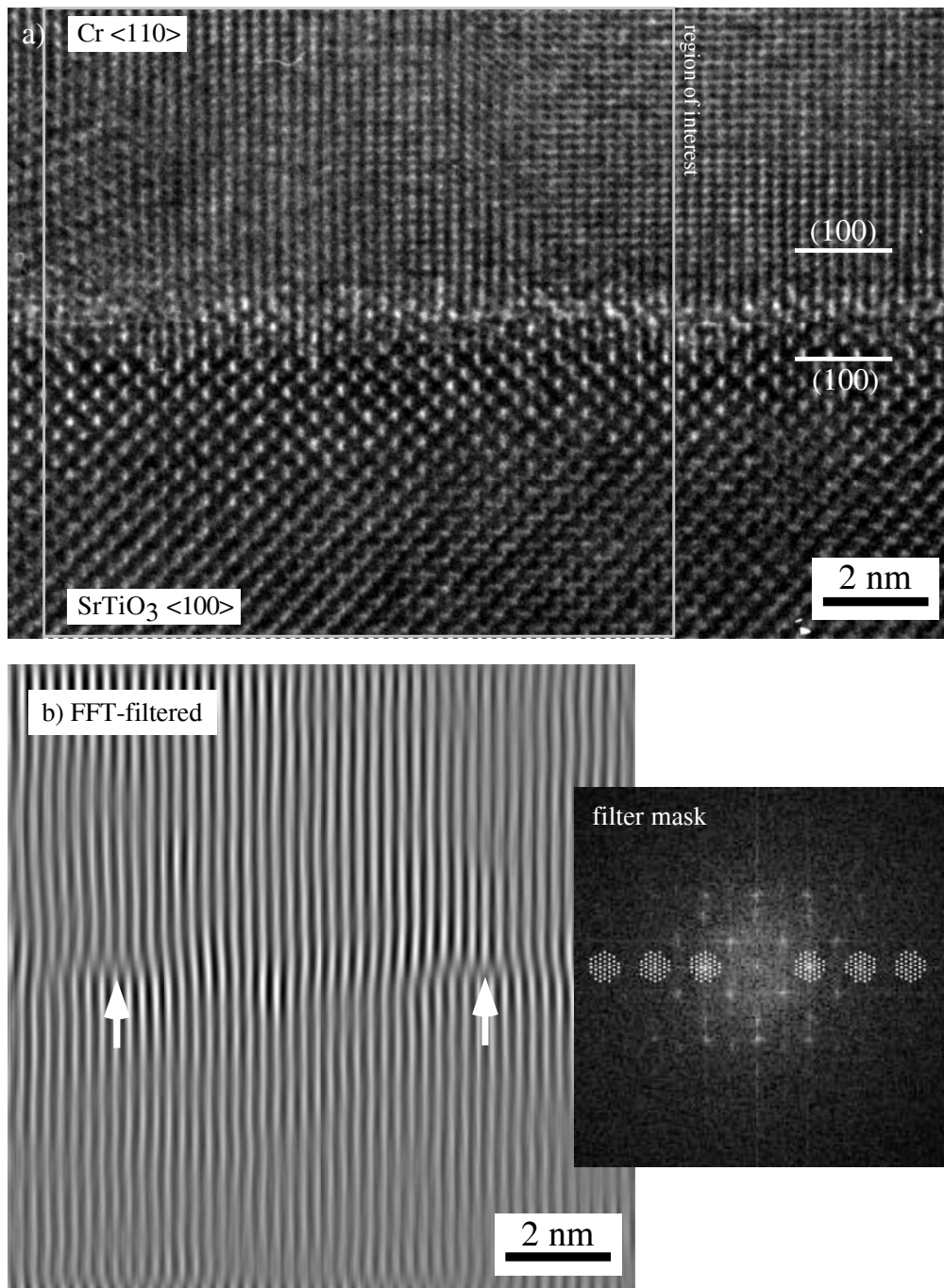


Figure 9.3: HRTEM micrograph of the Cr/SrTiO₃ interface in $\langle 100 \rangle$ zone-axis orientation. In b) the marked region of interest was Fourier-filtered in order to visualize the displacements of the lattice planes, which are perpendicular to the interface.

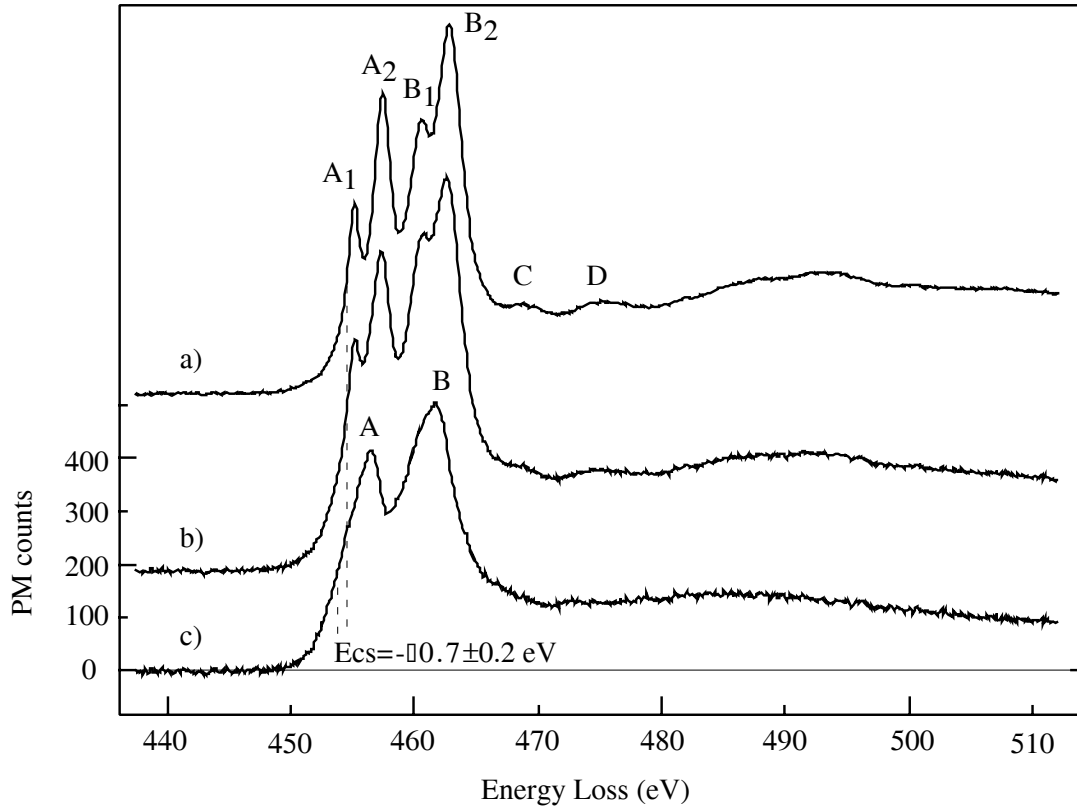


Figure 9.4: Ti L_{2,3}-edges of the Cr/SrTiO₃ interfaces. Plotted are the edges measured in bulk SrTiO₃ (a) and in region containing the interface (b), together with the extracted interface specific component (c).

20 eV–25 eV beyond the edge onset are analysed, edge overlaps are of minor importance in this case. Besides that, in the current study, mainly peak energies rather than absolute peak intensities are analysed.

In Figure 9.4 the Ti L_{2,3}-edges recorded for the Cr/SrTiO₃ interface are plotted. The interface specific Ti L_{2,3}-ELNES (c) was extracted from the spectrum recorded in the interfacial region (b) by the spatial difference method using a scaling factor of $\mu = 0.21$. For each Ti L-edge, the difference spectrum exhibits one broad peak (A for the L₃-edge and B for the L₂-edge) instead of two clearly resolved peaks as in bulk SrTiO₃, which are separated by the 2.4 eV crystal field splitting. Calculating the second derivatives of the difference spectra one can observe that in the interface specific ELNES, each of the Ti L-edges is formed by two peaks separated by 1.6 ± 0.2 eV. Therefore, a reduction of the crystal field splitting of the Ti e_g and t_{2g} states of 0.8 ± 0.2 eV is observed at the interface compared to bulk SrTiO₃. In addition, the interface specific component of the Ti L_{2,3}-edges is shifted by 0.7 ± 0.2 eV towards lower energy-losses. Peaks C and D visible in the bulk ELNES are no longer clearly resolved in the difference spectrum.

The results, which were obtained for the O K-edges at the Cr/SrTiO₃ interface are

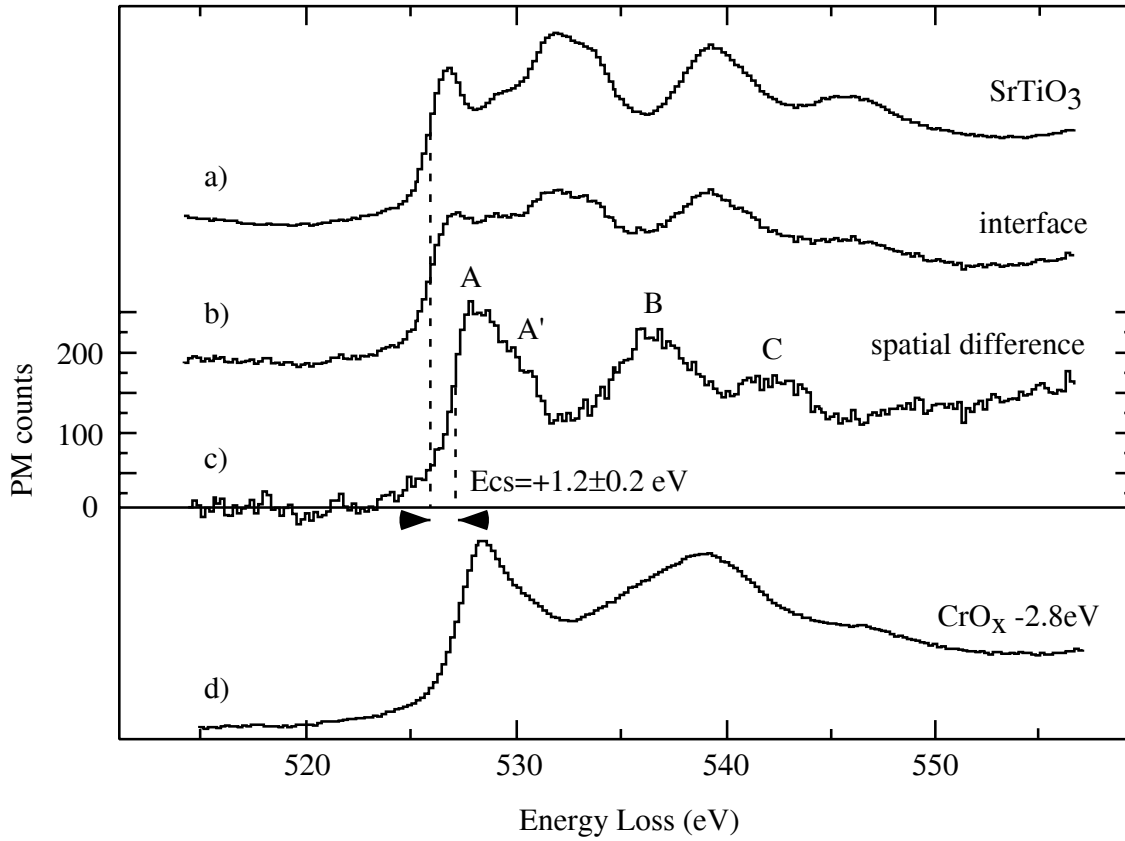


Figure 9.5: O K-edges of the Cr/SrTiO₃ interfaces. Plotted are the edges measured in bulk SrTiO₃ (a) and in a region containing the interface (b), together with the extracted interface specific component (c). A reference spectrum measured in a completely oxidised Cr film (d) with a composition of CrO_x is plotted in addition.

plotted in Figure 9.5. Similar to the Ni/SrTiO₃ interface, the difference spectrum of the O K-edge shows a completely different line shape than in bulk SrTiO₃, which was already indicated by the spectrum measured in the interface region. The interface specific ELNES of the O K-edge is dominated by 3 peaks *A*, *B* and *C*, while peak *A* exhibits a shoulder *A'* at an energy-loss of 531 eV on its high energy-loss wing. Peaks *B* and *C* occur at energy-losses of 532 eV and 537 eV, respectively. For the O K-edge, the interface specific component is shifted by 1.2 ± 0.2 eV towards higher energy-losses. Figure 9.5d shows the O K-edge measured in a completely oxidised Cr film. This ELNES line shape is in good agreement with O K-edges measured for hexagonal Cr₂O₃ and cubic CrO₂ by de Groot et al. [de Groot, 1989] and Manoubi et al. [Manoubi, 1990]. Although the O K-ELNES line shapes of these materials are not identical with the interface specific component of the Cr/SrTiO₃ interface (Figure 9.5c), similarities for peak *A* are clearly observable between the spectra 9.5c and 9.5d, as far as the edge onset and the asymmetric peak shape are concerned. In the energy regime where the difference spectrum shows two peaks *B* and *C*, the oxidic reference spectrum shows a broad feature with its maximum in between the energy positions of peaks *B* and *C*. The edge onset

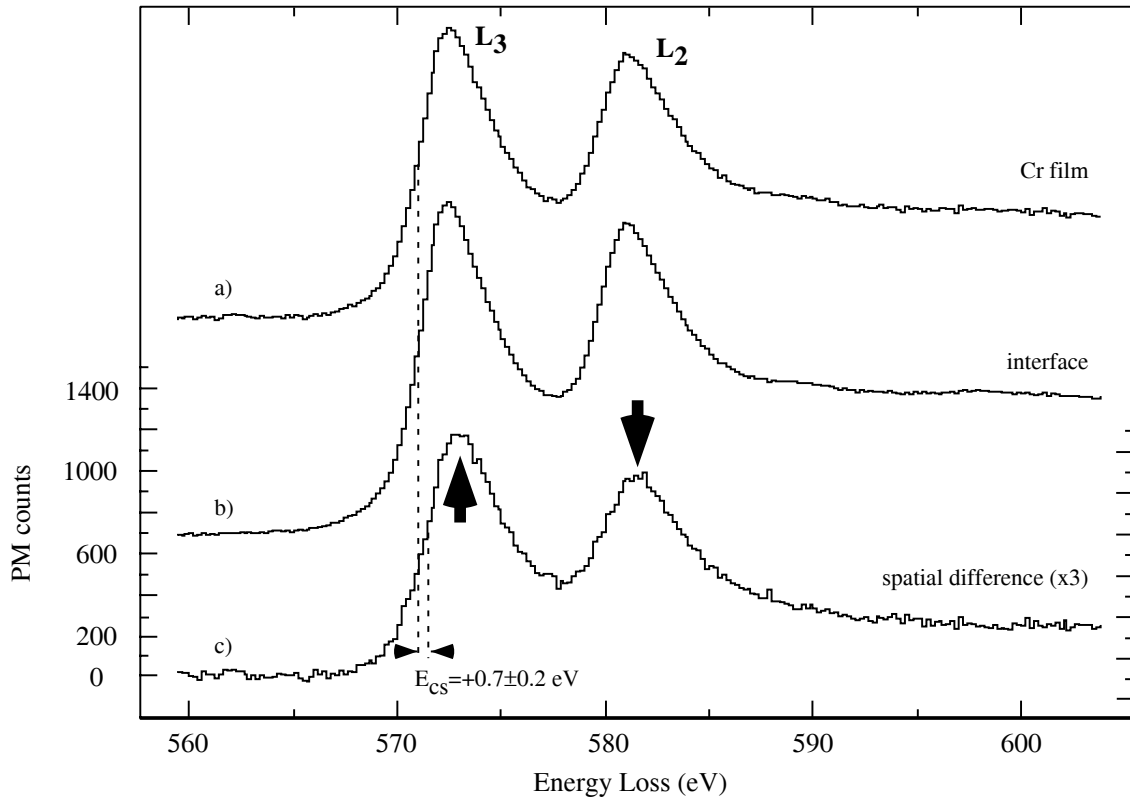


Figure 9.6: Cr $L_{2,3}$ -edges of the Cr/SrTiO₃ interfaces. Plotted are the edges measured in the chromium film (a) and in a region containing the interface (b), together with the extracted interface specific component (c).

of the difference spectrum has undergone a chemical shift and is positioned in between the edge onset energies for bulk SrTiO₃ and the oxidised Cr layer.

Figure 9.6 shows the experimental ELNES results for the Cr $L_{2,3}$ -edge. For the interface specific ELNES component the same white line shapes are observed as in the Cr film some 10 nm away from the Cr/SrTiO₃ interface. However, the edge onsets are both shifted by 0.7 ± 0.2 eV towards lower energy-losses compared to metallic chromium. A qualitative comparison of the L_3/L_2 intensity ratios, determined as discussed in section 8.3.2, shows an increase at the interface compared to the metallic Cr film. The widths of the white lines remain unchanged at the interface.

9.2 Discussion

In the following, the experimental results obtained for the Cr/SrTiO₃ interface are discussed in detail. Since no calculated results exist, a model to describe the bonding between the film and the substrate is developed only on the basis of the experimental observations. However, in a parallel study the Mo/SrTiO₃ interface was investigated theoretically by *ab initio* band

structure calculations [Classen, 2001a]. Since the valence electronic structure of Cr is similar to that of Mo, the results of the Mo/SrTiO₃ calculations can be used in the future to analyse the Cr/SrTiO₃ interface theoretically in a similar way as it was done for the Ni/SrTiO₃ interface.

9.2.1 Interface Structure

In situ RHEED observations during the MBE growth process revealed a 3-dimensional growth mode for Cr on the (100)SrTiO₃ surface at 65°C. An island formation was also observed by STM studies of samples with a low Cr coverage, whereas CTEM investigations revealed a continuous Cr film after a deposition of nominally 35 nm. Therefore, one can conclude that near room temperature, Cr grows in a 3-dimensional mode (Volmer-Weber growth mode) on (100)SrTiO₃ surfaces with a high density of nucleation sites and therefore also with a higher island density compared to Ni and Pd. A further deposition of Cr leads to coalescence processes of the different islands and finally to the formation of a continuous Cr layer. However, this growth behaviour indicates that for larger Cr clusters the interface energy $\gamma_{sf,Cr}$ is smaller than the free surface energy $\gamma_{fv,Cr}$ for Cr clusters and therefore Cr grows laterally on the surface rather than vertically. A more detailed investigation of the growth behaviour of Cr on the (100)SrTiO₃ surface is given by Fu and co-workers [Fu, 2001], who also included the effects of the different substrate temperatures in their investigations. They found epitaxial metallic Cr layers for substrate temperatures up to 640°C. The orientation relationship between the film and the substrate given in equation 9.1 was found to be stable for substrate temperatures up to 280°C. Above this temperature range O ions become mobile, which lead to an oxidation of the Cr layers. Above 700°C interdiffusion processes of Ti and Cr were observed [Fu, 2001].

During the whole growth process an epitaxial orientation relationship was observed in which the Cr lattice is rotated by 45° around the interface normal compared to a cube-on-cube orientation. This orientation relationship is energetically preferred against the cube-on-cube epitaxy since the lattice mismatch of $m = +4.3\%$ between the film and the substrate is significantly smaller in this configuration. For the continuous film this orientation relationship is predominant, although some polycrystalline components of the film were observed by RHEED.

Recording images of the interface with TEM under high resolution conditions, it could be shown that a semi-coherent interface between *bcc* Cr and the (100)SrTiO₃ substrate is formed. This observation is based on the appearance of localized misfit dislocations within the interfacial plane, as Figure 9.3b demonstrates. In the HRTEM micrographs, no reaction phase or reaction layer could be observed by a qualitative image analysis. Therefore, the interface seems to be abrupt which can only be proved by a quantitative HRTEM analysis including image simulations using a previous theoretically determined atomistic structure model of the Cr/SrTiO₃ interface.

9.2.2 ELNES-analysis

The crystal field splitting in bulk SrTiO₃ within the Ti L₃- and the Ti L₂-edges of 2.4 eV is strongly reduced by 0.6 ± 0.2 eV directly at the interface (cf. Figure 9.4). This indicates a disturbance of the ligand field for Ti at the interfacial sites. This effect is however expected for the interfacial Ti sites since the surrounding octahedron of O atoms is replaced on one side by the Cr film. The interface specific Ti L_{2,3}-edges show a chemical shift of 0.7 ± 0.2 eV towards lower energy-losses. Leapman et al. [Leapman, 1982] have ascribed this phenomenon to a reduction of the nominal oxidation state for Ti. They observed a chemical shift of 1.0 eV for Cr₂O₃ compared to metallic Cr. In the framework of the Cr/SrTiO₃ interface, the experimentally observed chemical shift also indicates a nominal reduction of the interfacial Ti atoms. This can be interpreted that Cr forms a bonding with the interfacial O atoms of the first substrate layer. Therefore, interfacial Ti atoms and Cr atoms share the interfacial O atoms so that nominally less O atoms participate in a bonding to interfacial Ti atoms.

The interfacial O K-ELNES shows a completely different line shape compared to bulk SrTiO₃, indicating that the unoccupied O p-PDOS changes drastically at the interface. However, no direct conclusions can be drawn for the local 3-dimensional band structure at the Cr/SrTiO₃ interface based on these observations. A comparison of the difference spectrum with the O K-ELNES of a chromium oxide of CrO_x composition shows similarities in the line shape of the first ELNES peak labeled *A*. Since the edge onset is sensitive on the coordination of the excited atom, one can conclude that at the Cr/SrTiO₃ interface, Cr–O bonds are formed by an O-2p–Cr-3d hybridization. The bonding characteristic seems to be similar to those in CrO_x compounds. This is also underlined by the chemical shift of the interfacial O K edge onset, which is energetically situated between the edge onsets for bulk SrTiO₃ and for the different chromium oxides. Therefore, the assumption of an oxidation of Cr at the interface with a simultaneous nominal reduction of Ti can also be stated on the basis of the O K-edge analysis. The formation of the peaks *B* and *C* in the interface specific O K-ELNES can only be understood in detail by an analysis of theoretically determined PDOS, which were not available in the current study. However, it can be assumed that the origin of the corresponding states is a modified crystal field at the interfacial O site, similar to that observed for the Pd/SrTiO₃ interface.

As in the metallic Cr film, the Cr L_{2,3} spatial difference spectrum (cf. Figure 9.6) exhibits two white lines which are energetically shifted by 0.7 ± 0.2 eV towards higher energy-losses. The L₃/L₂ intensity ratio is increased at the interface compared to the metallic Cr film, indicating a decreased number of electrons at the Cr sites and therefore an electron transfer from the lower Cr-3d levels to the O-2p levels. The chemical shift of the Cr L_{2,3}-edges reflects an increased nominal oxidation state of Cr at the Cr/SrTiO₃ interface [Leapman, 1982].

To summarize, based on a detailed analysis of the experimental ELNES spectra of the Cr/SrTiO₃ interface, Cr is found to form bonds to O atoms of the substrate surface. An oxidation of Cr atoms on the costs of the nominal Ti oxidation states is found indicating a reduced bonding of Ti–O in the substrate surface and a hybridization of Cr-3d and O-2p states. The Cr–O bonds across the interface show a mixed ionic–covalent character due to

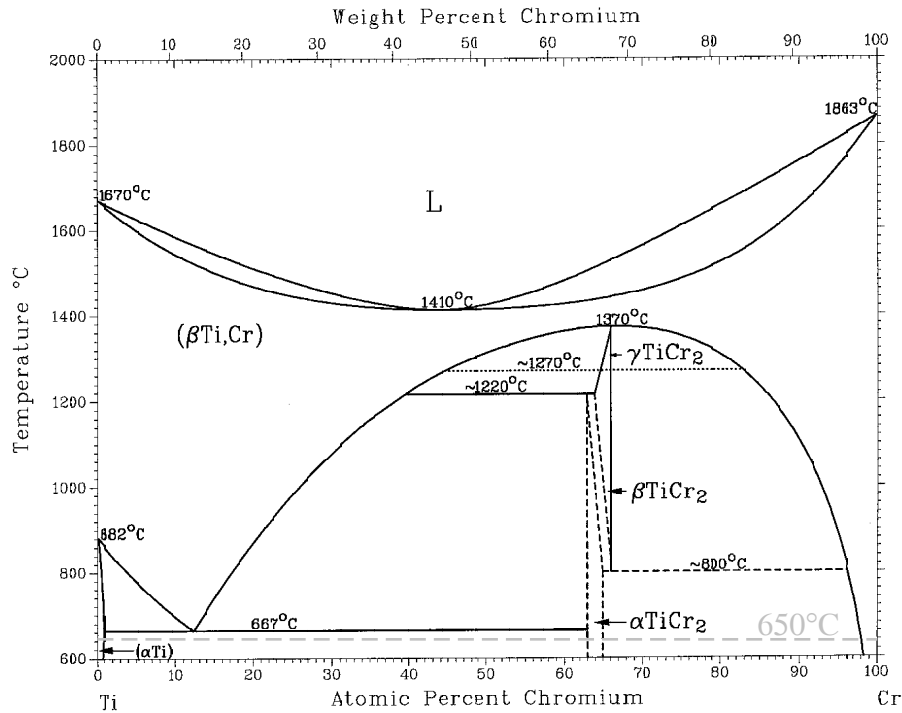


Figure 9.7: Binary phase diagram for the Cr–Ti system [Massalski, 1990].

the observed electron transfer from Cr to O. In many cases, intermetallic bondings stabilize the adhesion between metallic films and oxidic substrates [Tanaka, 1998], as was also found for the Pd/SrTiO₃ in section 7.3.3. In Figure 9.7 the binary phase diagram is plotted for the Cr–Ti system. Although an intermetallic Cr–Ti bonding is possible, like in the α – $TiCr_2$ phase at low temperatures, evidence for such a bonding can only be given by a parallel investigation using *ab initio* band structure calculations, which were not performed with this study.

In *in situ* heating experiments on the Cr/SrTiO₃ interface, Cr was found to diffuse into the substrate where it probably forms a ternary oxide with Ti [Tsukimoto, 2001]. However, at substrate temperatures of 65°C, the diffusion coefficient of Cr in single crystalline SrTiO₃ is expected to be so small that diffusion processes do not play a role [Fu, 2001].

Chapter 10

Final Discussion

In this chapter an overall discussion is given concerning the performed investigations on bulk SrTiO_3 and on the different metal/ SrTiO_3 interfaces investigated in this thesis.

10.1 Bulk SrTiO_3

For bulk SrTiO_3 the influences of the core-hole effects on the experimental Ti $L_{2,3}$ -, the O K-, and the Sr $L_{2,3}$ -edges were investigated theoretically by the so-called $Z + 1$ approximation. The final result is, that the consideration of core-hole effects is crucial for an understanding and interpretation of the Ti $L_{2,3}$ - and the O K-absorption edges in the electron energy-loss spectrum. For the Sr $L_{2,3}$ -edges no necessity of including core-hole effects into the calculations was found due to both, a high screening of the electron hole by the remaining core electrons, and the experimental energy resolution limits. Only by consideration of the core-hole effects for the absorbing atom, the 2.4 eV crystal field splitting of the Ti t_{2g} and e_g states, which is observable in the experiment, can be reproduced by the LDFT calculations. Therefore, the ELNES line shape with a peak separation of the 2.4 eV can be understood as a quantum-mechanical effect due to an interaction of the local band structure of the specimen and the measuring process itself, which is in agreement with previous investigations [de Groot, 1994] [Mo, 1999] [Ogasawara, 2001]. The crystal field splitting in relaxed bulk SrTiO_3 was calculated to be 1.7 eV. Ogasawara and co-workers were able to achieve an even higher reproducibility of the experimental Ti $L_{2,3}$ -edges by an atomic multiplet many-body calculation, in which configuration interactions are additionally considered. Using this approach not only peak positions but also relative peak intensities are reproduced excellently. For the O K-edge in bulk SrTiO_3 , core-hole effects also play an important role for a reliable ELNES interpretation, especially as far as the energy regime within the first 8 eV beyond the edge onset is concerned. Without considering any core-hole effects a small but significant spectral feature labeled B_1 in Figures 6.14 and 6.9 does not appear in the LDFT calculations of the O p-PDOS. In the $Z + 1$ approximation an additional peak occurs in the calculated O p_x -PDOS which coincides in energy with the experimental peak B_1 . Furthermore, the asymmetric ELNES line shape formed by the peaks B_i and the asymmetry of peak C are better

reproduced than without inclusion of the core-hole effect. From a more detailed analysis of the calculated PDOS, it could be concluded that the core-hole effect is dominantly affecting the O–Ti bonds and therefore shows an anisotropic shape. The $Z+1$ approximation seems to still underestimate the core-hole effect, since peak B_1 is not clearly resolved in the summed p-PDOS. This effect can either origin in neglecting the transition matrix elements in the present calculations or in an insufficient description of the core-hole effects in SrTiO_3 by the $Z+1$ approximation. The same observations were made in the results of ELNES calculations performed using a full multiple scattering approach, in which the transition matrix element is included. In these investigations, the $Z+1$ approximation as well as the Z^* approximation of the core-hole effect were also not able to reproduce the experimental ELNES line shapes.

For bulk SrTiO_3 low-loss EELS measurements were performed to analyse the valence electronic structure. By a synthesis of experiment and total densities of states calculations an assignment of the experimentally observed transition energies to distinct transitions became possible. Furthermore, by a FFT-based Kramers-Kronig transformation of the single scattering low-loss spectra, all optical properties are obtainable from the previously calculated complex dielectric function. The calculated spectra for the energy-loss function, the reflectivity, the complex index of refraction, and the interband transition strength were calculated from the acquired VEELS data and reproduce the results from optical VUV spectroscopy measurements. Even so, the energy resolution in the optical experiments is by a factor of 3 better than in the VEELS experiments, the determined results from both techniques agree with each other reasonably well for both, absolute intensities and absolute peak energies. Furthermore, the results are in good agreement with available data from previous studies reported in the literature [Bäuerle, 1978] [Ryen, 1999]. In the energy range below 15 eV, optical spectroscopy is superior to VEELS because in spectroscopic ellipsometry high intensities could be recorded with a high signal-to-noise ratio, whereas the VEELS data are susceptible to artifacts due to the fitting and subtraction of the zero-loss peak in this energy regime. Above approximately 15 eV, VEELS is superior because of high counting statistics. Even more, the Kramers-Kronig analysis is much more reliable for the VEELS data extending to higher energies than the VUV data. Especially by the advent of new CCD-based EELS detectors with a significantly improved point-spread function (or modulation transfer function), such as the UHV Enfina system [Hunt, 2001], VEELS data also become more reliable for energy-losses below 15 eV. Finally it will be possible to directly measure band gap energies of ceramics and probably also of semiconductors. Due to the high spatial resolution in a STEM, also valence electronic structure studies of defects are possible by VEELS (see for example [French, 2000] and [van Benthem, 2001a]). The present study therefore creates a basis set of understanding of the valence electronic structure of bulk SrTiO_3 which can finally be used for the analysis of, e.g., grain boundaries in SrTiO_3 . In SrTiO_3 delocalization effects of the inelastic scattering process appear to be dominant only below an energy-loss of approximately 15 eV [van Benthem, 2001a].

10.2 The metal/SrTiO₃ Interfaces

By a combination of ELNES experiments and local density functional theory the local electronic structure of the Pd/SrTiO₃ interface was investigated. Due to the low oxygen affinity of Pd (compare Table 2.1) and a lattice mismatch between the Pd film and the SrTiO₃ substrate of almost 0%, this interface is regarded as a model interface for coherent and non-reactive metal/ceramic interfaces. CTEM and HRTEM studies indeed showed Pd growing as islands with a coherent interfacial structure on the (100)SrTiO₃ surface. From the 3-dimensional growth mechanism also observed by *in situ* RHEED measurements, it becomes obvious that for a substrate temperature of 650°C the formation of free Pd surfaces is energetically favoured compared to the Pd/SrTiO₃ interface formation. Spatially resolved ELNES measurements by using the spatial difference technique revealed similar results as *ab initio* band structure calculations of the site and symmetry projected densities of states. For these calculations, a previously theoretically determined atomistic structure model [Ochs, 2000] was used. For the investigated ELNES line shapes of the Ti L_{2,3}-, the O K-, and the Sr L_{2,3}-edges the experimentally determined results could be reproduced by the LDFT calculations. By the comparison of experiment and theory a detailed understanding especially of the O K-ELNES could be achieved. However, comparisons were limited to peak energies rather than on peak intensities since no transition matrix elements were considered in the calculations. By the agreement of experiment and theory, the validity of the atomistic structure model, which corresponds to the atomic configuration with the lowest total energy [Ochs, 2000] [Ochs, 2001], could be proven. Assuming the validity of the atomistic interface model, the presence of a TiO₂ termination of the (100)SrTiO₃ substrate could be shown by a synergy of experiment and theory (cf. Figure 7.20). Furthermore, it was possible to reproduce a theoretically provided ELNES line shape by an independent measurement of the interface specific ELNES using the spatial difference technique. Therefore, this technique is reliable for the determination of interface specific ELNES components, as far as the in section 4.1.3 discussed rules are followed. After the validation of the atomistic structure model for the Pd/SrTiO₃ interface, the calculation of the occupied densities of states was used to analyse the bonding between the Pd film and the (100)SrTiO₃ surface. This analysis showed a hybridization of Pd-3d_{z²} and O-2p_z states, forming a σ -bonding across the interface. Moreover, also a Pd-Ti intermetallic bonding was observed. Mizuno et al. [Mizuno, 1998] and Tanaka et al. [Tanaka, 1998] also reported intermetallic bonds for the metal/MgO system stabilizing the interface between the two materials. This behaviour could also be observed in this work by an analysis of the bonding strengths for the Pd-O and the Pd-Ti bondings. In addition metal-induced gap-states (MIGS) were observed at the Pd/SrTiO₃ interface, which have their origins in the Pd-3d to O-2p as well as in the Pd-3d_{xz} to Ti-3d_{xz} hybridizations.

The analysis of bonding for the model system Pd/SrTiO₃ can be used for an interpretation of the more reactive Ni/SrTiO₃ and Cr/SrTiO₃ interfaces. Although *in situ* RHEED measurements showed a 3-dimensional growth behaviour for both Ni and Cr on the (100)SrTiO₃ surface at 650°C and 65°C, respectively, STM measurements showed a significantly higher island density for Ni compared to Pd, and even higher for Cr. Therefore, one can conclude

that the wetting probability on SrTiO₃ is highest for Cr, medium for Ni, and lowest for Pd. CTEM investigations showed Ni islands with larger lateral sizes as for Pd, and a continuous film for Cr. The wetting probability can therefore directly be connected to the oxygen affinity or the heat of oxide formation $-\Delta H_0$ for the different elements (compare Table 2.1). HRTEM micrographs of both interfaces do not exhibit any reaction phase at the interface, although some additional contrasts in the interfacial regions are present, which could only be analysed by a quantitative HRTEM image analysis.

For the Ni/SrTiO₃ interface LDFT calculations were performed for the O p-PDOS using the atomistic structure model calculated for the Pd/SrTiO₃ interface. This approach is reasonable since Ni and Pd have a comparable valence electronic structure and can therefore be treated similar in the pseudopotential approach. Furthermore, only small interatomic forces appeared in the Ni/SrTiO₃ supercell perpendicular to the interface and could therefore be neglected. However, no agreement of the local interfacial O p-PDOS with the experimentally determined O K-ELNES could be achieved. Therefore, the calculated atomistic structure of the Pd/SrTiO₃ interface model is not valid for the real structure of the investigated Ni/SrTiO₃ interface. A comparison of the O K-edge for bulk NiO showed strong similarities to the interface specific component. For the Ti L_{2,3}-edges, a reduction of the nominal oxidation state of the interfacial Ti atoms was observed, while the Ni L_{2,3}-edges showed a significant broadening of their white lines, probably due to a modified crystal field at the interfacial Ni sites. Therefore, it can be concluded that an oxidation of Ni at the Ni/SrTiO₃ interface takes place. Since the Ni L_{2,3}-edges do not behave in their chemical shifts and in their L₃/L₂ intensity ratio as it is expected for NiO [Leapman, 1982], a possible description can be the formation of a 2-dimensional NiO phase at the interface. For this reason, discrepancies between the O K-edges for the Ni/SrTiO₃ interface and for bulk NiO are revealed.

In case of the Cr/SrTiO₃ interface, so far no theoretically determined atomistic structure model is achievable. Therefore, the ELNES analysis was only based on comparisons with other experimental data. The results for the Ti L_{2,3}-, O K-, and Cr L_{2,3}-edges exhibit a bonding between Cr and O across the interface due to a Cr-3d-O-2p hybridization. Simultaneously, also for this interface a reduction in the nominal oxidation state for the interfacial Ti atoms is observed, whereas the interfacial Cr atoms show an increased nominal oxidation state by a chemical shift of the Cr L_{2,3}-edges towards higher energy-losses. The Cr L_{2,3}-edges also show an amount of ionic bonding between the Cr film and the substrate by an increased L₃/L₂-intensity ratio.

Comparing the three investigated interfaces one can clearly infer that the wetting of the (100)SrTiO₃ surface is best for Cr for depositions near room temperature. The Cr-O bonds are suggested to be strongest since not only a covalent but also a significant ionic bonding characteristic is detectable forced by oxidation processes of Cr directly at the interface. The wetting by Ni is still stronger than for Pd, both deposited at a substrate temperature of $T_{\text{substrate}} = 650^\circ\text{C}$. However, in the case of the Ni/SrTiO₃ interface the formation of a 2-dimensional reaction layer between the film and the substrate is a possible suggestion to describe the adhesion between the film and the substrate. An ionic bonding was not observed, neither for Ni nor for Pd.

To summarize, the bonding behaviour at metal/ceramic interfaces can efficiently be investigated by a combination of experiment and theory. A theoretically determined atomistic structure model, which is given by the atomic configuration with the lowest total energy, can be used for a further calculation of the site and symmetry projected densities of states or for a quantitative HRTEM image analysis.

For a comparison the local PDOS with experimental ELNES data, core-hole effects have to be considered for PDOS calculations. These effects appear to be crucial for K-edges and for L-edges with a small screening of the core-hole by the remaining core electrons, like, e.g., for the Ti $L_{2,3}$ -edges.

The advent of new EELS spectrometers with a more narrow PSF in combination with cold field emitters as electron sources in the transmission electron microscope, will enable the recording of EELS spectra with very high energy resolutions below 0.5 eV . The use of monochromators will further decrease the width of the energy distribution of the beam electrons to probably 0.1 eV and lower. The use of C_s correcting elements in the electron microscope can be used to decrease the spherical aberration of the objective lens and therefore increases the spatial resolution in the experiment, e.g., by reducing the spot size in the STEM.

Currently, *ab initio* band structure calculations are mainly limited by computation times to small supercells containing less than ~ 150 atoms. Thus, only defect structures with a short spatial periodicity length can be calculated in a reliable way, since for larger periodicities the supercells have to be significantly increased in size. The calculations of crystal defects, such as metal/ceramic interfaces with a non-zero lattice mismatch, are therefore mainly limited due to computational reasons, which can be partly overcome by parallelized program codes running on multi-processor computers [Classen, 2001a].

Appendix A

Image Formation Theory in the STEM

For conventional TEM applications, a large area of the specimen is illuminated by a nearly parallel electron beam. In a STEM the electron beam is focussed to form a small probe on the surface of the specimen. This probe is scanned over a rectangular area. The illumination in a STEM is convergent. The scattered electrons are finally recorded on angular detectors and readout to a monitor. The spatial resolution of a STEM is governed by the diameter of the probe. Therefore, in contrast to a conventional TEM, the high precision electron optics are located in front of the specimen. Thus, the objective lens in the STEM acts like the condensor lens in a TEM.

In general, the propagation of electron waves is described by the Schrödinger equation in the time-dependent form:

$$i\hbar \frac{\partial \Psi}{\partial t} = \hat{H} \Psi. \quad (\text{A.1})$$

Therein, \hbar is Planck's constant, $\Psi(\vec{r}, t)$ denotes the space and time dependent wave function of the electrons and \hat{H} is the corresponding Hamiltonian, given by.

$$\hat{H} = \frac{1}{2m}(\vec{p} + e\vec{A})^2 - e\phi. \quad (\text{A.2})$$

\vec{p} is the momentum, m is the relativistic mass of the electron, e is the elementary charge, \vec{A} and ϕ denote the 3-dimensional and the 1-dimensional potential, respectively.

The propagation of electron waves through the electron microscope can be divided into different parts. In principle, only two different cases have to be considered in this description: (a) the propagation in the field-free space and (b) the propagation through the electron optical lenses.

The solution of the Schrödinger equation (equation A.1) for the propagation of electrons in the field-free space is given by the Sommerfeld equation:

$$\Psi(\vec{r}, t) = \frac{i}{\lambda} \int \int \Psi_0 \frac{\exp(i\vec{k}\vec{r})}{r} \cos(\theta) d\sigma. \quad (\text{A.3})$$

λ is the wavelength of the electrons and \vec{k} is the corresponding wave vector. The integration is performed throughout the whole plane denoted by z_0 . For the observer located at the

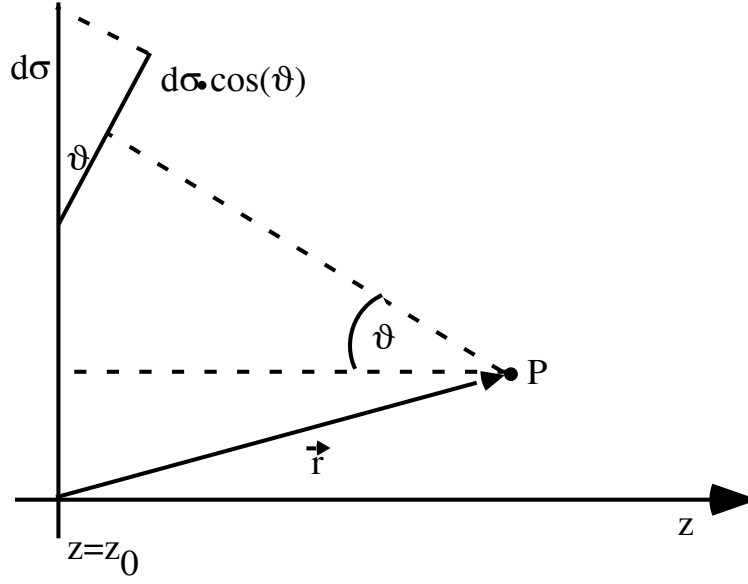


Figure A.1: Geometrical details to Sommerfeld's equation.

site P (cf. Figure A.1 the surface element $d\sigma$ has a size of $d\sigma \cdot \cos(\theta)$). Figure A.1 shows a schematic drawing of the geometries underlying the Sommerfeld equation. In this equation the electron wave can be calculated for every location in field-free space if it is known for one location. It should be mentioned that this equation is valid only for the case of $r \gg \lambda$, when higher order terms become negligible in the original formalism (cf. Huygens's principle in [Reimer, 1997] [Rose, 2000]).

For a substitution of $a := z - z_0$, \vec{r} can be written as

$$\begin{aligned} \vec{r} &= \sqrt{a^2 + (x - x_0)^2 + (y - y_0)^2} \\ &\approx a + \frac{1}{2} \frac{(x - x_0)^2}{a} + \frac{1}{2} \frac{(y - y_0)^2}{a} + \dots \end{aligned} \quad (\text{A.4})$$

In praxi, because of spherical aberrations, beams with high distances from the optical axis are removed by apertures. Therefore, equation A.3 can be changed to the so-called Fresnel-approximation (equation A.5) in the near-field, i.e. for small values of r (small values of a). By applying the Taylor series for the exponential function and for the cosine terms in equation A.3, and by using equation A.4, the Sommerfeld equation can be written as

$$\Psi(\vec{r}) \approx \frac{\exp(ika)}{i\lambda a} \iint \Psi_0 \exp\left(\frac{ik}{2a}[(x - x_0)^2 + (y - y_0)^2]\right) d\sigma \quad (\text{A.5})$$

In addition to the general description of the propagation of electrons in the field-free space, the influence of apertures have to be considered. Apertures are used e.g. to extract only electron beams penetrating through the microscope column with a small distance from the optical axis. In this case, lens aberrations like the spherical aberration, can be minimized. The disadvantage of using apertures is that the electron beam is diffracted by the apertures

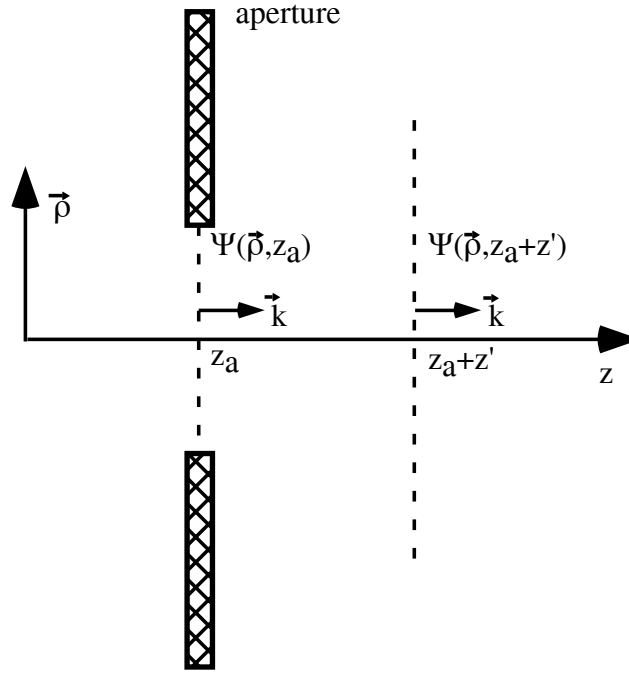


Figure A.2: Geometrical drawing of the influence of an aperture on the electron wave.

which decreases the spatial resolution, as it was mentioned earlier in section 4.1.1. In an approximation, apertures are considered to have an infinitesimal thickness and are changing the electron waves abruptly. A schematic drawing of the influence of apertures on the electron beam is given in Figure A.2.

A mathematical description of an aperture in the plane at $z - z_0$ is given by a transmission function $T(\vec{\rho}, z_a)$ with $\vec{\rho} = (x, y)$, following

$$\Psi(\vec{\rho}, (z_a + z')) = T(\vec{\rho}, z_a) \Psi(\vec{\rho}, z_a). \quad (\text{A.6})$$

In case of a thin spherical aperture with the radius b the transmission function of the aperture becomes

$$T(\vec{\rho}) = T(\rho) = \begin{cases} 1 & : \quad \rho \leq b \\ 0 & : \quad \rho > b \end{cases}. \quad (\text{A.7})$$

This description is valid in the case that all electrons are completely absorbed if they have a distance larger than b from to the optical axis. If there is more than one aperture inside the column, the wave function can be either calculated by a successive use of Sommerfeld's equation between the different lenses or by using one effective aperture, which has the size of the smallest aperture existing in the microscope.

The propagation of the electron waves through a magnetic lens has to be described in a different way since phase shifts appear. A solution of Schrödinger's equation is given by the

so-called WKB-ansatz ¹

$$\Psi = a \cdot \exp\left(\frac{i}{\hbar}W\right). \quad (\text{A.8})$$

$a = a^* = a(\vec{r})$ is the real amplitude of the electron wave function and $W = W(\vec{r})$ describes the phase of the wave function. Its dimension is the one of work function. If $W(\vec{r}) = W_0 = \text{const.}$, a surface of constant phase in real space and is produced, which is referred to as wavefront. In a static magnetic field, $W(\vec{r})$ can be described as

$$W = \int_0^P \vec{p} d\vec{s} = \int_0^P (m\vec{v} - e\vec{A}) ds. \quad (\text{A.9})$$

In this equation \vec{v} is the velocity of the electron, respectively. The work function and therefore the optical path of the electrons is determined by the Hamilton principle. The optical path of the electrons is determined by the path, for which the integral in equation A.8 is an extremum. This formalism for the static case is equivalent to Fermat's principle in light optics [Reimer, 1997] [Rose, 2000].

Similar to the description of apertures in the electron microscope, a magnetic lens is considered to be infinitesimally thin [Born, 1964] so that it changes the phase of the electron wave abruptly. This is realized mathematically by introducing the phase term $e^{\frac{iW}{2a}}$:

$$\Psi(\vec{r}) = \frac{1}{ia\lambda} \int \int \Psi_0 \exp\left\{\frac{iW\vec{r}\vec{p}}{2a}\right\} d^2\vec{\rho}. \quad (\text{A.10})$$

This description is exact for an ideal lens. For real lenses it is not sufficient since phase shifts appear inhomogeneous in the plane of the lens due to lens aberrations and due to non-ideal incoming electron waves. For a correct solution in the case of real lenses, one has to consider higher-order terms $\gamma(\vec{\rho})$ in calculating the work function

$$W(\vec{\rho}) = W'(\vec{\rho}) + \gamma(\vec{\rho}). \quad (\text{A.11})$$

$\gamma(\vec{\rho})$ is the lens aberration function and acts like an additional phase factor of the electron wave function. It includes all lens aberrations, which are discussed in section 4.1.1.

The spatial resolution of a dedicated STEM is governed by the diameter of the focussed electron beam on the specimen. As can be inferred from Figure 4.1, an image of the tip is demagnified by the condensor lens system into the plane of the selected area diffraction aperture. The objective lens further demagnifies this virtual image of the electron source and images it onto the surface of the specimen. For both lens systems, the propagation of the electron waves can be described by a successive use of the equations given above. By the transmission of the electrons through the sample, phase shifts of the wave functions occur. For thin samples, where absorption effects can be neglected, these phaseshifts $\Phi(\vec{r})$ are proportional to the projected crystal potential $U(\vec{r})$ [Glauber, 1959]. The mathematical

¹WKB-method: solution of the time invariant of Schrödinger's equation, which was provided independently by Wentzel, Kramers, and Brillouin in 1926.

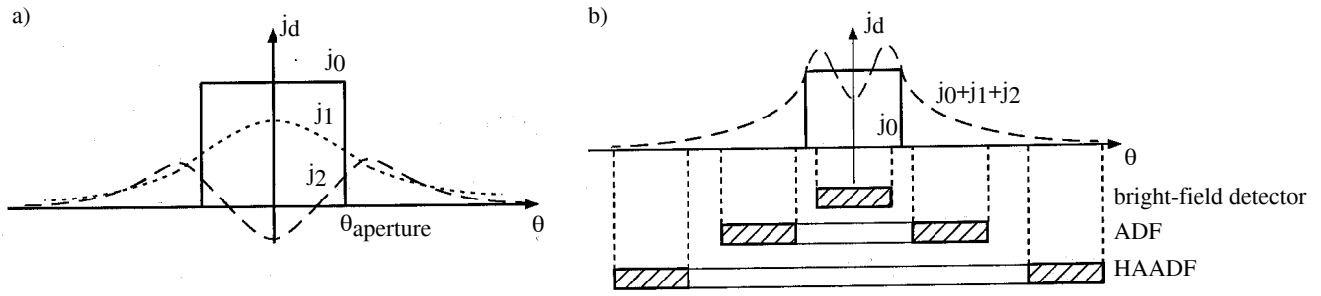


Figure A.3: Current density distribution in the detector plane. Figure (a) shows the three different components of the current density as a function of the emission angle. (b) shows the total current density as a function of the emission angle and the corresponding detectors in the VG STEM.

description of these effects again uses a transmission function for the sample T_{sample} , which acts abruptly on the back plane of the specimen:

$$\Psi_{sample}(\vec{r}) = \Psi_0 \cdot T_{sample} = \Psi_0 \cdot \exp\left\{-\frac{ik}{2E} \int_{-\infty}^{+\infty} U(\vec{r}) dz\right\}. \quad (\text{A.12})$$

E denotes the kinetic energy of the electrons. This approximation is only valid for plane waves whose wave vector \vec{k} is parallel to the optical axis. Inelastically scattered electrons were not considered in the description of the electron propagation through the microscope. However, the propagation from the specimen to the detector plane can be calculated using Sommerfeld's equation (equation A.3), since in a dedicated STEM no additional lens is following the specimen.

In the VG STEM the electrons are detected by one circular detector (bright-field detector) and two angular detectors (ADF and HAADF), as is shown in Figure 4.1. The detected current density j_d is given by

$$j_d = \Psi_d \Psi_d^* = \sum_{\nu} j_{\nu} \quad \nu = 0, 1, 2 \quad (\text{A.13})$$

The total current density j_d consists of 3 different parts (see also Figure A.3a). The current density with index ν denotes the ν^{th} power of the scattering amplitude f , which is the Fourier transform of $F = 1 - T_{sample}$. If no sample is present, the current densities j_1 and j_2 equal zero. The maximum angle $\theta_{aperture}$ is given by the effective aperture inserted into the microscope. Although no specimen is present, the current density distribution j_1 is smeared out due to diffraction effects of the inserted apertures (cf. Figure A.3). If the electron beam is transmitted through a thin specimen, j_1 and j_2 become non-zero. Interference effects of the elastically scattered electrons with the non-scattered electrons produce some phase contrast on the detector plane. Due to elastic scattering of the electrons the angular distribution of the current density is smeared out more strongly than without the specimen interaction.

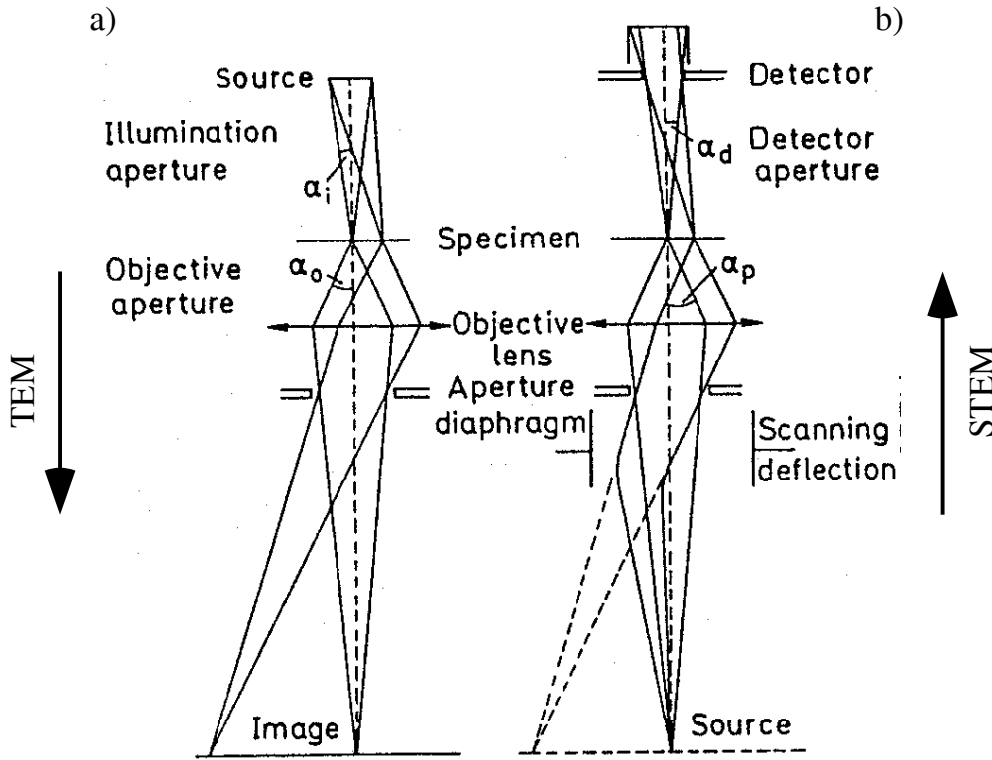


Figure A.4: Comparison of the electron beams penetrating a conventional TEM (a) and a dedicated STEM (b). The image formation theory for one can be used for the other microscope following the theorem of reciprocity, if certain requirements are fulfilled [Reimer, 1997].

Therefore, by a specific combination of different circular and angular detectors a difference of the corresponding signals can be used for phase contrast imaging in the STEM [Rose, 1974] [Rose, 1977]. Most commonly, only angular detectors are used in a STEM, which collect all electrons available, and therefore *no* phase contrast is available. Apart from the bright-field detector, two angular detectors are available, which collect electrons from different scattering angles: an annular dark field detector (19 mrad to 38 mrad) and an HAADF detector (53 mrad to 173 mrad, cf. Figure A.3). For large angles, which are in the HAADF regime, only the current density j_3 is dominant and no phase contrast appears. The electrons collected in this regime are incoherently scattered. Thus, the scattering can be explained by the Rutherford formalism, in which the intensity is proportional to the square of the atomic number Z^2 [Pennycook, 1988]. The resulting image therefore is referred as Z-contrast image. By tilting the specimen into a low-indexed zone-axis, this can be used to acquire atomically resolved STEM images including a so-called chemical contrast.

The image formation theory provided in this section was shown for the dedicated STEM, which was predominantly used in this work. However, the theoretical descriptions are of course valid for all TEMs. The elementary difference between a dedicated STEM and a

conventional TEM is the electron optical configuration. In a STEM, all electron optical lenses are located in front of the specimen, whereas in the conventional TEM the lens system for image formation is located behind the specimen. This fact is visualized in a schematical drawing of the electron beams in a STEM compared to a conventional TEM in Figure A.4. This analogon between the two different microscopes is called the *theorem of reciprocity*, which was first discussed by Helmholtz in 1860 for light optics [Reimer, 1997]. The theorem of reciprocity is in general only valid in the case that the illumination angle α_i in the CTEM equals the collecting angle α_d in the STEM (compare Figure A.4. However, in all other cases it is regarded to be approximately fulfilled. Detailed information on the theorem of reciprocity can be found in [Rose, 1988], [Reimer, 1997], and [Egerton, 1996]. The image formation in a TEM, such as the Jeol ARM1250 or the Jeol JEM2000FX, which were used in this work, can again be described by the successive use of equations A.3, A.5, and A.8.

Appendix B

Characterization of the PEELS Detectors

In this section, the performance of the two different PEELS detectors, which were used throughout the presented investigations, is reported with respect to the achieved energy resolution. Both detector systems are commercially available and were provided by Gatan Inc., Pleasanton, Ca., USA. One system is the so-called Gatan PEELS766 system, consisting of a photo diode array (in the following: PDA detector); the second detector is the newly designed UHV Enfina System [Hunt, 2001], which consists of a CCD array (in the following: CCD detector). Both detector systems were adapted to a parallel electron energy-loss spectrometer, which is mounted to a VG HB501 UX dedicated STEM.

Both detector systems consist of a scintillator module placed in UHV and a camera module. The scintillator systems of the two different detectors have different designs. However, both consist of a YAG scintillator, which is optically coupled to a fiber optic. The camera module contains either the PDA or the CCD chip, whereas the latter is placed in an extra vacuum chamber and is cooled by a thermostated thermoelectric cooler backed by water-cooling [Hunt, 2001]. The camera module and the scintillator module are oil-coupled to each other in both the PDA detector and the CCD detector.

A sketch view of the UHV Enfina system is shown in Figure B.1. To control acquisition times while recording EEL spectra, the electron beam is chopped by a shutter whose chopping frequency is software controlled. For this system, two different shutters are available: an electromagnetic shutter and an electrostatic shutter. The electromagnetic shutter is placed inside the spectrometer and removes the electron beam from the optical axis of the spectrometer to a grounded plate offside the optical axis. The electrostatic shutter is the beam blanker of the STEM in between the condensor lenses and the selected area diffraction aperture of the microscope (see Figure B.1). It can either be controlled by software or manually by an adapted frequency generator. For the PDA system, acquisition times were software controlled using a different type of electromagnetic shutter, which was also placed within the scintillator module, whereas the electrostatic shutter is the same for both systems.

The electron detector adapted to an energy-loss spectrometer records electrons in the

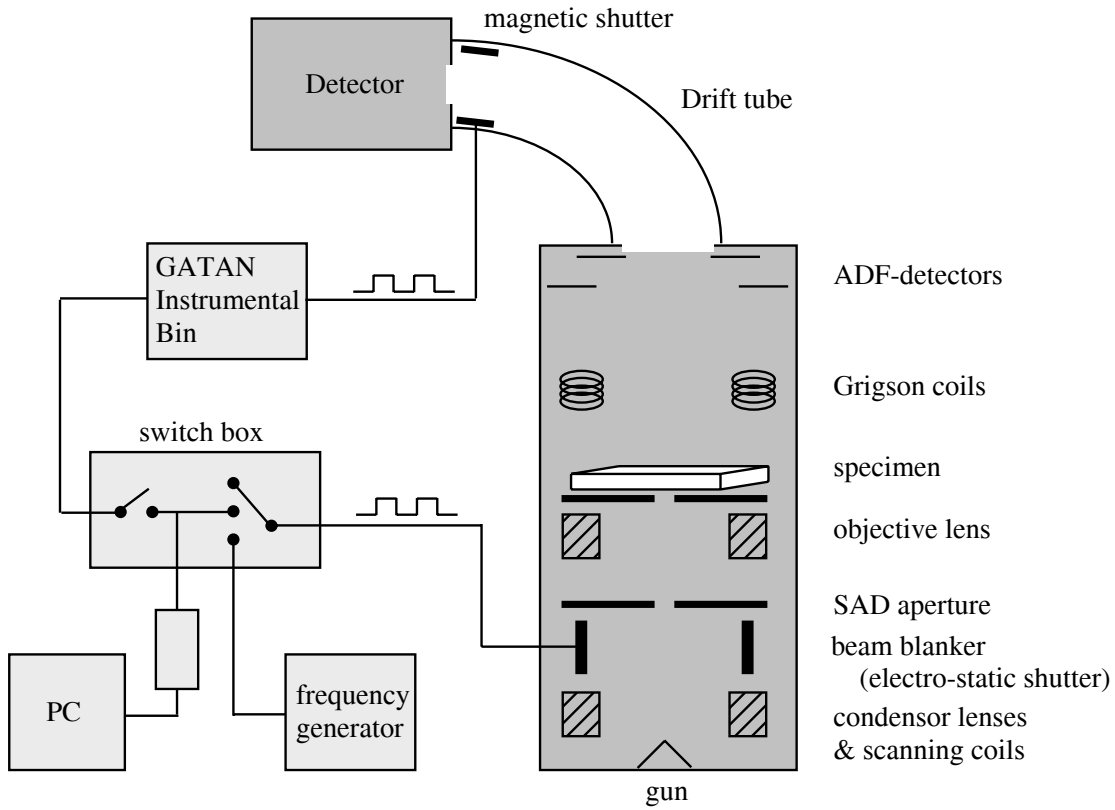


Figure B.1: Sketch view of the available shutters for the UHV Enfina system.

energy dispersive plane of the spectrometer. The spatial resolution s in the energy-dispersive plane determines the experimentally achievable energy resolution, as it was already shown in equation 4.7. Therefore, a blurring of the signal of an incident monochromatic electron inside the detector leads to an overall reduction of the energy resolution of the recorded data. Blurring effects can origin from the reflections of photons between the scintillator and the fiber optics or also from reflections within the fiber optics. These blurring effects can mathematically be described by the so-called point-spread function (PSF) [Dainty, 1974] and is the response of the detector on a δ -impulse. The PSF is a characteristic function for each detector.

The PSF of a PEELS detector can easily be measured by recording the zero-loss peak without any specimen interaction at a dispersion, which is larger than the FWHM of the corresponding energy distribution of the electron beam. In the case of the VG STEM this condition is fulfilled by using an energy-dispersion of 4.0 eV/channel. By using this setup, only one pixel of the detector array is regarded to be illuminated by the incident electron beam since its intrinsic width in energy is below 0.5 eV. Thus, the extended wing of the measured signals, after correction for the dark current and channel-to-channel gain variations, are due to a blurring of the signal inside the detector.

In Figure B.2 the results for the PSF measurements concerning the PDA detector and

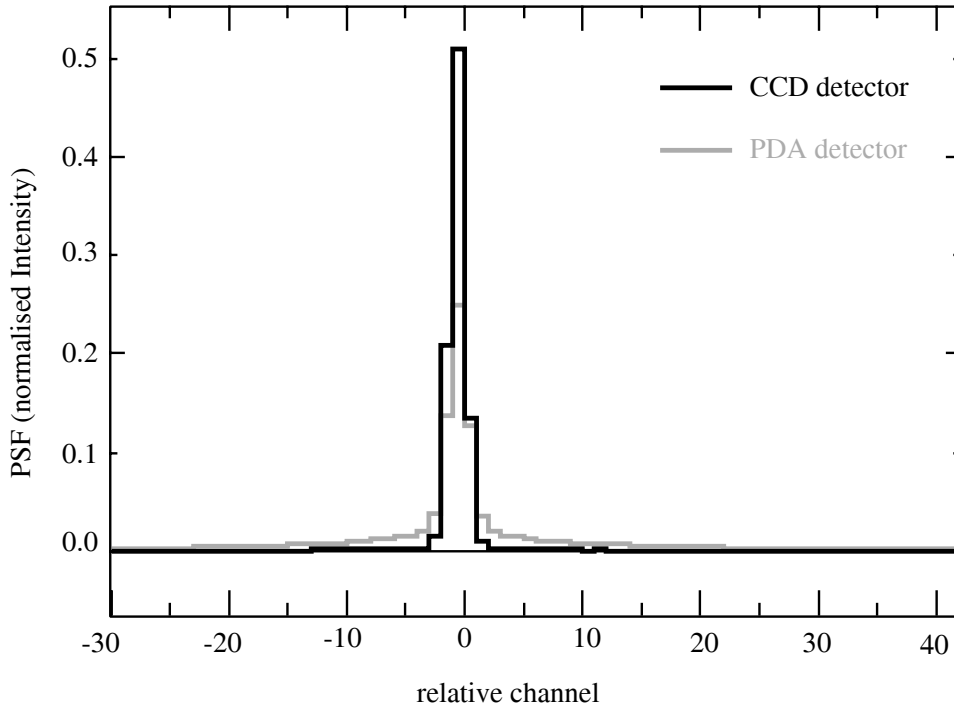


Figure B.2: Normalised point-spread functions of the DigiPEELS detector and the UHV Enfina system.

the CCD detector are plotted for comparison. Both spectra were normalised with respect to their integrated intensity. In this plot one can clearly observe that the tails of the PSF are significantly reduced in intensity for the CCD detector in comparison to the PDA system. As a consequence, the FWHM of the PSF is also reduced for the CCD array. Therefore, the CCD detector is able to record higher spatial frequencies in the spectra than the PDA detector, leading to an increased experimental energy resolution. For the formerly used PDA detector, in a standard setup of the VG STEM with a beam current of approximately 1 nA, an energy resolution of 0.8 eV, measured by the FWHM of the zero-loss peak, was achievable when an energy dispersion setting of 0.1 eV/channel was used. Using the CCD detector for the same setup, the improved PSF leads to an achievable energy resolution of 0.6 eV.

The scintillator of the detector transfers the kinetic energy of the incoming electrons into photons, which are registered either by a PDA or a CCD array. During this registration process photons produce free electronic charges within the detecting array, which are converted into electrical impulses, so-called counts. The ratio of incoming electrons N_i to the number of the finally produced counts N is called the conversion rate ξ of the detector system. ξ has a specific value for each different detector and gives information about the sensitivity of the detector system. In an ideal electron detector, each incoming electron produces one electronic count.

The conversion rate of the CCD detector was determined by measuring the beam currents (I_1 and I_2) for two different values of the extraction voltage of the tip at the switched-off

drift tube using the spectrometer as a Faraday cup. The corresponding intensities N_1 and N_2 for these settings were acquired in the spectroscopy mode using an energy dispersion of 0.05 electrons/channel. The zero-loss peak was defocussed on the energy-axis using the quadrupole lenses of the spectrometer in order to spread the electron beam over the whole CCD array. The conversion rate ξ in electrons/counts can be calculated by

$$\xi = \frac{I_1 - I_2}{N_1 - N_2} \cdot t_{int} \cdot 6.25 \cdot 10^{18} . \quad (\text{B.1})$$

t_{int} denotes the used integration time in the corresponding measurement. The determined conversion rates of the PDA detector and the CCD detector are $\xi_{PDA} = 13$ electrons/count and $\xi_{CCD} = (0.25 \pm 0.02)$ electrons/count, respectively. This strong reduction in the conversion rate demonstrates a higher sensitivity of the UHV Enfina System by a factor of approximately 50 compared to the PDA based DigiPEELS system. Therefore, the electron dose on the specimen, i.e., the beam current, and/or integration times can be significantly reduced in EELS experiments while the statistics of the recorded data remain constant. This leads to a lower beam damage propability on one hand, and in smaller specimen drifts due to shorter acquisition times on the other hand. Additionally, a higher sensitivity of the detector enables the measurement of absorption edges at high energy-losses, like, for example, the Sr $L_{2,3}$ -edge.

List of Tables

2.1	Heats of formation and oxygen affinities for different oxides.	28
3.1	Literature overview for Pd/ceramic systems	38
3.2	Literature overview for Ni/ceramic systems	41
3.3	Literature overview for Cr/ceramic systems	42
4.1	Electron configuration of Ti, V, Sr, Y, O, F, and Pd.	68
5.1	Processing Parameters during MBE growth	73
6.1	Interband transition energies for bulk SrTiO ₃	84
6.2	Band gap energies for bulk SrTiO ₃	86
6.3	Edge onsets in bulk SrTiO ₃	92
6.4	Total energy dependence on the supercell size	96

List of Figures

2.1	Coherence of interfacial structures	21
2.2	Different modi of wetting	22
2.3	Definition of the contact angle after the Young-Dupré equation	23
2.4	Growth modes as a function of temperature and sputter rate	24
2.5	Crystal structure of bulk SrTiO_3 at room temperature	25
2.6	Termination of the (100) SrTiO_3 surface	26
2.7	Crystal structures of <i>fcc</i> and <i>bcc</i> materials	27
3.1	Standard free Energy changes for different metal oxides	34
3.2	Channeling effects in the VG HB501 STEM	46
4.1	The VG HB501 UX dedicated STEM	50
4.2	Inelastic scattering of electrons	54
4.3	Electron energy-loss spectrum of SrTiO_3	55
4.4	Scattering geometry	56
4.5	Bandstructure vs. densities of states	58
4.6	Spectroscopy at high spatial resolution	60
4.7	Scanning areas for the spatial difference technique	61
4.8	Schematic drawing of the spatial-difference technique	63
4.9	Multiple scattering description for ELNES and EXELFS	69
4.10	Inelastic mean-free path Λ_i as a function of energy	70
5.1	TEM cross-sectional specimen praparation	74
5.2	Specimen damage due to ion-thinning	75
5.3	Monodirectional and bidirectional ion-thinning	76
5.4	Ion-milling from one direction	77
5.5	Specimen bending effects	78
6.1	Valence electron energy-loss spectrum of bulk SrTiO_3	80
6.2	Index of refraction of bulk SrTiO_3	82
6.3	Interband transition strength of bulk SrTiO_3	83
6.4	f-sum rule from EELS and VUV spectroscopy.	85
6.5	Comparison of energy-loss functions obtained by different techniques	86
6.6	Calculated densities of states of bulk SrTiO_3	87

6.7	Schematic energy level diagram for bulk SrTiO_3	90
6.8	Ti $L_{2,3}$ -edges in bulk SrTiO_3	93
6.9	O K-edge in bulk SrTiO_3	94
6.10	Sr $L_{2,3}$ -edges in bulk SrTiO_3	95
6.11	Titanium PDOS core-hole calculations for different supercell sizes	97
6.12	Ti $L_{2,3}$ -edge in bulk SrTiO_3 : core-hole effect	99
6.13	Oxygen PDOS core-hole calculations for different supercell sizes	100
6.14	O K-edge in bulk SrTiO_3 : core-hole effect	101
6.15	Sr $L_{2,3}$ -edge in bulk SrTiO_3 : core-hole effect	102
6.16	Ti $L_{2,3}$ -edge in bulk SrTiO_3 : different core-hole approximations	103
6.17	O K-edge in bulk SrTiO_3 : different core-hole approximations	104
6.18	Sr $L_{2,3}$ -edge in bulk SrTiO_3 : different core-hole approximations	105
6.19	Charge distribution plot for an oxygen core-hole in SrTiO_3	106
6.20	Charge distribution plot for an oxygen core-hole in SrTiO_3	108
7.1	Island growth of Pd on SrTiO_3 (RHEED & SEM)	112
7.2	CTEM micrograph of the Pd/ SrTiO_3 interface	113
7.3	HRTEM micrograph of the Pd/ SrTiO_3 interface in $\langle 110 \rangle$ zone-axis orientation.	114
7.4	HAADF micrograph of the Pd/ SrTiO_3 interface in $\langle 100 \rangle$ zone-axis orientation	115
7.5	HAADF micrograph of the Pd/ SrTiO_3 interface after digital image filtering	116
7.6	The Pd $M_{4,5}$ - and the Ti $L_{2,3}$ -edges at the Pd/ SrTiO_3 interface	117
7.7	Experimental results for the Ti $L_{2,3}$ -edge at the Pd/ SrTiO_3 interface	118
7.8	Experimental results for the O K-edge at the Pd/ SrTiO_3 interface	119
7.9	Influence of energy drifts on the spatial difference technique	120
7.10	Experimental results for the Sr $L_{2,3}$ -edges at the Pd/ SrTiO_3 interface	121
7.11	Supercell geometries for the Pd/ SrTiO_3 interface	122
7.12	Calculated V d-PDOS for the Pd/ SrTiO_3 interface	124
7.13	Local O p-PDOS projected for different sites in the supercell	125
7.14	Calculated O and F p-PDOS for the Pd/ SrTiO_3 interface	126
7.15	Spatial distribution of the local unoccupied O p-PDOS	127
7.16	O p-PDOS for a free surface and for the Pd/ SrTiO_3 interface	128
7.17	Calculated O p-PDOS for the Pd/ SrTiO_3 interface	129
7.18	Calculated Sr d-PDOS for the Pd/ SrTiO_3 interface	130
7.19	Interfacial Ti L_3 -edge: experiment and theory	133
7.20	O K-edge of the Pd/ SrTiO_3 interface: theory and experiment	135
7.21	Analysis of the O p-PDOS of the Pd/ SrTiO_3 interface	136
7.22	Atom arrangement at the Pd/ SrTiO_3 interface	137
7.23	Occupied local Ti d-PDOS at the Pd/ SrTiO_3 interface	139
7.24	Occupied local Pd d-PDOS at the Pd/ SrTiO_3 interface	141
7.25	Charge distribution plot of the Pd/ SrTiO_3 interface	143
7.26	Local PDOS in the band gap region at the interface	144
7.27	Spatial distribution of the total DOS in the band gap region	145

8.1	Island growth of Ni on SrTiO ₃ (RHEED & SEM)	147
8.2	CTEM micrograph of the Ni/SrTiO ₃ interface	148
8.3	HRTEM micrograph of the Ni/SrTiO ₃ interface	149
8.4	Ti L _{2,3} -edges of the Ni/SrTiO ₃ interface	150
8.5	O K-edges of the Ni/SrTiO ₃ interface	151
8.6	Ni L _{2,3} -edges of the Ni/SrTiO ₃ interface	152
8.7	O p-PDOS of the Ni/SrTiO ₃ interface	154
8.8	Spatial distribution of the local unoccupied O p-PDOS	155
8.9	Analysis of the interfacial O K-edge of the Ni/SrTiO ₃ interface	157
8.10	Binary phase diagram for the Ni–Ti system	159
9.1	<i>In situ</i> RHEED investigations of Cr/SrTiO ₃	161
9.2	CTEM micrograph of the Cr/SrTiO ₃ interface	162
9.3	a) HRTEM micrograph of the Cr/SrTiO ₃ interface	163
9.4	Ti L _{2,3} -edges of the Cr/SrTiO ₃ interface	164
9.5	O K-edges of the Cr/SrTiO ₃ interface	165
9.6	Cr L _{2,3} -edges of the Ni/SrTiO ₃ interface	166
9.7	Binary phase diagram for the Cr–Ti system	169
A.1	Geometrical details to Sommerfeld’s equation	176
A.2	The influence of an aperture	177
A.3	Current density distribution in the detector plane	179
A.4	Theorem of reciprocity	180
B.1	Sketch of the UHV Enfina system	183
B.2	PSF of the PEELS detectors	184

Bibliography

- [Adachi, 1999] Y. Adachi, S. Kohiki, K. Wagatsuma, and M. Oku, *Appl. Surf. Sci.* **143** (1999) 272.
- [Ahn, 1983] C. C. Ahn and O. L. Krivanek, *EELS atlas, A reference collection of electron energy-loss spectra covering all stable elements*, Gatan Inc., Pleasanton, Ca., USA (1983)
- [van Aken, 1998] P. A. van Aken, B. Liebscher, and V. J. Stryrsa, *Phys. Chem. Miner.* **25** (1998) 323.
- [Akhtar, 1995] M. J. Akhtar, Z. Akhtar, and R. A. Jackson, *J. Am. Ceram. Soc.* **78**, 421 (1995).
- [Andersen, 1990] J. E. T. Andersen and P. J. Møller, *Thin Solid Films* **186** (1990) 137.
- [Ankudinov, 1998] A. L. Ankudinov, B. Ravel, J. J. Rehr, and S. D. Conradson, *Phys. Rev. B* **58** (1998) 7565.
- [Ashcroft, 1976] N. W. Ashcroft and N. D. Mermin, *Solid State Physics*, CBS Publishing Asia Ltd. (1976).
- [Backhaus-Ricoult, 1988] M. Backhaus-Ricoult and D. Ricoult, *J. Mater. Sci.* **23** (1988) 1309.
- [Backhaus-Ricoult, 1994] M. Backhaus-Ricoult, S. Hagège, A. Peyrot, and P. Moreau, *J. Am. Ceram. Soc.* **77** (1994) 423.
- [Baluffi, 1981] R. Baluffi, P. Bristowe, and C. Sun, *J. Am. Ceram. Soc.* **138**, 457 (1981).
- [Barbier, 1998] A. Barbier, G. Renaud and O. Robach, *J. Appl. Phys.* **84** (1998) 4259.
- [Batson, 1993] P. E. Batson, *Nature* **366** (1993) .
- [Batson, 1994] P. E. Batson, N. D. Browning and D. A. Muller, *MSA Bulletin* **24** (1994) 371.

- [Bauer, 1958] E. Bauer, *Z. f. Krist.* **110**, 372 (1958), **110**, 385 (1958).
- [Bäuerle, 1978] D. Bäuerle, W. Braun, V. Saile, G. Sprüssel, and E. E. Koch, *Z. Phys. B* **29** (1978) 179.
- [Bäumer, 1999] M. Bäumer and H.-J. Freund, *Progress in Surface Science* **61** (1999) 127.
- [van Benthem, 2001a] K. van Benthem, R. H. French, W. Sigle, C. Elsässer, and M. Rühle, *Ultramicroscopy* **86**, 303 (2001).
- [van Benthem, 2001b] K. van Benthem, R. H. French, and C. Elsässer, *J. Appl. Phys.* **90** (2001) 6156.
- [Berger, 1982] S. D. Berger and S. J. Pennycook, *Nature* **298** (1982) 635.
- [Bethe, 1930] H. Bethe, *Ann. der Physik* **5** (1930) 325.
- [Bialas, 1977] H. Bialas and L.-S. Li, *phys. stat. sol. A* **42** (1977) 125
- [Bialas, 1994] H. Bialas and K. Heneka, *Vacuum* **45** (1994) 79.
- [Boersch, 1954] H. Boersch, *Zeitschrift für Physik* **139** (1954) 115.
- [Born, 1964] M. Born and E. Wolf, *Principles of Optics* Macmillan, New York (1964).
- [Brandes, 1992] E. A. Brandes and G. B. Brook, *Smithells Metals Reference Book*, 7th ed., Butterworth-Heinemann Ltd., Oxford (1992).
- [Bredow, 1999] T. Bredow and G. Pacchioni, *Surf. Sci.* **426** (1999) 106.
- [Brown, 1981] L. M. Brown, *J. Phys. F* **11** (1981) 1.
- [Browning, 1993a] N. D. Browning and S. J. Pennycook, *Microbeam Analysis* **2** (1993) 81.
- [Browning, 1993b] N. D. Browning, M. F. Chisholm and S. J. Pennycook, *Nature* **366** (1993) 143.
- [Browning, 1996] N. D. Browning and S. J. Pennycook, *J. Phys. D: Appl. Phys.* **29** (1996) 1779.
- [Browning, 1997] N. D. Browning, D. J. Wallis, P. D. Nellist, and S. J. Pennycook, *Micron* **28** (1997) 333.
- [Bruley, 1993] J. Bruley, *Microsc. Microanal. Microstruct.* **4** (1993) 23.
- [Brydson, 1991] R. Brydson, *EMSA Bulletin* **21** (1991) 57.

- [Brydson, 1992] R. Brydson, H. Sauer, W. Engel, and F. Hofer, *J. Phys.: Condens. Matter* **4**, 3429 (1992).
- [Brydson, 1995] R. Brydson, H. Mülleijans, J. Bruley, P. A. Trusty, X. Sun, J. A. Yeomans, and M. Rühle, *J. Microscopy* **177** (1995) 369.
- [Callaway, 1984] J. Callaway and N. H. March, in: *Solid State Physics. Advances in Research and Application*, H. Ehrenreich and D. Turnbull (eds.), Plenum Press, Orlando (1984) 135.
- [Calow, 1971a] C. A. Calow, P. D. Bayer and I. T. Porter, *J. Mater. Sci.* **6** (1971) 150.
- [Calow, 1971b] C. A. Calow, P. D. Bayer and I. T. Porter, *J. Mater. Sci.* **6** (1971) 156.
- [Cappellini, 2000] G. Cappellini, S. Bouette-Russo, B. Amadon, C. Noguera, and F. Finocchi, *J. Phys.: Condens. Matter* **12** (2000) 3671.
- [Cardona, 1965] M. Cardona, *Phys. Rev. A* **140**, 651 (1965).
- [Chapon, 1985] C. Chapon, C. R. Henry and A. Chemem, *Surf. Sci.* **162** (1985) 747.
- [Chiang, 1990] Y. M. Chiang and T. Takagi, *J. Am. Ceram. Soc.* **73**, 3278 (1990), **73**, 3286 (1990).
- [Chaudhari, 1987] P. Chaudhari, R. H. Koch, R. B. Laibowitz, T. R. McGuire, and R. J. Gambino, *Phys. Rev. Lett.* **58** (1987) 2684.
- [Chung, 1979] Y.-W. Chung and W. B. Weissbard, *Phys. Rev. B* **20** (1979) 3456.
- [Classen, 2001a] T. Classen, *Mikroskopische Struktur und Energetik von kohärenten Übergangsmetall-SrTiO₃-Grenzflächen*, Diplomarbeit, Universität Stuttgart (2001).
- [Classen, 2001b] T. Classen and C. Elsässer, *unpublished results* (2001).
- [Colliex, 1984] C. Colliex and C. Mory, in: *Quantitative Electron Microscopy*, J. N. Chapman and A. J. Craven (eds.) SUSSP publications, Edinburgh, UK (1984).
- [Conard, 1996] T. Conard, A.-C. Rousseau, L. M. Yu, J. Ghijsen, R. Sporken, R. Caudano, and R. L. Johnson, *Surf. Sci.* **359** (1996) 82.
- [Cox, 1995] P. A. Cox, *Transition Metal Oxides*, Clarendon Press, Oxford (1995).

- [Crewe, 1971] A. V. Crewe, M. Isaacson and D. Johnson, *Rev. Sci. Inst.* **42** (1971) 411.
- [Cyrot-Lackmann, 1967] F. Cyrot-Lackmann, *Adv. Phys.* **16** (1967) 393.
- [Dainty, 1974] J. C. Dainty and R. Shaw, *Image Science*, Academic Press, London, Uk (1974).
- [Dehm, 1995] G. Dehm, M. Rühle, G. Ding, and R. Raj, *Phil. Mag. B* **71** (1995), 1111.
- [Dehm, 1996] G. Dehm, F. Ernst, J. Mayer, G. Möbus, H. Mülleians, F. Phillipp, C. Scheu, and M. Rühle, *Z. für Metallkunde* **87** (1996), 898.
- [Dehm, 1997] G. Dehm, C. Scheu, G. Möbus, R. Brydson, and M. Rühle, *Ultramicroscopy* **67** (1997) 207.
- [Denk, 1995] I. Denk, W. Münch, and J. Maier, *J. Am. Ceram. Soc.* **78**, 3265 (1995).
- [Doben, 1988] P. Doben, M. Onellion, and Y. Kime, *Scann. Tunn. Microsc.* **2**, 177 (1988).
- [Dorneich, 1998] A. D. Dorneich, R. H. French, H. Mülleians, S. Loughin, and M. Rühle, *J. Microsc.* **191** (1998) 286.
- [Ducastelle, 1970] F. Ducastelle and F. Cyrot-Lackmann, *J. Phys. and Chem. Sol.* **31** (1970) 1295.
- [Durham, 1982] P. J. Durham, J. B. Pendry and C. H. Hodges, *Comput. Phys. Commun.* **25** (1982) 193.
- [Duscher, 1998] G. Duscher, N. D. Browning and S. J. Pennycook, *phys. stat sol.* **166** (1998) 327.
- [Egerton, 1996] R. F. Egerton, *Electron Energy-Loss Spectroscopy in the Electron Microscope* (2nd ed.), Plenum Press, New York and London (1996).
- [Elsässer, 1990] C. Elsaßer, *Untersuchung der Kohäsions-, Diffusions- und Schwingungseigenschaften von Wasserstoff in Übergangsmetallen mit einer ab-initio Pseudopotentialmethode*, PhD thesis, Universität Stuttgart, Stuttgart (1990)
- [Elsässer, 2001] C. Elsaßer and S. Köstlmeier, *Ultramicroscopy* **86** (2001) 325.

- [Elssner, 1990] G. Elssner and G. Petzow, *Metal/Ceramic Joining*, ISIJ International **30**, 1011 (1990).
- [Ernst, 1995] F. Ernst, *Materials Science and Engineering* **R 14** (1995) 97.
- [ESTools] The Electronic Structure Tools (EST) consists of a number of programs for the quantitative analysis of optical, VUV, and EELS spectra. It has been developed under Grams, a PC based spectroscopy environment. EST is available from *Deconvolution and Entropy Consulting*, 755 Snyder Hill Road, Ithaca NY 14850, or <http://www.deconvolution.com>.
- [Evans, 1996] J. Evans, B. E. Hayden and G. Lu, *Surf. Sci.* **360** (1996) 61.
- [Finnis, 1996] M. W. Finnis, *J. Phys. Condens. Matter* **8**(1996) 5811.
- [Fischmeister, 1993] H. F. Fischmeister, G. Elssner, B. Gibbesch, K.-H. Kadow, F. Kawa, D. Korn, and W. Mader, *Rev. Sci. Instrum.* **64**, 234 (1993).
- [Fitzsimmons, 1994] M. R. Fitzsimmons, G. S. Smith, R. Pynn, M. A. Nastasi, and E. Burkel, *Physica B* **198** (1994) 169.
- [French, 2000] R. H. French, *J. Am. Ceram. Soc.* **83** (2000) 2127.
- [Frye, 2001] A. Frye, R. H. French, and D. A. Bonnell, *unpublished* (2001).
- [Fu, 2001] Q. Fu and T. Wagner, *submitted to Surf. Sci.* (2001).
- [Fujikawa, 1983] T. Fujikawa, *Journal of the Physical Society of Japan* **52** (1983) 4001.
- [Fujishita, 1979] H. Fujishita, Y. Shiozaki, and E. Sawaguchi, *J. Phys. Soc. Japan* **46**, 581 (1979).
- [Gao, 1988] Y. Gao, P. Shewmon and S. A. Dregia, *Scripta Metallurgica* **22** (1988) 1521.
- [Garvie, 1998] L. A. J. Garvie and P. R. Buseck, *Nature* **396** (1998) 667.
- [Gaudette, 1997] F. Gaudette, S. Suresh, A. G. Evans, G. Dehm, and M. Rühle, *Acta mater.* **45** (1997) 3503.
- [Gautsch, 1995] O. Gautsch, *Materials Science and Engineering* **A194** (1995) L27.
- [Glauber, 1959] R. J. Glauber, *Interscience* (1959) 315.

- [Goniakowski, 1998] J. Goniakowski, *Phys. Rev. B* **57** (1998) 1935.
- [Goniakowski, 1999a] J. Goniakowski, *Phys. Rev. B* **59** (1999) 11047.
- [Goniakowski, 1999b] J. Goniakowski, *Phys. Rev. B* **60** (1999) 16120.
- [Gossmann, 1991] H. Gossmann and G. Fisanick, *Surf. Sci. Lett.* **244**, L117 (1991).
- [Goyhenex, 1996] C. Goyhenex, M. Meunier and C. R. Henry, *Surf. Sci.* **350** (1996) 103.
- [Graham, 1995] M. J. Graham and R. J. Hussey, *Oxidation of Metals* **44** (1995) 339.
- [de Groot, 1989] F. M. F. de Groot, M. Grioni, J. C. Fuggle, J. A. Ghijsen, G. Sawatzky, and H. Petersen, *Phys. Rev. B* **40**, 5715 (1989).
- [de Groot, 1993] F. M. F. de Groot, J. Faber, J. J. J. Michiels, M. T. Czyzyk, M. Abbate, and J. C. Fuggle *Phys. Rev. B* **48** (1993) 2074.
- [de Groot, 1994] F. M. F. de Groot, Z. W. Hu, M. F. Lopez, G. Kaindl, F. Guillot, and M. Tronc, *J. Chem. Phys.* **41** (1994) 12366.
- [Gu, 1999a] H. Gu, *Ultramicroscopy* **76** (1999) 159.
- [Gu, 1999b] H. Gu, *Ultramicroscopy* **76** (1999) 173.
- [Gutekunst, 1997a] G. Gutekunst, J. Mayer and M. Rühle, *Phil. Mag. A* **75** (1997) 1329.
- [Gutekunst, 1997b] G. Gutekunst, J. Mayer and M. Rühle, *Phil. Mag. A* **75** (1997) 1357.
- [Gyorffy, 1973] B. L. Gyorffy and M. J. Scott, in: *Band Structure Spectroscopy of Metals and Alloys*, D. J. Fabian and L. M. Watson (eds.), Academic Press, London, UK, (1973) 385.
- [Hamann, 1979] D. R. Hamann, M. Schlüter and C. Chiang, *Phys. Rev. Lett.* **43** (1979) 1494.
- [Hébert, 2000] C. Hébert, M. Kostner and P. Schattschneider, *Proc. 12th EU-REM2000, Brno, Czech Republic*, (2000) 1333.
- [Heidemann, 1973] A. Heidemann and H. Wettengel, *Z. Physik* **258**, 429 (1973).
- [Heine, 1965] V. Heine, *Phys. Rev.* **138A** (1965) 1689.
- [Henrich, 1978] V. E. Henrich, G. Dresselhaus and H. J. Zeiger, *Phys. Rev. B* **17** (1978) 4908.

- [Henry, 1991] C. R. Henry, C. Chapon, C. Duriez, and S. Giorgio, *Surf. Sci.* **253** (1991) 177.
- [Henry, 1998] C. R. Henry, *Surf. Sci. Rep.* **31** (1998) 231.
- [Heumann, 1957] T. Heumann and M. Kniepmeyer, *Z. Anorg. Allgem. Chem.* **290**, 191 (1957).
- [Hill, 1989] D. M. Hill, H. M. Meyer III and J. H. Weaver, *J. Appl. Phys.* **65** (1989) 4943.
- [Hoel, 1990] R. H. Hoel, J. M. Penisson and H. U. Habermeier, *Colloq. Phys.* **51** (1990) C1.
- [Hohenberg, 1964] P. Hohenberg and W. Kohn, *Phys. Rev.* **136** (1964) B864.
- [Hönlein, 1999] W. Hönlein, *Phys. Blätter* **55** (1999) 51.
- [Howe, 1997] J. M. Howe, *Interfaces in Materials*, John Wiley & Sons, Inc., New York, Chichester, Weinheim, Brisbane, Singapore, Toronto (1997).
- [Hull, 1984] D. Hull and D. J. Bacon, *Introduction to Dislocations*, Pergamon Press, 3rd ed., London/Oxford (1984).
- [Hunt, 2001] J. A. Hunt, F. E. Dickerson, A. A. Abbott, G. Szantai, and P. E. Mooney, *Proceedings of the Microscopy Society of America 2001 Annual Meeting* **7** (2001) .
- [Hussain, 1989] A. A. Hussain, *J. Phys.: Condens. Matter* **1** (1989) 9833.
- [Imhoff, 1999] D. Imhoff, S. Laurent, C. Colliex, and M. Backhaus-Ricoult, *Eur. Phys. J. AP* **5** (1999) 9.
- [Inkson, 1999] B. Inkson, R. Spolenak and T. Wagner, in: C. J. Kiely (ed.), *Electron Microscopy Analysing* Institute of Physics Conference Series **161** (1999) 335.
- [Isaacson, 1975] M. Isaacson and D. Johnson, *Ultramicroscopy* **1** (1975) 33.
- [Jackson, 1998] T. J. Jackson, B. A. Glowacki and J. E. Evetts, *Physica C* **296** (1998) 215.
- [James, 1999] E. M. James and N. D. Browning, *Ultramicroscopy* **78** (1999) 125.
- [Jacobs, 1985] H. Jacobs, W. Mokwa, D. Kohl, and G. Heiland, *Surf. Sci.* **160** (1985) 217.

- [Jiang, 1996] Q. Jiang and J. Zegenhagen, *Surf. Sci. Lett.* **367** (1996) L42.
- [Jeol] Jeol JEM 2000FX manual.
- [Jones, 1989] R. O. Jones and O. Gunnarson, *Reviews of Modern Physics* **61** (1989) 689.
- [Kawasaki, 1994] M. Kawasaki, K. Takahashi, T. Maeda, R. Tsuchiya, M. Shinohara, O. Ishiyama, T. Yonezawa, M. Yoshimoto, and H. Koinuma, *Science* **266** (1994) 1540.
- [Kennedy, 1995] R. J. Kennedy, *IEEE Transactions on Magnetics* **31** (1995) 3829.
- [Kido, 2000] Y. Kido, T. Nishimura and H. Namba, *Nuclear Instruments and Methods in Physics Research B* **161-163** (2000) 371.
- [Kienzle, 1999] O. Kienzle, *Atomistische Struktur und chemische Zusammensetzung innerer Grenzflächen in Strontiumtitanat*, PhD thesis, Universität Stuttgart, Stuttgart (1999).
- [Kiselev, 1989] N. I. Kiselev, Yu. I. Man'kov and V. G. Pyn'ko, *Sov. Phys. Solid State* **31** (1989) 685.
- [Köstlmeier, 2001] S. Köstlmeier, *Ultramicroscopy* **86** (2001) 319.
- [Kohn, 1954] W. Kohn and N. Rostocker, *Phys. Rev.* **94**, (1954) 1111.
- [Kohn, 1965] W. Kohn and L. J. Sham, *Physical Review* **140** (1965) A1133.
- [Kohn, 1983] W. Kohn and P. Vashishta, in: *Theory of the inhomogeneous Electron gas* S. Lundquist and N. D. March (eds.), Plenum Press, New York (1983).
- [Korringa, 1947] J. Korringa, *Physica* **13** (1947) 392.
- [Kramers, 1927] H. A. Kramers, *Atti Congr. Int. Fis. Como* **2** (1927) 545.
- [Krivanek, 1987] O. L. Krivanek, C. C. Ahn and R. B. Keeney, *Ultramicroscopy* **22** (1987) 103.
- [Kronig, 1926] R. Kronig, *J. Opt. Soc. Am.* **12** (1926) 547.
- [Landoldt, 1981] Landoldt-Börnstein, *Numerical Data and Functional Relationships in Science and Technology*, Vol. 16, Springer, K.-H. Hellwege (ed.), Berlin (1981).
- [Leapman, 1980] R. D. Leapman and R. D. Grunes, *Phys. Rev. Letters* **45**, 397 (1980).

- [Leapman, 1982] R. D. Leapman, R. D. Grunes, L. A. Fejes, and P. L. Silcox, *Phys. Rev. B* **26**, 614 (1982).
- [Leapman, 1991] R. D. Leapman and J. A. Hunt, *Microsc. Microanal. Microstruct.* **2** (1991) 231.
- [Levy, 1979] M. Levy, *Proc. of the National Academy of Sciences of the USA* **76** (1979) 6062.
- [Levy, 1982] M. Levy, *Phys. Rev. A* **26** (1982) 1200.
- [Liang, 1995] Y. Liang and D. Bonnell, *J. Am. Ceram. Soc.* **78** (1995) 2633.
- [Loane, 1988] R. F. Loane, E. J. Kirkland, and J. Silcox, *Acta Cryst. A* **44** (1988) 912.
- [Louie, 1975] S. G. Louie, J. R. Chelikowski, and M. L. Cohen, *Phys. Rev. Lett.* **34** (1975) 155.
- [Lytle, 1964] F. W. Lytle, *J. Appl. Phys.* **35**, 2212 (1964).
- [Manoubi, 1990] T. Manoubi, M. Tencé, M. G. Walls, and C. Colliex, *Microsc. Microanal. Microstruct.* **1** (1990) 23.
- [Markov, 1976] I. Markov and R. Kaischew, *Thin Solid Films* **32**, 163 (1976).
- [Markov, 1976] I. Markov and R. Kaischew, *Krist. Tech.* **11**, 685 (1976).
- [Maruyama, 1995] H. Maruyama, H. Qiu, H. Nakai, and M. Hashimoto, *J. Vac. Sci. Technol. A* **13** (1995) 2157.
- [Massalski, 1990] T. B. Massalski, *Binary Alloy Phase Diagrams* 2nd ed., Vol. 1-3, ASM International (1990).
- [Matsumoto, 1992] T. Matsumoto, H. Tanaka, T. Kwai, and S. Kwai, *Surf. Sci. Lett.* **278** (1992) L153.
- [Mattheiss, 1972] L. F. Mattheis, *Phys. Rev. B* **6** (1972) 4718.
- [Matveev, 1999] A. V. Matveev, K. M. Neyman, I. V. Yudanov, and N. Rösch, *Surf. Sci.* **426** (1999) 123.
- [Meijering, 1971] J. L. Meijering, Internal Oxidation in Alloys, in: *Advances in Materials Research*, H. Herman (ed.), John Wiley&Sons, New York (1971).
- [Meixner, 1995] H. Meixner, J. Gerblinger, U. Lampe, and M. Fleischer, *Sensors and Actuators B* **23** (1995) 119.

- [van der Merwe, 1993] J. van der Merwe, *Interf. Sci.* **1**, 77 (1993).
- [Meyer, 1998] B. Meyer, *Entwicklung eines neuen ab-initio mixed-basis-Pseudopotential-Programmes und Untersuchung atomarer Fehlstellen in Molybdän und intermetallischen Verbindungen*, PhD thesis, Universität Stuttgart, Stuttgart (1998).
- [Mizuno, 1998] M. Mizuno, I. Tanaka, and H. Adachi, *Acta mater.* **46** (1998) 1637.
- [Mo, 1999] S.-D. Mo, W. Y. Ching, M. F. Chisholm, and G. Duscher, *Phys. Rev. B* **60** (1990) 2416.
- [Moltaji, 2000] H. O. Moltaji, J. P. Buban, J. A. Zaborac, and N. D. Browning, *Micron* **31** (2000) 381.
- [Moodie, 1977] A. F. Moodie and C. E. Warble, *Phil. Mag.* **35** (1977) 201.
- [Moos, 1997] R. Moos and K. H. Härdtl, *J. Am. Ceram. Soc.* **80**, 2549 (1997).
- [Moreno, 1992] J. Moreno and J. M. Soler, *Phys. Rev. B* **45** (1992) 13891.
- [Muller, 1998] D. A. Muller, D. A. Shashkov, R. Benedek, L. H. Yang, and J. Silcox, *Phys. Rev. Lett.* **80** (1998) 4741.
- [Muller, 1999] D. A. Muller, *Ultramicroscopy* **78** (1999) 163.
- [Muller, 1999] D. A. Muller and M. J. Mills, *Materials Science and Engineering A* **260** (1999) 12.
- [Müllejans, 1994] H. Müllejans and J. Bruley, *Ultramicroscopy* **53** (1994) 351.
- [Müllejans, 1995] H. Müllejans and J. Bruley, *J. of Microscopy* **180** (1995) 12.
- [Müllejans, 1996] H. Müllejans and R. H. French, *J. Phys. D* **29** (1996) 1751.
- [Nakai, 1995] H. Nakai, H. Qui, M. Adamik, G. Sáfran, P. B. Barna, and M. Hashimoto, *Thin Solid Films* **263** (1995) 159.
- [Nassau, 1988] K. Nassau and A. E. Miller, *J. Cryst. Growth* **91**, 373 (1988).
- [Nufer, 2001a] S. Nufer, T. Gemming, C. Elsässer, S. Köstlmeier, and M. Rühle, *Ultramicroscopy* **86** (2001) 339.
- [Nufer, 2001b] S. Nufer, A. G. Marinopoulos, T. Gemming, C. Elsässer, W. Kurtz, S. Köstlmeier, and M. Rühle, *Phys. Rev. Lett.* **86** (2001) 5066.

- [Ochs, 2000] T. Ochs, *Theoretische Untersuchungen der atomaren und elektronischen Struktur an Korngrenzen in kubisch raumzentrierten Übergangsmetallen und an Metall/Keramik-Grenzflächen*, PhD thesis, Universität Stuttgart, Stuttgart, Germany (2000).
- [Ochs, 2001] T. Ochs, S. Köstlmeier, and C. Elässer *Integr. Ferroelectr.* **32** (2001) 959.
- [Ohring, 1992] M. Ohring, *The Materials Science of Thin Films*, Academic Press, Boston (1992).
- [Ogasawara, 2001] K. Ogasawara, T. Iwata, Y. Koyama, T. Ishii, I. Tanaka, and H. Adachi, *Phys. Rev. B* **64** (2001) 115413.
- [Ogawa, 1995] S. Ogawa and S. Ichikawa, *Phys. Rev. B* **51** (1995) 17231.
- [Pacchioni, 1996] G. Pacchioni and N. Rösch, *J. Chem. Phys.* **104** (1996) 7329.
- [Palik, 1991] E. D. Palik (ed.), *Handbook of optical constants of solids II*, Academic Press, Inc., San Diego, CA., USA (1991).
- [Pantelides, 1975] S. T. Pantelidis, *Phys. Rev. B* **11** (1975) 2391.
- [Pantelidis, 1985] S. T. Pantelidis, *Phys. Rev. B* **43** (1985) 8412.
- [Pennycook, 1988] S. J. Pennycook and L. A. Boatner, *Nature* **336** (1988) 565.
- [Phillipp, 1994] F. Phillipp, R. Höschen, G. Möbus, M. Osaki, and M. Rühle, *Ultramicroscopy* **56** (1994) 1.
- [Platzman, 1973] P. M. Platzmann and P. A. Wolff, in: *Solid State Physics. Advances in Research and Application*, H. Ehrenreich, F. Seitz and D. Turnbull (eds.), Academic Press, Orlando, USA (1973)
- [Polli, 1998] A. D. Polli and T. Wagner, unpublished results.
- [Polli, 1999] A. D. Polli, T. Wagner and M. Rühle, *Surf. Sci.* **429** (1999) 237.
- [Polli, 2000] A. D. Polli, T. Wagner, T. Gemming, and M. Rühle, *Surf. Sci.* **448** (2000) 279.
- [Qiu, 1994] H. Qiu, A. Kosuge, H. Maruyama, M. Adamik, G. Safran, P. B. Barna, and M. Hashimoto, *Thin Solid Films* **241** (1994) 9.
- [Raatz, 1989] G. Raatz and J. Woltersdorf, *phys. stat. sol. A* **113** (1989) 131

- [Reed, 1971] T. B. Reed, *Free Energy of Formation of Eumery Compounds, An Atlas of Charts for High Temperature Calculations*, The MIT Press Cambridge, Massachusetts, and London, England (1971).
- [Rehr, 1990] J. J. Rehr and R. C. Albers, *Phys. Rev. B* **41** (1990) 8139.
- [Rehr, 2000] J. J. Rehr and R. C. Albers, *Rev. Mod. Phys.* **72** (2000) 621.
- [Reimer, 1994] L. Reimer (ed.), *Energy-Filtering Transmission Electron Microscopy*, Springer Series in Optical Science, Springer-Verlag Berlin Heidelberg New York (1994).
- [Reimer, 1997] L. Reimer, *Transmission Electron Microscopy* (4th ed.), Springer Series in Optical Science, P. W. Hawkes (ed.), Springer-Verlag Berlin Heidelberg New York (1997).
- [Renaud, 1999] G. Renaud, A. Barbier and O. Robach, *Phys. Rev. B* **60** (1999) 5872.
- [Reniers, 1996] F. Reniers, M. P. Delplancke, A. Asskali, V. Rooryck, and O. Van Sinay, *Appl. Surf. Sci.* **92** (1996) 35.
- [Rez, 1991] P. Rez, X. Weng, and H. Ma, *Microsc. Microanal. Microstruct.* **2** (1991) 143.
- [Richter, 2000] G. Richter, *Charakterisierung der Keimbildung und des Wachstums dünner Pd-Schichten auf der SrTiO₃(001)-Oberfläche*, PhD thesis, Universität Stuttgart, Stuttgart, Germany (2000).
- [Romanov, 1998] A. E. Romanov, T. Wagner, and M. Rühle, *Scripta Materialia* **38**, 869 (1998).
- [Rösch, 1997] N. Rösch and G. Pacchioni, in: *Chemisorption and Reactivity on Supported Clusters and Thin Films*, edited by R. M. Lambert and G. Pacchioni, Kluwer–Academic, The Netherlands (1997) 353.
- [Rose, 1974] H. Rose, *Optik* **39** (1974) 416.
- [Rose, 1977] H. Rose, *Ultramicroscopy* **2** (1977) 251.
- [Rose, 1988] H. Rose, *Bildentstehung im Elektronenmikroskop*, Vorlesungsskript WS 1989/90, Technische Universität Darmstadt (1989).
- [Rose, 2000] H. Rose, *Bildentstehung im TEM*, Vorlesung am Max-Planck-Institut für Metallforschung Stuttgart, Stuttgart (2000).
- [Rühle, 1989] M. Rühle and A. G. Evans, *Mater. Sci. Eng. A* **107** (1989) 187.

- [Rühle, 1990] M. Rühle, A. G. Evans, M. F. Ashby, and J. P. Hirth (eds.), *Metal-Ceramic Interfaces*, Acta-Scripta Metallurgica Proceedings Series **4**, Pergamon Press, Oxford (1990).
- [Ryen, 1999] L. Ryen, X. Wang, U. Helmersson, and E. Olsson, *J. Appl. Phys.* **85** (1999) 2828.
- [Samsonov, 1973] G. V. Samsonov (ed.), *The Oxide Handbook*, IFI/Plenum, New York, Washington, London (1973).
- [Sato, 1962] H. Sato, R. S. Toth and R. W. Astrue, *J. Appl. Phys.* **33** (1962) 1113.
- [Sawatzky, 1991] G. A. Sawatzky, *Microsc. Microanal. Microstruct.* **2** (1991) 153.
- [Scheu, 1995] C. Scheu, G. Dehm, H. Müllejans, R. Brydson, and M. Rühle, *Microsc. Microanal. Microstruct.* **6** (1995) 19.
- [Scheu, 1996a] C. Scheu, G. Dehm, H. Müllejans, and M. Rühle, *Mat. Sci. Forum* **207-209** (1996) 181.
- [Scheu, 1996b] C. Scheu, PhD thesis, Universität Stuttgart, Germany, (1996).
- [Scheu, 1998] C. Scheu, G. Dehm, and M. Rühle, *Phil. Mag. A* **78** (1998) 439.
- [Scheu, 2000] C. Scheu, W. Stein and M. Rühle, *phys. stat. sol.* **222** (2000) 199.
- [Schweinfest, 1998] R. Schweinfest, PhD thesis, Universität Stuttgart (1998).
- [Seah, 1979] M. P. Seah and W. A. Dench, *Surf. Sci. Anal.* **1** (1979) 2.
- [Setter, 2000] N. Setter and R. Waser, *Acta mater.* **48** (2000) 151.
- [Shashkov, 1999] D. A. Shashkov, D. A. Muller and D. N. Seidman, *Acta mater.* **47** (1999) 3953.
- [Shiles, 1980] E. Shiles, T. Sasaki, M. Inokuti, D. Y. Smith, *Phys. Rev. B* **22** (1980) 1612.
- [Smith, 1985] D. Y. Smith, in: *Handbook of Optical Constants of Solids*, E. D. Palik (ed.), Academic Press, New York, USA, (1985) 35.
- [Stanzick, 1998] H. N. Stanzick, Diplomarbeit, Carl von Ossietzky Universität Oldenburg (1998).
- [Stoneham, 1983] A. M. Stoneham, *Appl. Surf. Sci.* **14** (1983) 249.

- [Strecker, 1993] A. Strecker, U. Salzberger and J. Mayer, *Prakt. Metallogr.* **30** (1993) 482.
- [Strecker, 2001a] A. Strecker, U. Bäder, U. Salzberger, M. Sycha, and M. Rühle, Dreiländertagung für Elektronenmikroskopie, Innsbruck, Austria, S:D2.P, 144 (2001).
- [Strecker, 2001b] A. Strecker, U. Bäder, K. van Benthem, G. Richter, S. Krämer, U. Salzberger, M. Sycha, A. Zern, and M. Rühle, Dreiländertagung für Elektronenmikroskopie, Innsbruck, Austria, S:D2.P, 144 (2001).
- [Šturm, 2001] Š. Šturm, unpublished results (2001).
- [Sutton, 1995] A. P. Sutton and R. W. Balluffi, *Interfaces in Crystalline Materials*, Clarendon Press, Oxford 1995).
- [Tanaka, 1994] H. Tanaka, T. Matsumoto, T. Kwai, and S. Kwai, *Surf. Sci.* **318** (1994) 29.
- [Tanaka, 1996] I. Tanaka and H. Adachi, *Phys. Rev. B* **54** (1996) 4604.
- [Tanaka, 1997] I. Tanaka, T. Nakajima, J. Kawai, H. Adachi, H. Gu, and M. Rühle, *Phil. Mag. Lett.* **75** (1997) 21..
- [Tanaka, 1998] I. Tanaka, M. Mizuno, S. Nakajyo, and H. Adachi, *Acta mater.* **46** (1998) 6511.
- [Tchernychova, 2001] E. Tchernychova, *unpublished results* (2001).
- [Thomas, 1993] J. Thomas, J. Bruley and H. Müllejans, *Optik* Supplement 39 (61), 20.6; Poster presented on the Dreiländertagung Elektronenmikroskopie, Zürich, Schweiz (1993).
- [Titchmarsh, 1989] J. M. Titchmarsh, *Ultramicroscopy* **28** (1989) 347.
- [Trampert, 1992] A. Trampert, F. Ernst, C. P. Flynn, H. F. Fischmeister, and M. Rühle, *Acta metall. mater.* **40** (1992) 227.
- [Tsao, 1993] J. Y. Tsao, *Materials Fundamentals of Molecular Beam Epitaxy* Academic Press, San Diego (1993).
- [Tsukimoto, 2001] S. Tsukimoto and C. Scheu, *personal communications* (2001).
- [Uchino, 1994] K. Uchino, in: M. Swain, R. W. Cahn, P. Haasen, and E. J. Kramer (eds.), *Ferroelectric Ceramics*, VCH, Weinheim (1994) 635.

- [Vanderbilt, 1985] D. Vanderbilt, *Phys. Rev. B* **32** (1985) 8412.
- [Vvedensky, 1986] D. D. Vvedensky, D. K. Saldin and J. B. Pendry, *Comput. Phys. Commun* **40** (1986) 421.
- [Xu, 1997] C. Xu, X. Lai, G. W. Zajac, and D. W. Goodmann, *Phys. Rev. B* **56** (1997) 13464.
- [Wagner, 2001a] T. Wagner, A. Polli, G. Richter, and H. Stanzick, *Z. für Metallkunde* **3** (2001) 507
- [Wagner, 2001b] T. Wagner, G. Richter and M. Rühle, *J. Appl. Phys.* **89** (2001) 2606.
- [Waser, 1990] R. Waser, T. Baiatu, and K.-H. Härtl, *J. Am. Ceram. Soc.* **73**, 1645 (1990), **73**, 1654 (1990), **73**, 1663 (1990).
- [Waser, 1991] R. Waser, *J. Am. Ceram. Soc.* **74**, 1934 (1991).
- [Winterbottom, 1967] W. L. Winterbottom, *Acta Metall.* **15**, 303 (1967).
- [Wallis, 1997] D. J. Wallis and N. D. Browning, *J. Am. Ceram. Soc.* **80** (1997) 781.
- [Wood, 1958] E. A. Wood and V. Compton, *Acta Cryst.* **11**, 429 (1958).
- [Wulff, 1901] G. Wulff, *Z. Kristallogr.* **34**, 449 (1901).
- [Yoshimoto, 1994] M. Yoshimoto, T. Maeda, K. Shimonzo, H. Koinuma, M. Shino-hara, O. Ishiyama, and F. Ohtani, *Appl. Phys. Lett.* **65** (1994) 3197.
- [Xu, 1990] Y.-N. Xu, W. Y. Ching and R. H. French, *Ferroelectrics* **111** (1990) 23.
- [Zhang, 1989] X.-G. Zhang and A. Gonis, *Phys. Rev. Lett.* **62** (1989) 1161.

Epilogue

This thesis was performed at the Max-Planck-Institut für Metallforschung Stuttgart, Stuttgart, Germany, in the time between January 1999 and February 2002.

One of the most difficult parts in writing a PhD thesis is building up the list of acknowledgements. Should I first mention all the people who helped me solving small and bigger problems during all-day working times; or is the financial supporter the one with the highest priority? And what about the supervisor, the advisors, and last but not least, my partner and friends? Therefore, I have decided to choose the conventional style for expressing gratitudes for all the help I got during preparing this work. Therefore:

- I greatly acknowledge Prof. Dr. Dr. h.c. M. Rühle who gave me the opportunity to prepare this study in his laboratory. I am thankful for his constant support and for his interest in forthcoming of this project.
- I thank Prof. Dr. F. Aldinger for taking over the *Mitbericht*.
- Special thanks are due to my advisors C. Scheu, W. Sigle and C. Elsässer for their invaluable help and their support during the past three years.
- T. Ochs, G. Richter and T. Wagner are acknowledged for all the scientific discussions regarding metal/SrTiO₃ interfaces.
- I acknowledge R. H. French for introducing me into the field of VEELS, and for his co-operation within the VEELS project.
- S. Šturm and M. Čeh are acknowledged for fruitful discussions and for giving me the opportunity to perform first Z-contrast studies on the Pd/SrTiO₃ interface in Ljubljana, Slovenia.
- Thanks to the TEM specimen preparation team, namely U. Salzberger, A. Strecker and M. Sycha for their support and for preparing excellent TEM specimens.
- I greatly appreciate all colleagues of the Stuttgart *VG group*, especially J. Thomas, for all their help during the STEM experiments and the excellent working conditions.
- Thanks are also due to all members of the group of Prof. Rühle, especially my former room-mate S. Nufer, for all the scientific and private discussions.

- I acknowledge B. Brown French and R. H. French for their friendship and for carefully reading the manuscript while correcting all the german-tongue mistakes in the english language.
- Last but not least I especially want to thank my fiancé Pia Göttert for strongly supporting me, and for spending so many lonely hours at home waiting for me.

If I forgot anybody in this list, it was done by mistake rather than intention.

Stuttgart, February 2002

Curriculum vitae

Name : Klaus van Benthem
Date of birth : July 2nd, 1974
Place of birth : Münster
Nationality : german
Marital status : single

1980 - 1984 : Paul-Gerhardt Grundschule Hiltrup, Münster

1984 - 1993 : Immanuel-Kant-Gymnasium Hiltrup, Münster

June 1993 : Allgemeine Hochschulreife (Abitur)

1993 - 1998 : Study of Physics at the Westfälische-Wilhelms Universität Münster

1997 - 1998 : Diplomarbeit in the group of Prof. Dr. H. Kohl
title of the thesis: *"Charakterisierung des Inversionsgrades
von Mg-Al-Spinellen anhand der Kantennahen Feinstrukturen
in Elektronen-Energieverlustspektren"*
*"Characterisation of the Degree of Inversion of Mg-Al-Spinels
using the Electron Energy-Loss Near-Edge Structure"*

November 1998 : Diploma (Dipl.-Phys.)

1999 - 2000 : Study of Materials Science at the Universität Stuttgart

since January 1999 : PhD student at the Max-Planck-Institut für Metallforschung Stuttgart
in Stuttgart in the group of Prof. Dr. Dr. h.c. M. Rühle

